Quasi-periodic invariant tori and retrieval of Near-Earth Asteroids using low-energy trajectories

Daniel Paricio Ezquerra

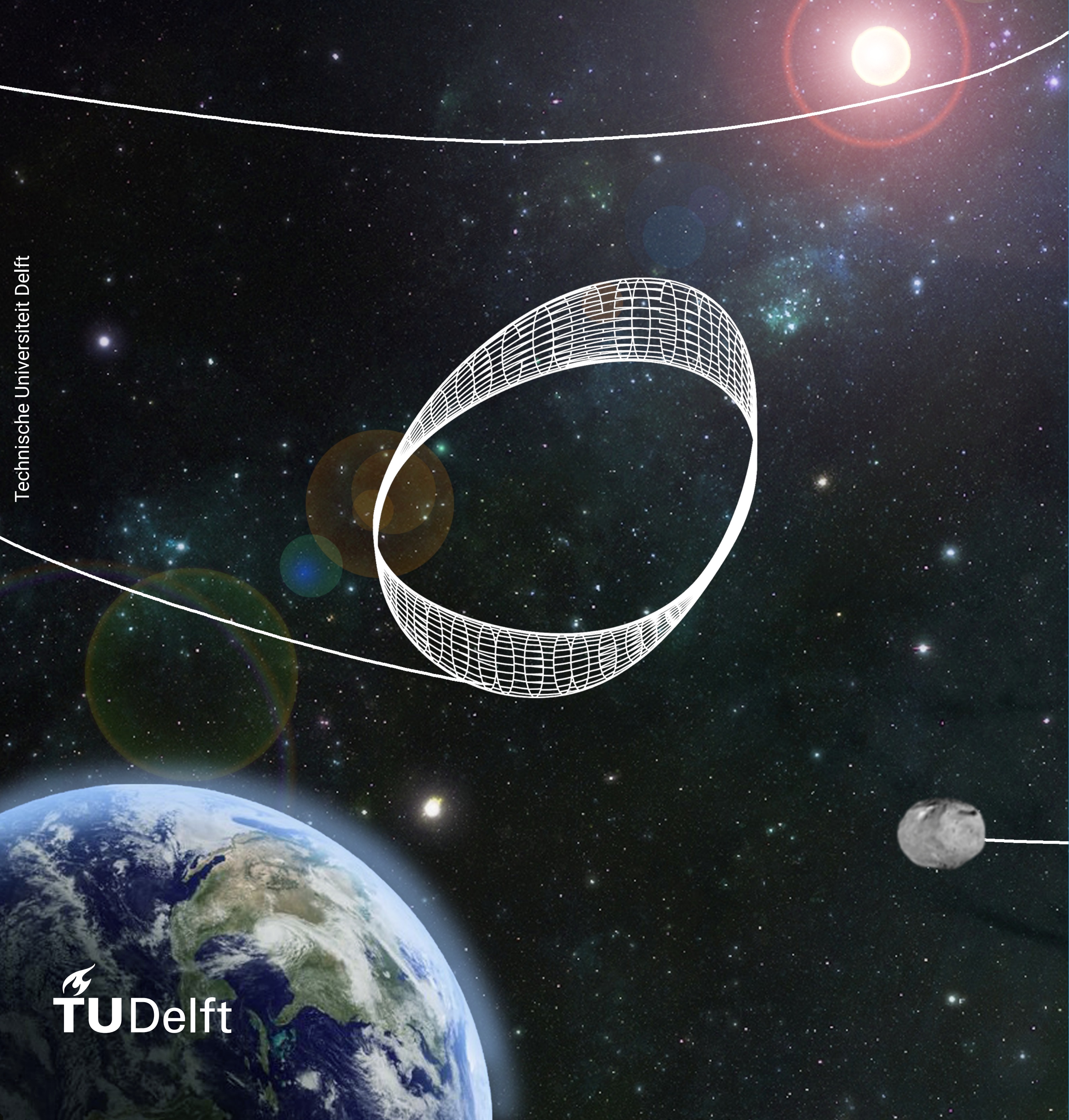

Technische Universiteit Delft

TU Delft

Quasi-periodic invariant tori and retrieval of Near-Earth Asteroids using low-energy trajectories

by

Daniel Paricio Ezquerra

to obtain the degree of Master of Science
at Delft University of Technology,
to be defended publicly on Wednesday August 25, 2021 at 14:00 PM.

Student number:	5028892	
Project duration:	October 15, 2020 – July 15, 2021	
Thesis committee:	Ir. R. Noomen,	TU Delft, supervisor
	Dr. ir. E.J.O. Schrama,	TU Delft
	Dr. S. Speretta,	TU Delft

This thesis is confidential and cannot be made public until December 31, 2021.

An electronic version of this thesis is available at `http://repository.tudelft.nl/`.
Cover pictures credit: VADIM SADOVSKI/SHUTTERSTOCK (Earth),
NASA/JPL-Caltech/UCAL/MPS/DLR/IDA (asteroid), wallpapersafari.com (background)

TU Delft

Preface

After two years in which I could learn more about my passion, have an enriching work experience, and meet incredible people, this master thesis represents the last part of my Master's in Space Flight at TU Delft. In a year where we all had to keep our distance from the others, stay indoors and switch completely online, it was a good moment to look up into the sky and reflect on the vast opportunities ahead of us, but also our responsibilities and limitations.
I m very glad of having had the opportunity to develop this work in a field I am personally interested in, and that I wanted to discover and explore more in-depth. I truly appreciate having the chance to work in something I like, without any limitations or constraints.

Special thanks to my tutor Ron Noomen for his continuous support through our weekly meetings, guidance, and positivity, which is always needed. I would also like to thank my mom and Xus for giving me strength and tenderness when it was most needed in these difficult times. Mil gracias.

I hope you find this work helpful or inspiring in any way.

Per aspera ***ad astra***

Daniel Paricio Ezquerra
Delft, July 2021

Contents

Acronyms

AB Adams-Bashfort-Moulton

AU Astronomical Unit

BS Bulirsch-Stoer

BVP Two-Point Boundary Value Problem

CR3BP Circular Restricted Three-Body Problem

DART Double Asteroid Redirection Test

DFT Discrete Fourier Transfer

ER3BP Elliptic Restricted Three-Body Problem

ERO Easy Retrievable Object

FLOSS Free/Libre and Open Source Software

KAM Kolmogorov–Arnold–Moser

MHACO Hypervolume-based ACO

MOEA/D Multi-objective EA with Decomposition

MOO Multi-Objective Optimization

NEA Near-Earth Asteroid

NEO Near-Earth Object

NES Natural Earth Satellite

NHATS Near-Earth Object Human Space Flight Target Study

NSGA2 Non-dominated Sorting GA

NSPSO Non-dominated Sorting PSO

PAGMO Parallel Global Multiobjective Optimization

PCR3BP Planar Circular Restricted 3-Body Problem

PDE Partial Differential Equation

PGM Platinum Group Metals

RK Runge-Kutta

SEA Small-Earth Approachers

TOF Time Of Flight

TUDAT TU Delft Astrodynamic Toolbox

List of Symbols

Latin Symbols

a	Semi-major axis	$[m]$
a_i	Asteroid i	
C	Jacobi constant	
C	Conservation chance	
CR	Cross over rate	
D	Discrete Fourier Matrix	
e	Eccentricity	
F	Jacobian of the flow	
F	Scale factor	
F	Objective function	
$\mathbf{F}$	Accumulated circle flow	
F_t	Quasi-periodic family	
$\mathbf{f}_0$	CR3BP flow equation	
G	Universal Gravitational constant	$[m^3 kg^{-1} s^{-2}]$
H	Asteroid Absolute magnitude	
H	Hamiltonian	
I	Identity matrix	
I_i	Local integral of motion	
i	Inclination	[rad]
J	Tisserand parameter	
L_i	Lagrange point	
l_k	Lagrange basis polynomial	
M	Monodromy matrix	
m	Collocation order	
n	Orbital mean motion	[rad / s]
n_{rev}	Number of revolutions	

P_i	Primary in CR3BP	
P_n	Legendre polynomial	
P_{sid}	Sidereal period	[s]
P_{syn}	Synodic period	[s]
p	Geometric albedo	
R	Rotation matrix	
$\mathbf{r}$	Position vector	[m]
S	Shift matrix in frequency domain	
s	Pseudo-arc length value	
T	Period	[s]
T	Neighbor size	
t_{begin}	Beginning time of transference	[s]
t_{trans}	Lambert transference time	[s]
$\mathbf{u}$	Cylinder function	
W^s	Stable invariant manifold	
W^u	Unstable invariant manifold	
$\mathbf{X}$	Accumulated circle state	
$\mathbf{x}_\pi$	Approximated solution of the differential equation	

Greek Symbols

γ	Periodic orbit	
γ_j	Normalized distance about L_j	
ΔV	Delta V value	$[m/s]$
ϵ	Small perturbation	
θ	True anomaly	[rad]
θ_m	Manifold angle	[rad]
λ	Eigenvalue	
λ	Unfolding parameter	
θ	Torus angles (θ_1 long, θ_2 lat)	
μ	Gravitational parameter	$[m^3 s^{-2}]$
$\boldsymbol{\nu}$	Torus function	
ρ	Rotation angle	[rad]
σ	Time shift	[s]

ϕ	State transition matrix	
$\phi(t)$	Periodic solution of differential equation	
Ψ	Stroboscopic map at T	
Ψ	Invariant circle of the monodromy matrix	
Ω	Longitude of the ascending node	[rad]
ω	Frequency (w_1 long, w_2 lat)	$[s^{-1}]$
ω	Argument of periapsis	[rad]

Abstract

Near-Earth Asteroids (NEAs) have attracted the attention of the scientific community in the last few years. Not only because of their importance to life on Earth but also their scientific potential and possible economic returns. This work explores the use of quasi-periodic orbits to bound the motion of NEAs close to the Earth's vicinity for their exploitation. The invariant manifolds emanating from these quasi-periodic tori are used to design NEA high-thrust, low-energy retrieval trajectories. A thorough characterization of the two-dimensional space in which the invariant tori can exist is conducted.

Three promising NEAs are selected, from which only two of them (2006 RH120 and 2020 CD3) permit transfers at extremely low ΔVs. For 2006 RH120, transfers that require between 20 and 2 times less ΔV than the existing results from literature were found. We prove that quasi-periodic orbits allow for better transfers than just considering manifolds from periodic families or no manifolds at all. The use of quasi-periodic tori also permits extended transfer windows and more flexibility in the mission design.

1

Introduction

There is a family of bodies in our Solar System that has especially captured researchers' attention in the last decades. These are the Near-Earth Asteroids (NEA), which are characterized for moving in orbits very close to the Earth, and even intersecting Earth's orbit at some points. Around $25,000$ NEAs have been discovered so far, mainly discovered during the Pan-STARRS1 and Catalina sky surveys [124]. NEA surveys were motivated by the need to understand and minimize the threat that the impact of some of these objects could cause to life on Earth, as it has happened in the past already. After almost all objects larger than 1 km were discovered (2011) the idea of deflecting a threatening NEA has become more appealing. In 2022 the mission AIDA will study the feasibility of using a kinetic impactor as a means to deflect a NEA [30].

Several missions have visited NEAs since the beginning of the century, such as the NASA NEAR mission (2002) [95] and the JAXA's Hayabusa mission (2005) [74] among others. Although these missions were mainly focused on exploration, scientific research, and technological demonstration, some more audacious missions have been planned. In 2012 the company Planetary Resources declared their plan to mine asteroids commercially [81]. The idea of asteroid mining is not new, but as resource depletion on Earth becomes more apparent, and space technologies improve, the idea of extracting resources from space starts to take shape. Even bolder ideas have been also proposed, such as asteroid tourism, or creating habitats inside them [123].

The idea of capturing a NEA into a bounded region around Earth's vicinity with relatively easy access has also been envisioned in recent years. That would allow to conduct more scientific research on them, use them as a mining source, tourism attraction, and even use them as a means of asteroid deflection for other NEAs.

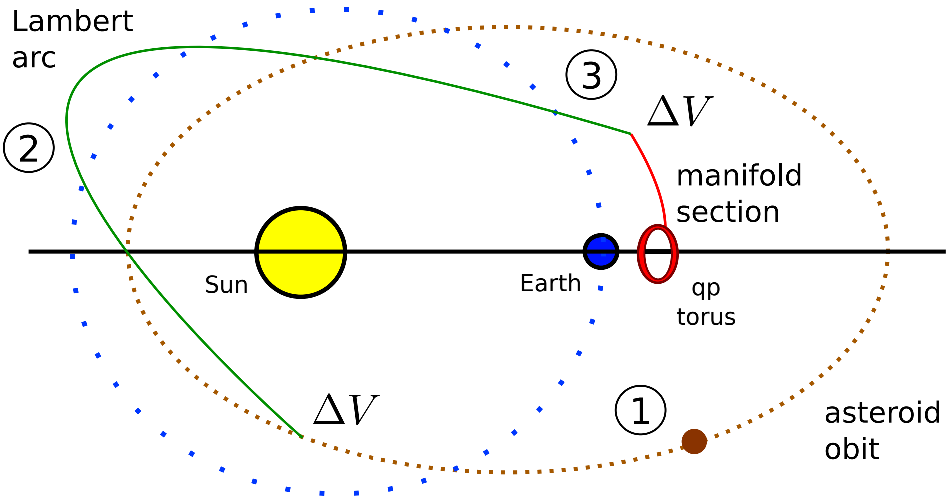

Figure 1.1: Schematic transfer from NEA orbit to quasi-periodic tori.

In this work, we will address the possibility of capturing one of these bodies into a so-called quasi-periodic torus or quasi-periodic orbit. In these orbits, a body would move on the surface of a torus, hence it is a bounded motion. One of the more attractive properties of these orbits is that, in the context of the Circular Restricted Three-Body Problem (CR3BP), they live in two-dimensional families, while periodic orbits only live in one-dimensional ones. From every point on the surface of these tori emerge so-called invariant manifolds, which are a series of low-energy trajectories that converge or diverge from the torus as time passes. The main idea is to use these manifolds as a means to connect the NEAs to trajectories leading to bounded motion close to the Earth, specifically about the equilibrium points of the Sun-Earth system. The asteroid orbit and manifold section will be connected by using a Lambert arc. Figure 1.1 shows a scheme of such transfer, where the main elements, namely the manifold section, Lambert arc and asteroid orbit are present. A ΔV is applied to change the asteroid from its orbit (1) to the tranfer Lambert arc (2), and finally a different ΔV is applied to transfer it from (2) to the manifold section (3) that leads to a quasi-periodic torus.

The research question and sub-questions that will be answered in this work are the following:

What possibilities and (dis)advantages provide quasi-periodic orbits for NEAs transfers to Earth's vicinity?

1. Do transfers designed using quasi-periodic manifolds offer cheaper (lower ΔV) transfer than using periodic orbits or no manifolds at all?
2. Do quasi-periodic orbits provide more flexible transfer windows?

This works aims at being self-contained, justified, and replicable so that future work can build on it, or extract data from it. Previous developments and work in the field are reviewed in Chapter 2. Chapter 3 explores the dynamical environment of the CR3BP, from the equations of motion and existence of equilibrium points to the methods to approximate and compute periodic orbits, and the use of continuation methods to obtain the whole families of orbits. This section explains the fundamental concepts upon which the rest of the work will be built. Chapter 4 explains how quasi-periodicity is defined and the different methods that were created to compute it. The stroboscopic method with Gauss-Legendre collocation is chosen and its formulation and implementation are described. Next, a database of invariant tori is created to be used afterward in our computations. Chapter 5 describes the general orbital and physical properties of NEAs, and some filters are applied in order to find in a rapid manner the more promising asteroids. Three asteroids come up as the most suitable ones for these transfers. Then, Chapter 6 defines the optimization problem using a Lambert arc to connect the NEA orbit with the invariant manifolds. A Monte Carlo analysis is used to explore the design space and further restrict some of the parameters. Finally, Chapter 7 contains an in-depth discussion of the optimization results, the effect of the main parameters, and the best results compared with previous literature.

2

Heritage

Some researchers have already explored the possibility of bringing a NEA to Earth's vicinity for its exploitation. Sánchez and McInnes [106] were one of the first ones to study the capture of small NEAs with relatively low energy by using a NEO distribution provided in [18]. They showed that just a tiny fraction of the NEA population lies in Keplerian regions where low-energy transfers to Earth with ballistic opportunities exist. Other studies [63, 107] have focused on capturing small NEAs in periodic orbits around the Sun-Earth $L_1 - L_2$ libration points. Of particular interest in this regard are the Easy Retrievable Objects (EROs) proposed by Yárnoz et al. [128]. This category includes all NEAs which could be captured into periodic orbits around the L_1 and L_2 libration points in the Sun-Earth circular restricted three-body problem with a total $\Delta V < 500$ m/s.

The use of the invariant manifolds that emanate from the periodic orbits about libration points in the CR3BP to transport NEAs has been studied in by some researchers. Some like [116] proposed to transfer the asteroid into the periodic orbits around the equilibrium points in the Earth-Moon problem, which would make them more accessible. Many derived studies from this topic also exist, for instance, Zimmer [130] explored the feasibility of using reusable cargo spacecraft in halo orbits of the Sun-Earth system to reduce the costs of missions to NEAs. From a different perspective, in 2012 Gao [53] studied how to use the Sun-Earth periodic orbits manifolds to obtain NEA flyby trajectories.

In [38, 82] the authors used periodic orbits with unstable characteristics to design low-energy ballistic transfers. The NEA has to be inserted onto the stable manifold associated with the target periodic orbit around the libration point of interest. Once it is inserted, it will be asymptotically captured without any other active measures.

Some authors have also studied the ballistic capture mechanics in the restricted three-body problem for creating transfers between NEAs and the libration points in the last years. For instance, Mingotti et al. [90] in 2014 proposed using low-thrust propulsion to capture NEAs to a target periodic orbit around the Sun-Earth L_1 and L_2 points by using the stable manifolds associated with the target periodic orbit. Farquhar et al. [49] in 2014 studied the Sun-Earth L_2 libration point as a potential parking orbit and gateway station for missions to NEAs and Mars. Tan et al. in 2017 [116] proposed a lunar capture based on two impulses that will insert the asteroid directly into the Earth-Moon L_2 periodic orbit.

The work presented by Yárnoz et al. [128] in 2013 has been very influential for this one. They defined the EROs population based on the discovered NEAs up to that date and some other assumptions based on the geometry of the invariant manifolds of the periodic orbits. They used the Tisserand parameter and the manifold orbital elements to develop a method for pruning the asteroid catalog.
This pruning allowed them to focus only on the asteroids with an estimated ΔV below 1 km/s. The NEO orbital elements were considered valid until their next close encounter with Earth. Then, the Lambert transfers between the asteroid initial orbit and the manifolds were optimized using EPIC, a global optimization method that uses a stochastic search blended with an automatic solution space decomposition technique [120]. They simply computed the manifolds of the planar Lyapunov, vertical Lyapunov, and Halo orbits around L_1 and L_2. The transfer between the NEO orbit and the manifold was calculated as a heliocentric Lambert arc of a restricted two-body problem with two impulsive burns, one to depart from the NEO, and the final one from the insertion into the manifold with the insertion constrained to take place before or at an arbitrarily located Poincaré section.

The authors showed that 12 asteroids of the whole NEO catalog can be retrieved at a cost lower than 500 m/s, ten of them around L_2 plus two Atens around L_1. They showed that, as expected, planar Lyapunov orbits are optimal for lower-inclination NEOs, while NEOs with higher inclinations favor transfers to vertical Lyapunov. The *cheapest* transfer found was for 2006 RH120, for which a

ΔV of 60 m/s was found to be needed to transfer it into a halo orbit. The total duration of the transfer ranged from 3 to 7.5 years; for longer transfers it was possible to find faster solutions with fewer revolutions in the Lambert arc at a small ΔV penalty [128].

Sánchez and Yárnoz [105] conducted a similar study but using the 2016 NEO database and further refining the results by including low-thrust propulsion. They found new EROs objects at lower ΔV. In 2010, Baoyin et al. [11] had conducted a similar study as [128], however, they only took into account periodic orbits around the libration points L_1 and L_2.

3

Dynamical Environment

This section addresses the dynamical framework in which our problem will be embedded. First, the equations of motion that describe the Circular Restricted Three-Body Problem (CR3BP) are explained. Then, the existence of equilibrium points, the so-called Lagrange points and the dynamics around them is discussed. Afterwards, we explain the importance of the periodic orbits in the CR3BP, and the main families that exist. The concept of invariant manifold is introduced and its importance for astrodynamics and this work in particular. The methods to compute an analytical approximation of periodic orbits, and two schemes to compute periodic orbits are described and compared. Finally, the continuation methods that are used to obtain all the family members are described. Most of the concepts that are explained in this chapter are also applicable or can be extrapolated to the computation of quasi-periodic orbits

3.1. Circular Restricted Three-Body Problem

The investigation of the dynamics of a third body within a system with two other massive bodies emerged naturally from the study of the Sun-Earth-Moon system in astronomy, and the study of the vicinity of the Earth-Moon system in astrodynamics. This problem turned out to be very complex and has fascinated many of the most brilliant scientists throughout the centuries. In an attempt to gain some more insight into the nature of the problem, some assumptions and simplifications were applied to the initial model, which came to be known as the Circular Restricted Three-Body Problem.

The CR3BP studies the dynamics of a pointless body P with an infinitesimal mass m_3, called the third body in the presence of two massive bodies, P_1 and P_2, with masses m_1 and m_2 respectively, which are called the primaries. These two bodies are assumed to move in circular orbits around their center of mass. The perturbation by the third body is not considered because its mass is treated as negligible compared to that of the primaries. The CR3BP reduces the original nine second-order differential equations (18th order) to three (6th order). Furthermore, if the mass of the third body is restricted to the orbital plane, then it is called the Planar Circular Restricted Three-Body problem (PCR3BP), which has been used extensively in research [33, 111, 126]. Regardless of the fact that the real orbits of the planets are not circular, but eccentric: this model has proved to add useful insight and solutions that can be extrapolated to more complex models, such as the existence of equilibrium points, periodic families and manifold solutions.

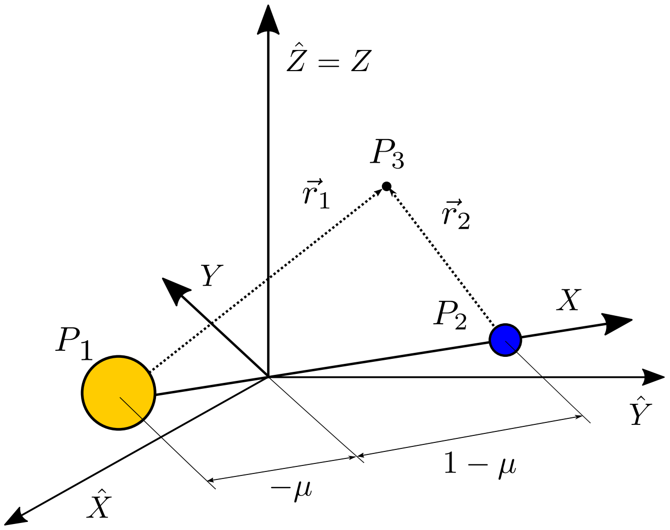

Figure 3.1: Inertial ($\hat{X}\hat{Y}\hat{Z}$) and rotating (XYZ) reference frame in the CR3BP and location of the primaries in non-dimensional units.

3.1.1. Equations of motion

Using Newton's second law and the law of gravitation, the three-body problem is formulated as

$$\ddot{\mathbf{r}}_i = G\frac{m_j}{r_{ij}^3}\mathbf{r}_{ij} + G\frac{m_k}{r_{ik}^3}\mathbf{r}_{ik} \quad \text{for} \quad i,j,k = 1,2,3 \tag{3.1}$$

where G is the gravitational constant and

$$\mathbf{r}_{ij} = \mathbf{r}_j - \mathbf{r}_i, \quad r_{ij} = |\mathbf{r}_{ij}| \tag{3.2}$$

Equation 3.1 is called the classical or Euler formulation of the Three Body Problem[125]. In order to transform Equation 3.1 into the CR3BP several transformations must be applied. First the following assumptions are made:

- The mass of the third body m_3 in negligible with respect to that of the other bodies, so its gravitational influence is not considered.
- The orbits of the two massive bodies are known and circular. Therefore, only the equations of motion for P_3 need to be solved.

Note that in this new formulation the conservation of energy and angular momentum are violated [125], so that they are no longer constants of motion. With the intention of transforming the problem into an autonomous dynamical system[1], the equations of the third body are expressed in a synodical reference system, which is a reference frame that rotates with constant angular velocity w (also expressed as mean motion n) around its $Z-$axis. The origin of this reference frame is set at the barycenter of the system and the $X-$axis coincides with the line that joins the primaries. Finally, the equations are also non-dimensionalized, so that the sum of the masses of the primaries, the distance between them and the modulus of the angular velocity of the rotating frame are unitary. Figure 3.1 illustrates both the inertial reference frame $\hat{X}\hat{Y}\hat{Z}$ and the synodical reference frame XYZ. It also shows that the more massive primary is located at $x_1 = -\mu$ while the smaller one is at $x_2 = 1 - \mu$. For the system with the Sun and the Earth as primaries, we will be using a value of $\mu = \mu_E/(\mu_S + \mu_E) = 3.0404390358 \cdot 10^{-6}$ [84] which combines the mass of the Earth and the Moon in

---

[1] A autonomous dynamical system does not depend explicitly on time. Note that in Equation 3.1 the position of the primaries depends on time, while in Equation 3.3is constant. Autonomous systems permit to study the solutions in the phase space and have some useful properties such as the translation property. For more on this see [121]

μ_E. After transforming the reference frame and units, the equations of motion can be written as

$$\begin{aligned} \ddot{x} - 2\dot{y} &= \frac{\partial U}{\partial x} = x - \frac{(1-\mu)}{r_1^3}(x+\mu) - \frac{\mu}{r_2^3}(x-1+\mu) \\ \ddot{y} + 2\dot{x} &= \frac{\partial U}{\partial y} = y - \frac{(1-\mu)}{r_1^3}y - \frac{\mu}{r_2^3}y \\ \ddot{z} &= \frac{\partial U}{\partial z} = -\frac{(1-\mu)}{r_1^3}z - \frac{\mu}{r_2^3}z \end{aligned} \tag{3.3}$$

with U the scalar function:

$$U(x,y,z) = \frac{1}{2}(x^2+y^2) + \frac{1-\mu}{r_1} + \frac{\mu}{r_2} \tag{3.4}$$

and where the distance from P_3 to P_1 and P_2 is respectively (Figure 3.1)

$$r_1^2 = (x+\mu)^2 + y^2 + z^2 \quad \text{and} \quad r_2^2 = (x-1+\mu)^2 + y^2 + z^2 \tag{3.5}$$

For the full derivation see [35]. Since Equation 3.3 is Hamiltonian and independent of time, it admits a first integral, the so-called Jacobi integral

$$C(x,y,z,\dot{x},\dot{y},\dot{z}) = 2U(x,y,z) - (\dot{x}^2 + \dot{y}^2 + \dot{z}^2) \tag{3.6}$$

When the velocity of the third body is zero, Equation 3.6 describes the so-called surfaces of Hill. These surfaces allow to determine which regions of the configuration space are accessible to the third body for a given value of the Jacobi constant C. By analyzing the evolution of these regions it can be seen that it is possible to obtain bounded motion by modifying the Jacobi constant of an object. For an object starting in the vicinity of any of the primaries and with $C_1 < C < C_2$ being C_i the Jacobi constant value at the equilibrium point L_i, see Section 3.2, we can ensure that the body will not escape the proximities of the primary for it is forbidden by Equation 3.6. Therefore, this method could be used to bound an asteroid to the Earth's vicinity. Nonetheless this method would imply a higher ΔV than the solutions that will be discussed in this paper, and would involve certain risks concerning planetary protection, which should also be accounted for.

3.1.2. Equations near equilibrium points

A modified version exist of the equations of motion for the CR3BP Equation 3.3, which is used to study the motion close to the equilibrium point. In this section xyz refer to the coordinates centered at the equilibrium point to study and the following simplification is taken

$$\begin{aligned} r_1 &= 1 \quad \text{for motion about} \quad L_1, L_2 \\ r_2 &= 1 \quad \text{for motion about} \quad L_3 \end{aligned} \tag{3.7}$$

the units of mass and time come from $G(m_1 + m_2) = n^2 a^3 = 1$ with n and a the orbital mean motion and distance of P_2 about P_1. Also the following dimensionless quantity is defined

$$\begin{aligned} \gamma_L &= \frac{r_1}{a} = n^{2/3} \quad \text{for} \quad L_1, L_2 \\ \gamma_L &= \frac{r_2}{a} = n^{2/3} \quad \text{for} \quad L_3 \end{aligned} \tag{3.8}$$

a new time variable $s = nt$ is introduced and Equation 3.3 is rewritten by expanding the non-linear terms using Legendre polynomials P_n [101]

$$\begin{aligned} \ddot{x} - 2\dot{y} - (1 + 2c_2)x &= \frac{\partial}{\partial x} \sum_{n\geq 3} c_n \rho^n P_n\left(\frac{x}{\rho}\right) \\ \ddot{y} + 2\dot{x} - (c_2 - 1)y &= \frac{\partial}{\partial y} \sum_{n\geq 3} c_n \rho^n P_n\left(\frac{x}{\rho}\right) \\ \ddot{z} + c_2 z &= \frac{\partial}{\partial z} \sum_{n\geq 3} c_n \rho^n P_n\left(\frac{x}{\rho}\right) \end{aligned} \tag{3.9}$$

where

$$\begin{aligned} c_n &= \frac{1}{\gamma_L^3}\left[(\pm 1)^n \mu + (-1)^n \frac{(1-\mu)\gamma_L^{n+1}}{(1 \mp \gamma_L)^{n+1}}\right], \quad \text{for} \quad L_1(\text{upper}),\ L_2(\text{lower}) \\ c_n &= \frac{1}{\gamma_L^3}\left[1 - \mu + \frac{\mu \gamma_L^{n+1}}{(1+\gamma_L)^{n+1}}\right], \quad \text{for} \quad L_3 \end{aligned} \tag{3.10}$$

Equation 3.9 allow to obtain all orders of the non-linear expansion recursively using the well-known Legendre polynomial relationships [76]. This form of the equations of motion is particularly useful when developing analytical approximations of periodic orbits, around L_1, L_2 and L_3, as it will be done in Section 3.4.

3.2. Libration Points

There are five different equilibrium points –or zero-dimensional tori– in the CR3BP, all of them lie in the xy-plane. Three of them, namely L_1, L_2 and L_3, are located along the $X-$axis that connects the primaries, these equilibrium points are called the *collinear Lagrange points.* Their location can be obtained by solving the well-known Szebehely quintic polynomial [115]:

$$\begin{aligned} \gamma_j^5 \mp (3-\mu)\gamma_j^4 + (3-2\mu)\gamma_j^3 - \mu\gamma_j^2 \pm 2\gamma_j - \mu = 0 \quad \text{for} \quad L_1(\text{upper}),\ L_2(\text{lower}) \\ \gamma_3^5 + (2+\mu)\gamma_3^4 + (1+2\mu)\gamma_3^3 - (1-\mu)\gamma_3^2 - 2(1-\mu)\gamma_3 - (1-\mu) = 0 \quad \text{for} \quad L_3 \end{aligned} \tag{3.11}$$

where γ_j for $j = 1,2$ is the distance from the smaller primary, the one with $m_2 = \mu$, to the equilibrium point L_j and γ_3 is the distance from the larger primary to L_3. Equation 3.11 can be solved numerically by using the Newton method and using as starting point $(\mu/3)^{1/3}$ for Equation 3.11a (L_1 and L_2), and $(1-7\mu/12)$ for Equation 3.11b (L_3) [72]. The L_4 and L_5 libration points are the so-called *triangular Lagrange points* since they form an equilateral triangle with the primaries. They are located at $(\mu-\frac{1}{2},\pm\frac{\sqrt{3}}{2},0)$ where the minus sign corresponds to L_4 and the plus sign is for L_5. Figure 3.7 shows a schematic of the location of the libration points within the CR3BP system.

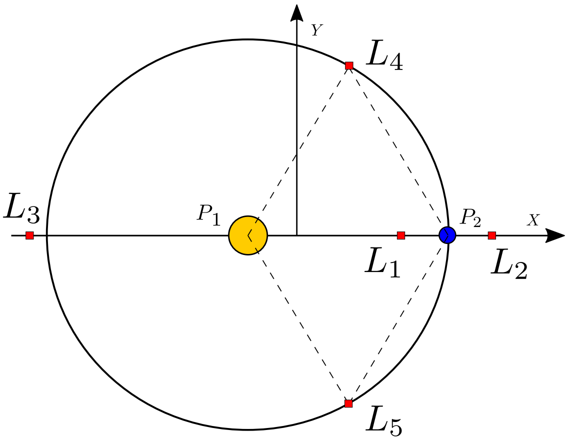

Figure 3.2: Location of the Lagrange equilibrium points in the CR3BP system.

Through this work we will be working only in the Sun-Earth system. Table 3.1 shows the location of the libration points with respect to the barycenter of the system in non-dimensional units. The results will be used during the rest of this work continuously. These data are validated using external sources in Chapter 8.

Table 3.1: Position of the equilibrium points in dimensionless units.

	L_1	L_2	L_3	L_4	L_5
x	0.989985965	1.010075217	-1.00000076	0.499996970	0.499996970
y	0.0	0.0	0.0	0.86602540	-0.86602540

3.2.1. Dynamics about libration points

The dynamics in the vicinity of the libration points can be studied by computing the eigenvalues of the linearized flow at the libration point and using the stable, unstable and center manifold theorem for continuous flows [59, 98]. It can be shown that the eigenvalues come in pairs due to the fact that the flow $\mathbf{f_0}$ is Hamiltonian [7], in other words they are symmetric with respect the real and imaginary axes [45].

An eigenvalue is classified as a *center* if it has zero real part, which implies an oscillatory motion. A *saddle* pair of eigenvalues will have a non-zero real part, and their real parts will have opposite signs. We will call *complex saddle* to four eigenvalues which are symmetric with respect both real and imaginary axes. The real part of the saddle eigenvalue contains the convergent/divergent behaviour, depending on the sign. Due to the fact that the eigenvalues always come in pairs, both the convergent (negative sign of real part) and divergent (positive sign of real part) values will appear in a saddle pair. The Jacobian matrix of the flow is a 6 × 6 matrix, so there will be three pairs of eigenvalues that define the dynamics close to the equilibrium points.

Table 3.2: Linearized motion at each of the libration points.

	$0 \leq \mu < \mu_r$	$\mu_r < \mu \leq 0.5$
L_1	center × center × saddle	
L_2	center × center × saddle	
L_3	center × center × saddle	
L_4	center × center × center	center × complex saddle
L_5	center × center × center	center × complex saddle

It can be shown that the collinear libration points behave has a center×center×saddle for all possible values of μ [72]. However, the stability of the triangular libration points changes depending on the mass parameter μ. For μ below the Routh critical value $\mu < \mu_r$ with $\mu_r = \frac{1}{2}(1 - \frac{\sqrt{69}}{9}) \approx 0.03852$, they are stable, otherwise they are unstable. Table 3.2 summarizes the types of eigenvalues that arise with respect to the mass parameter at each libration point. In this work we will only focus on the dynamics about L_1 and L_2 because they are the closest to the Earth. As seen in Table 3.2, they are always characterized by a center × center × saddle pair of eigenvalues no matter the value of μ.

The center × center eigenvalues create a 4-dimensional center invariant manifold about each of the collinear libration points. For a given energy level this is a 3-dimensional set which contains periodic and quasi-periodic solutions that form invariant tori [3]. Each of the center values is related to a particular planar or vertical frequency, and by combining these two frequencies we can obtain the periodic or quasi-periodic solutions. For a more detailed description of periodic orbits refer to Section 3.3 and for a description of quasi-periodic orbits, see Chapter 4. In order to better study this behavior, it is possible to isolate just the center × center component by using methods such as center manifold [2] or Poincaré-Lindstedt methods, Subsection 3.4.2 [73]. The saddle-type eigenvalue induces stable and unstable manifolds on each central orbit around the collinear point. It produces the hyperbolic behaviour that apprears for instance in periodic and quasi-periodic orbits and that provide new and innovative transfer solutions in astrodynamics. The stable and unstable invariant manifolds create cylinder tubes ($S^1 \times \mathbb{R}$) which act as separatrices [33] of the flow.

3.3. Periodic Orbits

The concept of periodic orbit is important to understand the dynamics of the CR3BP, and also the concept of quasi-periodic orbit which are key throughout this work. In dynamical systems theory [121] a periodic orbit can be defined as

Definition 1 *Let* $x = \Phi(t)$ *be a solution of the differential equation* $\dot{x} = f(x)$, $x \in D \subset \mathbb{R}^n$. *Suppose that a positive real number* T *exists such that* $\Phi(t) = \Phi(t+T)$ *for all* $t \in \mathbb{R}$. *Then* $\Phi(t)$ *is a periodic solution with period* T *[121].*

Note that, consequently, the periodic solution has also period $2T, 3T$, etc. When T is the smallest period, we say that $\Phi(t)$ is T-periodic. A periodic solution of an autonomous equation produces a closed orbit, a cycle, in the phase-space, and a closed orbit in the phase space corresponds with a periodic solution [121]. Equilibrium points are therefore a form of periodic solution which does not depend on time.

The search for periodic orbits in the context of the CR3BP may have begun when in 1892 the French mathematician Henri Poincaré wrote in his *Méthodes Nouvelles de la Mécanique Céleste* [99]:

> *'D'ailleurs, ce qui nous rend ces solutions périodiques si précieuses, c'est qu'elles sont, pour ainsi dire, la seule brèche par où nous puissions essayer de pénétrer dans une place jusqu'ici réputée inabordable.'*[2]

According to Poincaré, periodic solutions are the only way to decipher the otherwise unapproachable three-body problem. Building upon the astronomical intuition, he called a solution periodic if it behaves as such in some rotating frame, in other words if $\Phi(t+T) = Rx(t)$, where R is a rotation matrix. Poincaré showed the existence of periodic solutions in the neighborhood of the equilibrium points which agreed with Hill's intuition [29]. Poincaré's work was later extended by Bendixon who formulated the Poincaré-Bendixon theorem, which gives a criterion for the existence of periodic solutions. Their work led to systematic and thorough searches for periodic solutions in the Three-Body Problem and their classification by Darwin [36, 37], Moulton et al. [93], Strömgren and Pedersen [114], and many other researchers. In 1913, Birkhoff proved the 'Last Geometric Theorem' formulated by Poincaré which states that there are infinitely many periodic orbits near any stable periodic orbit, which also implies the existence of quasi-periodic orbits [94].

---

[2] 'Moreover, what makes these periodic solutions so precious to us is that they are, so to speak, the only breach through which we can try to enter a place previously deemed unaffordable.'

The different families of periodic orbits are connected. In other words, they share common members, creating a complex network. In 2007, Doedel et al [44] presented a clear overview of the elemental periodic orbits for different values of μ, and described their relationships by using bifurcation[3] diagrams.

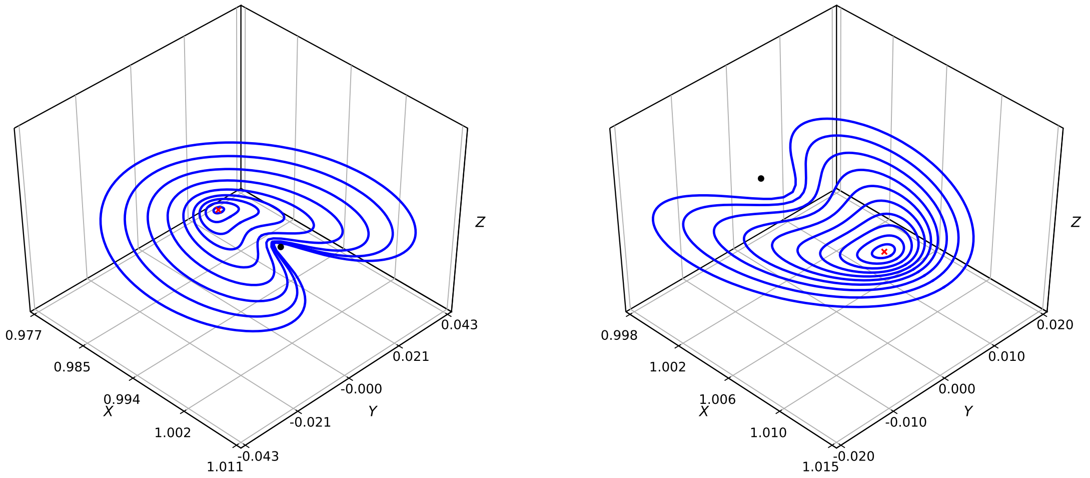

(a) L_1

(b) L_2

Figure 3.3: Part of the planar Lyapunov family about L_1 and L_2.

For this work we will just focus on four families, namely the planar and vertical Lyapunov orbits, and the northern and southern Halo orbits. Two of them –the planar and vertical Lyapunov families– emerge by virtue of the Lyapunov's center theorem [110]. The starting energy level for these families corresponds to the energy of the equilibrium point they are referred to. The terminating (largest) planar orbit around L_1 surrounds the larger primary and the equilibrium points L_2 and L_3. For L_2 it surrounds both primaries and L_1 and for L_3 it surrounds both primaries and all the collinear equilibrium points.

Vertical orbits terminate at bifurcating planar families. Planar families bifurcate into halo orbits as will be further explained afterwards. In order to compute the planar or vertical families we can start by creating an approximate solution in a close neighborhood of the libration point, Section 3.4, then the approximation is corrected by using a corrector algorithm (Section 3.5). Once one of the members of the family has been obtained the rest can be obtained by using a continuation method, Section 3.6.

---

[3] Bifurcation theory studies the changes in the qualitative structure of the flow associated with the dynamical system as parameters are varied. Bifurcation theory allows to identify bifurcation points without the need for the analytical solution, that is the points where there is a qualitative transition along families of solutions [67].

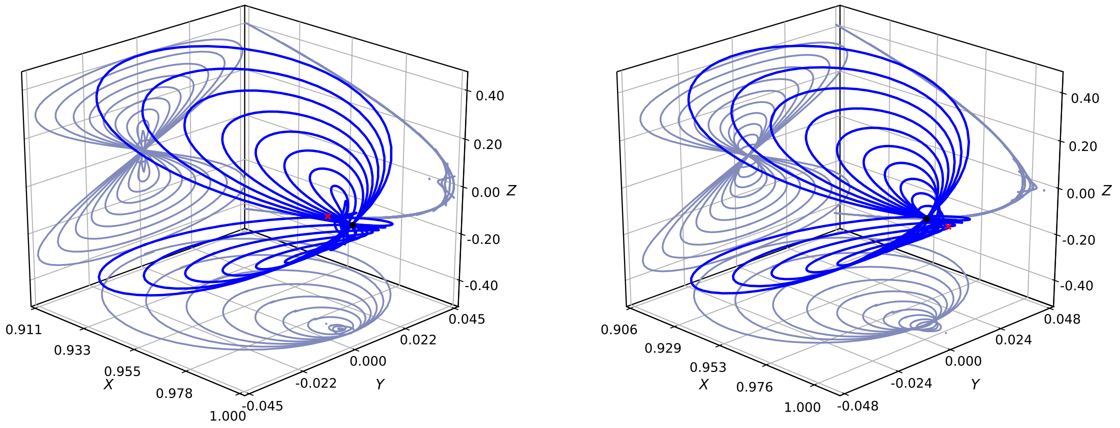

(a) L_1 (b) L_2

Figure 3.4: Part of the vertical Lyapunov family about L_1 and L_2.

The term 'halo orbit' was coined by Robert Farquhar in his PhD thesis in 1966 [50]. He found a family of three-dimensional almost periodic orbits around L_2 in the Earth-Moon system. He proposed using a communications station in such orbits for the Apollo 18 mission. The advantage of these orbits is that they allow continuous contact with both the far side of the Moon and the Earth. In the end, Apollo 18 was cancelled [66]. In 1973 Farquhar and Kamel [48] computed some members of the halo family by using the Poincaré-Lindsted method, Subsection 3.4.2. This work was further extended by Breakwell and Brown in 1979 [21].

Halo orbits bifurcate from the planar Lyapunov orbits for all collinear libration points. The bifurcation occurs when there is a $1:1$ resonance between the planar and the vertical frequencies, Subsection 3.4.3. At each bifurcation two orbits –north and south– emerge. They are divided into north and south halo families depending on whether they hover the equilibrium point at mostly positive z (north) or negative z (south). They are also symmetric with respect to the xz-plane. Similarly to the planar and vertical families, in order to compute halo orbits we require an accurate-enough initial guess, which must then be corrected to account for all the nonlinearities of the problem. Once a solution is obtained, we can use a continuation scheme to obtain the entire family.

A representative number of members of the planar Lyapunov family about L_1 and L_2 is shown in Figure 3.3 for decreasing Jacobi constant. Figure 3.4 illustrates the evolution of the vertical Lyapunov family. Finally, Figure 3.5 and Figure 3.6 show the north and south halo families from their bifurcation from the planar Lyapunov member until they collapse.

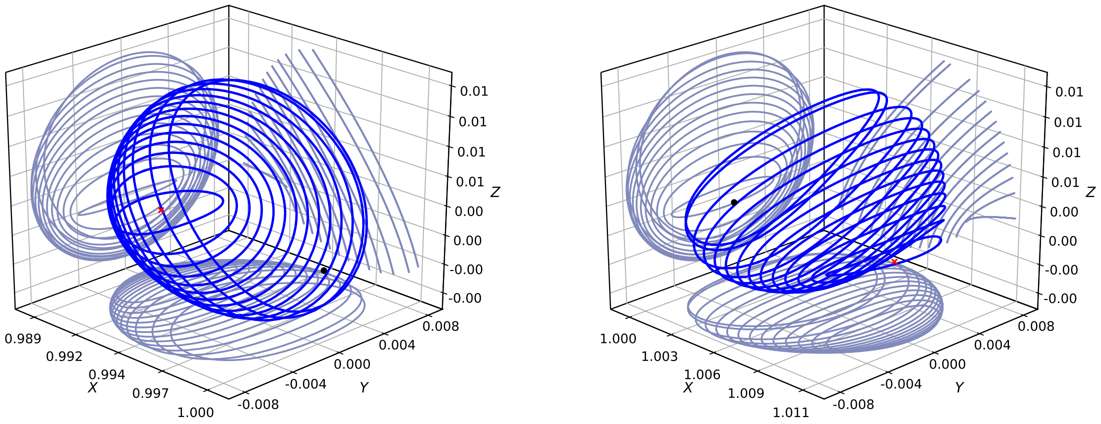

(a) L_1

(b) L_2

Figure 3.5: Part of the north halo family about L_1 and L_2.

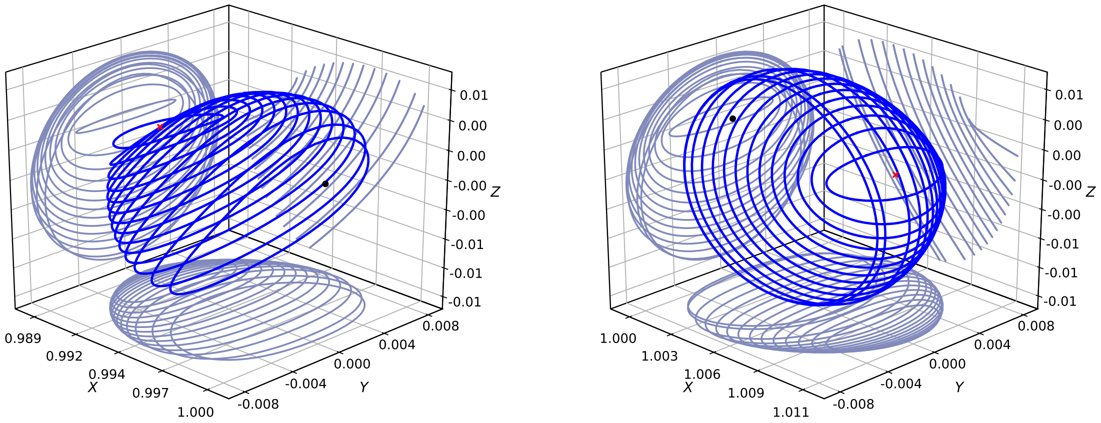

(a) L_1

(b) L_2

Figure 3.6: Part of the south halo family about L_1 and L_2.

3.3.1. Invariant Manifolds

The concept of invariant manifolds will be key throughout in this work, which will be built upon the existence of these kinds of structures. Although the invariant manifolds that will be used are related to quasi-periodic invariant tori instead of periodic orbits, this simpler case will be used for illustrative purposes and to gain a better understanding of the physical phenomenon.

The idea of invariant manifolds appears in dynamical systems theory and it is a broad concept; it refers to a variety of different structures that can emerge in these systems. In general, it denotes a topological manifold[4] that is invariant under the action of a dynamical system. There are several types of manifolds that fit in this definition. However, the concept of invariant manifold in the context of astrodynamics and the CR3BP commonly refers to a set of points in the system's phase space that tend toward a given limiting set as time moves to plus or minus infinity [54]; these are the so-called stable and unstable invariant manifolds respectively.

These invariant structures are very important in the dynamics of the CR3BP and provide insight into the transport of particles in the Solar System: asteroids, dust or even a spacecraft. Koon et al. [77] proved that, for a range of energy , the stable and unstable manifolds about the collinear libration points L_1 and L_2 form tubes that separate two types of motion: transit and non-transit orbits. The orbits that start inside those tubes can transit from one region to the other, in other words, they transit between orbiting one of the primaries to the other. On the other hand, the orbits that commence outside the tubes bounce back. In that sense, the stable and unstable invariant manifolds act as gate-keepers between the two regions. The invariant manifolds about libration points have been used in mission design, for instance in the Genesis mission [83].

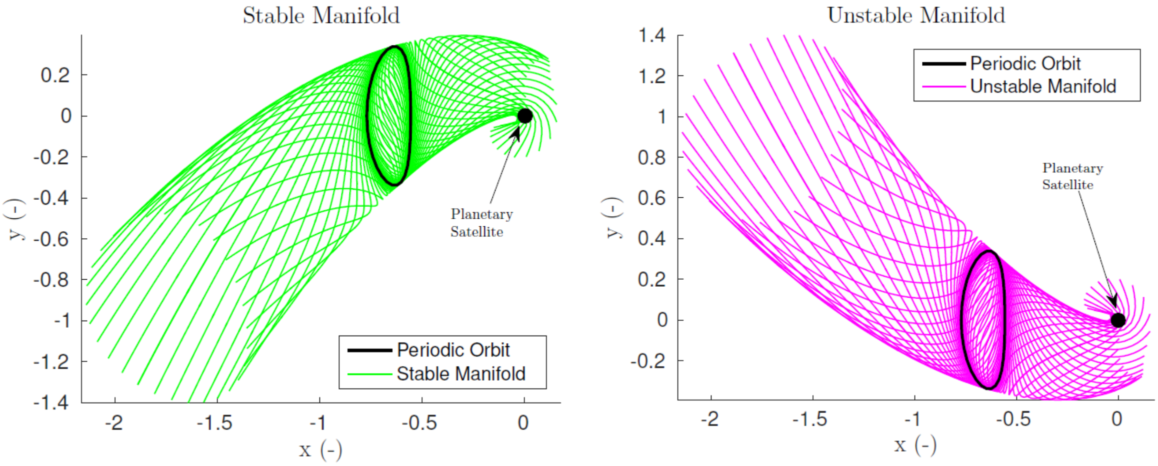

(a) Stable manifold (b) Unstable manifold

Figure 3.7: Stable and unstable manifolds from a periodic orbit [12].

---

[4] An $n-$dimensional manifold is a topological space for which every point has a neighbourhood homeomorphic to an Euclidean space $\mathbb{R}^n$, [121].

The main use of invariant manifolds in astrodynamics is to generate new low-energy spacecraft transfers emanating from periodic orbits that were not possible with more traditional methods. One of the advantages of these transfers is that they are ballistic, which means that no propellant is needed, the natural dynamics of the problem are harnessed to design the transfer orbit. In this context, the concept of heteroclinic and homoclinic connections emerges. In dynamical system theory, a heteroclinic orbit, or connection, is such that it connects two different equilibrium points –or periodic orbits– in the phase space. Note that heteroclinic connections between quasi-periodic tori are also possible, as shown in [97]. On the other hand, a homoclinic connection is such that it connects an orbit around an equilibrium point with itself [25]. In the CR3BP context, the phase space around the libration points L_1 and L_2 has a saddle component. Thus, there are orbits that asymptotically approach the periodic orbits in forward time (stable manifold) and orbits which leave it (unstable manifold). By matching a stable manifold with another unstable manifold, transfers at zero cost can be achieved. Because of the continuous dependence of the solutions with respect to the initial conditions and the asymptotic character of the manifolds, once one connection has been found there are infinitely many others in its vicinity [25]. This means that infinitely many connections can be found from any initial intersection on the Poincaré section. In general, connections with a small number of loops are preferred for the more practical applications.

In this work we will not try to find heteroclinic connections. Instead, we will find the best transfers between stable manifolds, that is the attractive manifolds, that emerge from quasi-periodic orbits and the orbits of NEO asteroids.

Let γ be a periodic orbit from which emerge the stable and unstable invariant manifolds, $W^s(\gamma)$ and $W^u(\gamma)$ respectively. Computing these manifolds essentially reduces to studying the stability of the linearized time-T mapping given by the monodromy matrix[5] for which the image of the periodic orbit is a fixed point. By studying the eigenvectors of the monodromy matrix we can obtain the directions that lead to hyperbolic behaviour, which can be propagated by using the corresponding state transition matrices. In this work, we will not compute the invariant manifolds associated with the periodic orbits of the CR3BP, however the interested reader can use the method explained in Section 4.8 to compute the manifolds from a periodic orbit collocation solver scheme.

---

[5] The monodromy matrix is the state transition matrix of the system evaluated at the period T of the periodic orbit.

3.4. Analytical approximations

As stated in Section 3.3, an analytical approximation of the periodic orbit is required in order to initialize the correction scheme. As seen in Subsection 3.1.1, the planar and the vertical motions in the CR3BP are decoupled; let us then make a difference between the orbits that lie on a two-dimensional space –planar Lyapunov family– and the orbits that span through the three-dimensional space –vertical and halo families. In this chapter we will provide an analytical approximation of each of these orbits so that they can be used to initialize a solver from which the analytical approximation is taken to obtain the real periodic orbit.

3.4.1. Planar approximation

Using the notation introduced in Equation 3.3, the linearized equations of motion in the xy-plane about an equilibrium point can be written as:

$$\begin{aligned} \ddot{x} - 2\dot{y} - (2K+1)x = 0 \\ \ddot{y} + 2\dot{x} + (K-1)y = 0 \end{aligned} \tag{3.12}$$

Where it can be shown that $K > 1$ for the collinear Lagrange points. Equation 3.12 is a system of homogeneous coupled linear differential equations with constant coefficients with the characteristic equation:

$$\lambda^4 + (2-K)\lambda^2 - (2K+1)(K-1) = 0 \tag{3.13}$$

and the solution of Equation 3.12 can be expressed in general as:

$$\begin{aligned} x = A_1 e^{\lambda_1 t} + A_2 e^{-\lambda_1 t} + A_3 e^{\lambda_3 t} + A_4 e^{-\lambda_3 t} \\ y = B_1 e^{\lambda_2 t} + B_2 e^{-\lambda_2 t} + B_3 e^{\lambda_4 t} + B_4 e^{-\lambda_4 t} \end{aligned} \tag{3.14}$$

with λ_3 and λ_4 pure imaginary. It can be shown that the coefficients A and B are not independent [125], and can be expressed as $B_i = \gamma_i A_i$ so that we can rewrite Equation 3.14 as:

$$\begin{aligned} x = A_1 e^{\lambda_1 t} + A_2 e^{-\lambda_1 t} + A_3 e^{\lambda_3 t} + A_4 e^{-\lambda_3 t} \\ y = \gamma_1 A_1 e^{\lambda_1 t} - \gamma_1 A_1 e^{-\lambda_1 t} + \gamma_3 A_3 e^{\lambda_3 t} - \gamma_3 A_4 e^{-\lambda_3 t} \end{aligned} \tag{3.15}$$

By inspecting Equation 3.15 it is noticeable that in order to have a periodic motion $A_1 = A_2 = 0$ so that the secular terms –those that grow exponentially with time– are removed. After substituting the initial conditions x_0 and y_0, solving for the constants A_3 and A_4, and performing some algebraic manipulations on Equation 3.15 we can write the linearized solution in the xy-plane as:

$$\begin{aligned} x = x_0 \cos st + \frac{y_0}{\nu} \sin st \\ y = y_0 \cos st - \nu x_0 \sin st \end{aligned} \tag{3.16}$$

with

$$s = \sqrt{\alpha + \sqrt{\alpha^2 + \beta^2}}, \quad \alpha = 1 - \frac{1}{2}K, \quad \beta^2 = (2K+1)(K-1) \quad \text{and} \quad \nu = \frac{s^2 + 2K + 1}{2s} \tag{3.17}$$

Equation 3.16 describes an ellipse in the xy-plane centered at the collinear libration point and with the semi-major axis aligned with the $y-$axis. The continuous approximation of the orbit can then be used to initialize corrector schemes such as multiple shooting or collocation. From Equation 3.16 the period of the linearized solution, and also the non-linear one is $T = 2\pi/s$ [125], which means that the period of the solution does not depend on the initial conditions, but only the equilibrium point. This fact can be exploited for formation flying, where several satellites are required to move close to each other at all times. Furthermore, differentiating at $t = 0$ allow us to obtain the following relationships:

$$\begin{aligned} \dot{x}_0 &= \frac{s}{\nu} y_0 \\ \dot{y}_0 &= -s\nu x_0 \end{aligned} \tag{3.18}$$

which are usually employed to define the starting conditions for single-shooting corrector schemes. However, the error of this linear approximation grows fast with increasing distance form the equilibrium point, so continuation is needed in order to ensure convergence, Section 3.6.

3.4.2. Poincaré-Lindstedt Method

The Poincaré-Lindstedt method allow us to find a convergent series approximation of periodic solutions by using the expansion theorem and the periodicity of the solution. The method can be applied to any differential equations with the form:

$$\ddot{x} + \dot{x} = \epsilon f(x, \dot{x}, \epsilon), \quad (x, \dot{x}) \in D \subset \mathbb{R}^2 \tag{3.19}$$

where we assume that periodic solutions exist for small positive values of ϵ. This form is obtained in the CR3BP context by expressing the equations of motion in the vicinity of the equilibrium points as seen in Subsection 3.1.2. The Poincaré method consists of using time-varying frequencies by setting $\tau = \omega t$ and considering the corrected frequency

$$\omega = 1 + \sum_{n \leq 1} \omega_n, \quad \omega_n < 1 \tag{3.20}$$

The method then consists of finding the appropriate values of ω_n so that the secular terms that emerge from the expansion and would cause it to blow up can be removed. The main advantage of the Poincaré-Lindstedt method is that it allows to obtain an approximation of the solution with an arbitrary good precision. This method has been extensively used in astrodynamics for computing approximations of periodic solutions and its manifolds [73, 87, 101].

3.4.3. Three-dimensional approximations

This section summarizes the most relevant results to compute three-dimensional analytic periodic orbit approximations, which were proposed in 1979 by Richardson [101]. We start by considering the linearized equations of motion centered at a libration point, given by:

$$\begin{aligned} \ddot{x} - 2\dot{y} - (1 + 2c_2)x &= 0 \\ \ddot{y} + 2\dot{x} + (c_2 - 1)y &= 0 \\ \ddot{z} + c_2 z &= 0 \end{aligned} \tag{3.21}$$

If the initial conditions are limited to non-divergent solutions the linearized solution can be expressed as:

$$\begin{aligned} x &= A_1 \cos\lambda t + A_2 \sin\lambda t \\ y &= -kA_1 \sin\lambda t + kA_2 \cos\lambda t \\ z &= B_1 \sin\nu t + B_2 \cos\nu t \end{aligned} \tag{3.22}$$

Where A_i and λ define the in-plane amplitude and frequency, and B_i and ν the analogues in the out-of-plane. If $\lambda/\nu \in \mathbb{P}$ then Equation 3.22 defines a first-order quasi-periodic approximation. Planar Lyapunov orbits bifurcate into halo orbits when the in-plane and out-of-plane amplitudes are large enough to make the non-linear contributions of the system produce frequencies that are 1 : 1 resonant [101]. The linear approximation of such orbits can be written as:

$$\begin{aligned} x &= -A_x \cos(\lambda t + \phi) \\ y &= kA_x \sin(\lambda t + \phi) \\ z &= A_z \sin(\lambda t + \psi) \end{aligned} \tag{3.23}$$

where A_x, A_y and A_z are usually referred as the $x-$excursion, $y-$excursion and $z-$excursion. Due to the fact that halo orbits are one-dimensional tori, it is clear that there must exist an algebraic relationship between A_x and A_z, and between ϕ and ψ. That means that non-linear terms are required in order to find these relationships. Richardson [101] developed a third-order analytical approximation of the halo family using the Poincaré-Lindstedt method. As he states in his paper, not any solution with the form Equation 3.23 will be a halo orbit, only those that meet some specific relationships between A_x/A_z and ϕ/ψ will be.

The main idea of this method is that the nonlinearities of the problem change the solutions of the linearized system. A correcting value $\Delta = \lambda^2 - c_2$ is added to Equation 3.21 so that the first-order out-of-plane equation can be rewritten as:

$$z_1'' + \lambda^2 z_1 = \Delta z_1 \tag{3.24}$$

When Δ is considered as a perturbation we can obtain Equation 3.23 as a first-order solution. In order to account for the nonlinearities the Lindsdtedt-Poincaré method uses time-varying frequencies which can be written as

$$\omega = 1 + \sum_n \omega_n \tag{3.25}$$

the value of ω_n is then chosen in such a way that the secular terms that appear during the development are removed. The development of the equations up to third-order is a lengthy process from which we will only review the conclusions and the main equations, the interested reader can check [101].

From the second-order equations he found that ω_1 is not needed so

$$\omega_1 = 0 \tag{3.26}$$

and from the third order expansion he found that

$$\omega_2 = s_1 A_x^2 + s_2 A_z^2 \tag{3.27}$$

where s_1 and s_2 are constants with long expressions. Furthermore, he showed that some of the secular terms that appear cannot only be removed by tweaking ω_n and that there must be a relationship between amplitudes and phases. The amplitude relationship can be expressed as

$$l_1 A_x^2 + l_2 A_z^2 + \Delta = 0 \tag{3.28}$$

where l_1 and l_2 are constants. The phase constraint is

$$\psi = \phi + n\frac{\pi}{2}, \quad n = 1,3 \tag{3.29}$$

where the value of n states whether the orbit belongs to either the north or south family. Finally, the third-order analytic approximation is found to be

$$\begin{gathered}
x = a_{21} A_x^2 + a_{22} A_z^2 - A_x \cos\tau_1 + (a_{23} A_x^2 - a_{24} A_z^2)\cos 2\tau_1 + (a_{31} A_x^3 - a_{32} A_x A_z^2)\cos 3\tau_1 \\
y = k A_x \sin\tau_1 + (b_{21} A_x^2 - b_{22} A_x^2)\sin 2\tau_1 + (b_{31} A_x^3 - b_{32} A_x A_z^2)\sin 3\tau_1 \\
z = \delta_n A_z \cos\tau_1 + \delta_n d_{21} A_x A_z(\cos 2\tau_1 - 3) + \delta(d_{32} A_z A_x^2 - d_{31} A_z^3)\cos 3\tau_1
\end{gathered} \tag{3.30}$$

where the value for all the constants can be found in [101]. Equation 3.30 allows then to compute the analytic approximation of halo orbits by simply evaluating the previous expression. Equation 3.30 can also be used to obtain the vertical Lyapunov family. In that case the expression does not change, but is has to be evaluated with $A_x = 0$.

3.5. Correction methods

The problem of finding a periodic or quasi-periodic orbit can be seen as a two-point boundary value problem (BVP). BVP arise commonly in astrodynamics, either in the computation of closed orbits, or in targeters such as the Lambert's problem [9]. A two-point boundary value problem can be expressed formally as:

$$\begin{gathered}\dot{\mathbf{x}}(t)+\mathbf{f}_0(t,\mathbf{x}(t))=0\\ \mathbf{x}(t_0)=\mathbf{x}_0,\quad \mathbf{x}(t_1)=\mathbf{x}_1\quad \text{or}\\ \mathbf{x}(t_0)=\mathbf{x}(t_1)\quad \dot{\mathbf{x}}(t_0)=\dot{\mathbf{x}}(t_1)\end{gathered}\tag{3.31}$$

These problems can be solved iteratively using methods such as shooting, where the BVP is converted to an initial-value problem; or relaxation methods, where the differential equations are replaced by difference equations, such as the collocation methods [47]. Each of these methods will be described and implemented; afterwards their performance, accuracy and stability will be discussed and compared.

3.5.1. Shooting technique

The idea behind the shooting method is to obtain a procedure that turns the BVP into an initial value problem [10]. Breakwell and Brown were one of the first ones to use this method to compute halo orbits in 1979 [21]. First, the equations of motion are linearized about the approximated orbit, then by applying a small perturbation $\delta\mathbf{x}$ we obtain a system of linear first-order differential equations such as $\dot{\mathbf{x}}=\mathbf{Ax}$. Using the 6×6 transition matrix $\Phi(t,t_0)$ allows us to obtain the state at any given time

$$\dot{\mathbf{x}}(t)=\Phi(t,t_0)\mathbf{x}(t_0)\tag{3.32}$$

by applying perturbation to Equation 3.32 we can compute the changes that need to be applied to the initial conditions in order to meet some final conditions.

$$\delta\dot{\mathbf{x}}(t)=\Phi(t,t_0)\delta\mathbf{x}(t_0)\tag{3.33}$$

Then it is possible to iteratively correct the initial state so that Equation 3.31 holds. The state transition is the matrix of partial derivatives $\frac{\partial\mathbf{x}(t)}{\partial\mathbf{x}(t_0)}$, and reflects how the variations in the initial state $\mathbf{x_0}$ affect a state $\mathbf{x}(t)$. The state transition matrix can be obtained by integrating the variational equations [47]

$$\dot{\mathbf{\Phi}}=F(t)\Phi(t,t_0)\tag{3.34}$$

where $F(t)=H[\mathbf{x}(t)]$ is obtained by computing the Hessian matrix of the state or the Jacobian of the flow and $\Phi(t_0,t_0)=I$. So the state transition matrix has to be propagated along with the equations of motion. For the CR3BP, $F(t)$ is given by [21]:

$$\mathbf{F}(t) = \begin{pmatrix} 0 & I \\ U_{xx} & 2\Omega \end{pmatrix} \tag{3.35}$$

where I is a 3×3 identity matrix and

$$\Omega = \begin{pmatrix} 0 & 1 & 0 \\ -1 & 0 & 0 \\ 0 & 0 & 0 \end{pmatrix} \tag{3.36}$$

and U_{xx} is the matrix of second partial derivatives of $\mathbf{U}$ with respect to x, y, z along the orbit:

$$\begin{aligned}
U_{x,x} &= 1 + \frac{3(1-\mu)(x-\mu)^2}{r_1^5} - \frac{(1-\mu)}{r_1^3} + \frac{3\mu(x+1-\mu)^2}{r_2^5} - \frac{\mu}{r_2^3} \\
U_{x,y} = U_{y,x} &= \frac{3(1-\mu)(x-\mu)y}{r_1^5} + \frac{3\mu(x+1-\mu)y}{r_2^5} \\
U_{x,z} = U_{z,x} &= \frac{3(1-\mu)(x-\mu)z}{r_1^5} + \frac{3\mu(x+1-\mu)z}{r_2^5} \\
U_{y,y} &= 1 + \frac{3(1-\mu)y^2}{r_1^5} - \frac{(1-\mu)}{r_1^3} + \frac{3\mu y^2}{r_2^5} - \frac{\mu}{r_2^3} \\
U_{y,z} = U_{z,y} &= \frac{3(1-\mu)yz}{r_1^5} + \frac{3\mu yz}{r_2^5} \\
U_{z,z} &= \frac{3(1-\mu)z^2}{r_1^5} - \frac{(1-\mu)}{r_1^3} + \frac{3\mu z^2}{r_2^5} - \frac{\mu}{r_2^3}
\end{aligned} \tag{3.37}$$

Note that Equation 3.33 does not account for the fact that changing the initial state will change the time it takes to intersect the plane we use to stop the integration, the Poincaré map. To correct this fact, Equation 3.33 is expanded in a Taylor series about the final state.

$$\delta\mathbf{x}(t_f + \delta t_f) = \Phi(t_f, t_0)\delta\mathbf{x}(t_0) + \left.\frac{\partial \mathbf{x}}{\partial t}\right|_{t_f} \delta t_f + \mathcal{O}(\delta t^2) \tag{3.38}$$

Equation 3.31 can be very sensible to initial condition deviations, in other words, small variations $\mathbf{x}_0$ give rise to large changes in the propagated flow after a long enough time has passed. Then, the shooting method will have problems converging to a solution or may not be able to find it if the initial guess is not accurate enough. The more general shooting method is usually simplified when computing periodic orbits. Commonly, we exploit the symmetries of the periodic orbit in order to reduce the propagation time and mitigate the potential intrinsic instabilities of the system. In order to deal with unstable problems, the multiple shooting method was developed [47]. This scheme divides the problem in intervals and performs shooting at each of them; the smaller the propagation time the more unlikely it is that instabilities become too large to avoid convergence. We will briefly explain how to compute each of the families by using the shooting method.

Planar Lyapunov orbits

The fact that this family lies in the xy-plane, and that it is symmetric with respect to the $y = 0$ plane is used to simplify the problem. To maximize the number of zero elements, the following initial conditions are typically used to compute planar Lyapunov orbits $\mathbf{x}_0 = (x_0, 0, 0, 0, \dot{y}_0, 0)^T$, which can be obtained from Equation 3.18. The propagation is stopped at the $x-$axis after half a revolution. Since the initial condition does not have any z-component, $\mathbf{x}(T/2)$ will not have either. Also, due to the fact that the orbit must be symmetric with respect to the $y = 0$ plane, it can be inferred that $\dot{x} = 0$ at the the plane intersection. Therefore, the corrector scheme will aim at iteratively reduce $\dot{x}$ to zero. Figure 3.8 illustrates how the correction scheme iteratively converges the Lyapunov orbit by nullifying $\dot{x}$.

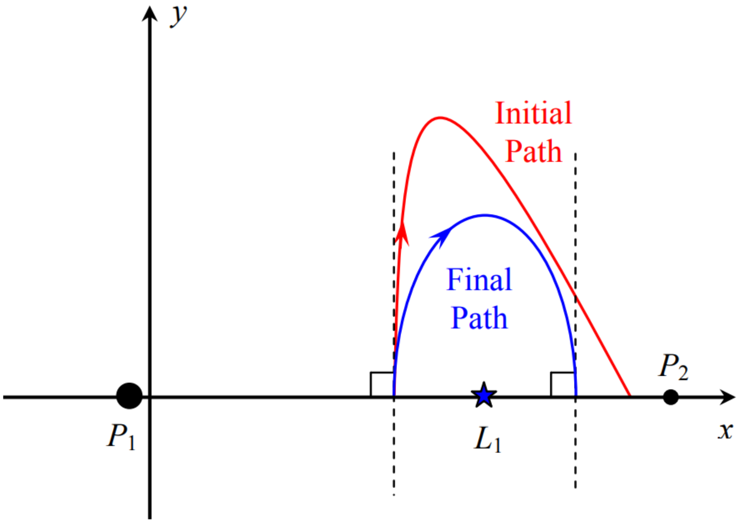

Figure 3.8: Initial guess and final orbit using single shooting for planar Lyapunov orbits [58].

Typically, although not necessary, either x_0 or $\dot{y}_0$ are taken as constant. This allow us to directly map errors from $\dot{x}$ to $\dot{y}_0$ for instance. The equations for the corrector scheme with x_0 fixed will be developed. Note that the process would be very similar for $\dot{y}_0$ fixed. We start by reducing Equation 3.38 by using the y_f and $\dot{x}_f$ rows:

$$\begin{pmatrix} \delta y_f \\ \delta \dot{x}_f \end{pmatrix} = \begin{bmatrix} \frac{\partial y_f}{\partial \dot{y}_0} & \dot{y} \\ \frac{\partial \dot{x}_f}{\partial \dot{y}_0} & \ddot{y} \end{bmatrix} \begin{pmatrix} \delta \dot{y}_0 \\ \delta \tau \end{pmatrix} \tag{3.39}$$

Since the propagation is stopped at $y = 0$ we can substitute it, solve for $\delta\tau$ and then write the remaining equation

$$\delta \dot{x}_f = \left(\frac{\partial \dot{x}_f}{\partial \dot{y}_0} - \frac{\ddot{y}}{\dot{y}} \frac{\partial y_f}{\partial \dot{y}_0} \right) \delta \dot{y}_0 = \left(\Phi_{45} - \frac{\ddot{y}}{\dot{y}} \Phi_{25} \right) \delta \dot{y}_0 \tag{3.40}$$

Equation 3.40 permits to compute the initial state correction $\delta \dot{y}_0$ to reduce $\dot{x}$ and make the orbit symmetric and thus periodic. If we propagate again after applying the correction once the orbit might not be yet periodic. We must iteratively apply this scheme until $|\dot{x}| < \epsilon$. Once this condition is met we can propagate the orbit over its complete period to get the trajectory of the planar Lyapunov orbit.

Vertical Lyapunov orbits

The vertical Lyapunov orbits are three-dimensional orbits, so it is not possible to use the simplifications used for planar Lyapunov orbits. Nonetheless, eight-shaped orbits are characterized by a double symmetry that can be exploited to simplify and improve the stability of the scheme. They are symmetric with respect to the $y = 0$ plane and the $z = 0$ plane, so it is only necessary to propagate until $t = T/4$ to be able to extrapolate the full orbit by symmetry. Although there are different options to choose as initial state, we choose the zenith of the orbit $\mathbf{x}_0 = (x_0, 0, z_0, 0, \dot{y}_0, 0)^T$ as the initial point [58]. Then, the initial state is propagated until it reaches $z = 0$. Due to its double symmetry, the vertical Lyapunov orbit must have $y = 0$ and $\dot{x} = 0$ at the $z = 0$ plane. These are the control parameters that will be used in the correction scheme. Similar to the planar Lyapunov orbits, one of the initial state parameters is fixed; in this case we choose to keep z_0 fixed.

Again the first step is to extract from Equation 3.38 the rows of interest, in this case $x, y, \dot{x}$.

$$\begin{pmatrix} \delta y_f \\ \delta z_f \\ \delta \dot{x}_f \end{pmatrix} = \begin{bmatrix} \frac{\partial y_f}{\partial x_0} & \frac{\partial y_f}{\partial \dot{y}_0} & \dot{x}_f \\ \frac{\partial z_f}{\partial x_0} & \frac{\partial z_f}{\partial \dot{y}_0} & \dot{y}_f \\ \frac{\partial \dot{x}_f}{\partial x_0} & \frac{\partial \dot{x}_f}{\partial \dot{y}_0} & \ddot{x}_f \end{bmatrix} \begin{pmatrix} \delta x_0 \\ \delta \dot{y}_0 \\ \delta \tau \end{pmatrix} \tag{3.41}$$

Since the integration is stopped at the $z = 0$ plane, $z_f = 0$ so Equation 3.41 can be expressed as:

$$\begin{pmatrix} \delta y_f \\ \delta \dot{x}_f \end{pmatrix} = \begin{bmatrix} \frac{\partial y_f}{\partial x_0} - \frac{\dot{x}}{\dot{y}} \frac{\partial z_f}{\partial x_0} & \frac{\partial y_f}{\partial \dot{y}_0} - \frac{\dot{x}}{\dot{y}} \frac{\partial z_f}{\partial \dot{y}_0} \\ \frac{\partial \dot{x}_f}{\partial x_0} - \frac{\ddot{x}}{\dot{y}} \frac{\partial z_f}{\partial x_0} & \frac{\partial \dot{x}_f}{\partial \dot{y}_0} - \frac{\ddot{x}}{\dot{y}} \frac{\partial z_f}{\partial \dot{y}_0} \end{bmatrix} \begin{pmatrix} \delta x_0 \\ \delta \dot{y}_0 \end{pmatrix} = \begin{pmatrix} \Phi_{21} - \frac{\dot{x}}{\dot{y}} \Phi_{31} & \Phi_{25} - \frac{\dot{x}}{\dot{y}} \Phi_{35} \\ \Phi_{41} - \frac{\ddot{x}}{\dot{y}} \Phi_{31} & \Phi_{45} - \frac{\ddot{x}}{\dot{y}} \Phi_{35} \end{pmatrix} \begin{pmatrix} \delta x_0 \\ \delta \dot{y}_0 \end{pmatrix} \tag{3.42}$$

Using Equation 3.42 we can find the corrections that need to be applied to the initial state to remove the errors when crossing the $z = 0$ plane. The process is repeated until $|y| < \epsilon$ and $|\dot{x}| < \epsilon$. Similar equations can be obtained by fixing any other of the initial state components.

Halo orbits

Halo orbits are also three-dimensional orbits, but they only have one symmetry with respect to the $z = 0$ plane, which will be exploited to simplify the computations. Similarly to the vertical orbits, the initial state is located at the zenith $\mathbf{x}_0 = (x_0, 0, z_0, 0, \dot{y}_0, 0)^T$, and one of them will be kept constant, in this case z_0. The initial state is propagated until in reaches again the $y = 0$ plane, where we will require the velocity vector to be perpendicular to the plane in order to ensure that the orbit is symmetric. The control variables will be thus $\dot{x}$ and $\dot{z}$.

The scheme is derived again from Equation 3.38 from where we retain the rows corresponding to $y_f, \dot{x}_f$ and $\dot{z}_f$ which yields

$$\begin{pmatrix} \delta y_f \\ \delta \dot{x}_f \\ \delta \dot{z}_f \end{pmatrix} = \begin{bmatrix} \frac{\partial y_f}{\partial x_0} & \frac{\partial y_f}{\partial \dot{y}_0} & \dot{y}_f \\ \frac{\partial \dot{x}_f}{\partial x_0} & \frac{\partial \dot{x}_f}{\partial \dot{y}_0} & \ddot{x}_f \\ \frac{\partial \dot{z}_f}{\partial x_0} & \frac{\partial \dot{z}_f}{\partial \dot{y}_0} & \ddot{z}_f \end{bmatrix} \begin{pmatrix} \delta x_0 \\ \delta \dot{y}_0 \\ \delta \tau \end{pmatrix} \tag{3.43}$$

and because the integration is stopped at $y = 0$ we can rearrange Equation 3.43 into

$$\begin{pmatrix} \delta \dot{x}_f \\ \delta \dot{z}_f \end{pmatrix} = \begin{bmatrix} \frac{\partial \dot{x}_f}{\partial x_0} - \frac{\ddot{x}_f}{\dot{y}_f}\frac{\partial y_f}{\partial x_0} & \frac{\partial \dot{x}_f}{\partial \dot{y}_0} - \frac{\ddot{x}_f}{\dot{y}_f}\frac{\partial y_f}{\partial \dot{y}_0} \\ \frac{\partial \dot{z}_f}{\partial x_0} - \frac{\ddot{z}_f}{\dot{y}_f}\frac{\partial y_f}{\partial x_0} & \frac{\partial \dot{z}_f}{\partial \dot{y}_0} - \frac{\ddot{z}_f}{\dot{y}_f}\frac{\partial y_f}{\partial \dot{y}_0} \end{bmatrix} \begin{pmatrix} \delta x_0 \\ \delta \dot{y}_0 \end{pmatrix} = \begin{pmatrix} \Phi_{41} - \frac{\ddot{x}_f}{\dot{y}_f}\Phi_{21} & \Phi_{45} - \frac{\ddot{x}_f}{\dot{y}_f}\Phi_{25} \\ \Phi_{61} - \frac{\ddot{z}_f}{\dot{y}_f}\Phi_{21} & \Phi_{65} - \frac{\ddot{z}_f}{\dot{y}_f}\Phi_{25} \end{pmatrix} \begin{pmatrix} \delta x_0 \\ \delta \dot{y}_0 \end{pmatrix} \tag{3.44}$$

Equation 3.44 allows to find the halo orbit by mapping the control parameters, namely $\dot{x}$ and $\dot{z}$, into initial state corrections. The process has to be repeated until $|\dot{x}| < \epsilon$ and $|\dot{z}| < \epsilon$. Then we can propagate the orbit to get the full period.

3.5.2. Collocation methods

A collocation method essentially consists of creating an approximate solution $\mathbf{x}_\pi$ of the differential equation as a linear combination of functions. The collocation method using piecewise polynomials to solve two-point boundary problems was first developed by Russell and Shampine in 1971 [103]. In this method, the trajectory is firstly discretized into N equally-spaced intervals, with $N + 1$ break points

$$0 \leq \tau_{0,0} < \tau_{1,0} < ... < \tau_{N,0} = 1 \tag{3.45}$$

where each of the polynomials forming the piecewise polynomial will be computed. Note that the domain has been normalized such that is covers $[0, 1]$. Then each of the intervals is subdivided into m points where the differential equations must be satisfied, these are the collocation points

$$\tau_{i,1} < \tau_{i,2} < ... < \tau_{i,m} \tag{3.46}$$

The most common collocation points are [52]:

- Gauss-Legendre points: The points $\tau_k,\ k = 1, 2...m$ are the roots of the Legendre polynomial of degree m mapped to the interval $[0, 1]$. Because the roots of the Legendre polynomial $\sigma_k,\ k = 1, 2...m$ are defined on $[-1, 1]$ they have to be shifted and resized $\tau_k = (1 + \sigma_k)/2$. The extremes of the interval are never part of the collocation points. For $m = 1$ this scheme produces the midpoint rule. The accuracy of the scheme is $\mathcal{O}(h^{2m})$ where h is the size of the largest interval $|\tau_k + 1 - \tau_k|$.

- Radau points: the extremes of the interval $[0,1]$ are part of the collocation points τ_1 and τ_m, and the rest are obtained from the roots of the Radau polynomial of degree m. The point-wise accuracy of the scheme is $\mathcal{O}(h^{2m-1})$.
- Lobatto points: Similar to Gauss-Legendre, but the extremes are included and then the $m-2$ remaining points are the roots of the Legendre polynomial. The point-wise accuracy of the scheme is $\mathcal{O}(h^{2m-1})$.

Gauss-Legendre collocation is specially appealing for several reasons. It is symplectic, which means that it preserves the symplectic nature of the Hamiltonian [129], i.i. it conserves the energy. In general Runge-Kutta methods transform the Hamiltonian into dissipative (non-Hamiltonian) systems, which has a completely different long-term behaviour [26]. It exhibits *superconvergence* at the mesh boundaries where its state accuracy is $\mathcal{O}(h^{2m-1})$ [97]. Moreover, it presents great stability (A-stability and B-stability) [60]. For all of that, Gauss-Legendre collocation is a good choice for solving Hamiltonian systems, and it is the one chosen for this work. The sum of the equally-spaced and collocation points form a mesh where the solution, either the periodic or quasi-periodic orbit, will be obtained, see Figure 3.9.

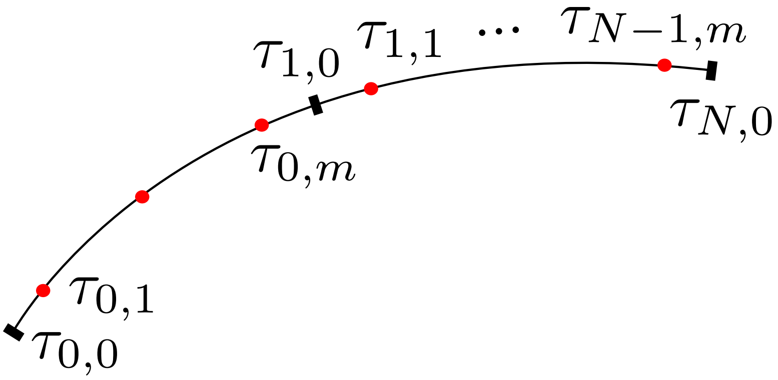

Figure 3.9: A figure showing an example of the Gauss-Legendre mesh

Also, note that all collocation methods are indeed implicit Runge-Kutta methods, however not all Runge-Kutta methods are collocation techniques [68].

In order to solve a non-linear autonomous boundary value problem by collocation we impose the following conditions

$$\mathbf{x}_\pi(t_i) = \mathbf{x}_i \quad \text{and} \quad \mathbf{x}'_\pi(t_{ij}) = \mathbf{f}(x_{ij}) \tag{3.47}$$

for $1 \leq i \leq N$ and $1 \leq j \leq m$. This means that the boundary conditions must be satisfied at the break points $\mathbf{x}_i$ and that the flow has to be tangent to the collocation points x_{ij}. In general, the problem is solved by assuming that the approximated solution can by expressed by a linear combination of n given functions $\Psi_0(\tau), ..., \Psi_n$ [8]

$$\mathbf{x}(\tau) \approx \mathbf{X}(\tau) = \sum_{j=0}^{m} c_j \Psi_j(\tau) \tag{3.48}$$

where it is assumed that all $\Psi_j(\tau)$ satisfy the boundary conditions and so any linear combination will also meet them. Normally, the coefficients $c_1, ..., c_n$ are obtained by demanding the approximated function $\mathbf{x}_\pi$ at the collocation points to be tangent to the flow.
With all of that, we can create a Lagrange interpolation polynomial of degree m

$$\mathbf{X}(\tau) = \sum_{k=0}^{m} \mathbf{X}_{i,k} l_k(\hat{\tau}) \quad \text{with} \quad \hat{\tau} = \frac{\tau - \tau_{i,0}}{\tau_{i+1,0} - \tau_{i,0}} \tag{3.49}$$

and $l_k(\hat{\tau})$ is the Lagrange basis polynomials

$$l_k(\hat{\tau}) = \prod_{\substack{j=0 \\ j\neq k}}^{m} \frac{\hat{\tau} - \hat{\tau}_j}{\hat{\tau}_k - \hat{\tau}_j} \tag{3.50}$$

which satisfy the following properties

$$l_k(\hat{\tau}_k) = 1 \quad \text{and} \quad l_k(\hat{\tau}_l) = 0 \quad \text{when} \quad l \neq k \tag{3.51}$$

The Lagrange form is one of the standard ways to define the interpolation polynomial [85]. However, this is not the only one, other options exist using Laguerre polynomial or Hermite splines. Throughout this work, only the case with Lagrange interpolation is presented and developed.

By comparing Equation 3.48 and Equation 3.49, it is clear that if we use Lagrange interpolation, the approximated states $\mathbf{X}_{i,j}$ are the coefficients to be determined. The Gauss-Legendre collocation requires the flow to be tangent to the derivative of the approximation at the collocation points. So the collocation condition is generically

$$\sum_{k=0}^{m} \mathbf{X}_{i,k} \frac{dl_k}{d\hat{\tau}_j} = \mathbf{F}(\mathbf{X}_{i,j}, \tau_{i,j}) \tag{3.52}$$

and must hold at all intervals $i = 0, ...N-1$ for all the collocation times $\tau_{i,j}, j = 1, ..., m$. Note that Equation 3.52 is applied at all collocation times, but the interpolation polynomial not only includes the collocation points but also $\tau_{i,0}$. Since $\mathbf{X}(\tau)$ must be continuous along the whole domain, the continuity between each of the polynomials can be imposed as

$$\sum_{j=0}^{m} \mathbf{X}_{i,j} l_j(1) = \mathbf{X}_{i+1,0} \tag{3.53}$$

for all $i = 0, ..., N-1$. If we sum the collocation conditions Equation 3.52 and the continuity conditions Equation 3.53 we have $N(m+1)$ vector equations, and there are $N(m+1)+1$ vector states that define the mesh. Therefore, one more vector equation is needed in order to be able to solve the problem. This is the periodicity condition

$$\mathbf{X}_{N,0} = \mathbf{X}_{0,0} \tag{3.54}$$

Together Equation 3.52, Equation 3.53, and Equation 3.54 form a system with the form $\mathbf{F}(\mathbf{X}) = 0$ which can be solved by using the Newton-Raphson method. A similar development is presented in Subsection 4.9.3

3.5.3. Shooting vs Collocation

In Subsection 3.5.1 and Subsection 3.5.2 the theory and implementation details behind the shooting and collocation methods for computing periodic orbits were presented. At this point, it is clear that these two methods are inherently different, concerning the initial data that is required, the computational effort, and stability among others. In this section, these topics will be discussed and both methods' performance and implementations will be compared.

A (single) shooting method only requires an initial state to be initialized, this is particularly helpful since it is relatively easy to find starting conditions in literature. After having computed a closed periodic orbit we can obtain the full family by continuation, Section 3.6, avoiding the lengthy expressions that appear in the 3^{rd}-order approximations of the three-dimensional orbits. On the other hand, the collocation method requires to have an approximation of the states at every point of the mesh, so the full analytical approximation needs to be computed beforehand. Not only that, but the Gauss-Legendre collocation method requires to have a very specific and not-uniform mesh. This means that in some cases an additional step exists which transforms the approximation into one with the collocation mesh, which will add a small overhead.

When using the shooting technique, the initial state is propagated by following the vector field flow, and then corrections are computed iteratively until the orbit converges. In that way the shooting scheme always follows the flow (meets the differential equations), and it converges once a closed orbit is obtained. On the other hand, collocation methods start with a full representation of the orbit which does not need to satisfy the dynamics of the system. Then, the collocation points –and eventually the break points after convergence– are forced to satisfy the flow iteratively by solving a system of algebraic equation. Figure 3.10 illustrates this fundamental difference between both methods

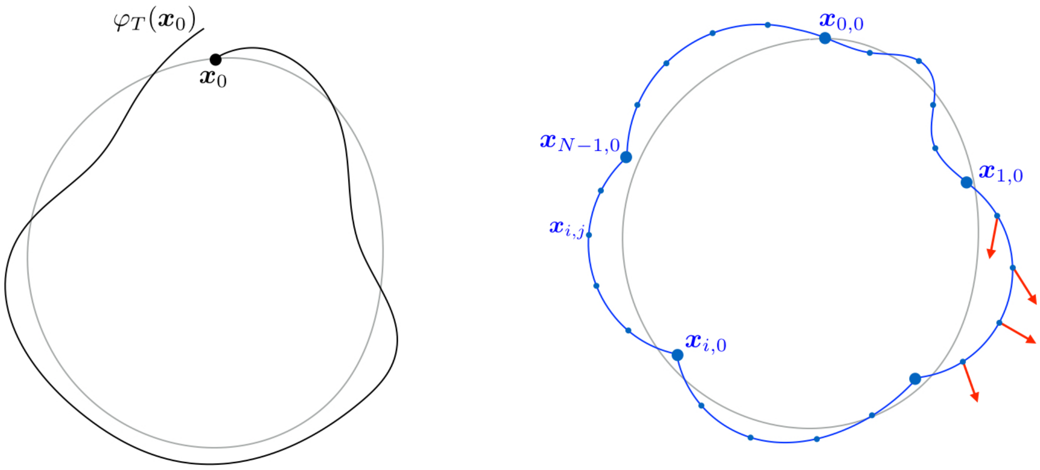

(a) Single Shooting method

(b) Collocation method

Figure 3.10: Shooting and collocation scheme for computing periodic orbits.

In both cases, the Newton-Rapson method is fundamentally used iteratively. However, while in the shooting methods we deal with a system of a few equations, the collocation method entails inverting very large matrices multiple times. In that sense, the shooting methods seems like a promising alternative; however, there is an important drawback. As it has been seen, Subsection 3.5.1, it suffers from a strong initial-guess dependency, in other words, that for inherently chaotic systems such as the CR3BP, small deviations in the initial conditions can cause large deviations in the final state, which can impede the scheme to converge. In order to mitigate that, a multiple shooting method would need to be used. However, by involving much more segments that need to be solved together we would lose the main advantage of the shooting method: its simplicity and computational speed. Furthermore, it has an excellent accuracy and a large attraction basis, this means that it is very robust for poor initial guesses. So, the Gauss-Collocation will make it simpler to compute the full families of quasi-periodic invariant tori that are required to solve our problem. For all those reasons, a Gauss-Collocation scheme will be used to find both the periodic orbits and the quasi-periodic invariant tori.

3.6. Continuation methods

In Section 3.4 we reviewed how to obtain an analytical approximation of members of the main four families of periodic orbits. Later in Section 3.5 we reviewed the two main methods, shooting (Subsection 3.5.1) and collocation (Subsection 3.5.2) to numerically converge an approximation to an exact periodic orbit. In this section, we will address the continuation methods. Continuation methods allow to step over the different members of a family without the necessity to first compute an approximation, and then the full solution of each member. Retrieving the full family of solutions can be advantageous to gain a better understanding of the dynamics of the system, see for instance [44]. Nonetheless, it can be challenging to make the correction scheme converge for an analytical approximation of a periodic orbit in very unstable regions, this is usually far form the equilibrium point. Continuation methods allow us to first compute a member of the family that lies in a more stable area and then use continuation iteratively and step over the different members until the aimed orbit is reached.

Most of the existing continuation algorithms were devised for computing one-dimensional manifolds [42, 100], although some exists for higher-dimensional manifolds [65]. In this work we will only review and work with one-dimensional solution branches. The two more common methods for computing families of periodic solutions in the context of the CR3BP are the natural parameter continuation and the pseudo-arclength continuation. Both methods will provide a better approximation of the periodic orbit than the analytical methods so that it can be fed to the differential correction method in order to find a solution.

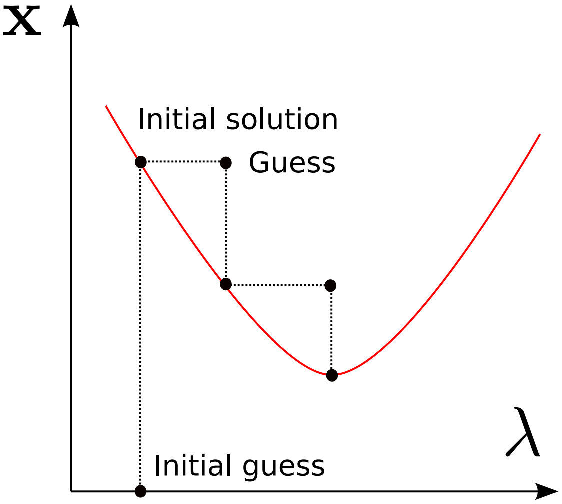

Figure 3.11: Natural parameter continuation.

3.6.1. Natural parameter continuation

Let the flow of the dynamical system by given by the finite-dimensional equation

$$\mathbf{f}_0(\mathbf{x},\lambda) = 0, \quad \mathbf{f}: \mathbb{R}^{n+1} \to \mathbb{R}^n \tag{3.55}$$

with $\mathbf{f}$ assumed to be sufficiently smooth. If $(\mathbf{x}_0,\lambda_0)$ is a solution of the problem, there is in general a one-dimensional branch that passes through it. In this method, a parameter of the system λ characterizes the family and it is used for continuation. A near member of the family $(\mathbf{x}_1,\lambda_1)$ can be computed by solving the extended system

$$\begin{aligned} \mathbf{f}(\mathbf{x},\lambda) &= 0 \\ \lambda &= \lambda_0 + \Delta\lambda \end{aligned} \tag{3.56}$$

and then using $(\mathbf{x}_0,\lambda_1)$ as an initial guess for the differential corrector method. This method assumes that $(\mathbf{x}_0,\lambda_1)$ lies on the basis of attraction of the corrector procedure to find $(\mathbf{x}_1,\lambda_1)$ [41].

Note that in the CR3BP there is not a explicit parameter in the equations that parameterizes the family (Section 3.1), nonetheless the different members of each family can be characterized by their Jacobi constant value. In order to add explicitly the extra parameter to the flow equation $\mathbf{f}_0$ we can use to so-called unfolding parameters, see Section 4.4 for more on that. This method is very simple to implement, however it can suffer from convergence problems because it does not take into account the local shape of the solution curve. If the slope with respect to the λ parameter is too steep the differential corrector scheme may not be able to converge, which will require to make $\Delta\lambda$ smaller, and consequently the algorithm would be less efficient.

3.6.2. Pseudo-arclength continuation

The pseudo-arclength continuation method was developed to solve the main problem of natural parameter continuation, to take into account the local shape of the solution manifold. It uses an already known orbit of the family to obtain a new guess. Let us clarify what this really means. Let $\mathbf{f}_0(\mathbf{x},\lambda) = 0$ be the flow of the system. If x_0, λ_0 is an already known solution of the vector field, we can construct an approximation of another solution $\mathbf{x}_1$ as

$$\tilde{\mathbf{x}}_1 = \mathbf{x}_0 + \dot{\mathbf{x}}_0 \Delta s \tag{3.57}$$

where Δs is the step-size of the continuation and $\dot{\mathbf{x}}_0$ is the unit tangent to the solution curve at $\mathbf{x}_0$ [41]. By differentiating Equation 3.55 with respect to the arclength s at $\mathbf{x}_0$ we obtain $\mathbf{f}_{\mathbf{x}}(\mathbf{x}_0,\lambda_0)\dot{\mathbf{x}}_0 = 0$. So $\dot{\mathbf{x}}_0$ is a null vector of the Jacobi matrix. The pseudo-arclength constraint can be expressed then as

$$(\mathbf{x}_1 - \mathbf{x}_0)\dot{\mathbf{x}}_0 - \Delta s = 0 \tag{3.58}$$

with $\mathbf{x}_1$ the solution for the current iteration which can be computed by extending Equation 3.55 with the arc-length continuation constraint

$$\begin{gathered}\mathbf{f}(\mathbf{x},\lambda)=0\\(\mathbf{x}_1-\mathbf{x}_0)\dot{\mathbf{x}}_0-\Delta s=0\end{gathered}\tag{3.59}$$

where Δs is adapted along the branch depending on the convergence rate of the Newton method. The main advantage of this method is that it does not require *a priori* knowledge of the evolution of the family and that it allows to use larger steps since the scheme accounts for the local shape of the solution curve.

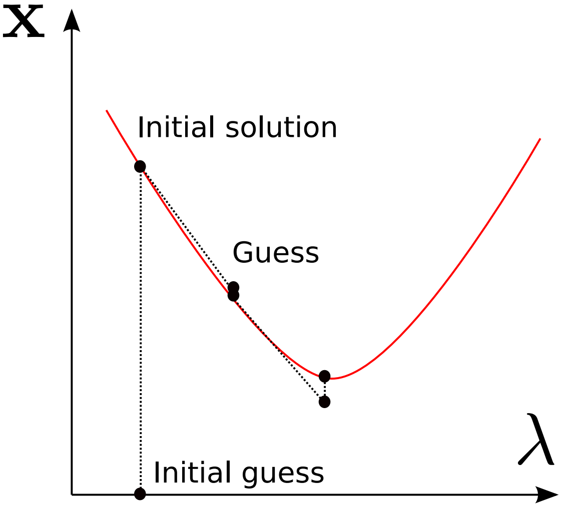

Figure 3.12: Pseudo-arclength continuation.

Figure 3.11 displays how typically natural parameter continuation works, while Figure 3.12 shows how the pseudo-arclength continuation.

4

Quasi-periodic orbits

This chapter contains the main formulation to obtain quasi-periodic orbits or invariant tori in the context of the CR3BP. First, the main formulation and the different methods to compute these tori are explained. The stroboscopic method that will be used is formulated and the extra constraints, namely phase and torus family, are described and formulated. Also, the augmented flow equation that will be used is presented. Then, the numerical implementation of a Gauss-Legendre collocation solver is explained together with some practicalities, such as how to compute the analytical approximations that will be used as first guess and the domain of existence of these tori. Next, the method used to compute the invariant manifold of tori is presented. The last part of the chapter addresses the creation of a database to be used in the optimization problem, how the solvers were implemented, a discussion about the parametrization used, and some other practicalities.

4.1. Introduction

The different kinds of bounded motions that appear in the CR3BP can be characterized by their dimensionality; in other words, the flow of all these bounded motions lies on a $n-$dimensional torus. Each $n-$dimensional torus has n fundamental frequencies that characterize the flow on it. The simplest case is the $0-$dimensional torus; these are the five equilibrium points at which the third body remains static in the synodical reference frame, Subsection 3.2.1. The center component of the libration points gives rise to the different families of periodic orbits that have already been studied, Section 3.3. Their motion lies on a $1-$dimensional torus and it is characterized by just one frequency. Similarly to the libration points, some of these periodic orbits have center components, which produce the so-called quasi-periodic orbits. Quasi-periodic motion lies on $2-$dimensional tori and it is characterized by two fundamental different frequencies.

The equilibrium points offer very promising possibilities for mission design: their hyperbolic (saddle) component allows to either arrive or depart from them at no cost, taking advantage of low-energy transfers. However, in the CR3BP there are just five $0-$dimensional tori, so the transfer space is very limited. On the other hand, periodic orbits also present a saddle component, therefore it is also possible to arrive/depart from them exploiting low-energy transfers. Nonetheless, there is only one periodic orbit of each family for a given Jacobi constant, so again the transfer space for a given energy level is rather limited. Here quasi-periodic orbits offer a very interesting alternative: for each Jacobi constant value there is a whole family of two-dimensional tori from where low-energy transfers can be envisioned, so the transfer space is richer and more varied.

Quasi-periodic orbits offer similar advantages to periodic orbits, but also new ones. They both present a bounded motion and have stable and unstable manifolds emanating from them, that allow for low-energy transfers. Another interesting fact about quasi-periodic orbits is that in more complex models periodic obits are more scarce and they degenerate into quasi-periodic orbits. For instance, in the Elliptic Restricted Three-Body Problem (ER3BP) the only periodic orbits that exist are the ones that are resonant with the primaries. The rest of the periodic orbits that appear in the CR3BP become quasi-periodic orbits in this problem. In this work we will only focus on two-dimensional tori in the context of the CR3BP, however tori with a dimensionality greater than two also exist.

4.2. Invariant Torus Formulation

Quasi-periodic motion occurs on a quasi-periodic invariant torus which is densely filled with quasi-periodic orbits [22, 109]. These quasi-periodic invariant tori are characterized by two fundamental frequencies: the longitudinal frequency w_1 and the latitudinal frequency w_2; the frequency vector is then given by $\boldsymbol{\omega} = (\omega_1, \omega_2)$. Consequently, a location on the surface of the torus can be described by two angles: longitude θ_1 and latitude θ_2, so that the angle vector is $\boldsymbol{\theta} = (\theta_1, \theta_2)$. Note that throughout this work, the angles will be normalized into a unit interval, in other words, all angles will be defined on $[0, 1)$ rather than $[0, 2\pi)$.

In general, the dynamics of the system can depend on the state of the third body, but also on a set of angles $\boldsymbol{\theta}$ changing at constant rates $\boldsymbol{\omega}$. This is not the case for the CR3BP, where the equations of motion can be written simply as

$$\dot{\mathbf{x}} = \mathbf{f}_0(\mathbf{x}) \tag{4.1}$$

but it appears in slightly more complex models such as the ER3BP. A formal description of the problem in the ER3BP is developed by Olikara in her PhD thesis [97].

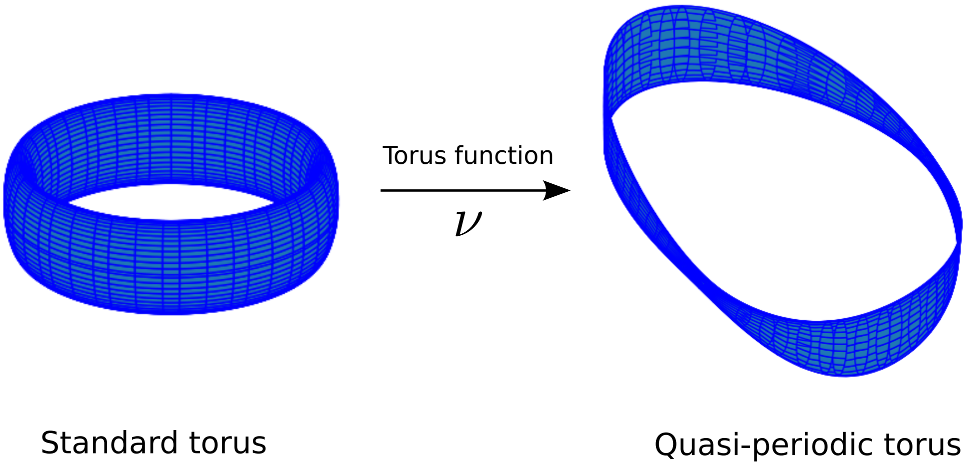

Figure 4.1: Mapping from the standard torus to the quasi-periodic torus using the torus function.

4.2.1. Invariance Equation

The torus function $\boldsymbol{v} : \mathbb{T}^p \to \mathbb{R}^n$ parameterizes the states on the standard torus using the angle vector $\boldsymbol{\theta}$, with $\mathbb{T}^p$ being the p−dimensional standard torus parameterized over $[0, 1)$. Figure 4.1 displays how the torus function maps points on the standard torus to states in the configuration state.

The search for a torus that describes quasi-periodic motion consists in finding a torus function v

whose image $T = \{\boldsymbol{v}(\boldsymbol{\theta})|\boldsymbol{\theta} \in \mathbb{T}^p\}$ in invariant under the flow of Equation 4.1. Let's focus on two-dimensional invariant tori, that is where $p = 2$. In order for the tori to be invariant under the flow $\mathbf{f}_0 : \mathbb{R}^n \to \mathbb{R}^n$ their surface has to be tangent to it. Substituting the torus function into Equation 4.1, imposing that $\mathbf{x} = \mathbf{v}(\boldsymbol{\theta})$, and using the chain rule yields the following invariance equation

$$\omega_1 \frac{\partial \mathbf{v}}{\partial \theta_1}(\boldsymbol{\theta}) + \omega_2 \frac{\partial \mathbf{v}}{\partial \theta_2}(\boldsymbol{\theta}) = \mathbf{f}(\mathbf{v}(\boldsymbol{\theta}), \boldsymbol{\theta}) \tag{4.2}$$

Equation 4.2 provides an equation for v, but the vector $\boldsymbol{\omega}$ is also unknown. In order to overcome this issue we could fix $\boldsymbol{\omega}$ or add more equations. Note that the frequency vector $\boldsymbol{\omega}$ must be rationally independent or not resonant, because the quasi-periodic invariant torus must be densely covered by quasi-periodic orbits. In other words, the ratio between ω_1 and ω_2 has to be irrational. If the ratio between w_1 and w_2 is rational the torus will not exist, due to this fact the tori family structure will resemble a Cantor set. This can generate problems to compute the tori when the continuation scheme falls into one of these resonant gaps.

There are two different approaches to compute the quasi-periodic invariant tori. The first one is to solve a system of Partial Differential Equations (PDE) –the invariance equation– on a grid of points. This is the most straightforward method, was proposed first by Schilder et al. [109] and leads to a full parametrization of the torus. The second method consists of computing invariant curves of maps. As they use objects of one dimension less, they are less susceptible to the curse of dimensionality[1]

Baresi et al. [13] studied and compared these methods. Specifically, he surveyed two PDE solvers, one based on Central Differences and the Discrete Fourier Transform and two based on invariant map solvers they called GMOS and KKG. GMOS is a modified version of the numerical method introduced by Gómez and Montero [55] which computed the Fourier coefficients of quasi-periodic orbits using stroboscopic mapping[2]. The modified version by Olikara and Scheeres [96] works directly with the states instead of the Fourier coefficients and the torus is computed by solving a two-point boundary problem. On the other hand, KKG uses similar ideas, but uses Poincaré maps rather than stroboscopic maps. They found GMOS to be the most accurate and flexible of all the methods. That is why, in this work, we will use this method to compute the quasi-periodic invariant tori.

---

[1] It refers to phenomena where the samples needed to estimate an arbitrary function with a given level of accuracy grows exponentially with respect to the number of input variables of the function.

[2] A stroboscopic map is a special case of Poincaré map for periodically driven systems.

4.2.2. The stroboscopic method

The key idea of the method proposed by Olikara et al. [97] is to reduce the dimension of the invariance equation. They achieve it by converting the flow into a stroboscopic map with associated time $T = 1/\omega_1$. By fixing a value of θ_1 and integrating over time T we arrive at θ_1 again because $\theta_1 = \theta_1 + 1$. However, the map in the θ_2 dimension gets shifted by a value $\rho = T\omega_2 = \omega_2/\omega_1$, the so-called rotation number. Since the ratio between ω_1 and ω_2 has to be irrational, the rotation parameter will also be irrational.

Instead of finding the torus function, a function that maps points from the standard torus to states on the tori as shown in Figure 4.1, we are interested in finding the circle function $\mathbf{w} = \mathbf{u}(\boldsymbol{\theta}_1, \cdot) : \mathbb{T}^1 \to \mathbb{R}^n$ that maps points on a standard circle to states on the stroboscopic map. So that the invariance equation can be rewritten as

$$\mathbf{w}(\theta_2 + \rho) = \boldsymbol{\phi}(\mathbf{w}(\theta_2)) \tag{4.3}$$

where $\boldsymbol{\phi}$ is the stroboscopic map at T. Equation 4.3 states that each of the states for a given θ_1 and θ_2 gets shifted by ρ in the θ_2, latitudinal direction, after the state is integrated over T. This equation applies to all $\theta_2 \in \mathbb{T}^1$ and for successive turns creates a dense torus, because ρ is irrational, that is, not resonant.

It is possible to create a boundary value problem by imposing that Equation 4.3 holds at each θ_2 and adding the following boundary condition: that the extreme on one side must be equal to the other one shifted by $-\rho$. In [97] this is formalized by defining a cylinder function $\mathbf{u} : [0,1] \times \mathbb{T}^1 \to \mathbb{R}^n$. Within the cylinder all trajectories are parallel, which means a trajectory is defined by a constant θ_2. For that reason from now on θ_1 and τ will be used interchangeably. The torus is created by twisting and closing the cylinder. The boundary value problem is then defined by

$$\frac{d\mathbf{u}}{d\tau}(\tau, \theta_2) = T\mathbf{f}(\mathbf{u}(\tau, \theta_2), \lambda_1, \lambda_2) \tag{4.4}$$

$$\mathbf{u}(0, \theta_2) = \mathbf{u}(1, \theta_2 - \rho) \tag{4.5}$$

4.3. Adding Constraints

4.3.1. Phase constraints

It has already been mentioned that autonomous dynamical systems such as the CR3BP have some peculiarities that have to be born in mind. One of these is that they permit time shifts, this means that a solution shifted in time is still a solution of the problem $\mathbf{u}(t) = \mathbf{u}(t + \sigma)$.

When computing periodic orbits a phase constraint had to be introduced, because otherwise the solution could only be obtained up to a phase shift. Periodic orbits are one-dimensional tori, the motion within the orbits can be fully described by a single parameter, and therefore its phase is constrained by one equation. Quasi-periodic orbits are two-dimensional tori and, analogously, two equations would be required.

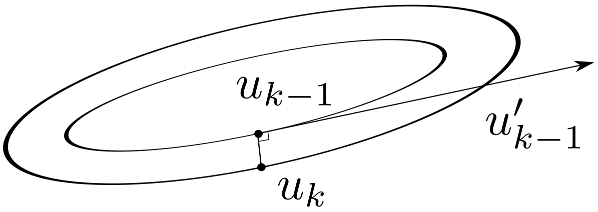

Figure 4.2: Geometric representation of the phase constraint.

One option could be to fix a point of the orbit to always have certain restrictions so that the phase ambiguity is removed, however better methods exist. In AUTO [43, 91], this problem was solved by using an ’anchor equation’ that tries to minimize the distance between neighboring solutions with respect to a change in phase [78]. This method has proved to be more robust in calculations and it is commonly used. Figure 4.2 displays how the phase constraint is constructed. The orbits are defined in such a way that it minimizes the distance with respect to a previously known solution. The phase constraints for an invariant torus are given by

$$\int_0^1 \langle \mathbf{u}(0,\theta_2) - \tilde{\mathbf{u}}(0,\theta_2), \frac{d\tilde{\mathbf{u}}}{d\tau}(0,\theta_2)\rangle d\theta_2 = 0 \tag{4.6}$$

$$\int_0^1 \langle \mathbf{u}(0,\theta_2) - \tilde{\mathbf{u}}(0,\theta_2), \frac{\partial\tilde{\mathbf{u}}}{\partial\theta_2}(0,\theta_2)\rangle d\theta_2 = 0 \tag{4.7}$$

where $\mathbf{u}$ is the solution we aim to obtain and $\tilde{\mathbf{u}}$ is a previously known solution. The concrete expressions to compute and implement the derivative terms will be explained in Section 4.5.

4.3.2. Torus family constraints

The Kolmogorov-Arnold-Moser (KAM) theory describes the properties of quasi-periodic solutions and has been extensively developed in the last decades. Due to the fact that this work builds on using quasi-periodic orbits for mission design rather than studying quasi-periodic motion itself, only the most relevant and useful results of KAM theory to our applications will be covered.

KAM theory states that for a $d-$dimensional quasi-periodic torus that exists in an autonomous Hamiltonian dynamical system which depends on r external parameters, the torus will lie in a

$(d-r)-$parameter family. Since quasi-periodic orbits are 2-dimensional tori, and the CR3BP has no external forcing parameters, each torus will lie in a 2-dimensional family. One way to parameterize them is by using their frequencies w_1 and w_2. In more complex models with forcing parameters such as the ER3BP, one-dimensional tori families will appear. Note that these families are not continuous due to the frequency resonances and topologically resemble a Cantor space.

The goal here is to obtain a set of equations that uniquely describe each torus, therefore two more equations are needed to select a single torus from the 2-dimensional family. Commonly the following constraints are used

$$\int_0^1 H(\mathbf{u}(0,\theta_2)d\theta_2 = H_{ref} \tag{4.8}$$

$$\int_0^1 \langle \mathbf{u}(0,\theta_2) - \tilde{\mathbf{u}}(0,\theta_2), \tilde{\mathbf{u}}'(0,\theta_2)\rangle d\theta_2 = \Delta s \tag{4.9}$$

Equation 4.8 is the energy constraint and fixes the value of the Hamiltonian at H_{ref}. By fixing the Hamiltonian we can uniquely relate quasi-periodic tori to periodic orbits with the same energy value, which will permit to initialize tori from their associated periodic orbit ,Section 4.6.

Equation 4.9 is the pseudo-arclength constraint. It sets a distance Δs between two tori with the same Jacobi constant value. $\tilde{\mathbf{u}}$ is a previously known solution, and $\tilde{\mathbf{u}}'$ is the tangent direction onto which the difference vector is projected. The tangent direction is computed as the difference between two known solutions. When the first torus is initialized, the tangent direction can be approximated by the difference between the first guess and the periodic orbits, which has shown to provide good results. Two more scalar equations will be needed in order to be able to use either T, ρ and ω_1, ω_2 indistinctly in the problem.

$$T\omega_1 = 1 \tag{4.10}$$

$$T\omega_2 = \rho \tag{4.11}$$

All the above equations describe the system of equations that needs to be solved in order to obtain each of the tori of the families. Equation 4.9 will allow us to step over these families to obtain the desired individual member.

4.4. Unfolding parameters

In the previous sections a complete description of the equations that define the problem of searching for a quasi-periodic torus has been provided. It has been seen that a torus is uniquely defined by two vector equations (4.10, 4.11) and six scalar equations (4.4-4.9). However, the original formulation of the problem only contains four free parameters. This is a common problem in Hamiltonian dynamical systems, and can be solved by adding two new free parameters λ_1, λ_2 –the so-called unfolding parameters– so that there is an equal number of equations and parameters. Another reasonable alternative could be to remove two scalar equations, however that would make the problem indeterminate since we would not be able to find a single torus from the 2-dimensional family. A different approach could be to use a non-linear least-squares method to avoid the problem of having more equations than parameters. Nonetheless, we will use unfolding parameters to create a fully determined system that can be solved using a Newton method for instance.

In the case that the system has integrals of motion, they can be used to augment the vector field with their gradient. This is very convenient when computing periodic orbits since they exist in only one parameter family. In that case, the vector field can be augmented as

$$\mathbf{f}(\mathbf{x}) = \mathbf{f}_0(\mathbf{x}) + \lambda \frac{\partial H}{\partial \mathbf{x}}(\mathbf{x}) \tag{4.12}$$

where it can be proved that only periodic solutions exist when $\lambda = 0$. The problem with computing invariant tori is that they exist in two-parameter families, and the CR3BP has only one integral of motion. So one extra expression is required to augment the vector field. Olikara [97] proposes using the following vector field

$$\mathbf{f}(\mathbf{x}, \lambda_1, \lambda_2) = \mathbf{f}_0(\mathbf{x}) + \lambda_1 \frac{\partial I_1}{\partial \mathbf{x}}(\mathbf{x}) + \lambda_2 \frac{\partial I_2}{\partial \mathbf{x}}(\mathbf{x}) \tag{4.13}$$

and using the torus action, which behave like local integrals of motion to obtain

$$\begin{aligned} \frac{\partial I_1}{\partial x}(u, T, \rho)\bigg|_{\tau,\theta_2} &= -\Big(\frac{\partial y}{\partial x}^T \mathbf{J} \frac{\partial y}{\partial x}\Big)\Big(T\mathbf{f}_0(\mathbf{u}, \theta - \rho \frac{\partial u}{\theta}\Big) \\ \frac{\partial I_2}{\partial x}(u)\bigg|_{\tau,\theta_2} &= -\Big(\frac{\partial y}{\partial x}^T \mathbf{J} \frac{\partial y}{\partial x}\Big)\frac{\partial u}{\partial \theta}\bigg|_{\tau,\theta_2} \end{aligned} \tag{4.14}$$

However instead of I_1, it is simpler to use the Hamiltonian, which can be used to replace any of the actions. So the augmented vector field that will be used for computing the tori is

$$\mathbf{f}(\mathbf{x}, \lambda_1, \lambda_2) = \mathbf{f}_0(\mathbf{x}) + \lambda_1 \frac{\partial H}{\partial \mathbf{x}}(\mathbf{x}) + \lambda_2 \frac{\partial I_2}{\partial \mathbf{x}}(\mathbf{x}) \tag{4.15}$$

where specifically in the CRBP3 the following applies

$$-\frac{\partial y}{\partial x}^T \mathbf{J} \frac{\partial y}{\partial x} = \begin{pmatrix} 0 & 0 & +2 & -1 & 0 & 0 \\ -2 & 0 & 0 & 0 & -1 & 0 \\ 0 & 0 & 0 & 0 & 0 & -1 \\ +1 & 0 & 0 & 0 & 0 & 0 \\ 0 & +1 & 0 & 0 & 0 & 0 \\ 0 & 0 & +1 & 0 & 0 & 0 \end{pmatrix} \tag{4.16}$$

4.5. Numerical computation

This chapter addresses the implementation of the set of equations that define the invariant quasi-periodic torus. By solving this set of equations we will obtain the cylinder function **u** that defines the torus and T, ρ, ω_1 and ω_2. For that, we need to discretize the domain in order to impose Equation 4.1 at every mesh node.

Firstly, the angle $\theta_1 = \tau$ is discretized using a continuous piece-wise polynomial with N_1 intervals, so $N_1 + 1$ break points. Then, Gauss-Legendre collocation will be applied to every interval. Gauss-Legendre collocation consist of taking very specific points, where the flow equation must hold. The m collocation points must be the roots of the Legendre polynomial of degree m, which must be scaled and translated to meet the boundaries of each interval since the domain of the Legendre polynomial is $[-1, +1]$, Subsection 3.5.2. For instance if x is a root of the m-degree Legendre polynomial over $[-1, +1]$, we obtain its transformation x' to $(\tau_{i,0}, \tau_{i+1,0})$ by using

$$x' = \frac{2x - (\tau_{i+1,0} + \tau_{i,0})}{\tau_{i+1,0} - \tau_{i,0}} \tag{4.17}$$

The notation $\tau_{i,j}$ is used to refer to the j^{th} collocation point within the $i+1$ interval. With this notation we can write the piece-wise discretization as

$$0 = \tau_{0,0} < \tau_{1,0} < ... < \tau_{N_1-1,0} < \tau_{N_1,0} = 1 \tag{4.18}$$

and the collocation points at the $i+1$-th interval are

$$\tau_{i,1} < ... < \tau_{i,m-1} < \tau_{i,m} \tag{4.19}$$

Equation 4.1 must hold at all collocation points. Take into account that under this condition $\tau_{i,0}$ would not be required to meet the flow condition. This is because these points will be used to impose the continuity condition between the different segments in the piece-wise polynomia, Figure 3.9. However, once the scheme has converged the flow equation will also hold at these points.

The second angle θ_2 is divided in $N_2 - 1$ evenly spaced intervals. For a given $\theta_1 = \tau$ the cylinder function becomes a circle function which has been typically represented via a truncated Fourier transform [56]. Yet, it is more meaningful to work with the states rather than the Fourier coefficients. For that Olikara [96] suggested transforming the Fourier coefficients into states by using the Discrete Fourier Transform (DFT), a linear and invertible operation. The circle function is then defined as

$$\mathbf{X}(\tau) = \{\mathbf{u}(\tau, k/N-2) |\ k = 0...N_2 - 1\} \tag{4.20}$$

The vector $\mathbf{X}(\tau)$ contains $6 \times N_2$ elements, that is, all the states on the discretized circle. Analogously, the vector field that acts on $\mathbf{X}(\tau)$ is

$$\mathbf{F}(\mathbf{X}(\tau)) = \{\mathbf{f}(\mathbf{X}(\tau)|k = 0, ..., N_2 - 1\} \tag{4.21}$$

which also contains $6 \times N_2$ elements. It is possible then to re-write Equation 4.1 as

$$\frac{d\mathbf{X}}{d\tau}(\tau) = T\mathbf{F}(\mathbf{X}(\tau)) \tag{4.22}$$

which must hold for all $\tau \in [0, 1]$. The boundary condition Equation 4.5 can also be expressed in terms of $\mathbf{X}(\tau)$

$$\mathbf{X}(0) = R(-\rho)\mathbf{X}(1) \tag{4.23}$$

The key idea of the collocation method is that we can express $\mathbf{X}(\tau)$ with $\tau \in [\tau_{i,0}, \tau_{i+1,0})$ as the interpolation polynomial in the Lagrange form

$$\mathbf{X}(\tau) = \sum_{k=0}^{m} \mathbf{X}_{i,k} l_k(\hat{\tau}) \quad \text{with} \quad \hat{\tau} = \frac{\tau - \tau_{i,0}}{\tau_{i+1,0} - \tau_{i,0}} \tag{4.24}$$

where $l_k(\hat{\tau})$ are the Lagrange basis polynomials

$$l_k(\hat{\tau}) = \prod_{\substack{j=0 \\ j \neq k}}^{m} \frac{\hat{\tau} - \hat{\tau}_j}{\hat{\tau}_k - \hat{\tau}_j} \tag{4.25}$$

By substituting Equation 4.24 into Equation 4.20 we obtain the final form of the vector field equation that will be later implemented

$$\sum_{k=0}^{m} \mathbf{X}_{i,k} \frac{dl_k}{d\hat{\tau}_j}(\hat{\tau}_j) = (\tau_{i+1,0} - \tau_{i,0}) T\mathbf{F}(\mathbf{X}_{i,j}(\tau_{i,j})) \tag{4.26}$$

where the derivative of the Lagrange basis function is

$$\frac{dl_k}{d\hat{\tau}_j} = \sum_{\substack{i=0 \\ i \neq k}} \left[\frac{1}{\hat{\tau}_k - \hat{\tau}_i} \prod_{\substack{j=0 \\ j \neq (i,k)}}^{m} \frac{\hat{\tau} - \hat{\tau}_j}{\hat{\tau}_k - \hat{\tau}_j} \right] \tag{4.27}$$

Equation 4.26 has to hold at all collocation points $\tau_{i,1}, ...\tau_{i,m}$. Note that even though the summation starts at $j = 0$, the flow equation is not imposed at that $\tau_{i,0}$; there is a difference between the points used in the interpolation and the ones where the vector field conditions have to hold. The sections at the extremes $\tau_{i,0}$ are used to ensure continuity of the piece-wise polynomial

$$\sum_{j=0}^{m} \mathbf{X}_{i,j} l_j(1) = \mathbf{X}_{i+1,0} \tag{4.28}$$

which must be met at $i = 0, ..., N_1 - 1$. Next, the quasi-periodic boundary condition Equation 4.23 can be written as

$$\mathbf{X}_{0,0} = R(-\rho)\mathbf{X}_{N_1,0} \tag{4.29}$$

where $R(-\rho)$ is a matrix that shifts the last section to match the first one, and that can be constructed by a composition of DFT. We illustrate how to construct this matrix by starting with one component of all the states in $\mathbf{X}(\tau)$, that is a vector with dimension N_2. The DFT matrix D for a single component will then be an $N_2 \times N_2$ matrix that transforms all the state space into the frequency space where it is shifted and transformed back to the state space by using the DFT inverse D^{-1}. In matrix form this operator can be expressed as

$$R(-\rho) = D^{-1} S(-\rho) D \tag{4.30}$$

where $S(\rho)$ is the $N_2 \times N_2$ shift matrix which can be written as $S(\rho) = I\mathbf{G}(\rho)$ with $\mathbf{G}$ a vector with N_2 elements given by [80]

$$G_k = \begin{cases} e^{-2\pi i \rho k} & k = 0 \ldots N_2'/2 - 1 \\ e^{-2\pi i \rho (k - N_2)} & k = N_2'/2 \ldots N_2 - 1 \end{cases} \tag{4.31}$$

where

$$N' = \begin{cases} N & \text{if N is even} \\ N+1 & \text{if N is odd} \end{cases} \tag{4.32}$$

Once the matrix R with dimensions $N_2 \times N_2$ has been obtained we can get R $(6N_2 \times 6N_2)$ by computing

$$R(\rho) = I'_{6N_2 \times N_2} R(\rho)_{N_2 \times N_2} I'_{N_2 \times 6N_2} \tag{4.33}$$

where $I'_{pN_2 \times N_2}$ contains p $N_2 \times N_2$ identity matrix stacked in the appropriate direction.
The derivative of R with respect to ρ will also be required as part of the Jacobian matrix, however, once the implementation of D, D^{-1} and $S(\rho)$ is clear its derivative is trivial.
Equation 4.26 Equation 4.28 and Equation 4.30 describe the set of vector equations of the invariant tori. They consists of $N_1(m+1)+1$ vector equations for $\mathbf{X}_{i,j}$, which means a system of $6N_2(N_1(m+1)+1)$ equations in total. Finally, the scalar equations can be straightforwardly implemented. The phase constraints would be

$$\frac{1}{N_2(N_1(m+1)+1)} \sum_{i=0}^{N} \left((\mathbf{X}_{i,0} - \tilde{\mathbf{X}}_{i,0}) \cdot \frac{d\mathbf{X}_{i,0}}{d\tau} + \sum_{\substack{j=1 \\ i \neq N}}^{m} (\mathbf{X}_{i,j} - \tilde{\mathbf{X}}_{i,j}) \cdot \frac{d\tilde{\mathbf{X}}_{i,j}}{d\tau} \right) = 0 \tag{4.34}$$

$$\frac{1}{N_2(N_1(m+1)+1)} \sum_{i=0}^{N} \left((\mathbf{X}_{i,0} - \tilde{\mathbf{X}}_{i,0}) \cdot \frac{d\mathbf{X}_{i,0}}{d\tau} + \sum_{\substack{j=1 \\ i \neq N}}^{m} (\mathbf{X}_{i,j} - \tilde{\mathbf{X}}_{i,j}) \cdot \frac{\partial\tilde{\mathbf{X}}_{i,j}}{\partial\theta_2} \right) = 0 \tag{4.35}$$

where $\frac{\partial \mathbf{X}_{i,j}}{\partial \theta_2}$ is the state derivative on the θ_2 coordinate and can be obtained again by using the DFT on each $\mathbf{X}_{i,j}$ as in Equation 4.30, but using as new $\mathbf{G}$

$$G_k = \begin{cases} ik & k = 0 \ldots N_2'/2 - 1 \\ i(k - N_2) & k = N_2'/2 \ldots N_2 - 1 \end{cases} \tag{4.36}$$

Once $\partial\mathbf{X}_{i,j}/\partial\theta_2$ is obtained we can use the invariance equation Equation 4.2 to obtain the derivative with respect to $\tau = \theta_1$

$$\frac{d\tilde{\mathbf{X}}_{i,j}}{d\tau} = \frac{1}{\tilde{\omega}_1}\left[\tilde{\mathbf{F}}_{i,j} - \tilde{\omega}_2\frac{\partial\tilde{\mathbf{X}}_{i,j}}{\partial\theta_2}\right] \tag{4.37}$$

Similarly, the constraints to select a single member of the family can be written as

$$\frac{1}{N_2(N_1(m+1)+1)}\sum_T H(\mathbf{X}_{i,j}) = H_{ref} \tag{4.38}$$

$$\frac{1}{N_2(N_1(m+1)+1)}\sum_T \left[(\mathbf{X}_{i,j} - \tilde{\mathbf{X}}_{i,j})\cdot\tilde{\mathbf{X}}'_{i,j}\right] = \Delta s \tag{4.39}$$

where $\sum_T$ stands for the summation over all discretized points on the torus. The last two equations are Equation 4.10 and Equation 4.11, which do not need any transformation.

$$\mathbf{G}(\mathbf{X}_{i,j}, T, \rho, \omega_1, \omega_2, \lambda_1, \lambda_2) = \begin{pmatrix} \mathbf{g}_{flow}(\mathbf{X}_{0,j}, T, \lambda_1, \lambda_2) \\ \mathbf{g}_{cont}(\mathbf{X}_{0,j}, \mathbf{X}_{1,0}) \\ \vdots \\ \mathbf{g}_{flow}(\mathbf{X}_{N_1-1,j}, T, \lambda_1, \lambda_2) \\ \mathbf{g}_{cont}(\mathbf{X}_{N_1-1,j}, \mathbf{X}_{N_1,0}) \\ \mathbf{g}_{per}(\mathbf{X}_{0,0}, \mathbf{X}_{N_1,0}, \rho) \\ g_{ph1}(\mathbf{X}_{i,j}, \tilde{\mathbf{X}}_{i,j}, d\tilde{\mathbf{X}}_{i,j}/d\tau) \\ g_{ph2}(\mathbf{X}_{i,j}, \tilde{\mathbf{X}}_{i,j}, \partial\tilde{\mathbf{X}}_{i,j}/\partial\theta_2) \\ g_{ham}(\mathbf{X}_{i,j}, H_{ref}) \\ g_{ext1}(\omega_1, T) \\ g_{ext1}(\omega_2, T, \rho) \end{pmatrix} = 0 \tag{4.40}$$

All these equations then form a $(N_1(m+1)+1)+6$ system with $\mathbf{X}_{i,j}, T, \rho, \omega_1, \omega_2, \lambda_1, \lambda_2$ as unknowns. We can write these equations as $\mathbf{G}(\mathbf{X}_{i,j}, T, \rho, \omega_1, \omega_2, \lambda_1, \lambda_2) = 0$ and apply the Newton method to solve it iteratively. In order to apply the Newton method we need to evaluate two things: the function $\mathbf{G}(\mathbf{X}_{i,j}, T, \rho, \omega_1, \omega_2, \lambda_1, \lambda_2)$ and its Jacobian. The equations are ordered as in Equation 4.40 in order to keep a geometrical logical order and consistency from now on.

The main advantage of using an already divided domain (i.e. to apply the collocation method) is that we end up with a very sparse Jacobian matrix, which is very advantageous from a computational point of view. Furthermore the divisions in τ allow us to use relatively small values of collocation order $m \approx 5$, which are values that are known to work well in these kinds of methods, Subsection 4.9.1. By inspecting Equation 4.40 it is clear that the partial derivatives of the vector field Equation 4.26

and continuity condition Equation 4.28 will account for a large part of the Jacobian matrix.

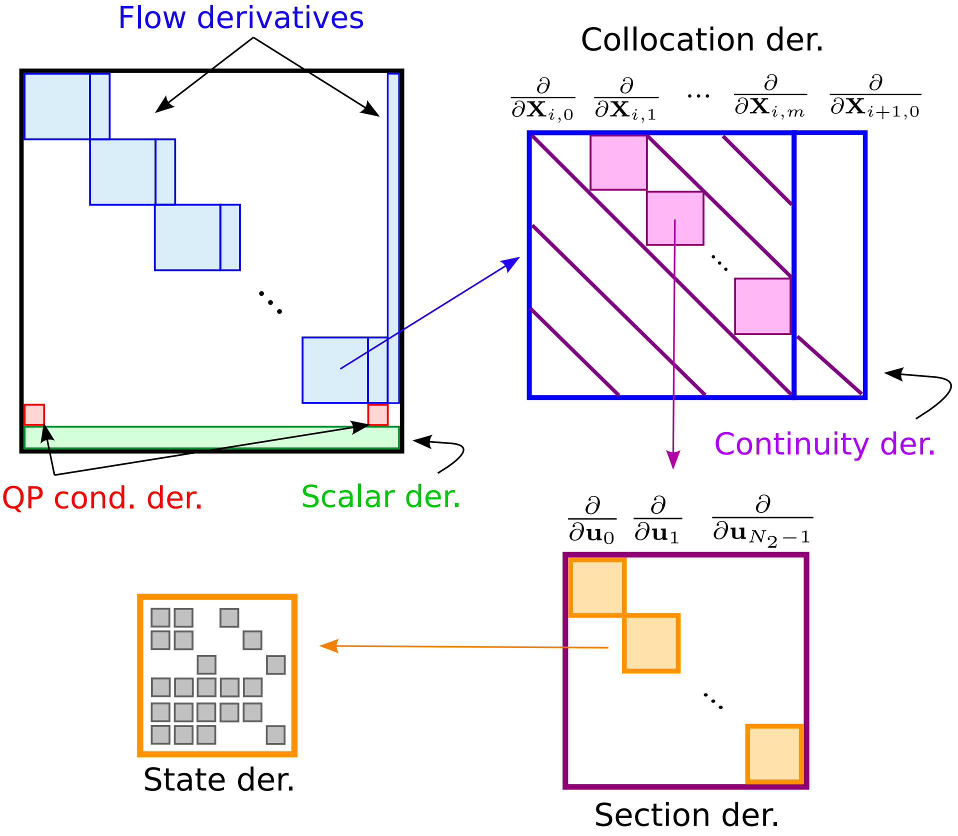

Figure 4.3: Jacobian matrix structure of the collocation problem.

Figure 4.3 shows how the sparse Jacobian matrix will look like. It can be seen that this very large matrix ($\sim 10^5 - 10^6$) will be composed by blocks of dimension $6N_2(m+1) \times 6N_2(m+2)$. These blocks contain all the vector field or flow derivatives except for the free parameters which should be added to the latest rows. Inside each of these blocks there are three different parts: there are shifted blocks (since the accumulated state vector used starts at $(\mathbf{X}_{0,1})$, and has a dimension of $6N_2 \times 6N_2$). It contains the Jacobian of the flow $\mathbf{F}(\mathbf{X}_{i,j})$ at each of the states of a circle section $\mathbf{X}_i$. Likewise, these blocks are sparse and diagonal with 6×6 smaller compact blocks inside. Finally, there are diagonal patterns which begin every $6N_2$ elements which account for the derivatives of the states that form the interpolation function. Finally, the last row contains the continuity condition and spans $6N_2(m+2)$ columns. The blocks associated with adjacent segments must "clash", this represents the continuity condition. Following this logic, the first element of the next block will contain the state derivative of $\mathbf{X}_{i+1,j}$.

The terms of order $\mathcal{O}(\lambda_1, \lambda_2)$ that appear when differentiating the vector field equation with respect to the states are not included in the jacobian. This increases considerably the sparsity of the Jaco-

bian and does not affect the convergence as noted by [97]. The derivative of the vector field with respect to λ_1 and λ_2 must be added to the Jacobian though.
The periodicity condition will start at the row $6N_2N_1(m+1)$ and only fills the first $6N_2 \times 6N_2$ blocks, and one of the latest. Finally, since most of the scalar equations depend almost on all the parameters, their representation in the Jacobian will be a compact segment which spans the whole matrix but very thin, with height 6 (Figure 4.3).

Once the set of equations and its Jacobian have been constructed and provided that an initial guess is known, see Section 4.6, we can apply the Newton method to converge the torus iteratively to its solution [97] with an arbitrary precision by using

$$\mathbf{s}_{i+1} = \mathbf{s}_i - J_{\mathbf{G}_i}^{-1}\mathbf{G}_i \tag{4.41}$$

where $\mathbf{s}$ stands for the accumulated variables of the problem, namely $\mathbf{s} = \{\mathbf{X}_{i,j}, T, \rho, \omega_1, \omega_2, \lambda_1, \lambda_2\}$. Once a member is computed and its family tangent is known we can obtain the next guess by linearly extrapolating the torus and using the same algorithm using a coherent value of Δs.

4.6. Initial Approximation

We have seen that in order to obtain a quasi-periodic invariant torus we need to provide the scheme described in Section 4.5 an approximation of the solution in order to initialize it. This approximate torus can come from an analytical approximation, or from the torus that emanates from an equilibrium point or periodic orbit. The latest is the approach that we will be using for this work. Note that for more complex systems, periodic orbits from the CR3BP will degenerate naturally to quasi-periodic tori, and thus they could simply be used as the initial guess.

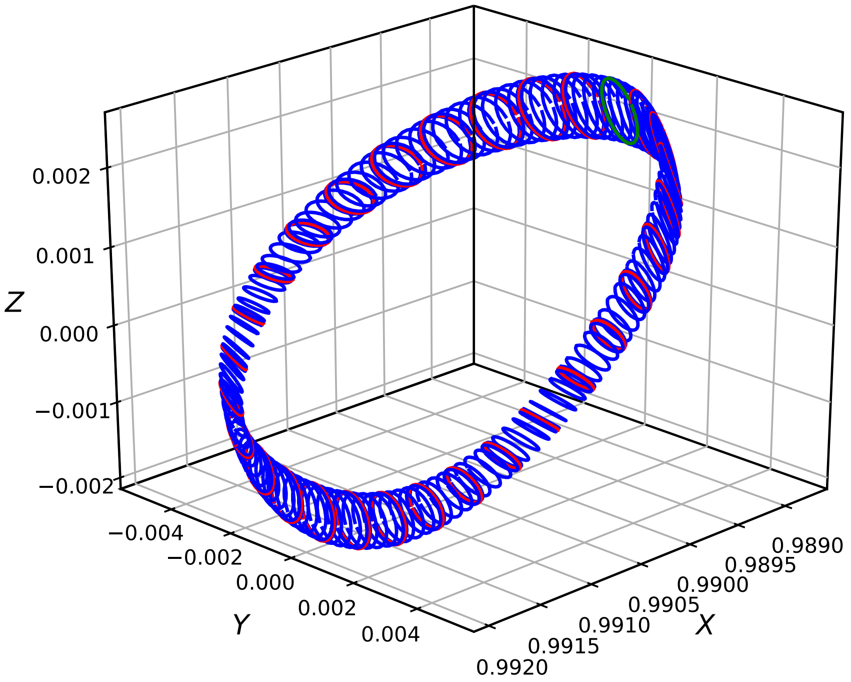

Figure 4.4: Initial approximation of the quasi-periodic torus. In yellow and green (overlapped) first and last sections respectively, in red section used for continuity and in blue collocation sections.

Consider $\mathbf{x}(t)$ a periodic orbit whose monodromy matrix M admits one pair of unitary magnitude complex conjugate eigenvalues such as $\lambda_1 = e^{i\rho}$, $1/\lambda_1 = e^{-i\rho}$ and let $\mathbf{y}$ be its associated eigenvector. Kolemen et al. [75] proved that the following curve is invariant under the monodromy matrix, see their paper for a rigorous proof.

$$\boldsymbol{\psi}(\theta_1) = K[\cos\theta_1 \operatorname{Re}(\mathbf{y}) - \sin\theta_1 \operatorname{Im}(\mathbf{y})] \tag{4.42}$$

with $K << 1$. $\boldsymbol{\psi}(\theta_1)$ is called the invariant circle of the monodromy map and it meets that $M\boldsymbol{\psi}(\theta_1) = \boldsymbol{\psi}(\theta_1 - \rho)$, so it is invariant under the monodromy matrix. As Kolemen et al. states, by using trigonometric manipulations it can be shown that the monodromy matrix maps this curve onto itself with an angle shift [75]. Therefore, it is a good first guess for initializing the invariant torus. As Baresi et al. noted, this curve shall not be confused with the invariant set of the Poincaré section that is used in some methods, Section 4.1, to obtain the invariant torus. It is simply a linear approximation of the relative distance between the quasi-periodic torus and the periodic orbit used to initialize it [12]. Figure 4.4 displays the skeleton of an initial-guess torus created generated from a north-halo orbit.

Once the invariant circle is obtained, it is possible to propagate it to create the torus by using the state transition matrix

$$\boldsymbol{\psi}_i^j = e^{-i\rho t_i/T}\Phi(t_i, t_0)\boldsymbol{\psi}^j \tag{4.43}$$

with $t_i = iT/N_1, i = 0, \dots N_1 - 1$ and T the period of the periodic orbit. The term $e^{-i\rho t_i/T}$ is introduced to undo the effects of the winding frequency ω_2, which acts in the latitudinal direction. This term allows to continuously change the shift to get in the end $\boldsymbol{\phi}(\theta_1) = \boldsymbol{\phi}(\theta_1 - \rho)$, which is the invariance condition (Equation 4.2).

Take into account that the set of state transition matrices that are normally obtained from the propagation of the periodic orbit will not match the required intervals that the Gauss-Legendre collocation imposes, unless the periodic orbit has been computed using a Gauss-Legendre collocation method with the same parametrization. Therefore after computing a first approximation, generally a new approximated torus with a collocation grid with the desired values of N_1, N_2 and m, as explained in Section 4.5, would need to be computed using interpolation.

4.7. Domain of existence

It has been seen that in order to initialize a quasi-periodic torus approximation, the invariant monodromy circle is required. This invariant circle can only be generated from periodic orbits that contain a center component which can produce the quasi-periodic motion, in other words those periodic orbits whose monodromy matrix possesses at least one pair of nontrivial eigenvalues on the unit circle. In Section 3.3, we saw that there exist four main families of periodic orbits. This section will study the domain of existence of quasi-periodic tori, or to put it in another way: the periodic orbits that contain a center component, the different families of quasi-periodic orbits that emerge from them and how they are interrelated. By computing the eigenvalues associated to the monodromy matrix of a large set of periodic orbits, and assessing whether they contain quasi-periodic components or not we can estimate the range of existence of quasi-periodic orbits related to the periodic orbits they emerge from. The following plots represent (in blue), the members that could produce quasi-periodic motion and (in red) the ones that could not, for each family of periodic orbits and for different energy levels.

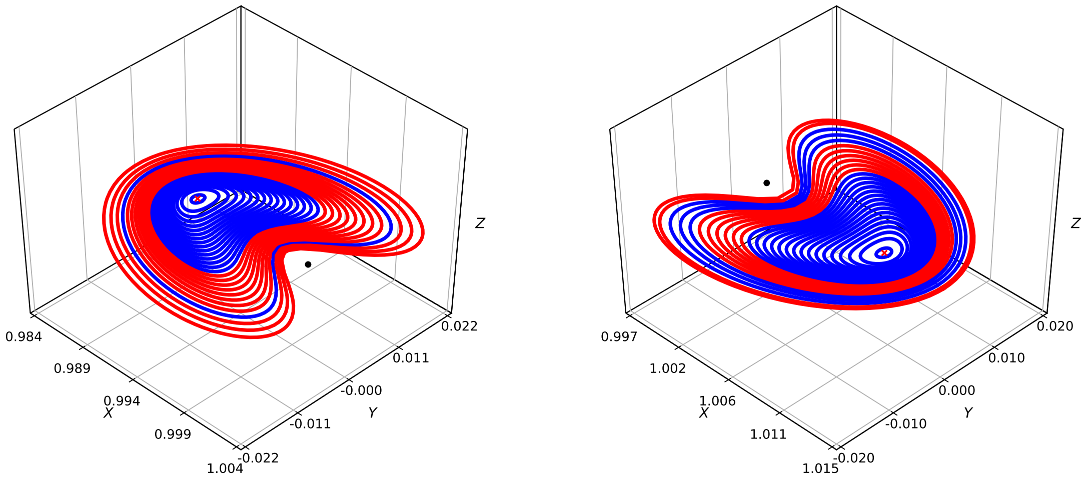

(a) L1

(b) L2

Figure 4.5: Planar Lyapunov periodic orbits about L_1 and L_2. In blue the orbits from which tori can emanate and in red otherwise.

Figure 4.5 show the Lyapunov orbits with the center component around L_1. There are four clearly different areas: from the libration point to $C_1 = 3.000831$ and $C_2 = 3.000825$ respectively there exists an eigenvalue with a quasi-periodic center component. The orbits stop being elliptic –there is no longer a center eigenvalue– when a bifurcation occurs, and at that energy level the Lyapunov orbits bifurcate into the north/south halo families. Afterwards, the Lyapunov orbits recover their center component, check Table 4.1. The center component exists then until there is again another bifurcation, this time the vertical family bifurcates from the Lyapunov family, however they do not contain any quasi-periodic center component. After this bifurcation the Lyapunov family does not regain its center component any more.

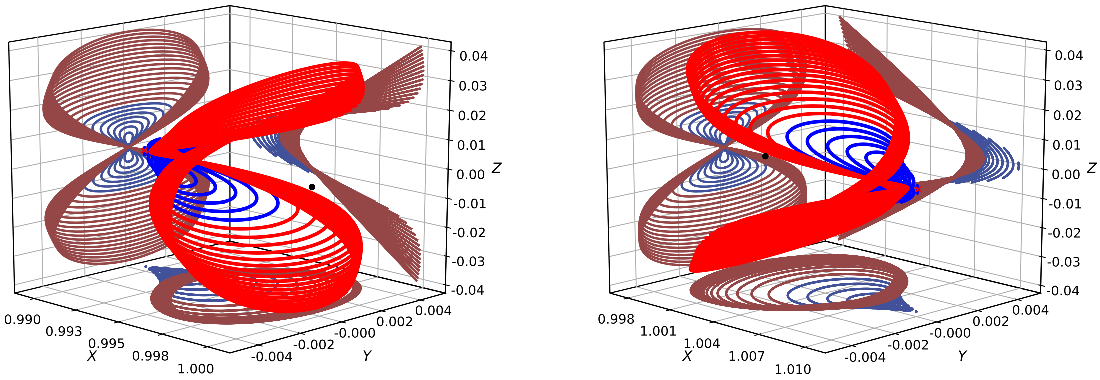

(a) L_1

(b) L_2

Figure 4.6: Vertical periodic orbits about L_1 and L_2. In blue the orbits from which tori can emanate and in red otherwise.

Figure 4.6 shows the vertical periodic orbits that contain a quasi-periodic center component (blue) or not (red) about L_1 and L_2. The most remarkable fact is that there is a relationship between the blue areas in the vertical and planar orbits (Figure 4.5 and Figure 4.6 respectively). As noted by Gómez et al. [55], this is due to the fact that the quasi-periodic invariant tori that emanate from the planar and vertical periodic orbits are, indeed, the same. They are connected, in other words, starting with a torus close to one of them and via continuation (with fixed energy), Section 3.6, it is possible to reach a torus that emanates from the other one. These kinds of quasi-periodic orbits have been traditionally called *Lissajous orbits*. This connection only exists in the first region with center components of Figure 4.5. At the second region of the planar family the bridge between both families has already bifurcated and independent tori around them arise.

Figure 4.7 illustrates the domain where a quasi-periodic center component exists in both north and south halo orbits and about L_1 and L_2. Halo orbits are symmetric with respect to the $z-$axis so the same results are expected for the north and south families. The quasi-periodic orbits that emerge from halo periodic orbits are normally differentiated from those who emerge from either

Table 4.1: Range of energies where quasi-periodic orbit exist for the different families.

	L_1	L_2
Planar	$(3.0008907-3.000831)$ - $(3.000177-3.000167)$	$(3.0008867-3.000825)$ - $(3.000211-3.000145)$
Vertical	$(3.0008907-3.000247)$	$(3.0008867-3.000256)$
Halo	$(3.000831, 3.0002105)$	$(3.000825, 3.000214531)$

planar or vertical Lyapunov orbits, and they are called *quasi-halo orbits.* For all cases quasi-periodic invariant tori exist for almost all members except the last ones –the ones with smallest energy. This is due to the fact that bifurcations from the halo to halo-type orbits occur in these regions. The interested reader can find more about this phenomenon in Gómez et al. [55].

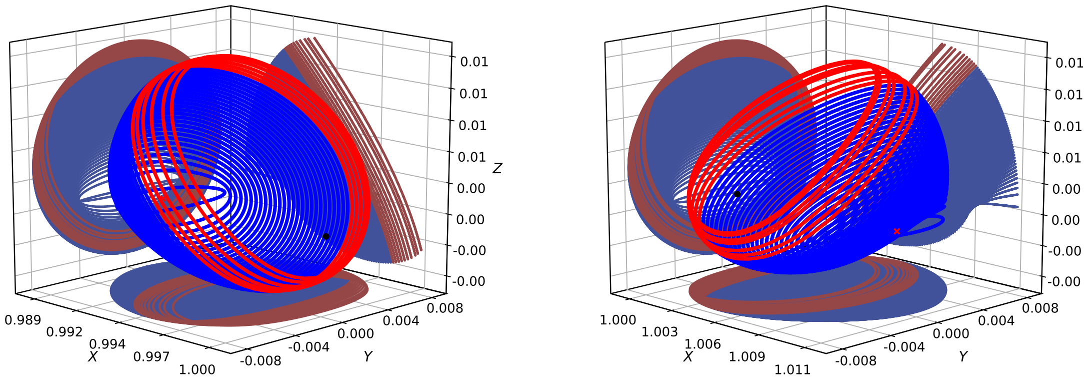

(a) North Halo L_1

(b) North Halo L_2

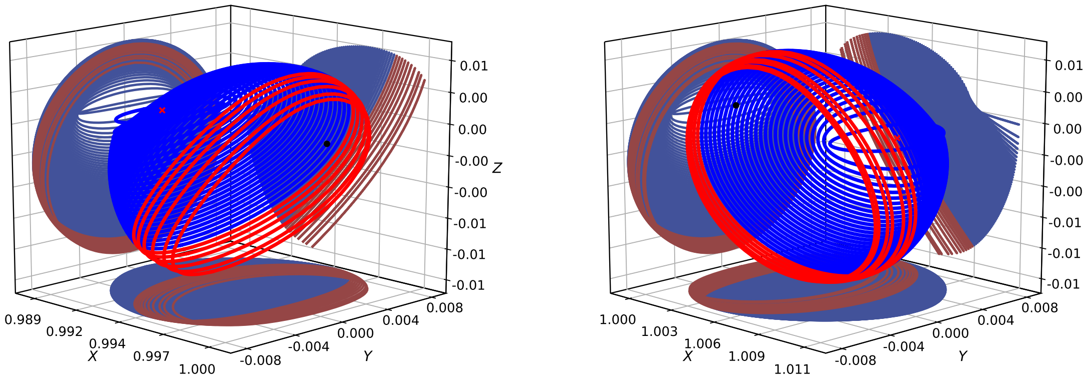

(c) South Halo L_1

(d) South Halo L_2

Figure 4.7: Halo orbits around L_1 and L_2. In blue orbits with a quasi-periodic center component, otherwise in red.

4.8. Stability and manifolds

The stability of any quasi-periodic torus can be evaluated by analyzing the linearized dynamics in the neighbourhood of the torus. In periodic orbits, the stability is assessed by reducing the periodic orbit to a fixed point on a stroboscopic map, since the characteristics of the orbit can be analyzed as a discrete time system. The method that will be used was proposed by Olikara [97] and assumes that the torus is reducible. This means that there is a coordinate transformation such that the differential of the stroboscopic map does not depend on the value of θ [71].
The method first computes the eigenvectors for a circle on the invariant torus, which are then propagated using the state transition matrices in a similar fashion as with periodic orbits. The eigenvectors associated with hyperbolic eigenvalues will generate the stable and unstable manifolds.

Let $\mathbf{w}$ be the circle function that defines an invariant circle of the time-T stroboscopic map $\boldsymbol{\phi}_T$. Due to the invariant condition all points obtained from the scheme are fixed points for the mapping

$$S(\mathbf{w}) = R_{-\rho}\boldsymbol{\phi}_T(\mathbf{w}) \tag{4.44}$$

where $R_{-\rho}$ rotates $\mathbf{w}$ over $-\rho$. The stability of the map can then be obtained by linearizing S

$$\Delta S = \frac{\partial \mathbf{S}}{\partial \mathbf{w}}(\mathbf{w})\delta\mathbf{w} = R_{-\rho}(\Phi_{N,0}(\mathbf{w}, T)\delta\mathbf{w}) = \mu\delta\mathbf{w} \tag{4.45}$$

where Φ is the state transition matrix after time T. It can be proved that the $6N_2$ eigenvalues μ can be related to the eigenvalues of the Floquet matrix λ by $\mu = \lambda e^{-ik2\pi\rho}$, therefore the eigenvalues μ lie on concentric circles in the complex plane, and each circle represents one eigenvalue λ of the Floquet matrix. Furthermore, due to the Hamiltonian nature of the problem the eigenvalues come in pairs and so, if one is greater than one, there must be other smaller than one. When this happens, the torus is hyperbolic, that is, it has stable and unstable invariant manifolds. Thus we seek the eigenvector associated with the real non-unity eigenvalues of μ, which will produce the invariant manifolds. In an entire torus surface, this results in concentric circles of eigenvalues, Figure 4.8.
A problem when extracting the eigenvalues from Equation 4.45 is how to obtain the state transition matrix Φ. However, it is possible to extract it from the Jacobian matrix computed during the Newton method during the torus convergence. Let $J'_{\mathbf{g}}$ be the Jacobian matrix where the rows related to scalar equations have been removed. Then the remaining Jacobian sub-term can be split as in

$$J'_{\mathbf{g}}\left(\begin{array}{c} \delta\mathbf{X}_{0,0} \\ \hline \delta\mathbf{X}_{0,1} \\ \vdots \\ \delta\mathbf{X}_{N_1,0} \\ \hline \delta\boldsymbol{\Lambda} \end{array}\right) = \begin{pmatrix} A & B & C \end{pmatrix}\left(\begin{array}{c} \delta\mathbf{X}_{0,0} \\ \hline \delta\mathbf{X}_{0,1} \\ \vdots \\ \delta\mathbf{X}_{N_1,0} \\ \hline \delta\boldsymbol{\Lambda} \end{array}\right) = 0 \tag{4.46}$$

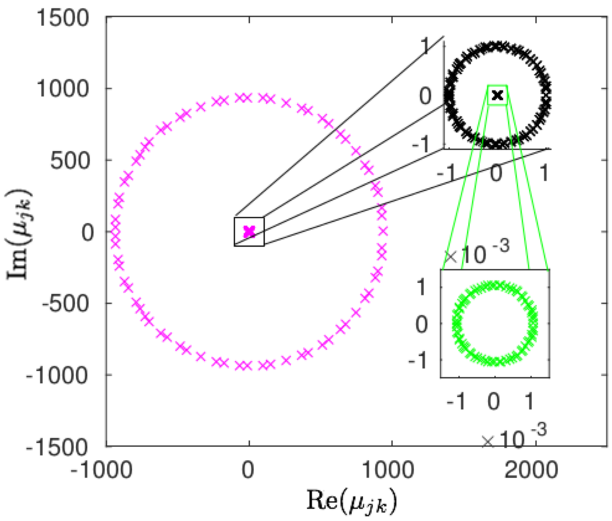

Figure 4.8: Eigenvalues from the torus section. The inner and outer rings contain the hyperbolic eigenvalues while the unit circle is formed by center eigenvalues [12].

where A is a matrix of dimensions $6N_2N_1(m+1)\times 6N_2$, B is a matrix of $6N_2N_1(m+1)\times 6N_2N_1(m+1)$ and C is a $6N_2N_1(m+1)\times 6$ matrix.

We can then rearrange Equation 4.46 in order to relate changes in the initial state $\delta\mathbf{X}_{0,0}$ and changes in the parameters $\delta\mathbf{\Lambda}$ to changes in the state along the trajectory

$$\delta\mathbf{X} = \Phi\delta\mathbf{X}_{0,0} + \Psi\delta\mathbf{\Lambda} = \begin{pmatrix} I \\ -BA^{-1} \end{pmatrix}\delta\mathbf{X}_{0,0} + \begin{pmatrix} 0 \\ -BC^{-1} \end{pmatrix}\delta\mathbf{\Lambda} \tag{4.47}$$

where $\mathbf{I}$ is the identity matrix and

$$\delta\mathbf{X} = \begin{pmatrix} \delta\mathbf{X}_{0,0} \\ \vdots \\ \delta\mathbf{X}_{N,0} \end{pmatrix}, \Phi = \begin{pmatrix} \Phi_{0,0} \\ \vdots \\ \Phi_{N,0} \end{pmatrix}, \Psi = \begin{pmatrix} \Psi_{0,0} \\ \vdots \\ \Psi_{N,0} \end{pmatrix} \tag{4.48}$$

where $\Phi_{i,j}$ is a $6N_2 \times 6N_2$ matrix and $\Psi_{i,j}$ is a matrix of dimension $6N_2 \times 6$. The element $\Phi_{N,0}$ is the monodromy matrix of the invariant torus and will allow us to compute its stability and eigenvectors associated with hyperbolic motion.

Once Φ is computed we cannot only compute the eigenvectors associated to the first circle segment $\mathbf{X}_0$, but also the rest of the state transition matrices of dimension $6N_2 \times 6N_2$ to propagate them to the rest of the torus and, therefore, obtain the full representation of the manifolds. Figure 4.9 displays eigenvectors generating the stable and unstable manifolds, for each of the points on the torus.

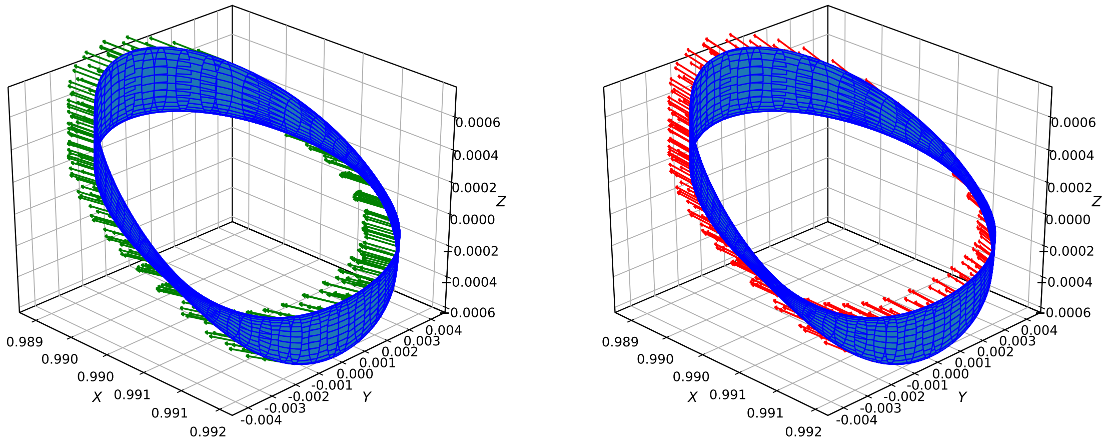

(a) Stable

(b) Unstable

Figure 4.9: Initial unstable and stable manifold vectors on the torus surface.

4.9. Database creation

The collocation scheme that was explained throughout this section permits to compute the invariant tori that emanate from any periodic orbit about any of the equilibrium points, and to continuate them to obtain the full family. The domain where these tori can exist is vast: not only are there two different libration points we will be using (L_1 and L_2), but also a range of types of periodic orbits (i.e. four), each of them with a family of orbits varying with C, and from each of them emanates a new family that can be continuated until it collapses [88]. As can be seen, the domain for just selecting a torus is extensive already, moreover, there are many more variables that will be used in the optimization problem of finding the best transfers (Section 6.5). Therefore, we will need to call, or access, these tori efficiently. The main problem here is that computing a single torus takes alone 1 minute, so implementing the tori solver in line in the optimization problem is most certainly not a feasible option, for it will definitely act as a bottle neck and blow up the computation times. For that reason, a database that contains all these tori in a table readable format will be created, so that the optimizer simply has to use a look-up table which will reduce the computing times enormously, for the tori would be calculated only once. In this section, we will first discuss some aspects of the implementation of the collocation solver and the encountered problems, afterwards a parametrization for the tori will be selected, and some practicalities that arose during the database generation will be explained.

4.9.1. Implementation

The implementation of the solvers was all done in C++, the library *Eigen* was used to perform all the matrix and vector operations, furthermore it provides also optimized routines for sparse matrices and their inverse, which will be required to invert the Jacobian matrix. The *boost* library was used for various purposes like obtaining the Legendre polynomial roots and for some root solvers (bisection and newton for periodic orbit computation). The interpolation routines were obtained from a John Burkardt implementation based on [34].

Figure 4.10 displays a scheme of the design. There, boxes represent abstract classes, which can include either solvers or complex data structures, and ellipses represent methods or functions. The small black arrows indicate the relationships between classes and methods and the big white arrows show the flow of data. The main structure of our implementation is based on two different classes: the *Torus* class and the *QPCollocationSolver* class, which inherits from an upper class since there is also a *POCollocationSolver* class to compute the periodic orbits. The *Torus* class constructor takes a periodic orbit, both its state and state transition matrix evolution, and a parametrization N_1, N_2 and m. The constructor then evaluates the eigenvalues of the monodromy matrix of the periodic orbit and evaluates whether the orbit permits a quasi-periodic torus to emerge from it or not. Next, it creates an approximation of the invariant torus by propagating the monodromy invariant circle, this means that the resulting torus will not meet the Gauss-Legendre τ required spacing. The method *toCollocationForm()* uses a linear interpolator to convert the original initial torus into one with a mesh that can be used in the collocation solver.

The method *solve* permits to obtain the quasi-periodic torus, but it requires some input data: an initial guess of the torus, which can be obtained by linearly extrapolating a previously known solution using the tangent direction of the family; a previously computed torus, for the first torus the approximated torus can be used since this is only used in the pseudo-arc length equation; the tangent direction of the family, which can be computed as the difference of two already computed tori or at the beginning as the direction between the approximated tori and the periodic orbit; and finally some extra parameters such as the reference Jacobi constant H_{ref} or the value of Δs for the pseudo-arc length continuation. Some extra parameters like the tolerance of the solver or the maximum number of iterations can also be set up.

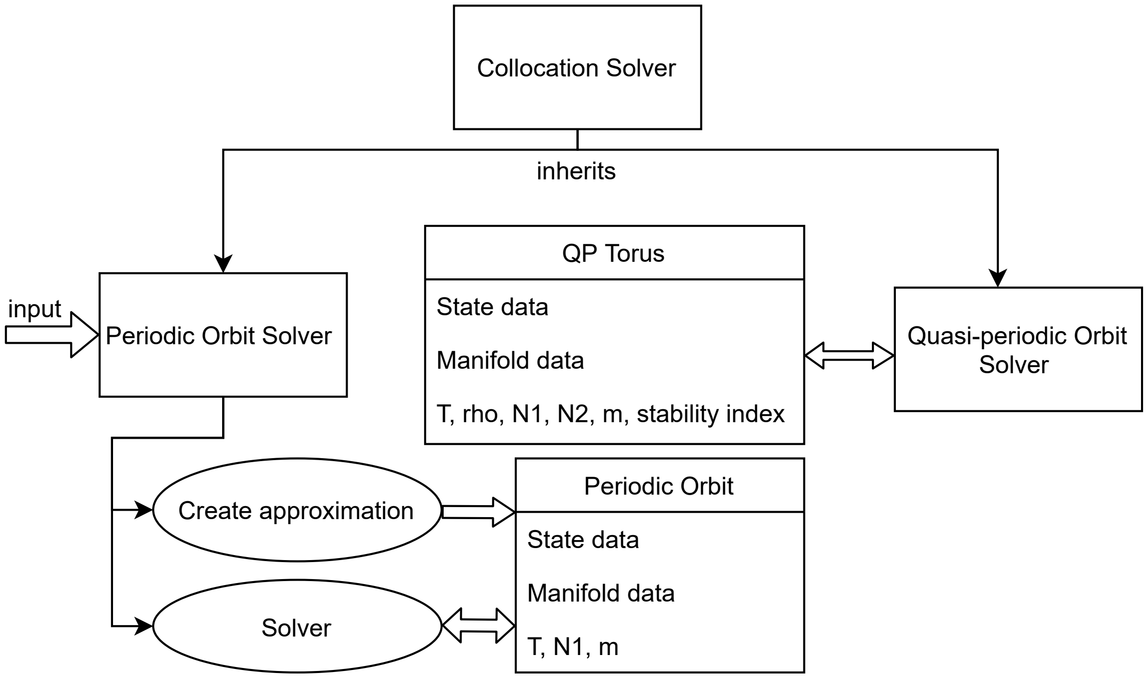

Figure 4.10: Scheme of the implementation. Boxes represent abstract objects and ellipses indicate methods. Black arrows refer to relationships between classes and white arrows to data flow.

This solver iteratively converges to the solution by evaluating the function **g** and its Jacobian, and computing the next guess by using the Newton method. In our implementation the vector **g** and its Jacobian are evaluated by different functions. Although this is the more human-readable way to write these functions, it has been noted that the efficiency of the solver can be increased considerably by using a single function call. The main problem when using two different calls is that these functions contain very large nested loops that are used to fill the expressions we need to evaluate; due to the large dimensions of the vector/matrix these loops do make a difference in terms of efficiency. By carefully planning on how to evaluate these expressions, we could mix them into one single call and reduce the loops to their minimum, at the expense of reducing readability of course.

There are several ways in which an *Eigen* sparse matrix can be filled. We found that using triplets[3] was the fastest, although filling by row or by column was not tried since the scheme computes the sections of the Jacobian by blocks. The sparse LU decomposition provided by *Eigen* offered the best results in terms of speed. Moreover, this algorithm permits solving in three steps: *analyzePattern*, which computes the ordering permutation vector from the structure of the Jaco-

---

[3] A structure that allows to declare the column, row and value for each of the elements

bian, *factorize* which performs the factorization, and *solve*, which solves the linear system. Since the structure of the Jacobian does not change it is possible to analyze the pattern only once within the solver loop, to be more efficient.

Once the torus has been solved we need to obtain the manifolds: the last Jacobian evaluated is transformed in order to get all the state transition matrices. The eigenvalues of the monodromy matrix of the invariant tori are evaluated and the eigenvectors associated with stable and unstable hyperbolic motion are obtained and propagated using the state transition matrices already computed. The metadata (period T, rotation angle ρ, Jacobi constant H, etc.), states and stable and unstable manifolds eigenvector are saved in an ASCII-type format we called the *torus exchange format* which will be used afterwards as a look-up table, which includes the state and manifold vector, in the optimization process.
A similar algorithm was used for computing the periodic orbits that are used as seed for the tori. The interested reader can check the code at `https://github.com/daniel-ezquerra/Master-Thesis`, where there is an implementation in both C++ and Python.

4.9.2. Tori parametrization

Before creating our database, we need to decide on a parametrization. This parametrization consists of selecting the correct values for N_1,N_2 and m so that the resulting tori meet two requirements:

- The torus mesh is fine enough so that there is not a qualitatively different behaviour between the stable manifolds of two contiguous nodes. We will assess this criterion by comparing the difference between two close hyperbolic eigenvectors. Although this criterion is not valid for arbitrary long time-scales due to the chaotic nature of the CR3BP, for the integration times that we will be using (never more that one turn around the Sun, i.e. the primary) it is valid.
- The torus mesh is coarse enough so that the computational load is as small as possible. Since the domain where tori exist is very large as has already be seen, if the computation time for computing a single member is not taken into account, the task of creating a thorough database may not be achievable in a reasonable amount of time, effectively prohibiting us from answering the main research question.

As can be seen, both requirements act in opposite directions; we must then achieve a reasonable compromise between them. First, the longitudinal dimension θ_1 of the torus will be discussed. In this dimension there are two variables that affect the parametrization, namely N_1 and m, Figure 3.9.

We will study the influence of these two variable in the complete definition of the manifold space and the computation time, and then make a most reasonable decision.

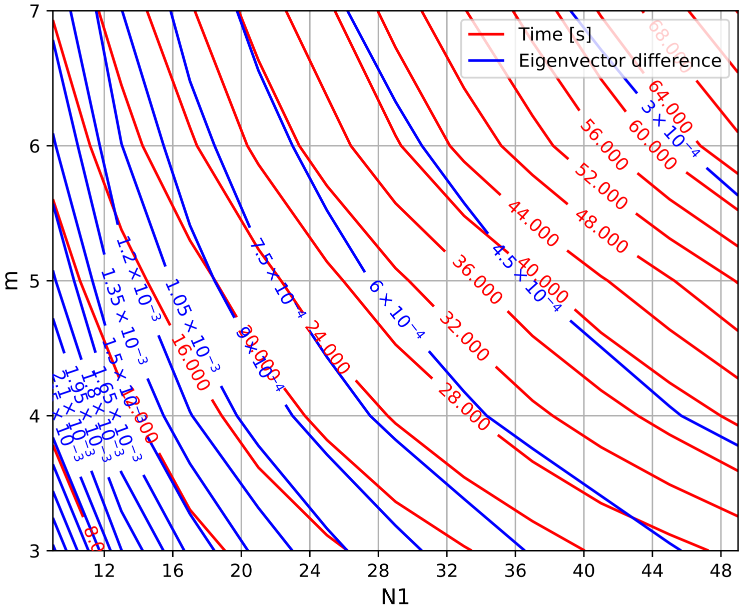

Figure 4.11: Parametric study in the θ_1 dimension. Computational time (red) and eigenvector difference (blue) vs N_1 and m.

Figure 4.11 displays along the $x-$axis the N_1 value and along the $y-$axis the m value selected. The red isobars shows the computation time and the blue ones the difference between adjacent hyperbolic eigenvectors. It can be seen that there are three regions. The one on the bottom left, that is, low values of N_1 and m, is an area where small changes in computation times imply big changes in eigenvector difference. In this area, a small change in either N_1 or m has a small impact on the computation time, but changes the completeness of the manifold space. On the other hand, the top-right area contains the opposite, large values of N_1 and m. There, a small change in either N_1 or m augments the computation time considerably, yet big differences in the eigenvectors do not exist. For that reason, the center area displays the most promising solutions. In this region changes in computation time and eigenvector differences appear balanced. Nevertheless, there are still some differences. Moving along any of the eigenvector difference isobars in the center region, it can be seen that if larger values of m are chosen at the expense of N_1, the computation time increases. Therefore, in principle, small values of m should be chosen. However, m defines the interpolating space in the collocation scheme, and so, if it is greatly reduced it will affect the stability of the scheme. For all of that, a value of $N_1 = 30$ and $m = 5$ was chosen. Note that we do not aim at studying the tori at points that are not nodes, for that reason the error of the states that will be used in the database generation is entirely controlled by the error that was imposed to the solver.

Next, we will study the parametrization in the latitudinal dimension θ_2. In this dimension, there is only one parameter that controls the evenly-spaced grid. Let us note that N_2 will greatly influence the computation time, since $N1(m+1) >> N_2$ and thus, small increments in N_2 will increase the total number of nodes on the grid greatly.

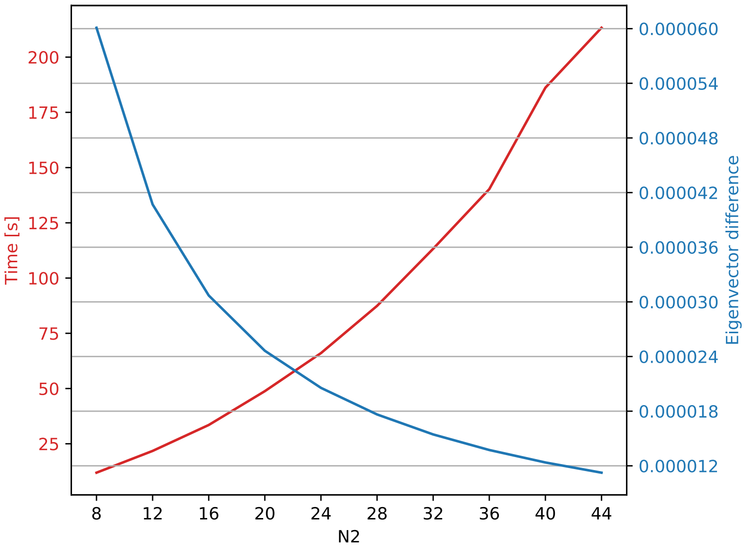

Figure 4.12: Parametric study on the θ_2 dimension. Computational time and eigenvector difference vs N_2.

Figure 4.12 shows the computational time in red, which increases quadratically with N_2 and the eigenvector difference in blue which decreases exponentially with N_2. In this case it is more difficult to assess what is the best decision, since all values between 20 and 30 are possible candidates. This is a region where the eigenvector difference has decreased significantly due to its exponential behaviour, but the CPU time is still not very large due to its quadratic behaviour. In the end a value of $N_2 = 26$ was selected.

Bear in mind that, even though the parametrization of the torus is important, we only need to be able to capture the behaviour of the manifold evolution. Even if this grid was somehow coarse we could perform a second round of optimization with only the most promising members and variables, which would be a much more realizable task than generating the whole database with an extremely fine grid. Anyway, the chosen grid is fine and captures accurately not only the first members of the family, which have a smaller circle section, but also the largest ones.

4.9.3. Practicalities

Once the tori parametrization has been selected, the next step is to select the number of periodic orbits that will be used to create each of the families, and the number of tori that will emerge out of that orbit, via continuation. Since periodic orbits can be computed relatively quickly, the following scheme was implemented to compute the set of periodic orbits that will be used afterwards. Periodic orbits are computed in such a way that the average difference between them in normalized coordinates is $\sim 10^{-4}$ which ensures that by using linear interpolation, any periodic orbit in the middle could be computed at the desired tolerance (10^{-12}) in about two iterations since the Newton method converges quadratically. This is possible with periodic orbits because they can be computed quickly so that different steps for continuation can be tried until the desired difference is obtained. With this setup most of the families contain about ~ 70 members.

The problem when deciding on the number of tori that emerge from each of the periodic orbits is that the computational cost of computing each torus is high, so we cannot use a similar scheme to adapt the step to obtain a desired difference. However, it was checked that using a value of 30 tori per family, periodic orbits yield average differences between adjacent tori of around 10^{-4} in normalized coordinates, so this value was selected.

Similarly to what happened with the torus parametrization, if this grid were coarse, we could increase its definition by focusing just on the most promising areas. The cost of having a very fine grid in either number of periodic orbits or members per periodic orbit is immense with an order of computation of weeks if not more, also the storage capacity for such a database would be very large. As an estimate, for the current setting the database generated weight about 25 Gb.

In Section 4.7, we saw that the planar family of quasi-periodic orbits has two regions, Figure 4.5. The first one is connected to the vertical family and it spans a large range of values of the Jacobi constant. On the other hand, the second one is decoupled and is extremely small. For that reason, the planar quasi-periodic orbits will only be considered in the region that they appear as an extension of the vertical family, and thus they will no longer be utilized as an independent family. The quasi-periodic families that will be used in the optimization problems are then the vertical, north, and south halo.

The corresponding validation for the computation of periodic orbit, quasi-periodic tori, and their associated invariant manifolds can be found in Chapter 8.

5

Near-Earth Asteroids

This chapter addresses the general ideas about Near-Earth Asteroids. We discuss the different classifications that exist and their orbital and physical properties. The scientific and economic motivation behind focusing our attention, and that of many others, on these bodies, is addressed. Some filters will be used in order only to retain the asteroids with the most advantageous orbital and physical properties. The need for such filters is driven by the fact that the database we will be using contains thousands of NEAs, and most of them would not be interesting for us. In the end, some relevant data about the most promising candidates is presented.

5.1. General Concepts

The NEAs are defined as the group of asteroids in our Solar System that orbit the Sun with a perihelion distance smaller than 1.3 AU and an aphelion distance larger than 0.983 AU [106]. NEAs belong to a more general category called Near-Earth Objects (NEOs), which can include many diverse objects such as meteorites, comets, interstellar dust particles, interplanetary dust particles, and space junk. Note that only a very small fraction of NEOs has been catalogued as comets, and most of the objects in the NEO catalog are NEAs.

There are two main groups of asteroids in our Solar System. On one hand, the asteroids in the belt between Mars and Jupiter, and on the other hand, two groups of Trojans at 60° ahead and behind Jupiter. The principal comet reservoirs are in the Kuiper belt and Oort cloud.
NEAs originate in these large asteroid reservoirs. Some of the bodies in these reservoirs leak slowly due to the chaotic dynamics of the Solar System, and other effects such as the Yarkovsky effect[1], resonances such as $3:1$ resonance with Jupiter, and the ν_6 secular resonance. Eventually, some of them arrive close to the Earth's orbit to become a NEO.

The first NEO was discovered in 1898 (433 Eros) and since then, more NEAs have been discovered every year. It is believed that over 90% of these bodies larger than one kilometer have already been discovered [61].

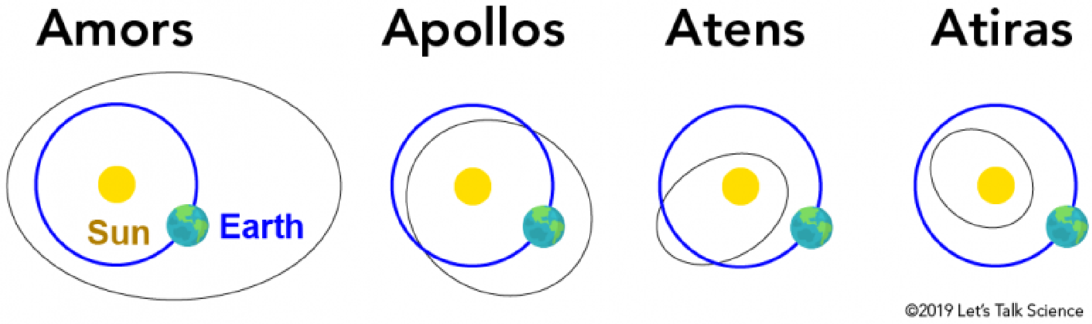

Figure 5.1: Different families of NEA according to their orbital elements[117].

---

[1] The Yarkovsky effect is a small, but significant force in small asteroids that appears in rotating bodies, and it is caused by the emission of thermal protons.

5.1.1. Families

NEOs have been traditionally classified into four different classes: Amors ($1.017 < r_{per} < 1.3$ AU), Apollos ($a > 1.0$ AU, $r_{per} < 1.017$ AU), Atens ($a < 1.0$ AU, $r_{ap} > 0.983$ AU) and Atiras ($0.7318 < r_{ap} < 0.983$ AU). The process of becoming a NEA is complex and long, and it is even longer and more complex when $a < 1.0$ AU, which explains why the Atens and Atira families are the least populated families, and also why their detection is more difficult. Atens and Apollos cross the Earth's orbit, and Amors have their orbits completely outside the Earth's orbit. Figure 5.1 illustrates the different types of NEAs according to the classification by orbital elements.

This classification is, nonetheless, controversial. Milani et al. [89] showed that over a time span of 200.000 years, the orbital precession and planetary perturbations will blur the boundaries between the established classes of NEAs. They proposed a different classification with six dynamical classes called after the most representative member of each one: Geographos, Toro, Alinda, Kozai, Oljato, and Eros.

The increasing interest in these kinds of bodies has made some scientists create new classifications to accommodate their needs. Arjunas were defined, for instance, as NEOs in exceptionally Earth-like orbits [17] with low eccentricity, low inclination, and a semi-major axis close to that of the Earth. Another very similar classification was proposed by Brasser and Wiegert in 2008 [20], called Small-Earth Approachers (SEA). Some other classifications include objects that follow particular trajectories. For example, objects in horseshoe orbits, Earth's Trojans or objects that are weakly captured by Earth –called Natural Earth Satellites (NESs) or Temporarily Captured Orbiters [57]. In 2012, NASA began publishing the Near-Earth Object Human Space Flight Target study (NHATS) list [1]. Other classifications for NEOs exist according to the impact hazard, this is the Palermo scale [32].

Of particular interest for this work are the Easy Retrievable Objects (EROs) proposed by Yárnoz et al. [128]. These are the NEAs that can be captured into periodic orbits around the L_1 and L_2 libration points in the Sun-Earth circular restricted three-body problem (CRTBP) with a total ΔV cost below 500 m/s.

5.1.2. Physical properties

In the last decades, there has been an improvement and increment in measurements of NEA physical properties. These measurements have been taken *in-situ* by probes like Deep Space I or OSIRIS-

REx or using spectroscopic and rotation properties. However, only a few hundred objects have been studied thoroughly [14]. In general, only approximate guesses of albedos and diameters can be made based on the asteroid absolute magnitude H.

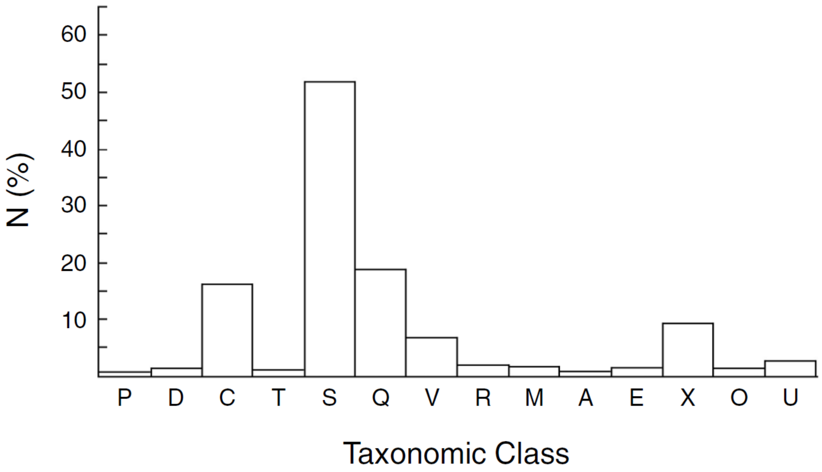

Figure 5.2: Histogram of the relative proportions of measured taxonomic properties for more than 300 of the largest NEAs [14].

Figure 5.2 shows a histogram of the relative proportions of measured properties for more than 300 NEAs [14]. The classification is based on the most abundant chemical component of the asteroid, and it is analogous to the one used regularly for classifying all asteroids. The data used to generate Figure 5.2 was extracted from a small batch of the largest asteroids only. Therefore, it does not fully represent the composition of the small asteroids we are interested in, as will be seen in Section 5.2.

5.1.3. Relevance

NEAs are the objects closest to the Earth, hence their name, and they have received special attention from researchers in the last decades for several reasons.

Earth planetary defence

NEAs can represent a potential danger for life on Earth. At this moment, it is widely accepted that asteroid impacts may have been the cause of mass extinctions in the past, such as the Cretaceous–Tertiary (K–T) extinction [28]. After the discovery of the first NEA that crosses the Earth's orbit (an Apollo) in 1932, it was clear that these kinds of objects deserve special attention. The Spaceguard Survey was created in 1998 with the intention of discovering 90% of the asteroids with a diameter larger than 1 km within one decade [61].

Asteroid mining

On the other hand, NEAs could offer important financial returns, first because some are energetically closer to the Earth than any other celestial body, including the Moon. As shown by Sánchez et al. in 2011 [104] NEAs allow access to resources at an incremental level of energy, while lunar resources always require a minimum threshold equal to the Moon's escape velocity.
The composition of these asteroids can only be obtained in a laboratory or from spectral reflectively studies. As described in [102] NEAs can be roughly classified according to their composition as C-type rich in water and carbon, S-type with anhydrous rocky material, silicates, sulphides, and metals, or M-type, metallic with a high radar reflectivity.

According to the Asteroid Mining Corporation [81] the main resources that can be obtained from asteroid mining are:

- **Volatiles**: Carbonaceous (C-type) asteroids contain large amounts of water. Access to water in space is crucial because it provides the basis for life-supporting systems, hydration, and breathable air. Plus, they could provide radiation shielding, industrial capabilities, and even be used to create rocket fuel. The idea of using *in-situ* resources to create propellant is common in the space-mining literature, and also opens the doors to an industry of space supply from asteroids [112].
- **Rare Metals**: It is known that some NEAs contain Platinum Group Metals (PGM) in a much higher concentration than Earth's most productive mines [81]. It is believed that a 500 m diameter asteroid would contain 1.5 times the known world reserves of PGM -specifically, ruthenium, rhodium, palladium, osmium, iridium, and platinum.
- **Others**: Asteroids could also be used as a source of common metallic elements such as iron, nickel, and cobalt; semiconductors and nonmetals used in microelectronics. Other volatiles such as nitrogen, CO, CO_2, and methane also exist in sufficient quantities to be extracted.

As can be seen, asteroid mining is a promising field with many future opportunities. However, many challenges still have to be solved. That is the reason why it has been a proliferous topic in the last few years [24, 46, 64].

Scientific missions

In the latest years, NEAs have become a popular destination for science and exploration space missions. Almost all of the main space agencies have had a mission targeting a NEA in the last decade.

NASA was the first one to do so. In 1996, they launched the probe NEAR Shoemaker (honoring the discoverer of the first NEA), which studied the NEA Eros (S-class asteroid) from a close orbit for over a year [95]. Later, the mission Deep Space 1, which was launched in 1998, visited the NEA 1992 KD as its first destination. In 2016, OSIRIS-REx traveled to the NEA Bennu, and it is intended to bring samples back to Earth in 2023.

The Japanese Space Agency JAXA has put great efforts in developing Hayabusa and Hayabusa 2 which were envisioned to bring samples from the NEA 25143 Itokawa, and 162173 Ryugu respectively.

Also, there are missions targeting a NEA that will be launched in the near future. In 2021, the Double Asteroid Redirection Test (DART) intends to evaluate the kinetic impact technique by striking one of the asteroids of the binary NEA system Didymos and Dimorphos. The NEA Scout mission is also to be launched soon, and it consists of a CubeSat, which will fly and return to the NEA 1991 VG. Both missions are being developed by NASA.

Other usages

Besides the more ’traditional’ usages for NEA asteroids, new and audacious ideas have also been suggested in the last decades. In 2019, Vermeulen et al. [122] proposed using asteroid resources to build settlements in space. Their main idea is to use differential 3D manufacturing to create and develop habitable spaces within an asteroid.

Having a NEA in a bounded and secure position could allow for having space tourism to these kinds of bodies. There, habitats (or hotels) would have to be created to host the space tourists during their trip. These kinds of ideas have been around since the start of the space era [112].

5.2. JPL Small-Body Database

The asteroid data used in this work has been retrieved from the JPL Small-Body Database, which provides physical and orbital data for all known asteroids and many comets. By the day the database was downloaded, 2^{nd} June 2021, information on 26,145 NEAs was available. By checking the existing literature [105], it can be verified that the database has almost doubled in the last five years. The JPL database permits to select the elements that the user needs to create customized databases. For this work, the following elements were used: name, the epoch of osculation in Julian day form, orbital elements $(a, e, i, \Omega, \omega, \theta)$, absolute magnitude H and sidereal orbital period.

The orbital elements and epoch osculation will permit us to associate the state of the asteroid to a precise moment, which will allow us to propagate its orbit in order to get its complete time history. The absolute value will allow us to estimate its diameter by using the following formula [19]

$$D = \frac{1329}{\sqrt{p}} 10^{-0.2H} \tag{5.1}$$

where H is the absolute magnitude of the asteroid, and p its geometric albedo. The main problem is that, for most of the asteroids, their geometric albedo is not known. However, it is known that the geometric albedo in NEAs ranges between 0.05 and 0.5, depending on whether they are very dark objects or not [62]. For this work, a value of $p = 0.05$ based on the peak of the albedo distribution model for NEAs created by Mainzer et al. [127] will be used.

The sidereal orbital period is the time it takes the asteroid to complete one orbit around the Sun, but since we are interested in creating transfers between the asteroid and the Earth's vicinity, we will use the synodic period. The synodic period is the time that takes the asteroid to return to the same position as seen from the Earth. The conversion between the sideral and the synodic period is given by [6] (all values in years)

$$P_{syn} = \frac{P_{sid}}{|P_{sid} - 1|} \tag{5.2}$$

5.2.1. Data analysis

In this section, we will analyze the data using the already mentioned parameters, in order to gain some insight into how the contents of the database are distributed. We will compare this data with some of the results derived from the creation of the tori database.

Figure 5.3 shows the distribution of the asteroids with respect to their Tisserand parameter. Note that the Jacobi constant is only defined in the context of the CR3BP, so we cannot use it directly. Instead, the so-called Tisserand parameter will be used

$$J \approx \frac{1}{a} + 2\sqrt{a(1-e^2)\cos i} \tag{5.3}$$

with $a, e,$ and i the semi-major axis in AU, eccentricity, and inclination respectively. The Tisserand criterion is derived from the Jacobi constant expression but simplified by assuming that one of the primaries is much larger than the other one and that the asteroid does not approach the primaries. It will be assumed that both assumptions are met and thus, the equation holds for this case. By using the Tisserand parameter we can connect the asteroid database to the CR3BP in the Sun-Earth system that we have extensively discussed.

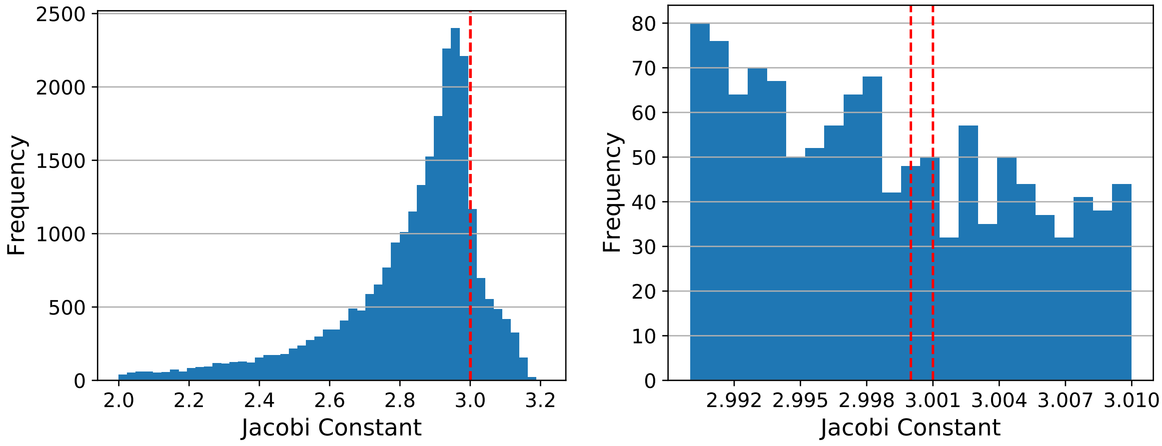

(a) Full distribution.

(b) Zoomed-in around area of interest.

Figure 5.3: Jacobi constant distribution for the NEA population.

Figure 5.3a displays the distribution of the whole spectrum of Jacobi constants C that contains the NEA family. It can be seen that, commonly, NEAs have a Jacobi constant of about 2.95. However, this is lower than the values that we will be interested in. In red, there are the constant limits that contain all the possible families of tori that were already computed $\sim (3.0, 3.001)$. It is apparent that most of the asteroids in the database have a constant out of the boundaries that we are interested in. Figure 5.3b shows an augmented section in which the span of the useful range of Jacobi constant values can be better visualized. By looking at the figure it can be seen that around 50 asteroids have a value of C in the range of the quasi-periodic tori derived here.

The next step is to analyze the distribution of the orbital elements of the asteroids. Figure 5.4 shows on the left side the distribution of eccentricity values among the NEAs. This distribution resembles a normal distribution with a mean of 0.444 and a standard deviation of 0.179. Ideally, the asteroid should be in an orbit very close to Earth's orbit ($e_E = 0.0167$). It is logical to think that asteroids with lower eccentricity will require lower ΔV to transfer to Earth's vicinity. 2020 AP2 is the asteroid with the lowest eccentricity with a value of 0.0028, and there are 151 asteroids with eccentricity smaller than 0.05.

Figure 5.4b shows an analogous distribution for the orbital inclination. It can be seen, that most of the asteroids have an inclination lower than 10°, which makes sense provided that they come from the asteroid belt and Jupiter Trojans. Following the same line of reasoning as with the eccentricity, we are interested in asteroids with inclinations closer to zero. 2013 GM3 has the lowest inclination with a value of 0.0133. Moreover, there are 7287 asteroids with an inclination lower than 5°.

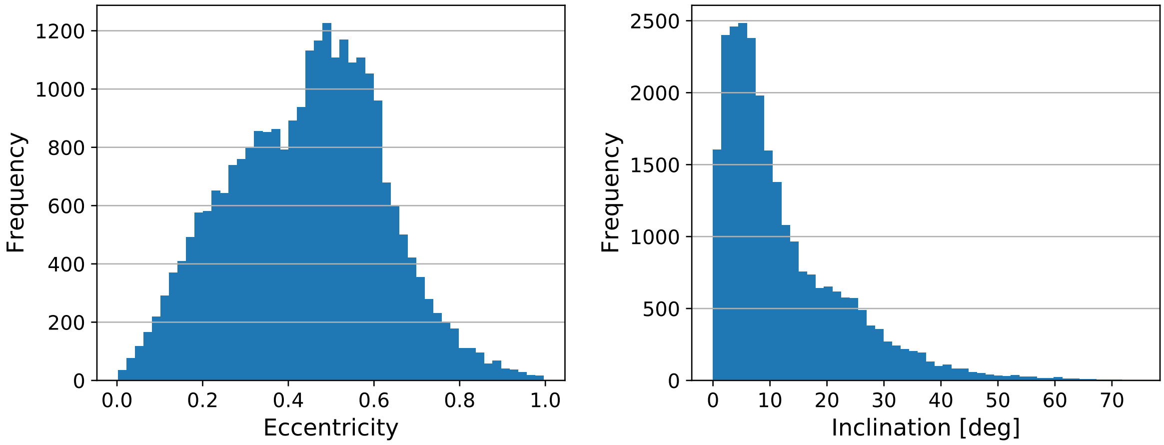

(a) Eccentricity histogram

(b) Inclination histogram

Figure 5.4: Distribution of eccentricity and inclination of the NEA database.

Promising candidates are those capable of generating cheap and fast transfers from their heliocentric orbit to Earth's vicinity. These asteroids have to meet one more requirement: not only the asteroid has to be in the appropriate C range and meet some geometrical conditions given by the orbital elements. If the asteroid is just too big to be transported, then it is not a feasible option. Sánchez et al. [107], building on the proposal of Keck [23], envisioned a spacecraft of 5500 kg dry mass, and 8100 kg of propellant at the NEA orbit. In that situation, a high-thrust engine with specific impulse 300 s would be able to carry from 44 to 400 tons. On the other hand, if a low-thrust engine with specific impulse of 3000 s were used, the maximum capacity could be increased one order of magnitude, up to 4000 tons.

The density of NEAs varies between 1.3 and 5.3 g/cm^3 [31]. In this work, a value of $\rho = 2.6\ g/cm^3$ will be taken since it is the average density of S-class asteroids, and as we have seen, they tend to be the most common NEAs, see Figure 5.2. Assuming that the asteroid is perfectly spherical, we can then conclude that the largest asteroid that could be transported under the above assumptions has a diameter smaller than $13-27$ m.

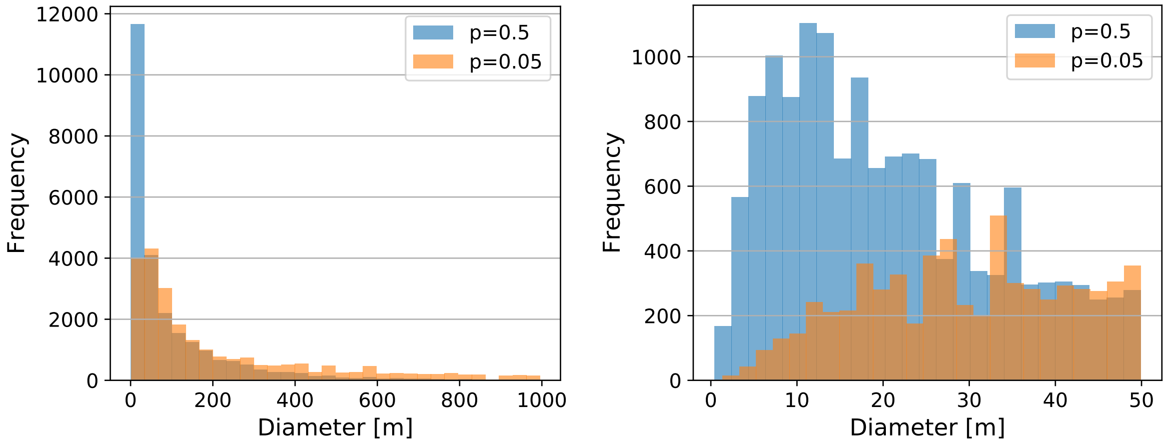

(a) General distribution overview.

(b) Augmented section of region of interest.

Figure 5.5: Distribution asteroid diameter estimation with $p = 0.05$ and $p = 0.5$.

Figure 5.5 shows the distribution of the NEAs by diameter. These values have been obtained using Equation 5.1 and using a geometric albedo values of $p = 0.5$ and $p = 0.05$. This will permit us to understand how the estimations would change by taking one value or the other. If the asteroids are assumed to be bright objects ($p = 0.5$) then Figure 5.5 shows that the number of asteroids with smaller diameters grows significantly. Figure 5.5b permits to appreciate better this difference. Considering that just an estimation of the asteroid's size can be obtained, it is more logical to use the most conservative criterion. Therefore, a value of $p = 0.05$ will be used from now on. It is also clear that there is an abundant number of asteroids within the range we are interested in, specifically, there are 2634 asteroids with a diameter smaller than 27 m.

Figure 5.6 illustrates the diverse range of asteroids that the JPL database contains. Every asteroid is plotted according to its semi-major axis and eccentricity, the size of the dot is proportional to its diameter. As has been discussed already, the potential candidates for being transferred to the Earth's vicinity must have low eccentricity, but also a semi-major axis close to unity, see the red and orange dots. The figure shows this area of interest magnified. The main observation there is that the set of valid asteroids is very small compared to the full domain. Another interesting observation is the shape of the domain. One could expect to have a randomly filled domain, yet there are clear boundaries that come from the definition of NEA, Section 5.1, and they coincide with the two solutions of Equation 5.3. The orange dots represent the asteroids that meet the C requirement, Figure 5.3, and have an inclination < 10°. Its shape comes from Equation 5.3, and it can be seen that about 10 promising candidates appear in the magnified area.

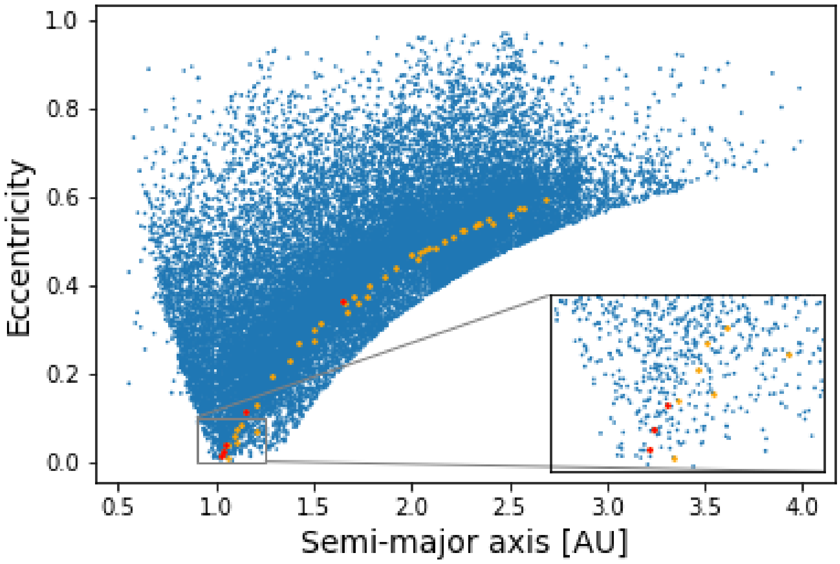

Figure 5.6: Semi-major axis vs eccentricity distribution for the full NEA family. In orange NEAs with low inclination, in red the ones from Figure 5.8.

Finally, we will merge our data from the database with the one obtained in the tori database. The maximum inclination that the manifold of each tori can achieve will be saved and plotted for each of the quasi-periodic families. Figure 5.8 represents this maximum inclination. The original signal was noisy, because a small part of the propagations fall into the primaries, distorting the results. For that reason, a smoothing filter has been applied.

Table 5.1: Most promising asteroids based on Jacobi constant and inclination from Figure 5.8.

Name	**Jacobi**	**a [AU]**	**e**	**i [deg]**	**H**
2006 RH120	3.000073	1.033154	0.025	0.595	29.50
2012 TF79	2.999948	1.050	0.038	1.005	27.39
2019 OY2	3.000096	1.650	0.363	0.527	24.70
2019 RP2	3.000599	1.154	0.114	1.224	28.90
2020 CD3	3.000309	1.028	0.012	0.634	31.80

In the figures, the resulting shape is plotted with a filled area. These curves span through the range of energies and inclinations where the tori exist. The differences between tori about L_1 and L_2 are very small, almost imperceptible. The most surprising result is that from the original 26.145 NEA asteroids only 4 meet these requirements, which are shown in Table 5.1.

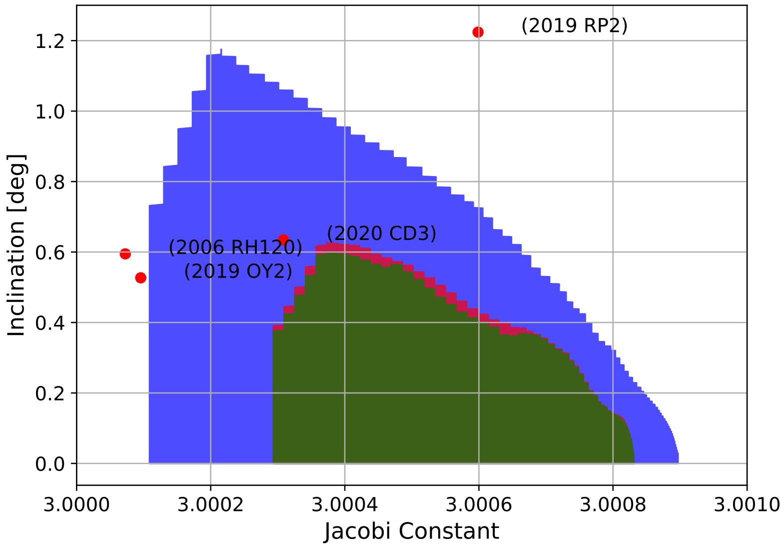

Figure 5.7: Maximum inclination of the tori families about L_1 for different values of Jacobi constant. In red dots, closest asteroids, which are further detailed in Table 5.1.

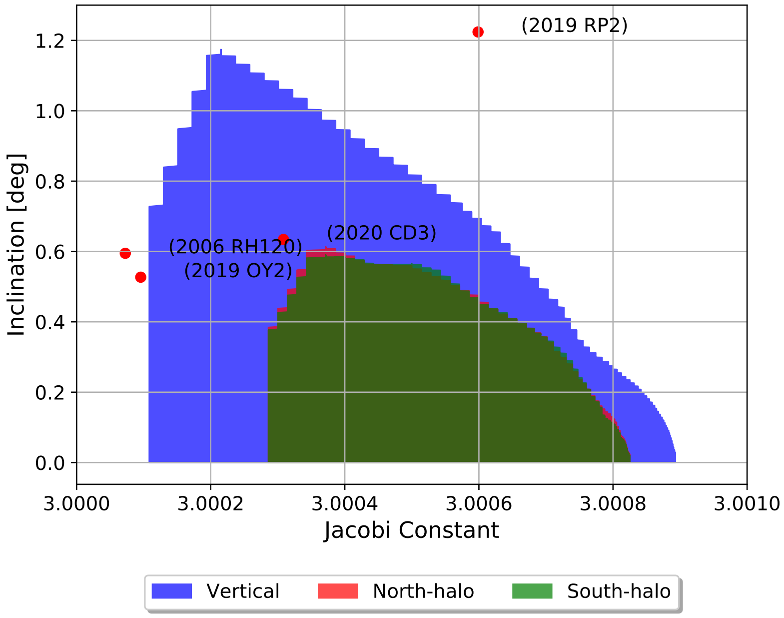

Figure 5.8: Maximum inclination of the tori families about L_2 for different values of Jacobi constant. In red dots, closest asteroids, which are further detailed in Table 5.1.

5.3. Pruning Method

We have seen in previous sections how vast and diverse the NEA database is, and that only a very small number of these asteroids can be used for designing low-energy transfers into a bounded region around the Earth. In this section, a pruning method consisting of different filters will be formalized. Note that, *a priori*, this filter should be applied to every quasi-periodic family at each Lagrange point individually, because there could be differences between them. However, it has been seen that the promising asteroids coincide for all quasi-periodic families and equilibrium points, so only one of these identical cases will be discussed here.

First, the Tisserand parameter of each asteroid is computed and checked if it is between the Jacobi constant ranges of each family, plus a small margin. As seen in Figure 5.3 this will filter out most of the database. Indeed, only 67 asteroids remain after applying the filter in our case.

The second filter was proposed by Sánchez et al., and it tests the geometry of the configuration. Take into account that during the pruning, any assumption that makes the asteroid more suitable or attractive is a valid assumption. A different discussion would be if, by doing that, we lose filter effectively. The second filter consists in computing the ΔV required for a Hohmann transfer from the asteroid to the manifolds. Some strong assumptions are made for the sake of simplicity, for instance, the lines of nodes are made to coincide with the lines of apsides so that the inclination changes can be applied at one of the apsides.

In order to apply this filter, we first need to compute the manifolds emanating from each torus and save the maximum inclination, and maximum and minimum distance so that they can be used as target points when applying the Hohmann formulas. The bi-impulsive burn required to match the semi-major axis of the asteroid with the invariant manifold can be computed as

$$\begin{aligned} \Delta v_{a1} &= \sqrt{\frac{\mu}{r_1}}\left(\sqrt{\frac{2r_2}{r_1+r_2}}-1\right) \\ \Delta v_{a2} &= \sqrt{\frac{\mu}{r_2}}\left(\sqrt{1-\frac{2r_1}{r_1+r_2}}\right) \end{aligned} \tag{5.4}$$

where r_1 is the radius of the inner orbit, r_2 the radius of the orbit, and μ the gravitational parameter of the Sun. Note that whether to choose the smaller or larger distance of the manifold depends on the initial asteroid position with respect to Earth's orbit. Furthermore, the ΔV required to produce a change Δi of the inclination is given by

$$\Delta v_i = 2v_1 \sin(\Delta i/2) \tag{5.5}$$

where $v_1 = \sqrt{\mu / r_1}$ is the velocity of the inner object at the initial orbit. The total ΔV of the Hohmann maneuver can be obtained as

$$\Delta v = \sqrt{\Delta v_{a1}^2 + \Delta v_{i1}^2} + \sqrt{\Delta v_{a2}^2 + \Delta v_{i2}^2} \tag{5.6}$$

where either Δv_{i1} or Δv_{i2} are included depending on whether the inclination change is performed at the perihelium of aphelion. Note that there exist four different combinations that accomplish the transfer: burn at aphelion to modify the perihelion, change of inclination at aphelion and circularization at perihelion; the analogous but changing the inclination at the perihelion and the rest can be obtained by modifying the perihelion first. The minimum of the four ΔV is the one used by the filter.

In our filter, a conservative threshold of $\Delta V = 1000$ m/s was used, and the database was reduced from 67 to 56 asteroids. This part of the filtering is expensive, because the manifolds of all existent tori have to be propagated compared and stored, and did not offer significant changes in the size of the pruned database.

The last part of the pruning process entails the size of the asteroid. It is very straightforward: the diameter of the asteroid is computed using Equation 5.1, and if it is larger than 15 m, it is discarded. The value of 15 m is a conservative estimate based on the maximum range admissible, Section 5.2.

After pruning the JPL database using the tori manifolds from our database, only three asteroids remained. Table 5.2 contains the candidates and some of their more relevant characteristics. Remarkably, all of them were also in Table 5.1, where conclusions were drawn using only graphical data and without computing the tori manifolds. In the next section, we will briefly address each of the candidates.

Table 5.2: Potential NEAs for generating low-energy transfers by using invariant manifolds form quasi-periodic tori.

Name	**Jacobi**	**a [AU]**	**e**	**i [deg]**	**d [m]**	**T [year]**
2006 RH120	3.000073	1.033	0.025	0.595	7.48	20.93
2019 RP2	3.000599	1.154	0.114	1.224	9.86	5.17
2020 CD3	3.000309	1.028	0.012	0.634	2.59	24.29

5.4. Potential Candidates

5.4.1. 2006 RH120

It was discovered in September 2006 by Eric Christensen. During that year, the asteroid was captured into orbit around the Earth-Moon system. At that time, it was the first natural object discovered to have been captured by the Earth's gravity. It is not estimated that it could collide with the Earth in the future, so it is not considered dangerous [113]. Nonetheless, at its closest 2006 RH120 passed at 0.02 AU from the Earth.

Originally, it was believed to be just space debris, because its spectrum matched the white titanium-oxide paint that was used in the Saturn V rocket. This had already happened, like the case of J002E3, which turned out to be the third stage of the Saturn IV-B [79]. Later, this was proved to be false and now, after several observations, 2006 RH120 is known to be a natural body.
More specialized works [79] have pointed that 2006 RH120 has an absolute magnitude of 29.9 ± 0.3. They also concluded that it must have a diameter between 2 and 7 m. It completes a revolution about its axis every 0.05 hours. 2006 RH120 has risen the interest of the scientific community to study these kinds of objects and potential retrieval missions, as is proved by the abundant works that have appeared since its discovery [4, 5, 118].

5.4.2. 2019 RP2

This asteroid belongs to the Amors group –full orbit out of the Earth's orbit. It was discovered in September 2019, and it is not classified as a dangerous asteroid. Besides the orbital and scarce physical information provided by the JPL database, no more studies have been focused on this asteroid, and no other sources could be found.

5.4.3. 2020 CD3

2020 CD3 was discovered in February 2021 by the Catalina Sky Survey when it was in a geocentric orbit. It was confirmed by astrometric and physical observations to be a natural body [51]. This discovery happened 14 years after the first discovery of 2006 RH120. It is estimated to have a rotation period of about 3 minutes and it is one of the smallest asteroids ever characterized. It is believed that it was originated in the inner Main Belt, due to its spectrum [16].

6

Tuning

In this section, the problem of designing a transfer from a NEA orbit to a stable manifold leading to an invariant torus using a Lambert arc is presented and parameterized. The cost function, which manages the reference frames transformations, and propagations is created. Then some of the tuning parameters of the cost function such as the integrator to use, the acceleration model, and integration steps are tweaked in order to find a compromise between accuracy and computational speed. Furthermore, a Monte Carlo analysis is conducted to explore the design space and constrain some of the parameters to help the optimizer later find an optimal solution. Finally, the optimization problem is defined and tuned to provide the best results for our problem.

6.1. Problem definition

Two very different problems have been studied throughout this work. The first one concerns the CR3BP, which is expressed in a rotating reference frame and dimensionless units. In the context of the CR3BP, it was seen that periodic solutions around the equilibrium points exist from which invariant manifolds emerge, Section 3.3. It was also seen, that these manifolds are particularly interesting in mission design, for they can allow low-energy cheap transfers between different regions or even between different periodic orbits, Subsection 3.3.1. Furthermore, we studied that periodic orbits can give rise to quasi-periodic orbits, which form a two-dimensional family of two-dimensional tori.

What is more remarkable is that from the quasi-periodic tori also emerge invariant manifolds that can be exploited to create low-energy transfers. Since the space in which these tori live is much larger than the one of the periodic orbits, it is reasonable to think that the design space to create interesting transfers using its associated manifolds will have also increased considerably.

The second part revolves around NEAs. It was seen that they have been increasingly gaining more attention from academia, but also private companies for mining and space travel purposes. On one hand, they entail a threat to life on Earth, but on the other hand, their applications are becoming more and more apparent. Their dynamics are complex and described by the interaction of the n-body problem and other physical phenomena.

In this chapter, both quasi-periodic invariant tori and NEAs are combined in order to figure out the best high-thrust transfer from the NEA orbit to a stable invariant manifold that leads to a quasi-periodic torus. The ΔV required to perform such transfers will be obtained by solving the so-called Lambert problem. Therefore, three different frameworks will be mixed to solve the problem: the n-body problem, which will be used to propagate the asteroid's orbit, the three-body problem where quasi-periodic tori and invariant manifolds exist, and the two-body problem to solve the Lambert problem.

6.1.1. Lambert's theorem

Lambert's theorem states that the time required to travel the elliptical arc of an orbit depends just on the semi-major axis of the ellipse, the sum of the distances from the attraction center to the initial and final points of the orbit, and the length of the arc that joins the initial and final points. The development of the equations is lengthy, the interested reader can check any astrodynamics textbook such as [125]. In general, the Lambert problem can be written as

$$\sqrt{\mu}\Delta t = f(a, r_1 + r_2, c) \tag{6.1}$$

Normally, there is one free parameter in Equation 6.1 which can be obtained iteratively until convergence. The main problem of Lambert's formulation is that there is not only a unique solution, there are various. For that reason, several formulations have been developed through the years in order to resolve this problem.

For this work, the multi-revolution Lambert solver integrated into the TU Delft Astrodynamic Toolbox (TUDAT) will be used. This function allows to obtain the total ΔV between two points, provided their states, time of flight (TOF), the gravitational parameter of the central body, and the number of complete revolutions. Both the right and left branches are computed, the one with the lowest ΔV will be used.

6.2. Dynamical model

In order to be able to compute and evaluate the most promising transfers, we first have to parameterize the problem. In an effort to harmonize the different problems, a reference frame with the origin at the barycenter of the Solar System and orientated towards the vernal equinox (ECLIP J2000) will be used. The JPL small-body database already provides its coordinates with respect to this reference frame, so no transformation will be required. After pruning the NEA database, three potential candidates were obtained, Chapter 5. For each of them, the problem of finding promising transfers to a torus will have to be solved. One of the parameters is then the selected asteroid a_i, out of the three possible options. Another parameter is the time at which the transfer from the NEA orbit to the Lambert arc starts t_{begin}. The lower limit for the starting epoch is defined at 1st of January 2022 onwards, and its upper limit is given by the synodic period of each asteroid as shown in Table 5.2.

First, a libration point L_i, and quasi-periodic family F_t, quasi-halos or vertical, have to be selected to characterize the tori. Due to the fact that quasi-periodic tori are two-dimensional objects which lie on two-dimensional families, four parameters are required to locate a point lying uniquely on a torus. One of them is related to the Jacobi constant of the periodic orbit used to initialize the family, C_t, and for the remaining dimension the rotation parameter ρ_t can be used. Once a particular torus has been selected, two parameters, θ_1 and θ_2, determine a point on its surface. Note that since a database was created to speed up the computations, Section 4.9, only a discrete number of tori from the whole family can be used. Nonetheless, the database was created to span the whole spectrum until it collapses. The angles θ_1 and θ_2 were also discretized. It would be possible to use interpolation to get more values, but for the sake of accuracy, it was preferred to use only points where the exact data is known (i.e. the database elements).

Once a point on the torus has been chosen, we know that a stable manifold leads asymptotically to it. In order to choose the point on the manifold where the insertion from the Lambert arc will be performed, another variable needs to be defined. For this purpose, the angle between a point on the manifold and the $x-$axis on the CR3BP framework was used, θ_m. This angle is defined clockwise for L_1 departing manifolds and anti-clockwise for L_2 because the stable manifolds that arrive at each of the equilibrium points move in different directions. A maximum value of θ_m of 200° is allowed, which corresponds to a manifold transfer time of about 10 years. Taking into account the Lambert transfer time as well, the total duration could double. So it would be a long mission, certainly according to the space mission standards nowadays.

The state at which the insertion from the Lambert arc to the manifold will occur can be obtained by propagating backward in time from the torus surface until reaching the desired value of θ_m. The state is then converted to dimensional units and rotated accordingly to match the J2000 orientation.

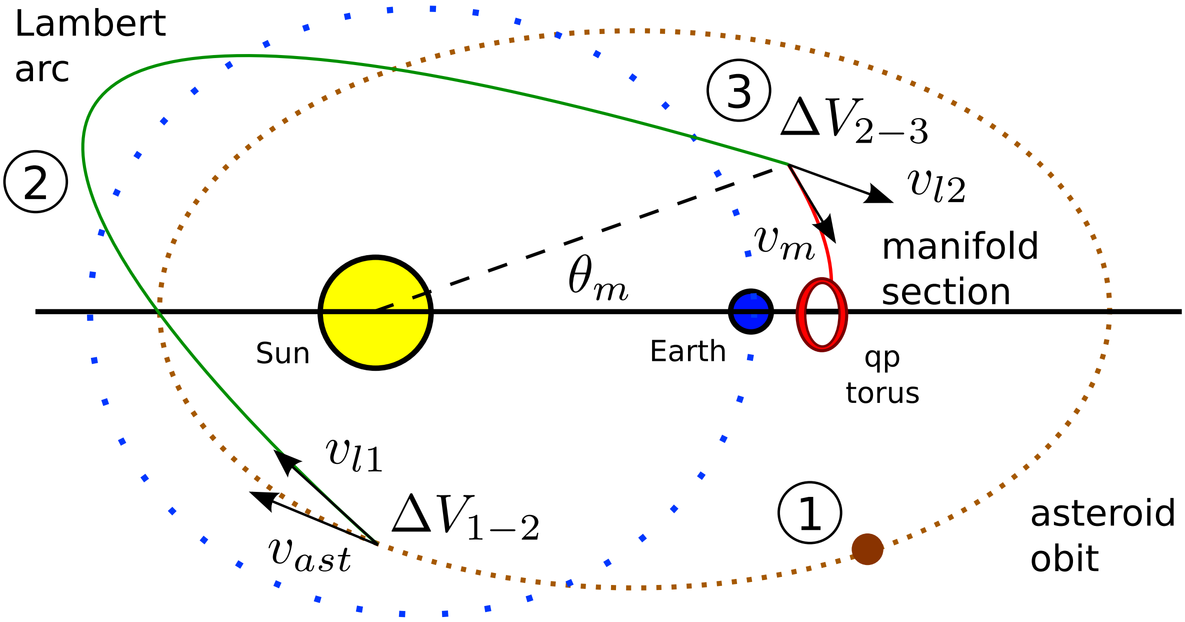

Figure 6.1: Scheme of the transfer from NEA to quasi-periodic orbits.

The state of departure in the NEA orbit and the state of the manifold at the insertion time define two parameters of the Lambert problem. The problem can be closed by adding two more parameters, the Lambert transfer time t_{trans} and the number of revolutions before insertion n_{rev}. t_{trans} was originally constrained to be between 1 and 5 years, although later in the Monte Carlo analysis it is shown that could be further restricted, Section 6.4. Once the Lambert problem is solved, the total ΔV can be obtained as

$$\Delta V = |\mathbf{v}_{ast} - \mathbf{v}_{l1}| + |\mathbf{v}_m - \mathbf{v}_{l2}| \tag{6.2}$$

where v_{ast} and v_m are the velocity in the NEA's orbit and manifold respectively, and v_{l1} and v_{l2} are the velocities at the Lambert arc at departure and insertion.

The total time of flight (TOF) can also be computed as

$$TOF = t_{trans} + t_m \tag{6.3}$$

where t_{trans} is one of the parameters of the problem, the time that is spent on the Lambert arc, and t_m is the traveling time from the insertion point to the quasi-periodic torus.

There are thus two opposite variables to optimize, the total ΔV and TOF, these are the two more common objectives in astrodynamics and the multi-objective optimization will depend upon 11 different parameters, namely $\mathbf{F}(a_i, t_{begin}, t_{trans}, L_i, F_t, C_t, \rho_t, \theta_1, \theta_2, \theta_m, n_{rev})$.

Table 6.1: Parameters of the transfer problem between NEA and manifold of quasi-periodic torus

Parameter	**Meaning**
a_i	NEA to be retrieved
t_{begin}	Time at which to start the transfer
t_{trans}	Time of transfer along the Lambert arc from NEA orbit to manifold
L_i	Lagrange point of the quasi-periodic orbit
F_t	Family of quasi-periodic orbit (quasi-halos, vertical)
C_t	Jacobi constant of the quasi-periodic orbit
ρ_t	Rotation parameter of the quasi-periodic orbit
θ_1	Longitudinal coordinate on the qp-torus where the manifold leads
θ_2	Latitudinal coordinate on the qp-torus where the manifold leads
θ_m	Angle between $x-$ axis an point of insertion in manifold
n_{rev}	Number of revolutions used in the Lambert problem

Table 6.1 contains a description of each of the parameters of the problem. By defining a combination of these a unique transfer from the NEA to a torus can be defined and its characteristics computed.
The cost function was implemented in TUDAT, so that the available modules for propagating the dynamics of the n-body problem, the CR3BP, and the Lambert solver can be used. Thus, there is no need to validate these computations, since modules which have been extensively tested and used will be employed. Only a check for proper usage and interpretation. Finally, the reference frame transformations that the cost function has to perform are validated in detail in Chapter 8.

Figure 6.1 show the geometry of such transfers. Starting from the NEA orbit (1) with $\mathbf{v}_{ast}$, a ΔV_{1-2} is applied to obtain a velocity $\mathbf{v}_{l1}$ which begins the transfer to the manifold along a Lambert arc (green). Later, a ΔV_{2-3} burn is applied to transform $\mathbf{v}_{l2}$ to $\mathbf{v}_m$. That manoeuvre introduces the asteroid into the manifold which will directly lead to a quasi-periodic torus about either L_1 or L_2.

6.3. Integration

The computation of the objective function contains some parameters that have to be adjusted. Ideally, the model should be as precise as possible, but the computational cost of such accuracy would be very high, and the optimization problem, which requires many iterations, would not be solved in reasonable times. For that reason, the balance between the accuracy of the solutions and performance will be addressed in three different problems: the accelerations used for the n-body simulation of the Solar System the integration scheme for both the n-body problem and CR3BP, and the time-steps or accuracy used.

Solar System acceleration model

It is necessary to address the influence of the different bodies of the Solar System in our simulation. Including fewer bodies in the simulation would speed up the computations. Yet, if the accelerations exerted are significant enough, the omission of errors would become unacceptably large for long integration.

To solve that problem, the influence of each of the main bodies on 2006 RH120 will be studied. A 21 year propagation (the synodic period of 2006 RH120) using a very fine time-step (15min!) will be used here. Then, similar propagations but omitting just one body will be conducted. The norm of the state difference between the reference and second simulation at the end of the integration will yield the effect that the missing body has on the integration. In this case, the full simulation will include Sun, Mercury, Venus, the Earth, the Moon, Mars, Jupiter, Saturn, Neptune and Uranus. Solar radiation pressure is also included, which is modeled using a cannonball radiation pressure model.

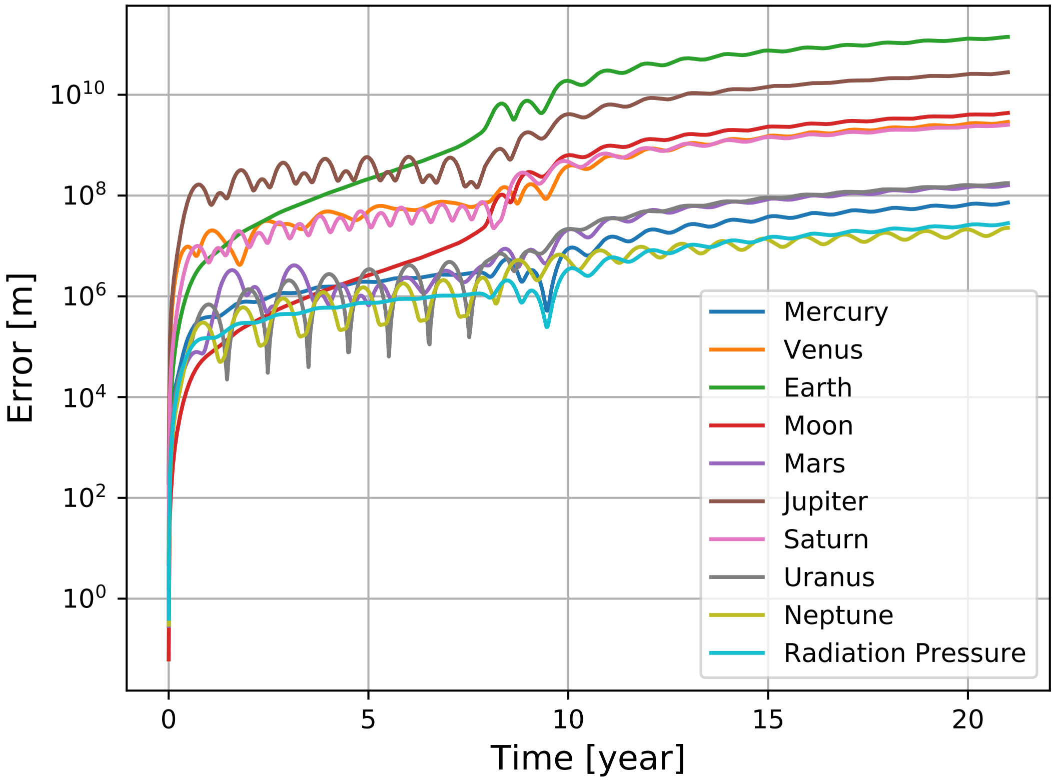

Figure 6.2: Effect of the different accelerations modelled in a full Solar System propagation.

Figure 6.2 shows the effect of the principal bodies and accelerations in the Solar System. It is not surprising to see the strong impact of Earth and the Moon, as long as NEAs are being studied. The substantial influence of Jupiter is also expected, for it is the second-largest object in the Solar System. Even the less important effects such as Mercury, Neptune, or the solar radiation pressure create errors of about 10.000 km over the 21 year integration. For that reason, it is decided that all contributions will be included in the propagation of the asteroid's trajectory.

Solar System integrator configuration

When doing the complete Solar System integrations, only variable step-size integrators will be considered. Allowing the integrator to choose the step size to meet an established tolerance is the best option for long interplanetary transfers because it can permit the use of larger step sizes at suitable points of the integration, which will result in lower computation times. We seek the fastest integrator for a given accuracy level. A common method to evaluate how well an algorithm will perform is to measure the cumulative number of function evaluations.

In this analysis, the following integrators will be compared: Runge-Kutta-Fehlberg (RK) 4(5), 5(6), 7(8), Runge-Kutta-Fehlberg 8(7) Dormand-Prince, Bulirsch-Stoer (BS) 6, 8, 10, and Adams-Bashfort-Moulton method (AB), with both absolute and relative tolerances ranging from 10^{-6} to 10^{-14}.

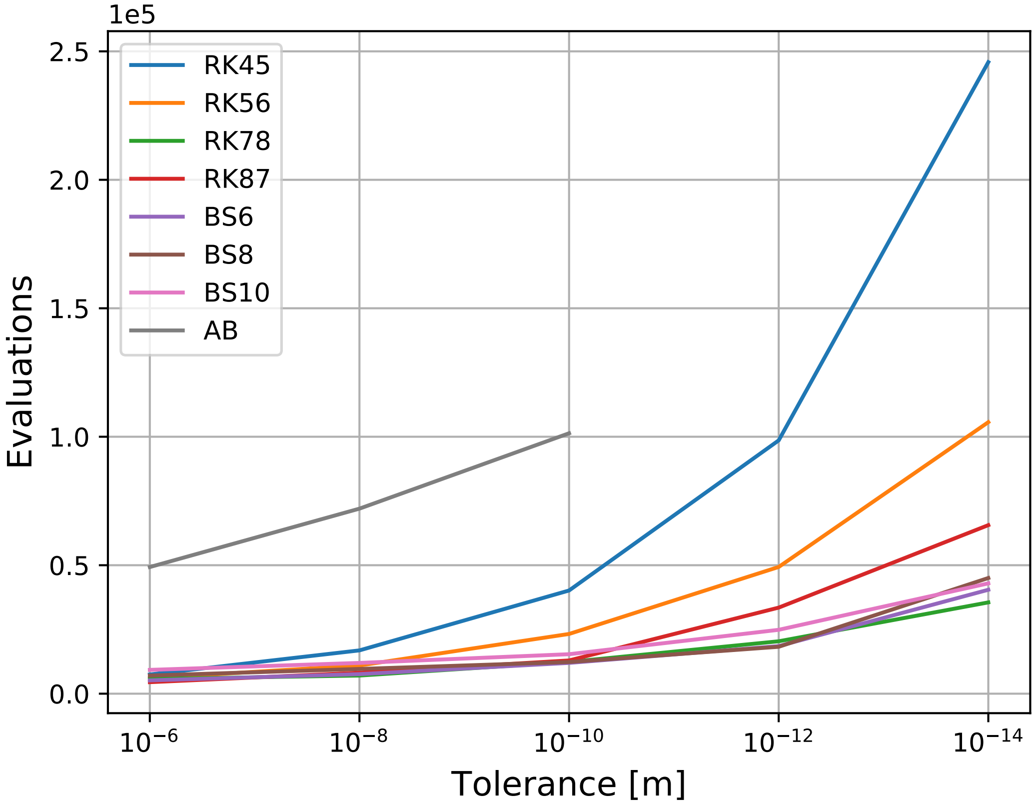

Figure 6.3: Number of evaluation required to meet the tolerance of the different variable step-size integrators.

Figure 6.3 shows the cumulative number of evaluations for the different integrators. At first sight, it can be seen that AB performs badly in this case. RK 4(5) and RK 5(6) also required a large number of function evaluations and thus are not suitable for this task. The best performance is obtained when using any of the BS methods or RK7(8). As is well known, the main advantage of BS methods is that they permit the use of extremely long time-steps [40], which is very favorable for integrating long time scales. That is why a BS method will be used to integrate the asteroid state.

Table 6.2: Selected integrators CPU time test

Scheme	**Error**	**Time [s]**
BS6	10^{-10}	1.0152
	10^{-12}	1.3129
BS8	10^{-10}	1.7400
	10^{-12}	1.9842

From Figure 6.3 the BS6 and BS8 seem to offer good results. Table 6.2 compares the computation speed of these two integrators for different values of error tolerance. BS6 is chosen for being the fastest one. Table 6.3 compares the error that BS6 provides for different tolerance values compared to a very fine RK4 integrator. Because most of the integrations in the optimization will last less than the synodic period, and thus the integration times are much lower than the ones shown in Table 6.2, a tolerance value of 10^{-10} is chosen in order to ensure a good quality of the results, but also good performance.

Table 6.3: Error at end of propagation using BS6 for different error values.

Integrator Tolerance [m]	**Error at last state [m]**
10^{-8}	11527100
10^{-10}	8223
10^{-12}	1106
10^{-14}	691

CR3BP Integrator configuration

The integration of the manifolds in the CR3BP problem is a logistically simpler task than the full state integration of all the Solar System elements. For that reason, a fixed-step Runge-Kutta 4 scheme will be used. The compromise between accuracy and performance is again critical. The best suitable time-step for this problem will be decided by computing the difference between the last state of an integration performed with a very fine time-step (time-step of 1 h), and the state obtained after integrations with different time-steps.

Figure 6.4 shows the evolution of the error at $\theta_m = 350°$ for different time-steps. The error grows exponentially for time-steps smaller than 5 days; any time-step beyond that leads to unacceptable errors. In the end, a time-step of 2 days is chosen for it provides an error of 10^4 m consistent with the error used for the asteroid propagation.

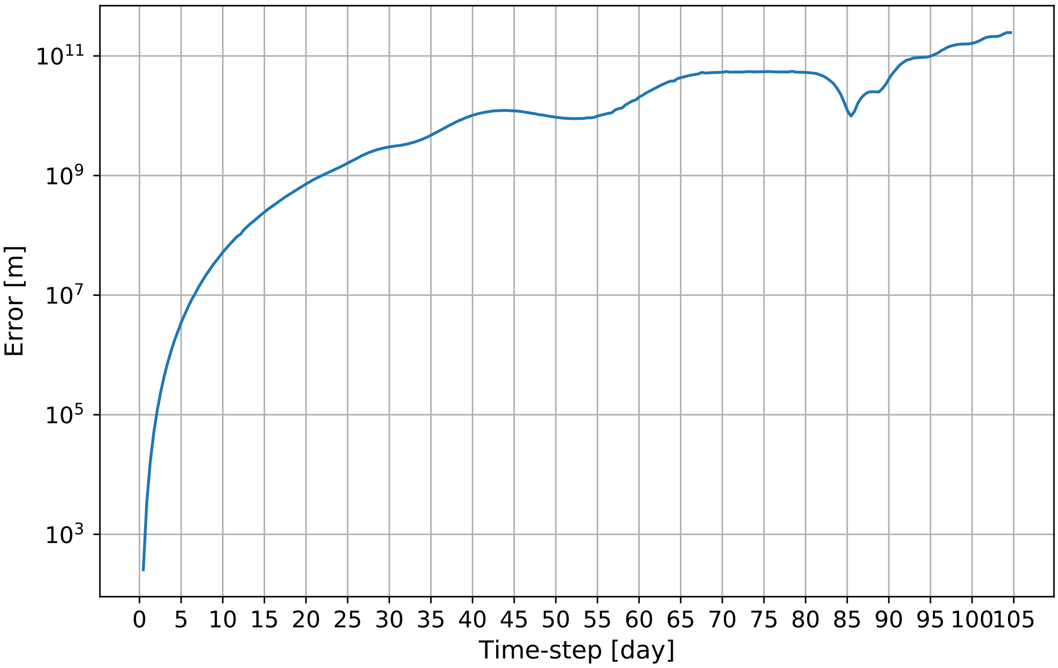

Figure 6.4: Error of manifold propagation with respect to the integration time-step.

Table 6.4 shows the computation times required for different time-steps. It can be seen that the reduction is more noticeable between using 1-2 days than between the rest. In any case, the values are so small compared with the time spent in the Solar System propagation, that is not worth bothering. Finally, a time-step of 2 days seems like a very reasonable choice.

Table 6.4: Computing times for manifold integrations with different time-steps until $\theta_m = 350°$

Time-step [day]	**Time [ms]**
1	6.462
2	2.865
3	1.617
4	1.203
5	1.015

6.4. Monte Carlo Search Space

It could be possible to start the optimization procedure right after defining the cost function. However, it is common practice to perform an exploration of the design space using a Monte Carlo method[1]. Exploring the design space prior to solving the optimization problem is a good practice and very useful for a number of reasons.

- It allows to redefine, and preferably reduce, the boundaries of the problem since it can show that some regions of the design space are unattractive compared to others others. This is very advantageous because the more we reduce the design space the less likely is the optimizer to get stuck in a local minimum afterward. Be aware that in multi-dimensional problems the different parameters can be extremely coupled, and thus, searching for the influence of individual variables can be a challenging task.

- It permits to gain insight into the order of magnitude of the solutions of the cost function, so it is easier to interpret the results afterward. In other words, by performing a random search of the design space we can understand how limited, or not, is the area at which a minimum can be found during the optimization phase. If the optimum is very sharp or more broad.

- The best individuals from the Monte-Carlo analysis can be used to initialize the optimizer. This will speed up the convergence of the optimization scheme significantly.

In our case, a different Monte-Carlo analysis was conducted for each of the asteroids. Even more, for each asteroid, a different Monte-Carlo run was done for each Lagrange point and family of quasi-periodic orbits. Furthermore, for the asteroids with a synodic period larger than 20 years (2006 RH120 and 2020 CD3), the domain for t_{begin} was split into five different parts to help find promising results, The asteroid 2019 RP2 has a synodic period of about 5 years, so its domain on beginning time was divided into two parts. Each Monte Carlo analysis will consist of 100,000 simulations using random values for the parameters, Table 6.1. Note that some of them have been already fixed or reduced in order to improve the exploration. With all of that, we can compute the number of simulations required to conduct the full Monte Carlo analysis

$$n_{sim} = \sum_{n_{ast}} n_{eq} \times n_{qpfam} \times n_{t_i} \times 100{,}000 = 7{,}200{,}000 \tag{6.4}$$

with $n_{ast} = 3$, $n_{eq} = 2$, $n_{qpfam} = 3$ and $n_{t_i} = 5, 2, 5$ for each of the asteroids.

---

[1] Monte Carlo methods rely on repeated random sampling to obtain numerical results. Its uses range from finance, engineering, science, and many others.

Since many runs are conducted and the search space has been divided, only one seed is used at this stage. Around 7 million simulations would be required to (try) characterize the design space. Now it is very clear why considerable efforts were put in creating a database to use a look-up table to find the tori manifolds, and finely tuning the propagations, instead of solving the problem 'on the fly'.

We assume that on average, evaluating the cost function takes around 1 second, which includes retrieving data from the database, CR3BP integration, n-body integration, and solving the Lambert problem. If that were the case, then we would need 84 days to do the Monte Carlo analyses, which would be 40% of the time available for this thesis work. However, the problem can be easily parallelizable, which would reduce the computational time enormously. For that reason, the TU Delft computer cluster was used. By running 14 simulations simultaneously the computational time could be reduced to a much more reasonable value of 6 days.

6.4.1. Error Analysis

Any combination of variables can appear during the Monte Carlo analyses. However, it was seen that some combinations did not provide a valid solution. There are three different causes to explain why a simulation failed in finding a solution:

- **Manifold**: The backward propagation of the invariant manifold fell into the primary. It was observed that, commonly, when this happens the orbital direction is reversed. In other words, if the stable manifold around L_2 falls into the primary it will, generally, orbit in a clockwise direction. Yet, the rest of the manifolds will move in an anti-clockwise direction.
- **Angle**: The value of θ_m, that is the value at which the backward propagation of the stable manifold should stop, is smaller than the initial θ_m at the surface of the torus. Since the values of the variables are randomly generated, this can occur sometimes. This problem could be solved by imposing a minimum value of θ_m. However, we preferred to leave it free in order to explore if using very small values of θ_m and thus, spending less time transferring along the manifold was the best option.
- **Lambert**: Due to the geometry of the problem, the Lambert solver sometimes failed to find a solution for the parameters used.

Figure 6.5 shows the distribution of the aforementioned error causes. It can be seen that the most common cause of problems is related to the Lambert solver, the second one is related to the manifold back-propagation falling into the primaries, and the last one, and most unlikely is that the θ_m angle is smaller than the one of the original state. In any case, around 10% of the simulations in the Monte Carlo analyses turned out to yield an error for one of those causes.

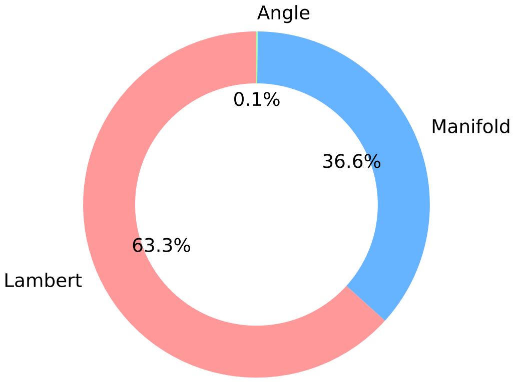

Figure 6.5: Distribution of the different causes of solver failure.

The relationship between the number of erroneous solutions and some of the main parameters was investigated. Figure 6.6a displays the distribution of errors with respect to the equilibrium points, and (b) the quasi-periodic family they belong to.

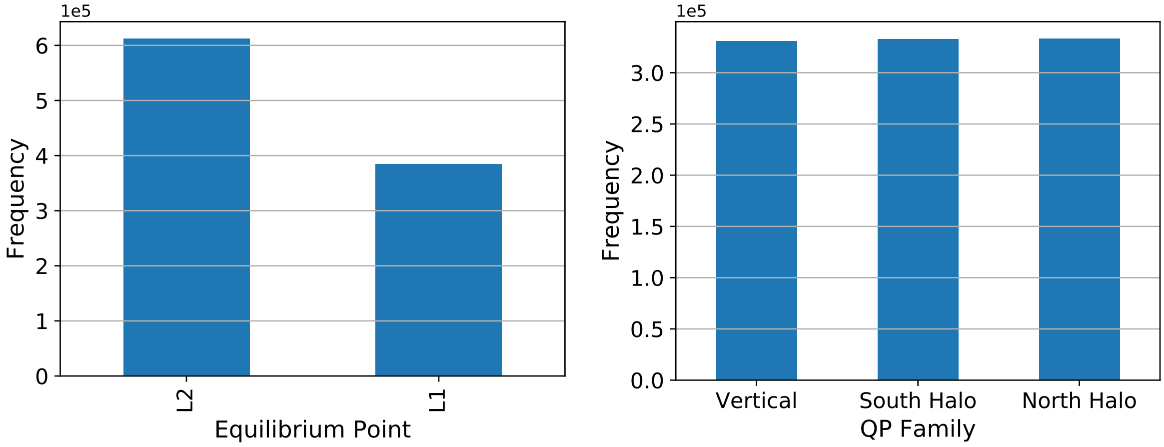

(a)

(b)

Figure 6.6: Distribution of the failed simulations with respect to the equilibrium point and quasi-periodic family.

It can be seen that the family of quasi periodic orbits does not have any effect. On the other hand, the equilibrium point does seem to have an effect. Geometries ending up at L_2 seem to be more prone to yield errors than the ones that end up around L_1.

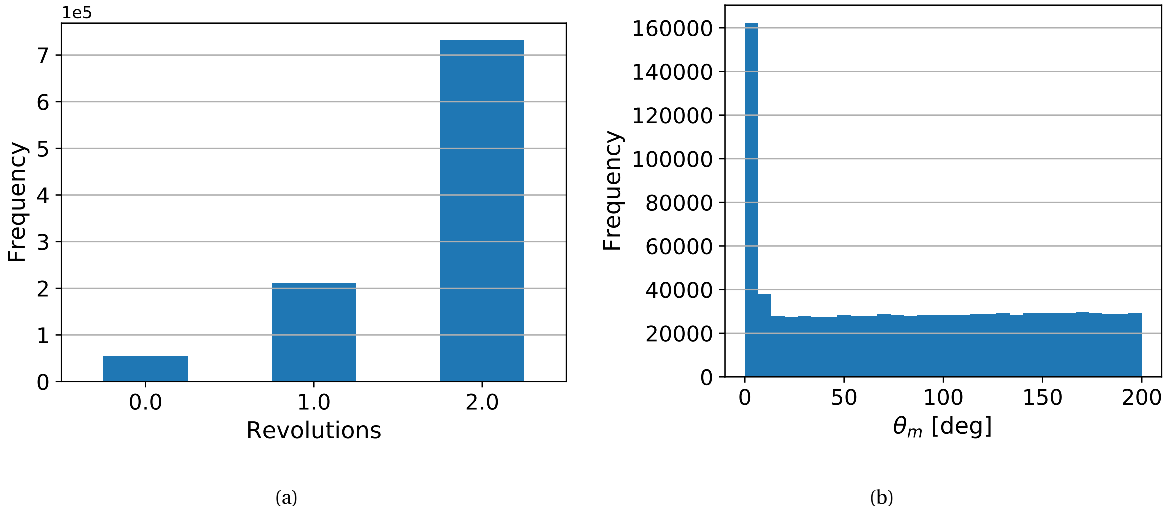

(a)

(b)

Figure 6.7: Distribution of the failed simulations with respect to the number of revolutions and manifold angle.

Figure 6.7 presents analogous data, but related to the number of revolutions (a) and the value of θ_m (b). Lower values of θ_m are related to larger occurrences of the error, which is the expression of the second error cause explained before (angle).

Using two revolutions seems to generate much more failed computations than when using zero or one. Since the number of revolutions used does not affect the propagation of the manifold, the increasing error for larger n_{rev} must be directly linked to the errors produced by the Lambert solver. In any case, due to the fact that, as it will be seen, using one or two revolutions produces the most promising transfers, these scenarios are kept.

6.4.2. 2006 RH120 Analysis

Next, we will examine the results of the Monte-Carlo analyses obtained for the NEA 2006 RH120. Note that some of the conclusions that are extracted from this analysis will also appear in the rest of the selected NEA, and these parts will not be repeated for them.

Histograms of the ΔV and TOF for each of the variables of the problem will be used to analyze their effect and distribution. Then we will try to extract conclusions from these graphs when possible, and relate them to the physics/geometry of the problem. Finally, this insight obtained will be used to reduce the design space by removing areas providing unrealistic ΔVs and TOFs.

Libration Point

Figure 6.8 shows the frequency of appearance of a specific ΔV and TOF for solutions that arrive to tori about L_1 and L_2. By looking at the ΔV, it is remarkable that both curves are similar in shape, but they are shifted. Specifically, the L_2 curve is displaced to lower values of ΔV. The physical explanation for this phenomenon is simple. The orbit of 2016 RH120 is larger in perihelion than the Earth's orbit, which means that it is energetically closer to L_2 than to L_1, hence lower ΔV is required to transfer from one to the other.

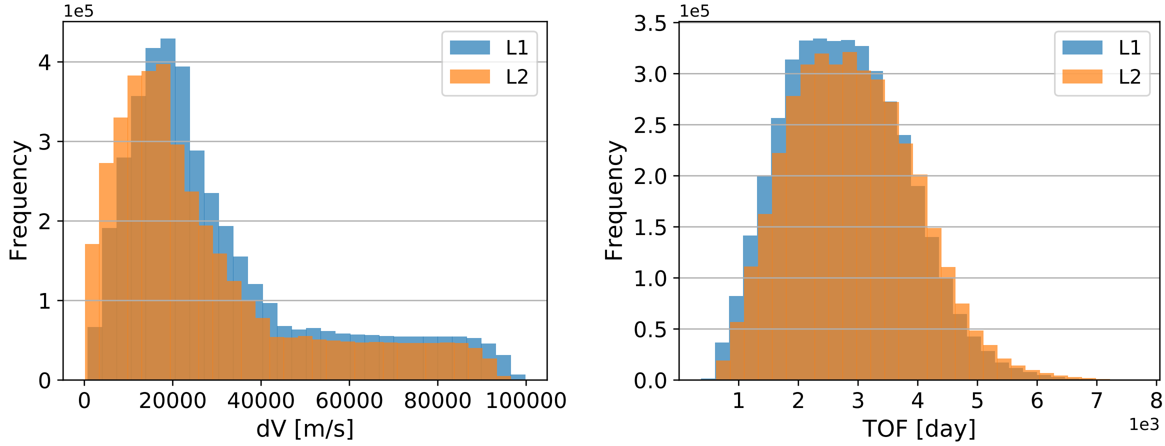

(a) ΔV

(b) TOF

Figure 6.8: Histogram of ΔV and TOF about each of the libration points.

Concerning the TOF, Figure 6.8b shows that there are slightly more transfers with lower TOFs to L_1 than L_2. However, both graphs are similar in shape and do not present a remarkable phase difference. For that reason, only transfers to tori around L_2 will be studied. This choice halves the full design space already.

Number of revolutions

Figure 6.9a shows the histogram of ΔV for different number of revolutions. On the right-hand side, there is a zoomed view for ΔV lower than 1 km/s. Practically none of the solutions for zero revolutions appear in the figure. Oppositely, there is a relative abundance of solutions in this region for $n_{rev} = 1,2$. Therefore, it is clear that using one or two revolutions yields the lowest ΔV values.

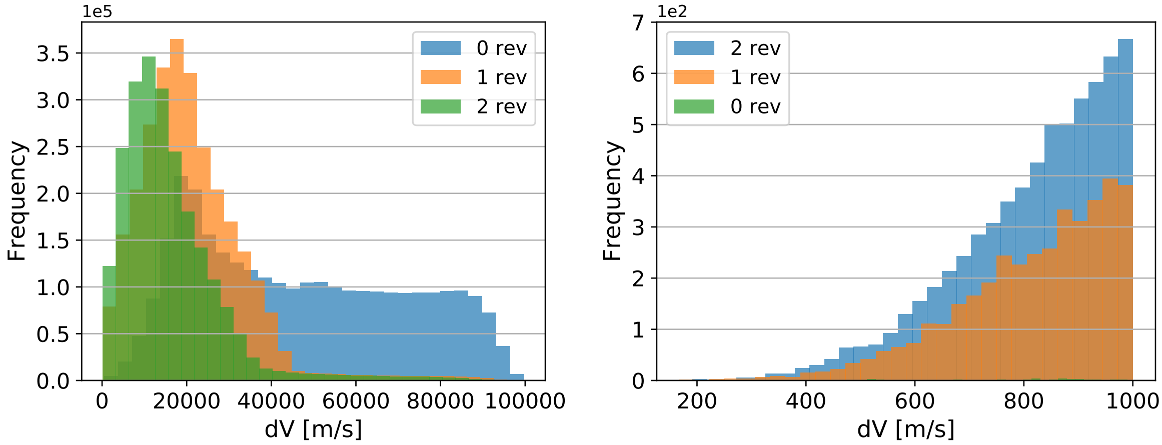

(a) General view

(b) Zoomed for $\Delta V < 1\ km/s$

Figure 6.9: Histogram of ΔV for different number of revolutions.

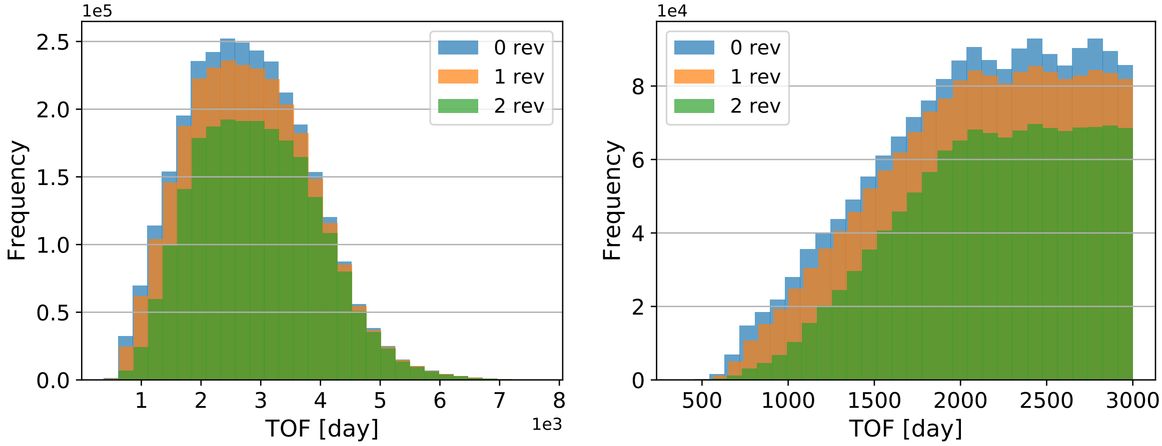

(a) General view

(b) Zoomed for $\Delta V < 1\ km/s$

Figure 6.10: Histogram of TOF for different number of revolutions.

A similar graph is displayed in Figure 6.10, but now for the TOF. On the right-hand side it can be seen that solutions that require two revolutions yield higher values of TOF, as expected. On the right-hand side, there is a zoomed section of TOF smaller than 3000 days. Solutions with smaller

TOF tend to use zero or one revolution. Moreover, the frequency difference between using 0 or 1 revolution is considerably smaller than for 1 or 2 revolutions.

We can conclude that the most promising option is to use one revolution. Nonetheless, also the case of two revolutions will be taken into account, for it could provide transfers at very low ΔVs and acceptable TOF.

Quasi-periodic family

As it happened with the asteroid, Lagrange point, and the number of revolutions, the quasi-periodic family is the only remaining variable that does not behave in a continuous fashion. If it could be further constrained, that is, to choose just one or some of them, it would be possible to reduce the design space considerably.

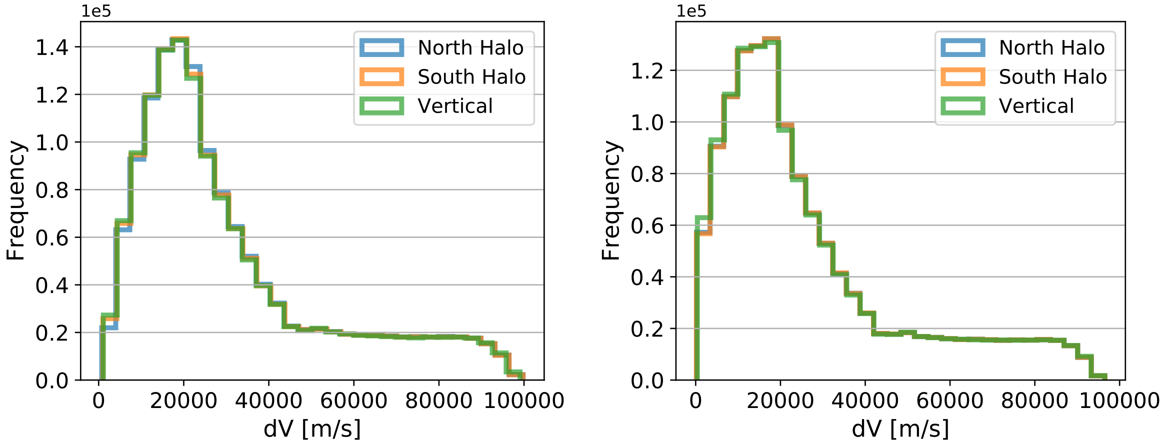

(a) ΔV L_1

(b) ΔV L_2

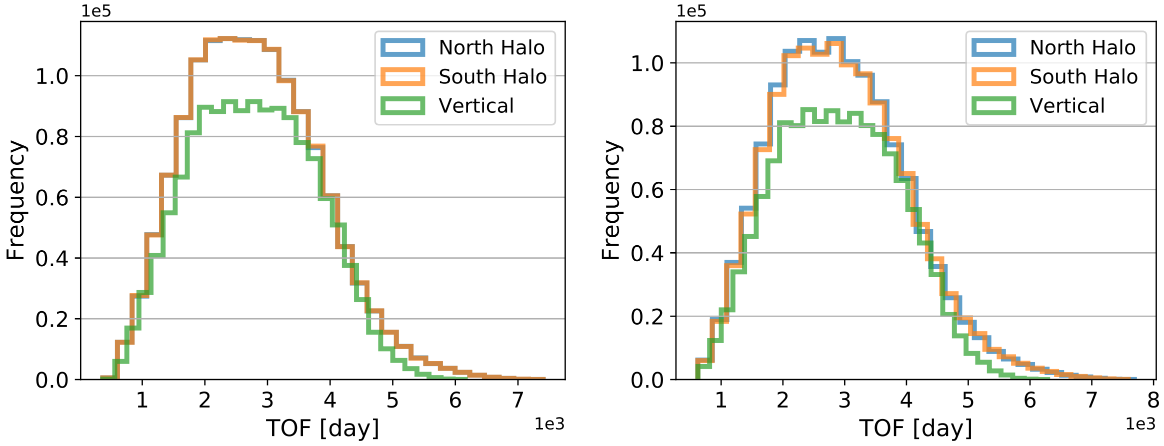

(c) TOF L_1

(d) TOF L_2

Figure 6.11: Histogram of ΔV and TOF for different quasi-periodic families about each libration point.

Figure 6.11 shows the ΔV and TOF histograms for the different quasi-periodic families. It seems that there is not a very large difference between the different families concerning ΔV in both L_1 and L_2. Figure 6.12 shows a zoomed section for families about L_1. On this scale, it is apparent that the north halo is the most promising family while the vertical Lyapunov is the least one, even though the differences are not very significant.

Regarding the TOF, vertical orbits seem to offer the best values, while both halo families perform a bit worse.

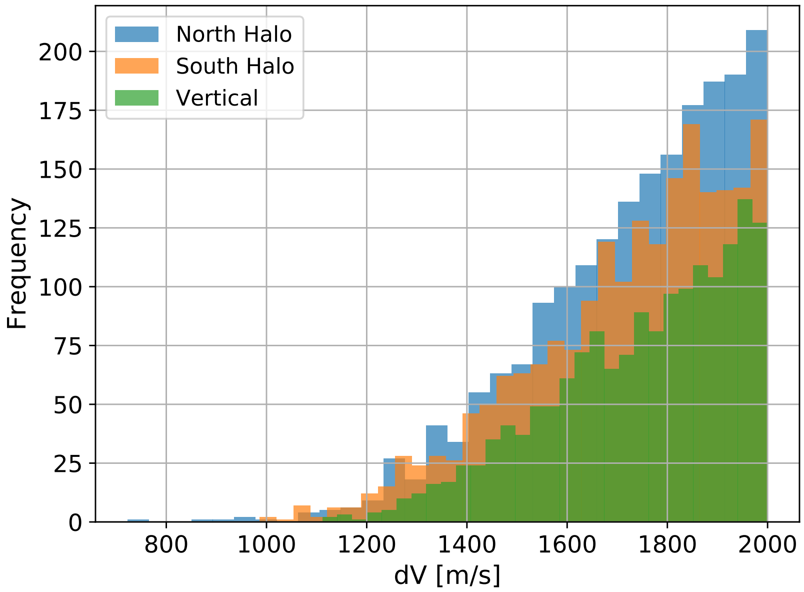

Figure 6.12: Zoomed $\Delta V < 2$ km/s histogram for different qp-families about L_1.

Jacobi energy

The Jacobi constant of the quasi-periodic torus is related to how far they are from its equilibrium point. More energetic orbits have a lower Jacobi constant. Figure 6.13a and b relates the Jacobi index of the tori with the ΔV of the solutions with $\Delta V < 1$ km/s for the halo and vertical families. The Jacobi index is the discretization of the Jacobi constant domain and allows us to compare tori from different families. It ranges from zero (i.e. close to the libration point) to the furthest quasi-periodic torus. It can be seen that for the halo families, a lower Jacobi constant seems to be related to lower ΔV. Since 2006 RH120 is above Earth's orbit, it is more energetic, hence it is logical that the most energetic orbits are the ones that offer the transfers with lower ΔV. On the other hand, the vertical family does not seem to exhibit this behavior, which could be linked to the required changes in inclination as will be discussed in Chapter 7. The TOF increases with decreasing Jacobi constant for both halos and vertical families. Figure 6.13c-d illustrates this behavior, which is potentially related to the existence of low ΔV transfers in these areas, which are also slower.

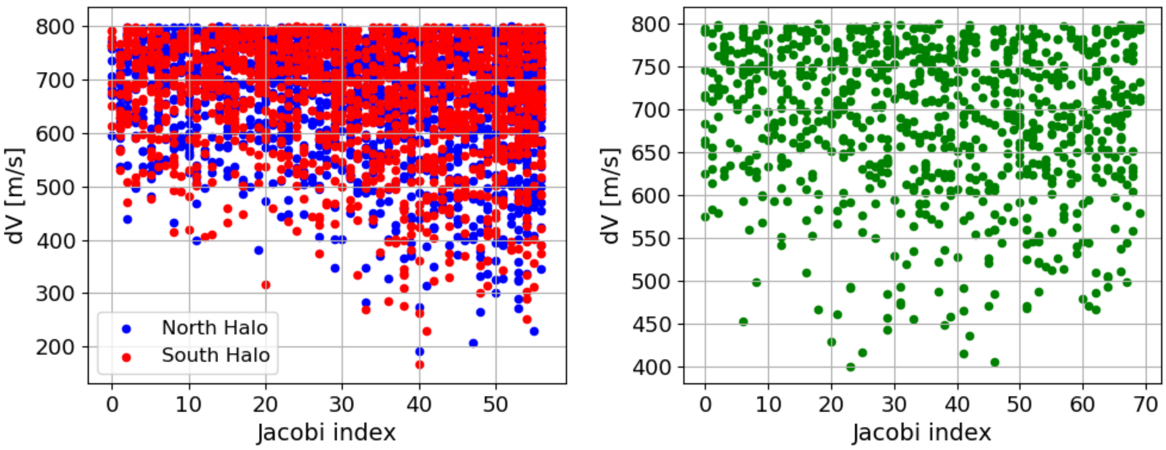

(a) ΔV and halo family

(b) ΔV and vertical family

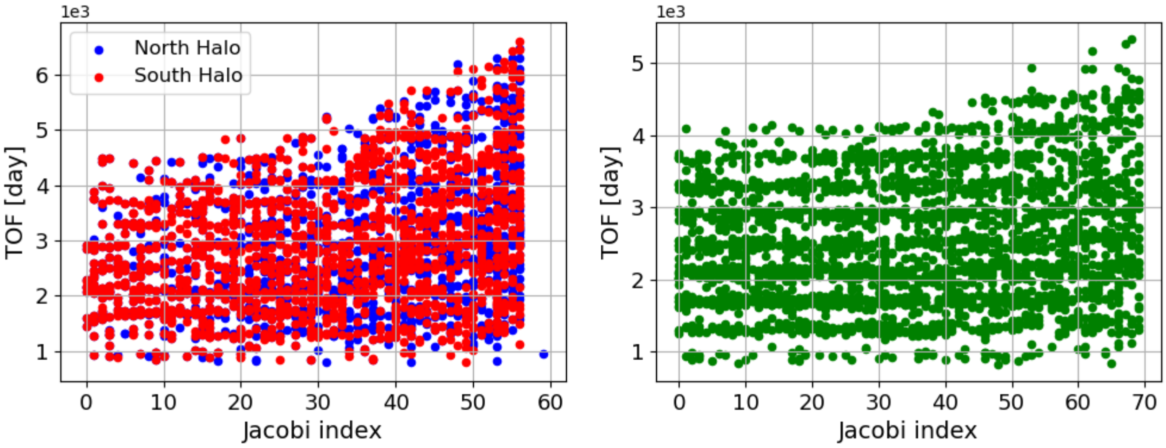

(c) TOF and halo family

(d) TOF and vertical family

Figure 6.13: ΔV and TOF with respect to Jacobi index. The Jacobi constant is discretized from the equilibrium point to the last value that admits quasi-periodic component.

Continuated family

As seen, the torus generated from a periodic orbit can be continuated until it collapses [88]. This direction is what we called here the continuated family, which could be characterized by the rotation angle for instance. The Monte Carlo analysis did not show any significant difference between the member of these families. Nonetheless, this is one of the dimensions we are more interested in. One of the goals of this work was to study if quasi-periodic orbits offer promising transfers, and this dimension is the one that differentiates quasi-periodic from periodic orbits. In Chapter 7 we will study the effect of this dimension in detail.

Manifold Angle

The effect of the angle where the insertion from the Lambert arc to the invariant manifold occurs is presented in Figure 6.14. By looking at the region close to zero angle in both figures it is apparent that there is a minimum θ_m value given by the angle of the initial state.

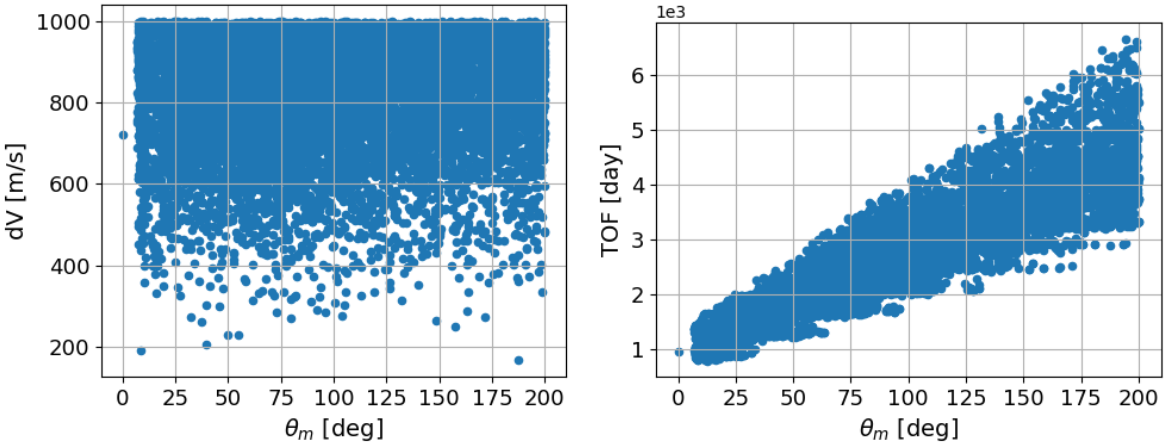

(a) ΔV

(b) TOF

Figure 6.14: Distribution of ΔV and TOF with respect to insertion manifold angle θ_m.

The left-hand figure shows the distribution of ΔV with respect to θ_m. There is no clear tendency; there are small ΔV values both at small and large angles, so no conclusion can be drawn for now. The right-hand figure shows that there is a linear relationship between θ_m and the TOF. This result is obvious because the manifolds are low-energy transfers, and hence, slow. The more time one spends on the manifold the longer the TOF will be.

Initial epoch

The initial epoch defines the moment when the asteroid is inserted into the Lambert orbit, and by definition begins on the 1st January 2022 which is the lower limit and reference value for this work. Figure 6.15a shows the beginning year for all transfers with a $\Delta V < 1$ km/s. It can be seen that there are two distinct regions that correspond to the best windows to begin the transfer during the synodic period of the asteroid. By simply looking at this graph we cannot choose the best one. However, by looking at Figure 6.15b, where the same points are plotted with respect to the TOF, it is clear that the left window offers much better transfers. For $t_{begin} \in (0, 7.5)$ it is possible to obtain transfers with low ΔV and TOF. Furthermore, it is possible to reduce the domain of this parameter to almost a third of its original value.

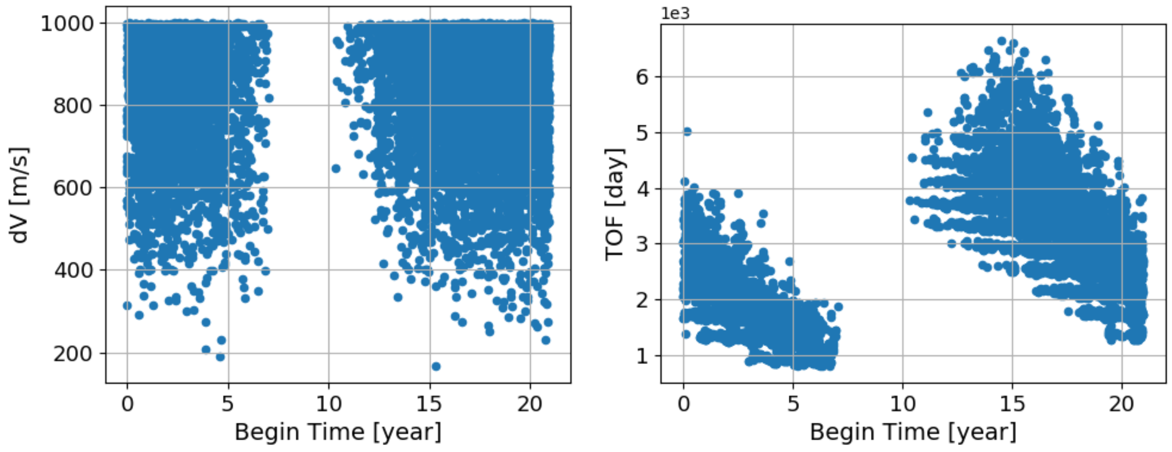

(a) ΔV

(b) TOF

Figure 6.15: Distribution of ΔV and TOF with respect to the transfer initial epoch.

Transfer Time

The domain of transfer time was originally constrained between 0 and 5 years. Similar to what has been done before we can plot the best transfers, with $\Delta V < 1$ km/s, to try to further constrain the domain.

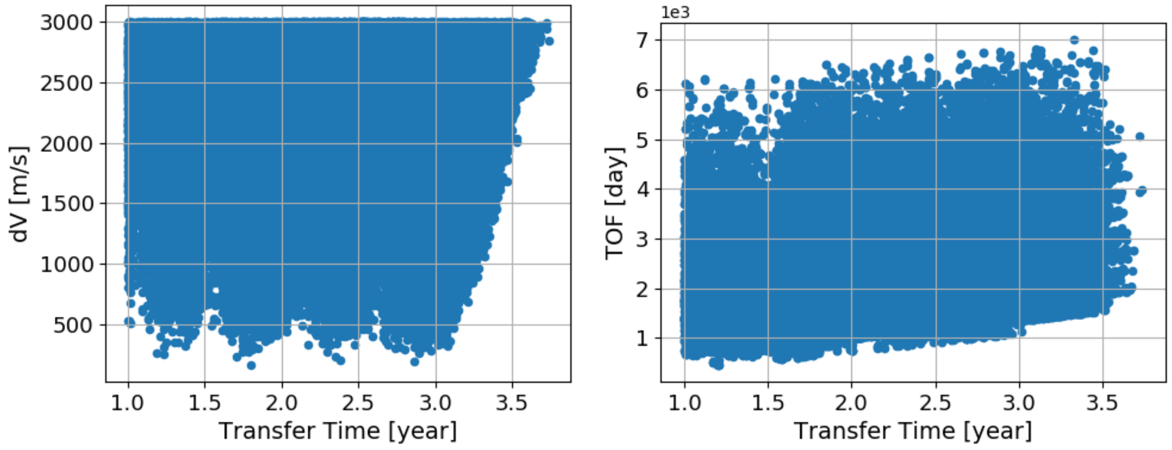

(a) ΔV

(b) TOF

Figure 6.16: Distribution of ΔV and TOF with respect to the transfer time.

Figure 6.16 shows the distribution of best transfers for both ΔV (left) and TOF (right) with respect to the years of transfer on the Lambert arc. Note that $TOF = t_{trans} + t_m$. It is unequivocal that the original domain was too large, and that a better approach is to use $t_{trans} \in [1, 3.2]$, reducing the domain of the variable by almost 40%.

Torus arriving position

As explained, the arrival position on the torus is parameterized by two angles θ_1 and θ_2, which define all points on its surface. The definition of these angles comes from the analytical approximation used to first compute the torus. We will try to clarify if there are some regions along θ_1 of θ_2 that yield better results in the Monte-Carlo analyses.

Figure 6.17 shows the distribution of transfers with $\Delta V < 600$ m/s (left) and TOF< 650 days. Figure 6.17a clearly displays that a relationship between the transfers with lower ΔV and its position on the torus exists. It seems that regions with $\theta_1 < 180°$ tend to be more favorable. The cause for this relationship will be further investigated in Chapter 7. On the other hand, no relationship seems to exist between the TOF and the arriving position on the torus, probably because this factor is greatly influenced only by the time spent on the manifold.

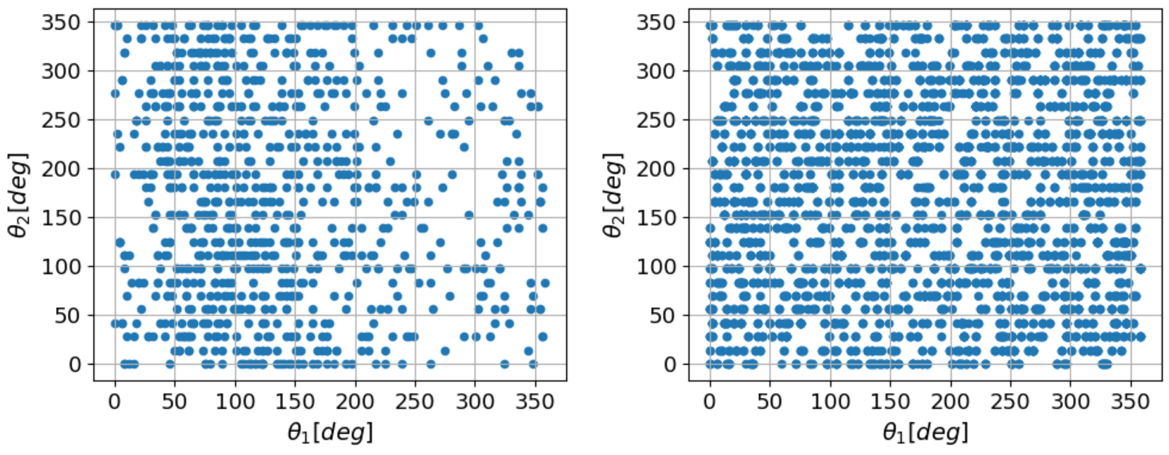

(a) ΔV

(b) TOF

Figure 6.17: Distribution of ΔV smaller than 600 m/s and TOF (< 650 days) with respect to the torus arriving position.

6.4.3. Redefined design space

Performing a Monte-Carlo study has allowed us to better understand the importance and influence of the parameters of the problem. It has also permitted us to get a sense of the order of magnitude of the solutions we can obtain. Figure 6.18 shows the best solutions that were obtained for one revolution. Since the problem deals with two objectives, a Pareto front representation is more useful. The points at this front are colored red. Only very few points reached some kind of optimality, considering the gigantic amount of simulations that were computed (7 million!). That seems to suggest that vast parts of the design space were not promising. Therefore, if we intend to converge the optimization scheme to an optimal solution, the design domain must be reduced first in order to focus only on the most promising regions.

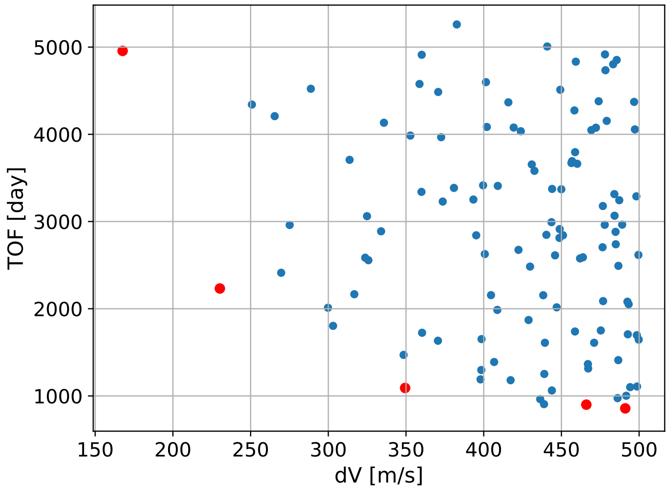

Figure 6.18: Estimated Pareto front from the Monte-Carlo analysis for 2006 RH120.

For all of the above, the original design space will now be constrained by:

- Only transfers that lead to tori about L_2 will be considered.
- Lambert orbits that perform only one or two revolutions will be used.
- The start epoch of the transfer is restricted to a maximum of 7.5 years.
- The maximum transfer time is further constrained between 1 and 3.1 years.

Moreover, we have seen that orbits with lower Jacobi constant (higher energy) are preferable, that quasi-periodic north halo families appear to be more promising and that $\theta_1 < 180°$ seems to offer the best results. Nevertheless, no constraints are applied to these parameters, in order to leave some flexibility. Also the differences between some of them were not strong enough to remove entire regions of the design space.

6.4.4. 2019 RP2 with Redefined domain

It was confirmed that many of the conclusions extracted from the Monte-Carlo analysis for 2006 RH120 also apply for 2019 RP2. Especially, those concerning the libration point and quasi-periodic family since both trajectories are beyond the Earth's orbit. However, some differences appear when defining the start point and transfer times. Figure 6.19 shows the ΔV distribution with respect to the initial epoch, on the left, and the transfer years, on the right.

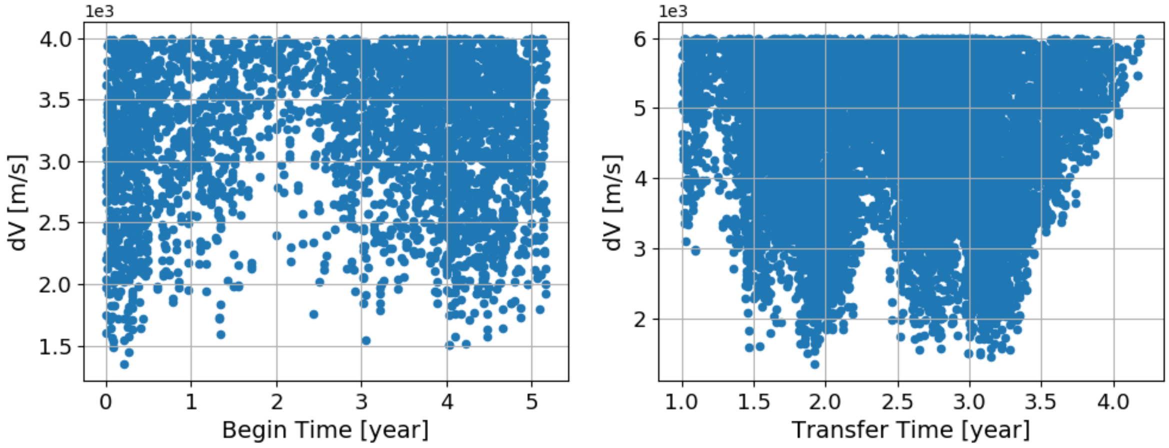

(a) (b)

Figure 6.19: Initial epoch and transfer year versus ΔV for 2019 RP2.

The year at which the transfer starts t_{begin} spans from 0, 1st of January 2022, to the synodic period of the asteroid. Contrary to the case of 2006 RH120, here all times seems to be able to provide minimum ΔVs of the same order. Furthermore, the synodic period of 2019 RP2 is 5.17 years, which is four times less than the synodic period of the other asteroids. Since the synodic period is relatively short and all regions seem to be equally promising, the initial epoch will not be restricted.

Figure 6.19b shows the most promising transfer times in regards to their ΔV. It can be seen that two regions seem to offer the best transfers, and that for $t_{trans} > 3.5$ years the transfer ΔV increases monotonically. For that reason, the transfer time will be restricted between 1 and 3.5 years.

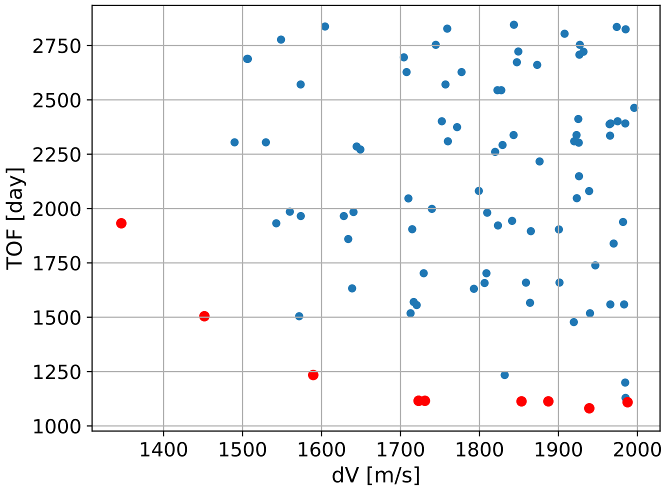

Figure 6.20: Estimated Pareto front from the best transfers in the Monte-Carlo analyses for 2019 RP2.

Figure 6.21 shows the best individuals that were obtained out of the Monte-Carlo analyses. Similar to what happened for 2006 RH120, Figure 6.21 contains only very few individuals considering the huge number of simulations performed during the Monte-Carlo analyses. This reinforces the fact that the domain must be further restricted before starting the optimization. It is remarkable that even the minimum ΔV values are large compared to the results obtained for 2006 RH120. The physical reason behind this fact will be addressed in Chapter 7.

6.4.5. 2020 CD3 with Redefined domain

Since the orbit of 2020 CD3 is also beyond the Earth's orbit, most of the main discussions are shared, as it happened with 2019 RP2 as well. The only different constraint concerns the begin time and transfer time. After analyzing the distribution using similar plots as in Figure 6.19, the beginning time was restricted between 10 and 24.29 years and the transfer time between 1 and 3.5 years.

Figure 6.21 displays the best individuals obtained from the random search. In red, there is the points that would belong to a possible Pareto front that yielded promising results. Note that the order of magnitude is similar to the ones obtained for 2006 RH120, which indicates that both asteroids have similar orbital parameters.

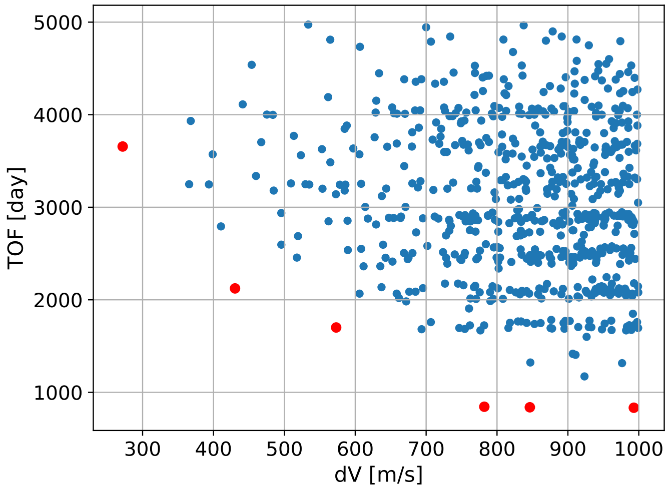

Figure 6.21: Estimated Pareto front from the best transfers in the Monte-Carlo analyses for 2020 CD3.

Table 6.5 shows the overview of the constraints that will be applied to the different parameters during the optimization process. NR stands for not restricted, which means that the original domain of the variable is kept unaltered. As explained, all asteroids share some common orbital properties, and therefore they also share the same kind of constraints on some parameters.

Table 6.5: Parameter constraints for each NEA asteroid. NR stands for Not-Restricted.

Asteroid	t_{begin}	t_{trans}	L_i	F_t	C_t	ρ_t	θ_1	θ_2	θ_m	n_{rev}
2006 RH120	$[0, 7.5]$	$[1, 3.2]$	L_2	NR	NR	NR	NR	NR	NR	1,2
2019 RP2	NR	$[1, 3.5]$								
2020 CD3	$[10, 24.29]$									

6.5. Multi-objective optimization tuning

A multi-objective optimization (MOO), also known as vector optimization or Pareto optimization, consists in optimizing simultaneously a collection of objective functions. It is a very common kind of problem in science and engineering that involves a trade-off between two or more objectives [27]. In our case, the two objectives that have to be optimized are ΔV and TOF, as already mentioned. Mathematically, these problems can be formalized as [86]:

$$\begin{gathered} \text{Minimize } \mathbf{F}(\mathbf{x}) = [F_1(\mathbf{x}), ..., F_k(\mathbf{x})]^T \\ \text{subject to } g_j(\mathbf{x}) \leq 0, j = 1, 2, ...m \quad h_l(\mathbf{x}) = 0, l = 1, 2, ..., e \end{gathered} \tag{6.5}$$

with k objective functions, m inequality conditions, e equality constraints, and $\mathbf{x}$ are the so-called design variables or decision variables.

In multi-objective problems, normally, there is no single global optimum; instead, there is a set of points that behave as an optimum. In this context, we talk about Pareto optimality, which is defined as [86]

Definition 2 *A point,* $\mathbf{x}^* \in \mathbf{X}$*, is Pareto optimal if there is no other point* $\mathbf{x} \in \mathbf{X}$*, such that* $\mathbf{F}(\mathbf{x}) \leq \mathbf{F}(\mathbf{x}^*)$*, and* $F_i(\mathbf{x}) < F_i(\mathbf{x}^*)$ *for at least one function.*

The goal of the optimization is then to find as many points as possible to constitute the Pareto optimal set. In other words, we seek the set of points where no individual can be better without making at least one criterion worse.

In this study, the library PaGMO (Parallel Global Multiobjective Optimizer) will be used. PaGMO was developed by Izzo and Biscani [15] under the FLOSS philosophy and is used by the Advanced Concepts Team of ESA. It offers a generalization of the island model [69], and in its latest version (2.17.0) offers the following multi-objective algorithms: Improved Harmony Search, Non-dominated

Sorting GA (NSGA2), Multi-objective EA with Decomposition (MOEA/D), Multi-objective Hypervolume-based ACO (MHACO), and Non-dominated Sorting PSO (NSPSO).

Based on the work of fellow TU Delft students such as Moreno Gonzalez [92] and Van der Heyden [119], the MOEA/D-DE algorithm was chosen. The MOEA/D-DE algorithm is based on the idea of problem decomposition. The problem is decomposed into individual sub-problems which are optimized separately, but simultaneously. Good solutions from neighboring problems are combined, which allows for a good convergence.
As indicated by Van der Heyden [119], MOEA/D-DE has proved in several studies to perform significantly better than other popular schemes such as NSGA2.

6.5.1. Algorithm tuning

Global optimization schemes usually depend on several parameters, which have to be tuned in order to optimize the algorithm performance. In this section, the MOEA/D-DE will be tuned so that it offers the best results for our particular problem. Table 6.6 contains the main parameters that control the algorithm. In this work, we will only focus on the population size, weight generation, decomposition method, neighbor size, and CR. The tuning was done optimizing north-halo quasi-periodic orbits about L_1 for 20 generations with three different seeds.

Table 6.6: Main parameters in the MOEA/D-DE algorithm.

Parameter	**Options**	**Description**
Population size	-	Number of individual solutions in a population
Weight Generation	Grid, Low Discrepancy, Random	Method used to generate the weights
Decomposition method	Weighted, Tchebycheff, Bi	Method used to decompose the objectives
Neighbor size (T)	-	Size of the neighborhood considered to generate a new solution
Cross-over rate (CR)	(0,1)	Crossover parameter of the Differential Evolution operator
Scale factor (F)	-	F parameter for the Differential evolution operator
Conservation chance	(0-1)	The chance that a neighborhood is considered at each generation, rather than the whole population

Population size

The population used during the optimization is kept constant for the entire optimization. The more members in the population, the more time it will take to evaluate and evolve each generation. On the other hand, the more individuals, the more ’genetic’ variability will exist in the population and the Pareto front will be better defined.

Once again, a trade-off between efficiency and accuracy or ’completeness’ has to be done. Figure 6.22a shows the minimum ΔV during 20 generations for populations from 100 to 1000 individuals. A value of 500 individuals will offer a good convergence while keeping the population relatively small. Figure 6.22b shows the analogous but for the total TOF. From now on, a population of 500 individuals is used for the rest of the simulations.

Decomposition Method

This parameter determines how the multiple objectives of the multi-objective problem are separated and ranked. By default, this is set to Tchebycheff. Figure 6.22c and Figure 6.22d contain the performance of the different options for ΔV and TOF. As can be seen, using a weighted decomposition approach seems to yield the best results.

Weight generation

This describes the method used to generate weights. According to Van der Heyden [119], the default value ’grid’ should be the best option, which agrees with our analysis. Figure 6.22e and Figure 6.22f show that using a grid weight generation method is indeed the best one.

Neighbors

The neighbor parameter controls the size of sub-solutions used for optimizing the algorithm. This is because two solutions can only be combined when they are neighbors in this algorithm, this rule is called mating restriction. The default value was 20, and according to the parametric study performed Figure 6.23a and Figure 6.23b, this is a good value.

Cross-over rate

This value is limited between 0 and 1 and indicates the probability to stop the inclusion of new variables into the mutant vector. Note that it does not mean that the population will be the same if $CR = 1$. That means that if $CR = 1$, the new individuals will all come from the combination of others in the population. F is the other parameter that controls the DE algorithm. It represents the weight by which the difference between two or more solutions is multiplied.

By default, CR is 1, which means that there is no external mutation. Nonetheless, Figure 6.23c and Figure 6.23d seem to suggest that adding small amount of randomness, such as values of 0.8 would offer better results.

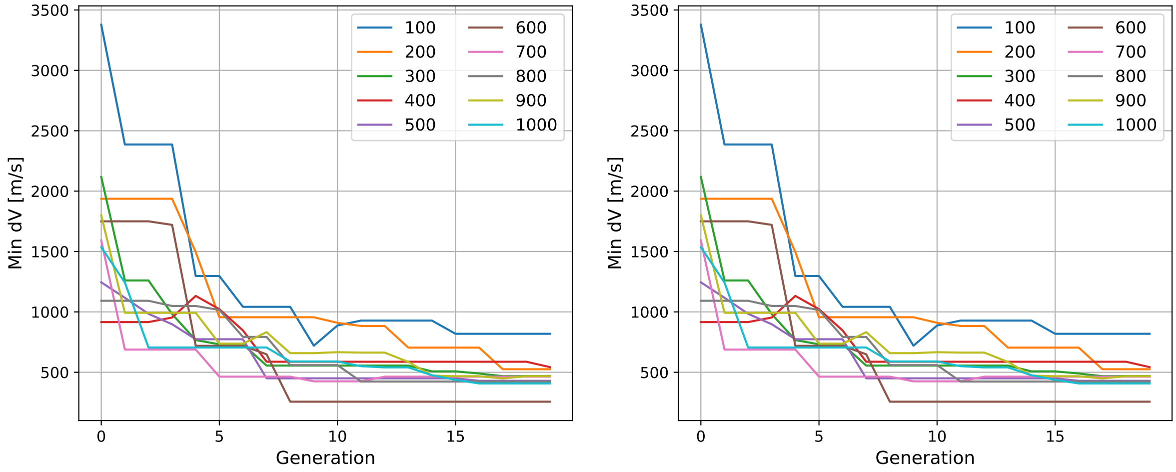

(a) Population versus min ΔV.

(b) Population versus min TOF.

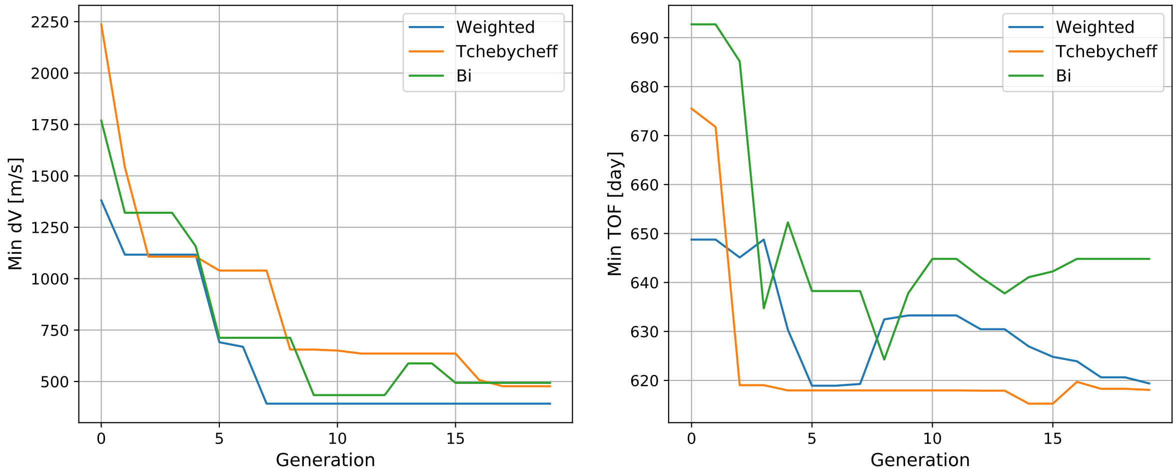

(c) Decomposition versus min ΔV.

(d) Decomposition versus min TOF.

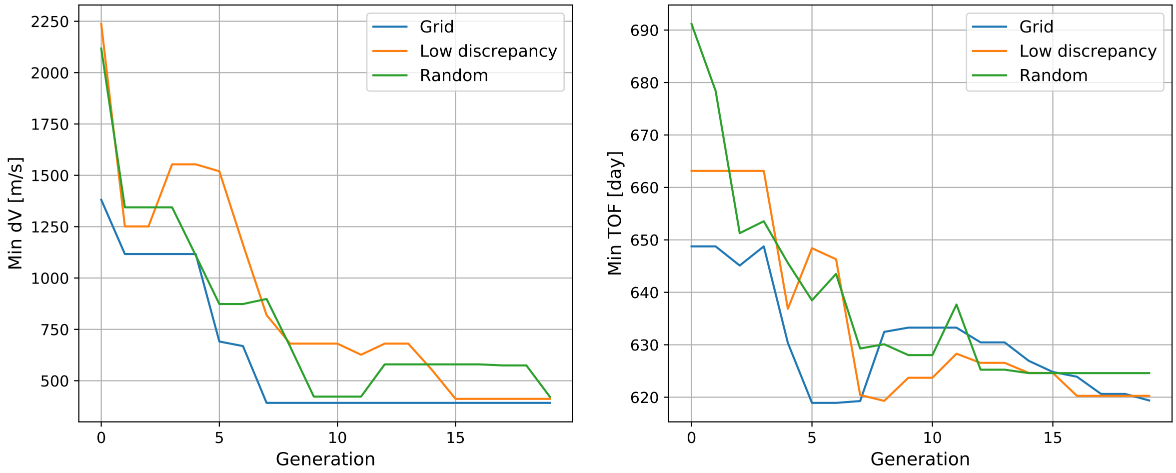

(e) Weight versus min ΔV.

(f) Weight versus min TOF.

Figure 6.22: Optimizer parametric study. Using north-halo quasi periodic family about L_1 and zero revolutions.

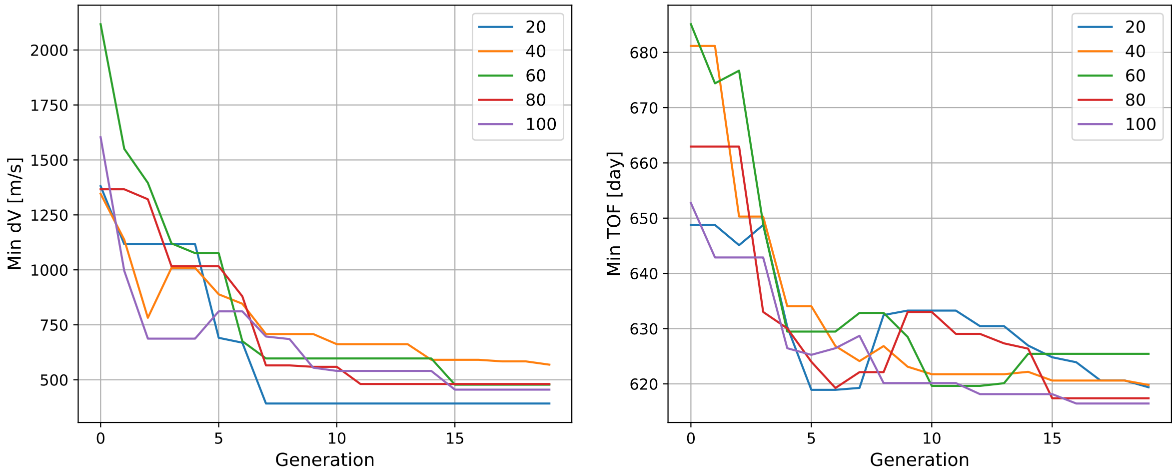

(a) Neighbors versus min ΔV.

(b) Neighbors versus min TOF.

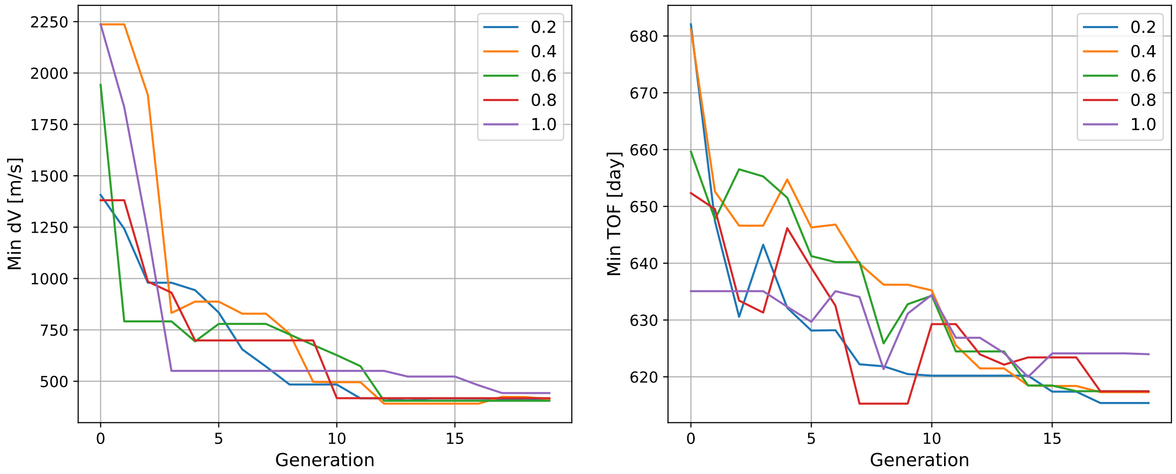

(c) CR versus min ΔV.

(d) CR versus min TOF.

Figure 6.23: Optimizer parametric study. Using north-halo quasi periodic family about L_1 and zero revolutions.

7

Results and Discussion

In his section, we will address the results obtained from the optimization. The complete optimization was run three times with different seeds to ensure the generality of the results. For each of the asteroids, the best results will be presented, and porkchop-like graphs are offered, which could be used for mission design. If the asteroid displayed undesirable results we will explain the reason why. For the sake of simplicity and brevity, the analysis will be developed more in-depth for 2006 RH120, and then, particularities and remarks of the solution for the other two asteroids will be commented on. For 2006 RH120 the effect of each of the parameters that make up the problem will be discussed individually.

7.1. 2006 RH120

This asteroid was the first known NEA to have been temporarily captured by the Earth, and for that, it has not only attracted the attention of many scientists as explained in Section 5.4, but also other researchers interested in the design of low-energy transfers to NEA as it will be explained in Subsection 7.1.8.

Table 7.1 contains the two more promising transfers for each quasi-periodic family and number of revolutions, these results are also presented as a Pareto front plot in Figure 7.1. The solutions were obtained by merging the results of three runs with different seeds. By looking at Table 7.1 (ordered by ΔV), it is clear that the northern halo family yields the best results. The most optimal transfer for 2006 RH120 was found to lead to a north halo torus, uses two revolutions, comes with a cost of 21.99 m/s and has a total TOF of around 4 years. This value is very low, not only compared to other's work but also other (sub)optimal solutions obtained in this work. The south-halo and vertical families also yielded solutions at low ΔV compared to other works, see Subsection 7.1.8.

Table 7.1: Best individuals for each family and number of revolutions for 2006 RH120.

Family	**Rev**	**Jac Idx**	**Cont Idx**	θ_1 **[deg]**	θ_2 **[deg]**	t_{begin} **[year]**	t_{trans} **[year]**	θ_m **[deg]**	ΔV **[m/s]**	**TOF [year]**
North Halo	2	41	29	96.56	55.38	3.42	2.86	12.32	22.00	3.95
North Halo	1	43	28	122.76	173.08	5.69	1.87	7.37	36.67	2.75
North Halo	2	50	29	155.44	124.62	4.99	2.41	8.09	42.53	3.46
North Halo	1	37	25	105.23	173.08	5.16	1.19	13.55	54.88	2.27
Vertical	2	46	29	108.56	145.38	3.04	2.54	11.07	94.05	3.48
South Halo	2	56	29	216.56	13.84	4.76	2.79	11.12	105.03	4.20
Vertical	2	44	29	110.77	0.0	3.07	2.50	12.37	106.44	3.46
South Halo	1	57	28	261.23	69.23	5.90	1.68	10.78	115.04	3.14
Vertical	1	44	28	102.0	0.0	2.98	1.66	29.40	136.40	3.52
South Halo	1	46	29	96.0	145.38	5.35	1.43	8.59	140.97	2.48
South Halo	2	40	29	117.23	110.77	2.20	2.86	25.72	170.12	4.80
Vertical	1	52	29	134.77	0.0	5.23	1.45	9.08	174.95	2.37

Figure 7.1 shows the Pareto fronts for the halo and vertical families, and one and two revolutions. The Pareto fronts of the halo families look rather complete and offer a wide range of possible transfers from low ΔV and relative high TOF to very small TOF with higher ΔVs. On the other hand, the vertical families do not seem to offer such a wide range. The Pareto front from of the vertical family with one revolution is not included in Figure 7.1.

The Pareto fronts confirm that the north halo family is the most preferable one. Whether to choose one or two revolutions would depend on the specific mission requirements. In general, the south-halo quasi-periodic tori show no advantage concerning the ΔV or TOF.

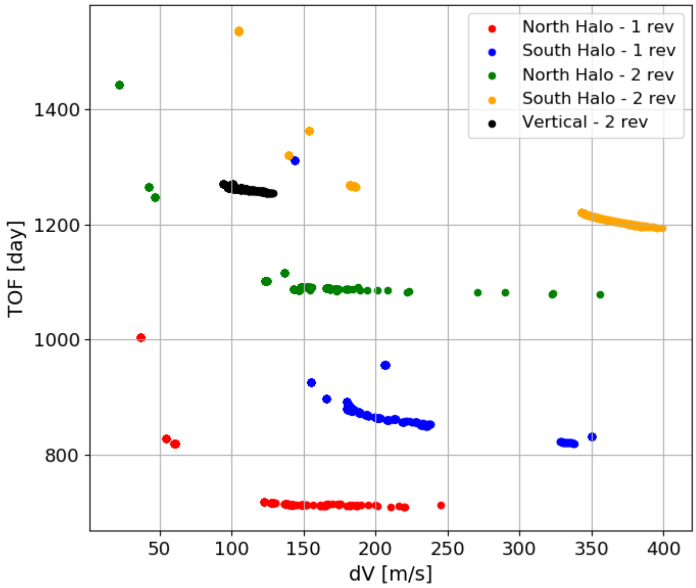

Figure 7.1: Pareto front for quasi-periodic halo families and a vertical family for one and two revolutions, for 2006 RH120.

7.1.1. Effect of Jacobi constant

The Monte Carlo analysis, see Section 6.4, suggested that using lower Jacobi constant values was preferable. To understand the effect of C on the transfers, the individual with the lowest ΔV has been saved and plotted for each family of tori with the same Jacobi index. In order to be able to compare the different families the x-axis does not show directly the Jacobi value, but a partition of the range where the invariant tori exists, as defined in Section 4.7.

The quasi-periodic orbits with a low Jacobi constant are those ones further from the equilibrium points, a larger Jacobi index, and these orbits are associated with higher energy. Moreover, all these asteroids that were obtained from the pruning are located beyond the Earth's orbit, which means that they are in more energetic orbits than the Earth, see Figure 5.8. For that reason, it was expected that the manifolds with higher energy (lower Jacobi constant) would provide the best transfers.

However, Figure 7.2 shows that the best transfers are not obtained with the highest Jacobi index, further from the equilibrium point, as could have been expected. The explanation for this phenomenon can be related to the relative inclination of manifold and asteroid. Figure 5.8 shows the maximum inclination of the asteroid with respect to the maximum inclination of the manifold for different values of the Jacobi constant. The maximum inclination of 2006 RH120 seems to match the inclination of the halo manifolds with low Jacobi constant values, but not the lowest. As is well known, inclination changes are a very expensive transfer in orbital mechanics. Hence, even though the 'highest' parts of Figure 5.8 could have yielded better transfers because their orbits have a closer Jacobi constant, the change in inclination increases the total ΔV. Therefore, the algorithm chooses a Jacobi constant/index region that minimizes the change in inclination.

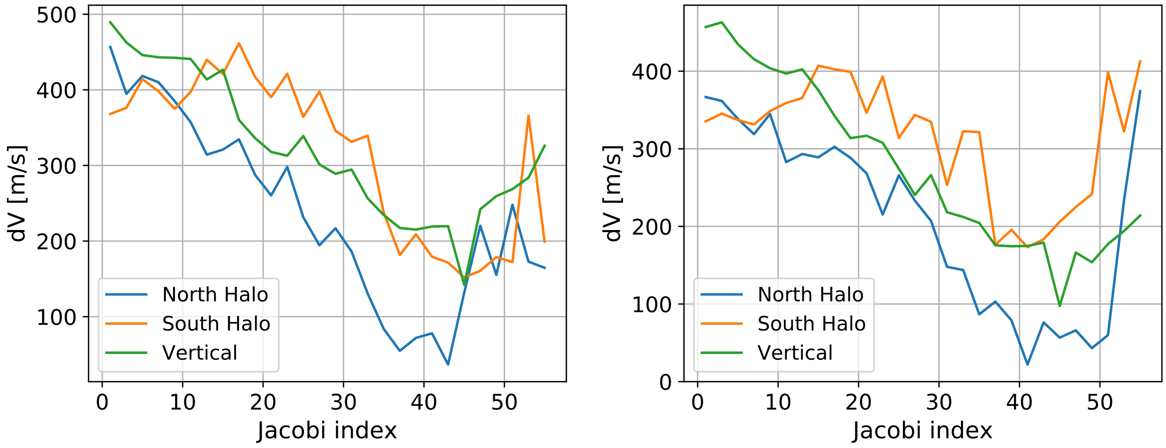

(a) One revolution

(b) Two revolutions

Figure 7.2: Transfer with lowest ΔV with respect to the Jacobi index for different families, and number of revolutions, for 2006 RH120.

2006 RH120 maximum inclination is slightly over the middle of the inclination range of the vertical family. Note that in Figure 7.2 the Jacobi index for the vertical family would extend further to the right, but it is not plotted to better compare both families.

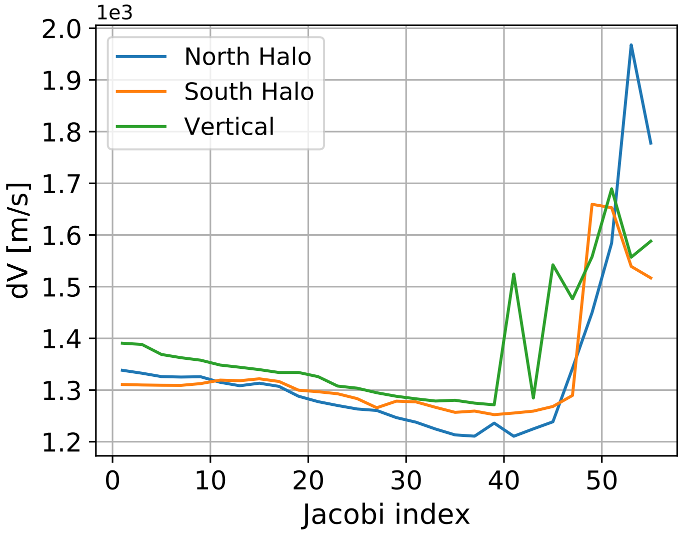

Figure 7.3: Minimum ΔV for different Jacobi constant tori for asteroid 2019 RP2 (one revolution).

Figure 7.3 shows the distribution of the minimum ΔV versus the Jacobi index for 2019 RP2 using one revolution. This asteroid is located in the middle of the Jacobi range, but at a larger inclination. There is not a remarkable peak like in the other case because in all of the tori, large inclination changes would be required in general.

7.1.2. Effect of the tori member

One of the main goals of this work was to prove if the use of the manifolds of quasi-periodic orbits for transporting NEA to the Earth's vicinity was more advantageous than using the manifolds from periodic orbits, or using a direct transfer. In this section, we will address whether that is true or not.

All individuals that existed in all generations used during the optimization, with a ΔV lower than a specific threshold, will be plotted against their continuation index. The continuation index reflects how far a particular quasi-periodic orbit is located away from the periodic orbit that was used to initialize it. An index equal to zero is a torus very close to the periodic orbit, and the 29th torus is the last one after which the tori calculations do not converge, they collapse [88]. Figure 7.6f shows this distribution of the different families of quasi-periodic orbits for one and two revolutions. By looking at the figures, it is clear that tori further from the periodic orbit always offer the lowest ΔV. This relationship becomes even more apparent in the vertical families.

Table 7.2: Comparison of two individuals with different continuation index from the vertical quasi-periodic family and two-revolutions case.

Jac Idx	Cont Idx	θ_1 [deg]	θ_2 [deg]	t_{begin} [year]	t_{trans} [year]	θ_m [deg]	dV [m/s]	TOF [day]
47	7	93.23	72	2.989	2.500	14.82	190.43	1278
45	29	117.23	345.6	3.074	2.557	10.51	97.46	1267

Table 7.2 compares two converged individuals with different continuation index. As can be seen, the difference between their parameters is very small, except for θ_2, which has a negligible effect as will be seen afterward, and the continuation index. Yet, the ΔV of the individual with a higher continuation index is less than half of the other one. Therefore, this seems to suggest that the individuals with the best values of ΔV share most of the parameters and that the distance to the original periodic orbit (i.e. continuation index) is key to reduce the ΔV considerably without the need to modify the time of flight.

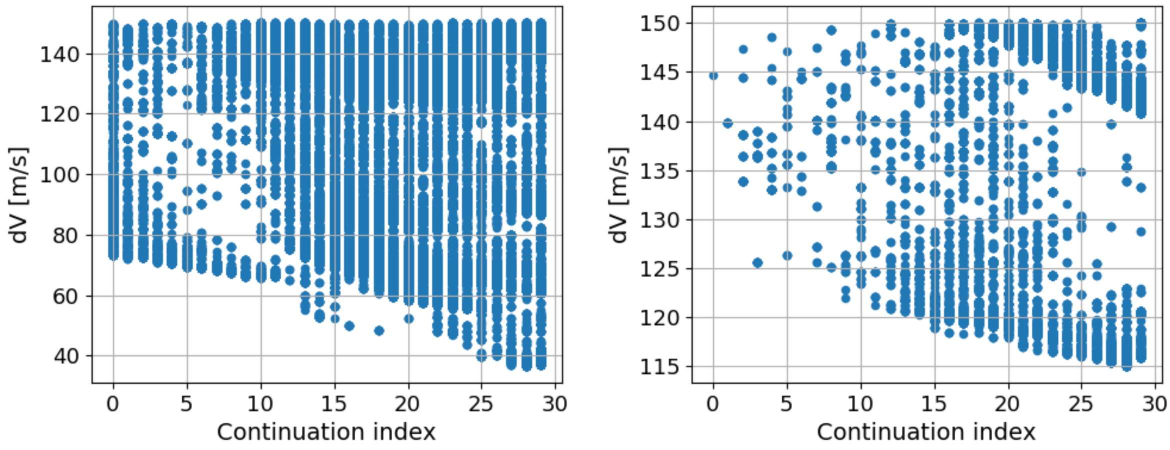

(a) North halo - 1 rev

(b) South halo - 1 rev

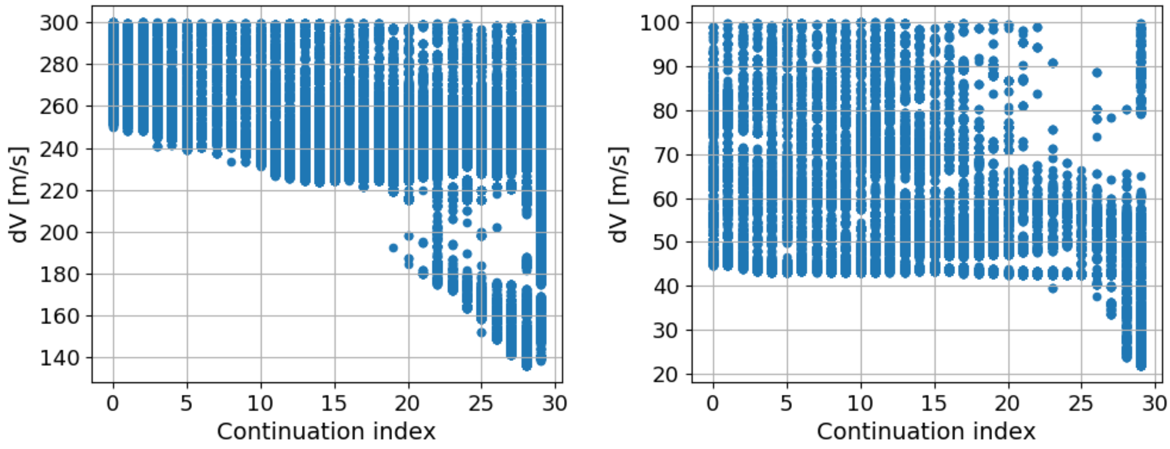

(c) Vertical - 1 rev

(d) North halo - 2 rev

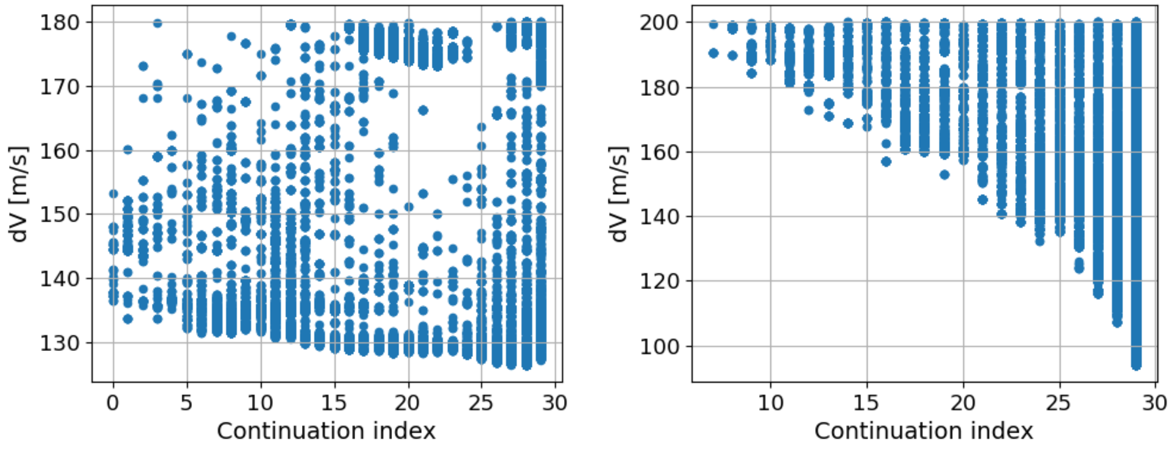

(e) South halo - 2 rev

(f) Vertical - 2 rev

Figure 7.4: ΔV distribution with respect to the continuation index for the different kinds of families, one and two revolutions.

Analyzing in-depth the results of 2006 RH120 is especially interesting because in 2016 Sánchez et al. [105] studied the possibility of retrieving asteroids by using the invariant manifolds of periodic orbits, and one of their candidates was 2006 RH120. The best result that they were able to obtain was a minimum ΔV of 58 m/s, and as can be seen in Figure 7.6d, quasi-periodic tori are able to provide many options with much better transfers. For more on this discussion, see Subsection 7.1.8.

Figure 7.5a shows all individuals of the north halo family with two revolutions with a ΔV smaller than 0.5 km/s, and their relationship with the Jacobi index and continuation index. These figures permit us to clearly identify both the region of interest of the Jacobi constant and the improvement along with the continuated family. Figure 7.5b shows the analogous, but with respect to the TOF, where the tendency is very clear. The lower the Jacobi index the lower the TOF, and no clear tendency can be seen along the continuation axis.

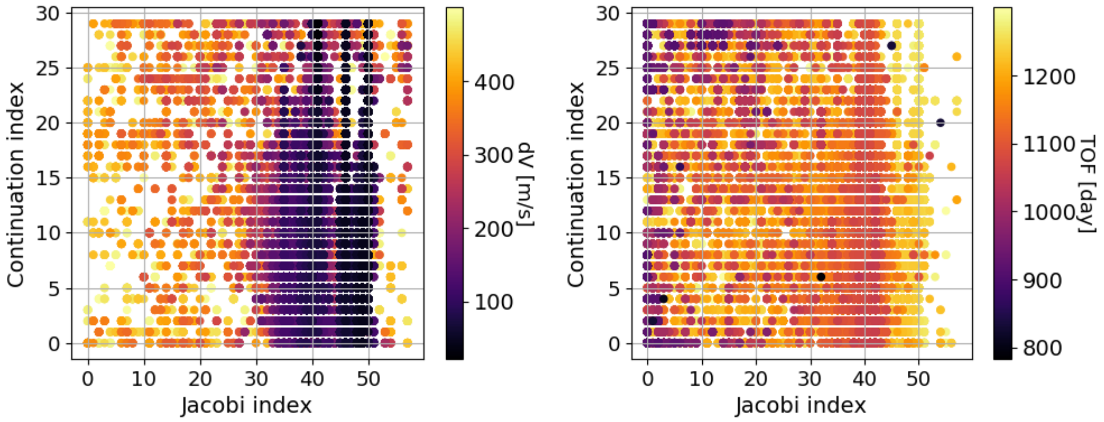

(a) $dV[m/s]$

(b) TOF [day]

Figure 7.5: Jacobi index versus continuation index versus ΔV and TOF for north-halo family and two revolutions.

7.1.3. Effect of initial epoch

Another question that this work aims to solve is whether using quasi-periodic orbits would allow for more frequent transfers at lower ΔVs. In this section, we will address this subject. For that, we will plot for each quasi-periodic family and number of revolutions the relationship between the continuation index and the initial epoch for individuals with a ΔV lower than a threshold. If there are individuals with an initial date that appears for only higher values of the continuation index, that means that using quasi-periodic orbits permits for more variety of transfer windows there. It can be seen in Figure 7.6 that for a given ΔV, the use of quasi-periodic orbits would allow for a transfer to happen at more and different times than when using periodic manifolds only (0 continuation index).

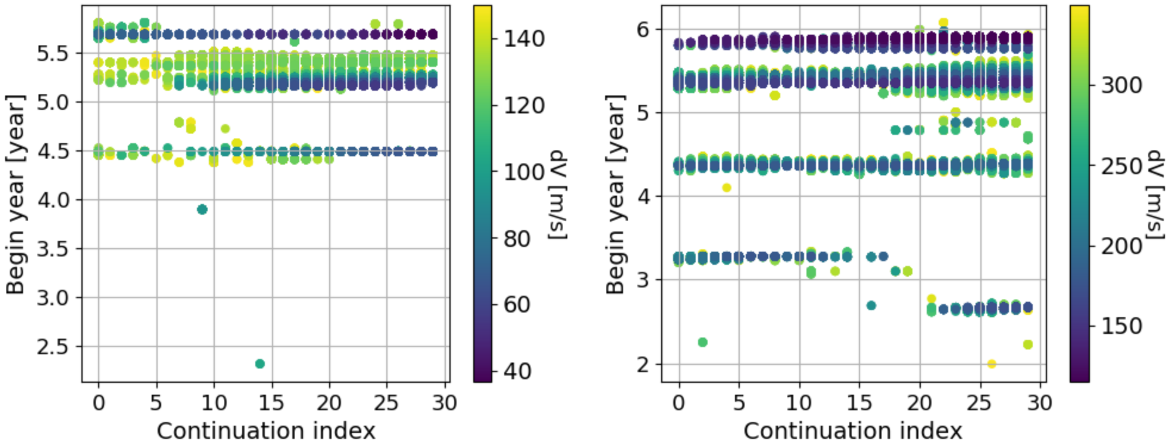

(a) North halo - 1 rev

(b) South halo - 1 rev

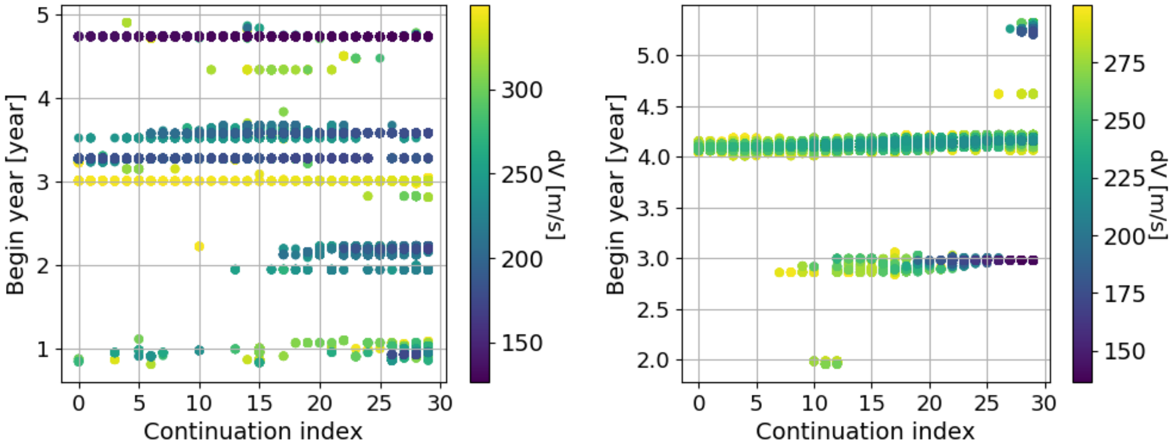

(c) Vertical - 1 rev

(d) North halo - 2 rev

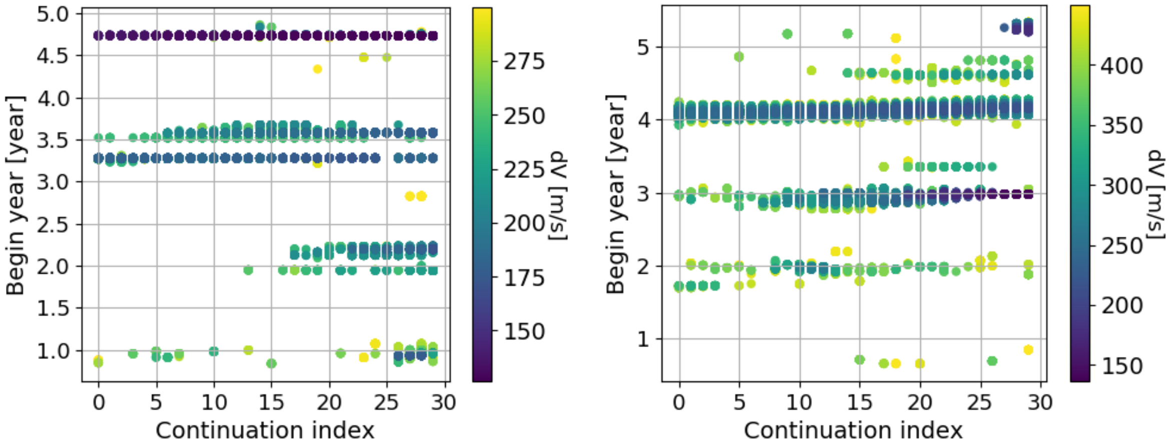

(e) South halo - 2 rev

(f) Vertical - 2 rev

Figure 7.6: Continuation index versus beginning time for individuals with ΔV lower than a given threshold.

In all the graphs, we can identify the following elements. There is a transfer window that spans all continuation indices, this tends to be also the transfers associated with the lowest ΔV. However, this is not the case for the north halo and south halo families with two revolutions where the window with the lowest ΔV does evolve smoothly along with the continuation index, and thus, it surpasses the threshold.

Note that these graphs are made from all the individuals in all generations for three different seeds, and therefore, some windows could be unexplored and not appear in these graphs. In order to obtain the complete picture, one should run the optimization algorithm by fixing the continuation index and initial epoch. However, due to the large number of individuals and runs used, the results are considered reliable.

7.1.4. Effect of transfer time

When analyzing the relationships between the most promising transfers and the time of the Lambert transfer t_m, one finds that in all cases two different regions appear. To illustrate this, Figure 7.7 shows on the left, the transfer time for the north-halo family and one revolution, and on the right, the vertical family and two revolutions. It can be seen that even though the transfer times are different, the difference between the regions is in both, and actually, all cases around five months.

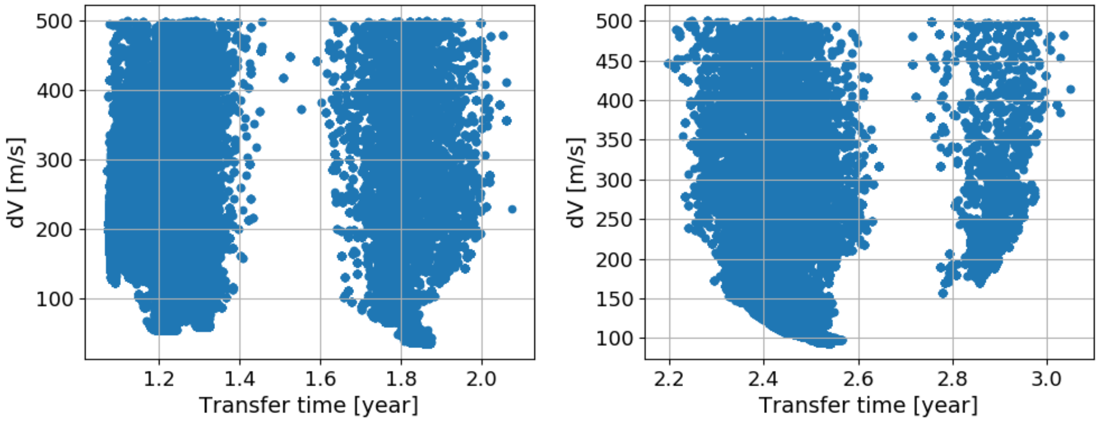

(a) North halo family - 1 rev.

(b) Vertical family - 2 revs.

Figure 7.7: Transfer time versus required ΔV for two different configurations.

By analyzing two individuals from each family and region, it can be seen that the two different transfer times that offer good results appear when the value of t_{begin} is modified, then in order to obtain relatively cheap transfers, the optimizer modifies the value of θ_m accordingly. This compromise between $t_{begin} - t_{trans} - \theta_m$ seems to be the cause of the two transfer regions that appear in Figure 7.7.

7.1.5. Effect of manifold angle

The manifold angle θ_m defines the moment when the insertion from the Lambert arc to the manifold is performed. In other words, it defines the point at which the low-energy transfer begins. When studying the data, it was found that a linear relationship between the initial epoch and θ_m exists when considering all individuals with a ΔV below a threshold.

Figure 7.8 shows an illustrative example from the vertical family with one revolution. The physical explanation behind this phenomenon is the following: the manifolds of the quasi-periodic tori permit that even when, due to phasing reasons, targeting the Earth's vicinity is very energetically expensive, it is possible to target always the manifolds. In that sense, using manifolds to design interplanetary transfers removes the phasing limitations in the classical sense. Since the optimizer tries to optimize both ΔV and TOF, it tries to find solutions that minimize low-energy transfers, because they are slow. However, when the initial epoch changes, and hence the phasing conditions, the optimizer has to sacrifice TOF in order to obtain transfers with low ΔV by pointing to an area further away from Earth's vicinity.

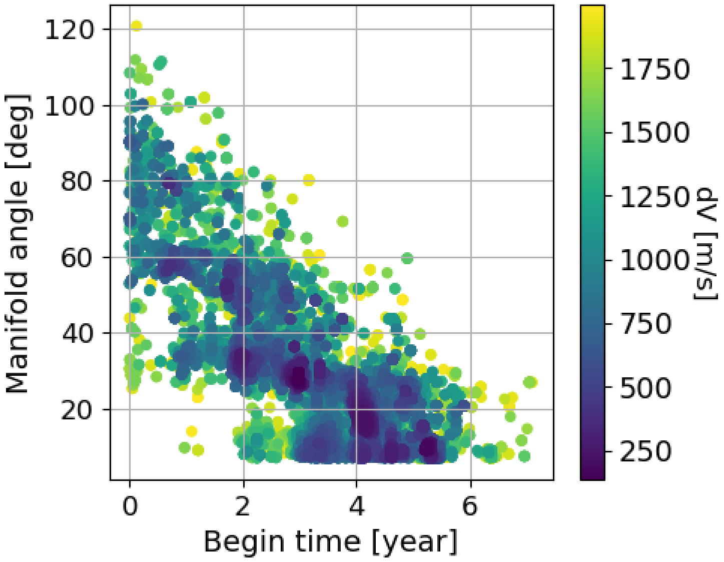

Figure 7.8: Initial epoch versus angle of insertion into the manifold and ΔV. Vertical family.

Why the optimizer tries to minimize the time on the manifold is obvious by looking at Figure 7.9. The figure on the left shows the relationship between the initial epoch and the TOF. It can be seen that its shape matches Figure 7.8 very much, which seems to indicate that θ_m is the main contributor to the total TOF. By looking at Figure 7.9b, which directly relates θ_m and TOF, it can be seen that the relationship is almost linear. Therefore, the larger θ_m, the larger the TOF, and since this is one of the objectives of our algorithm, the optimizer will always try to minimize θ_m when possible.

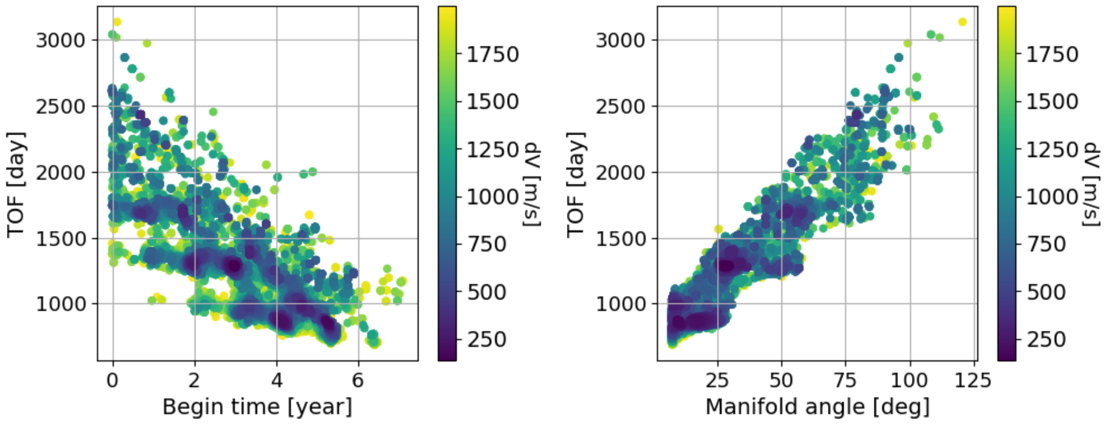

(a) t_{begin} vs TOF

(b) θ_m vs TOF

Figure 7.9: Linear relationship between θ_m, t_{begin}, and TOF.

7.1.6. Effect of tori arrival position

In order to study the influence of the arrival position on the tori we will plot the best individuals, those below an established threshold, with respect to their position on the tori, given by θ_1 and θ_2. Figure 7.11 displays an example obtained from the vertical family with one revolution. It can be seen that there is a strong influence of θ_1 on the quality of the solutions, while no effect of θ_2 is appreciated. It has been noticed that all the rest of the families and cases also present a similar pattern.

Table 7.3: Two individuals just differing on the value of θ_1.

Jac Idx	Cont Idx	θ_1 [deg]	θ_2 [deg]	t_{begin} [year]	t_{trans} [year]	θ_m [deg]	dV [m/s]	TOF [day]
49	19	50	99.44	2.995	2.344	17.93	202.84	1272
49	19	50	298.34	2.995	2.344	17.93	1300.43	1232

In order to examine what is the main cause behind this remarkable difference, we will look at the individuals which only differ in θ_1. Table 7.3 contains their full characterization. It can be seen that the ΔV difference between them is large, although they just differ in θ_1. Figure 7.10 shows these two transfers from different perspectives to help the reader get a three-dimensional picture of the trajectories. In blue, there is the asteroid orbit, and the point at which the Lambert orbits begin is marked in black. In red, there is the stable manifold of the individual with the most promising θ_1 and in pink the other one. Finally, the Lambert orbit that connects the asteroid orbit with the better individual is drawn in light green while the other is represented in darker green.

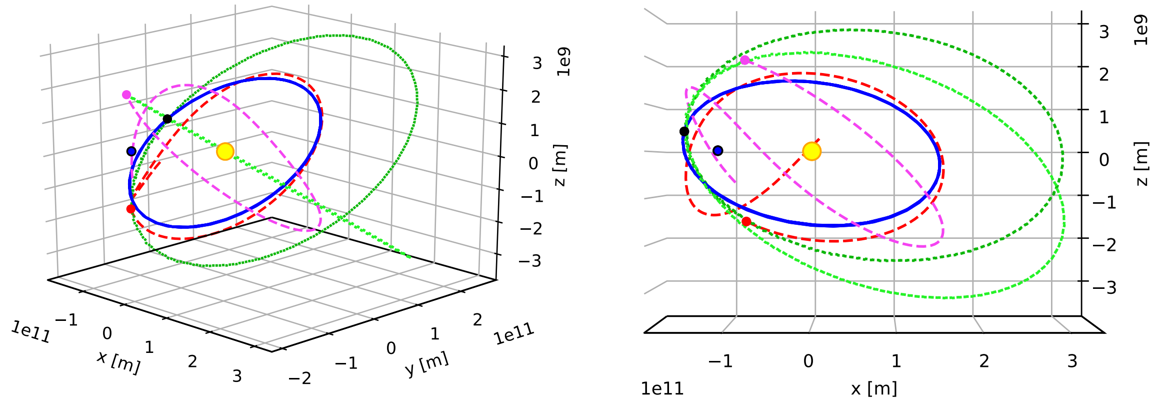

(a) 3D view.

(b) $x-z$ plane view.

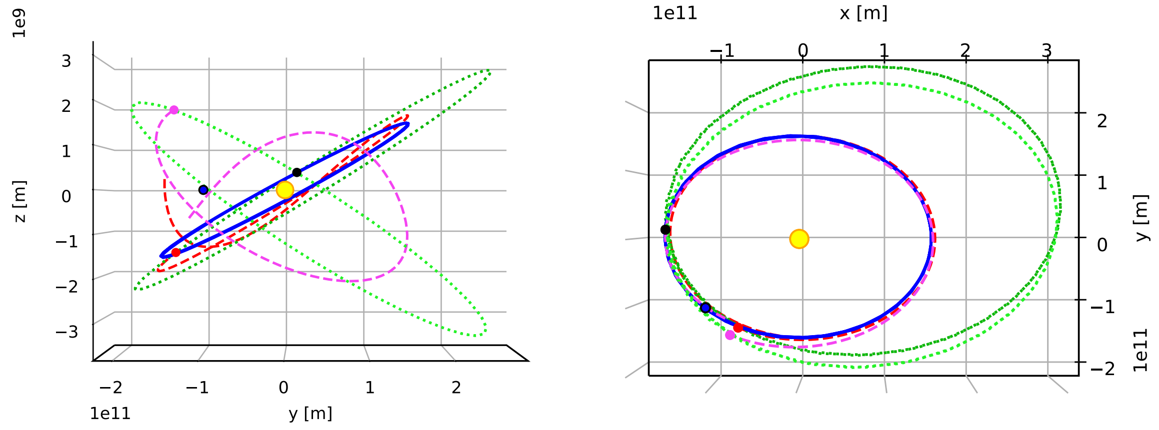

(c) $y-z$ plane view.

(d) $x-y$ plane view.

Figure 7.10: Two different trajectories which only differ in the value of θ_1 for 2006 RH120.

As can be observed in Figure 7.10c, the manifold that emanates from that region (red dotted line) has an inclination very close to the asteroid's orbit, which allows for low ΔV transfers. On the other hand, manifolds with different θ_1 do not achieve that inclination, which makes the transfers energetically much more expensive. Since all families are parameterized in the same way, that range of angles will also correspond to similar areas to some extend, which explains why Figure 7.11 looks similar in all cases.

Figure 7.10 also reveals the fact that using invariant manifolds can bring up interesting low-cost transfers by bringing two regions in space closer that would, otherwise, be unavoidably distant.

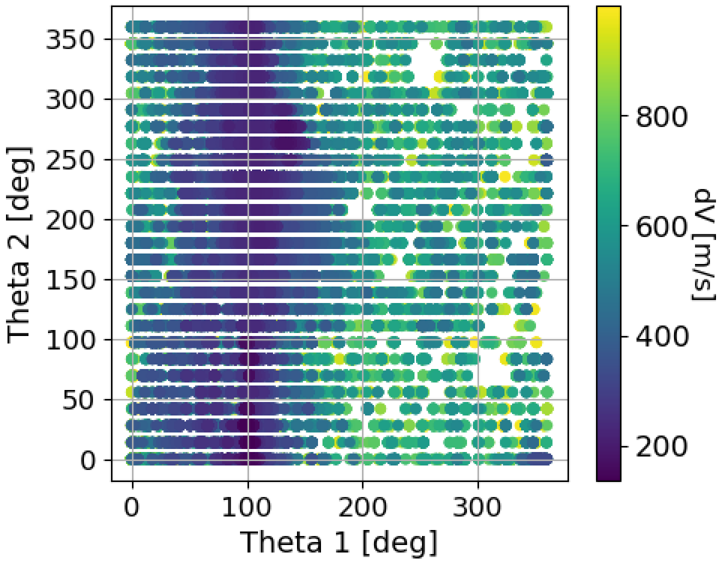

Figure 7.11: Distribution of ΔV with respect to the position on the torus surface from the vertical one revolution family.

7.1.7. Mission Design

Another main objective of this work was to provide clear results about the most promising transfer options in the next decades. In this section, we present the results obtained from the optimization process in porkchop-like plots. Porkchop maps are very common in mission planning and they commonly show contours of equal energy against a combination of launch and arrival date for the flight. These plots are used to identify promising launch windows that are compatible with the mission requirements in terms of ΔV mainly, but also TOF.

Figure 7.12 shows the porkchop-like maps for the north and south halo, and the vertical quasi-periodic families with one revolution. Figure 7.13 shows the analogous, but using two revolutions. It can be seen that all the figures contain points organized in an upper diagonal. The diagonal contains the points with the lowest TOF, in other words, the points that take the least advantage of the manifolds. Since our scheme tried to optimize both ΔV and TOF, many good results are found in these areas. If the time spent on traveling along the manifold was ignored, all points would lie on the diagonal of these porkchop-like maps. By looking at these graphs, it can be seen that one advantage of using the invariant manifolds is that transfers at low ΔV can be found outside the main window, although the arrival date in both cases is almost identical. For some scientific uses, having this early transfer window could be advantageous, and the extra time on the manifold could allow for more and better observations. Comparing the different families, it can be seen that not only the halo families provide the lowest ΔVs, but also the more flexible windows.

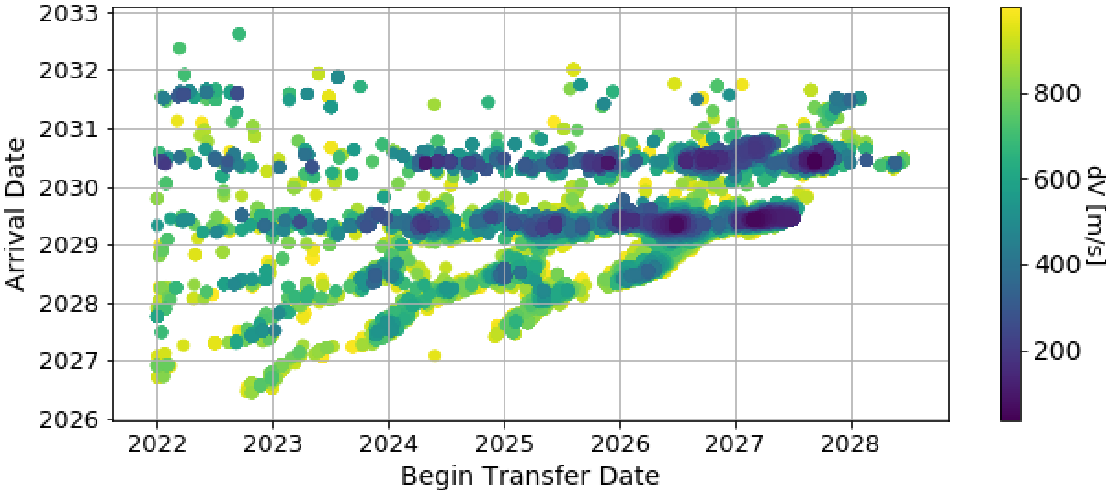

(a) North halo family

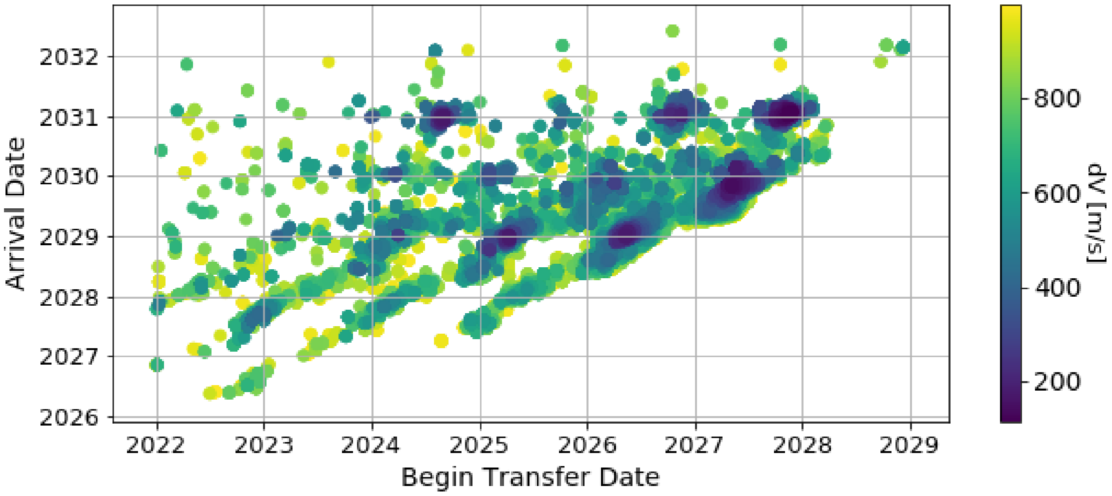

(b) South halo family

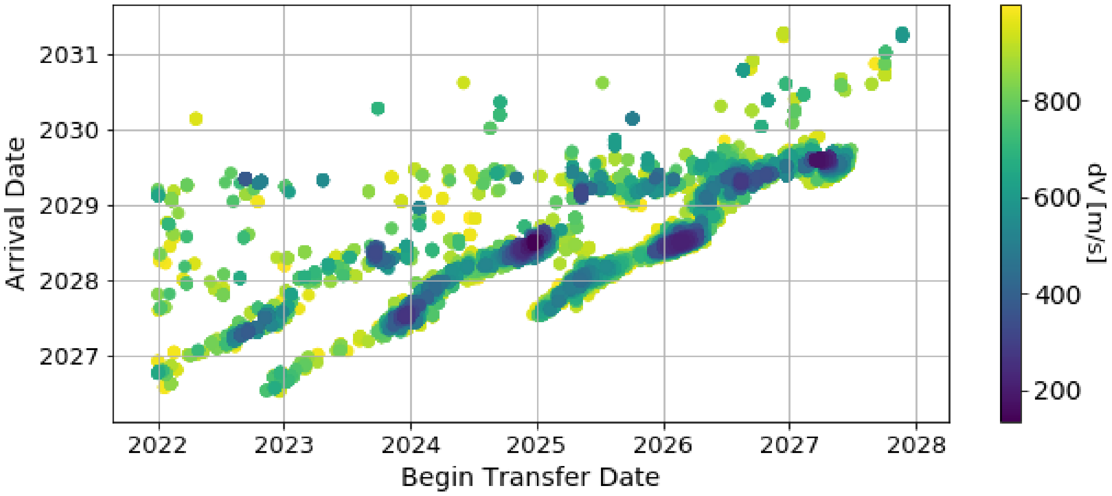

(c) Vertical family

Figure 7.12: Departure-arrival maps for one revolution and all quasi-periodic families for 2006 RH120.

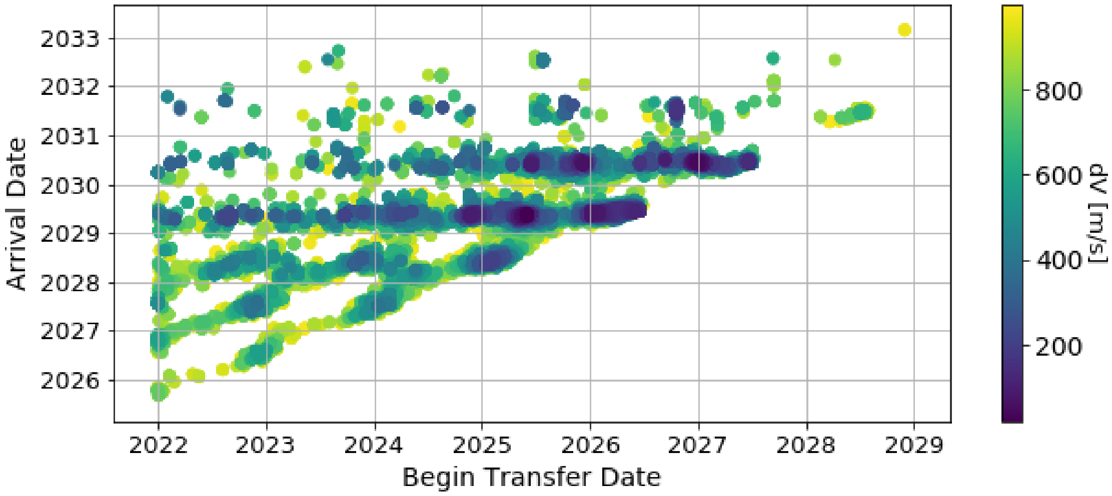

(a) North halo

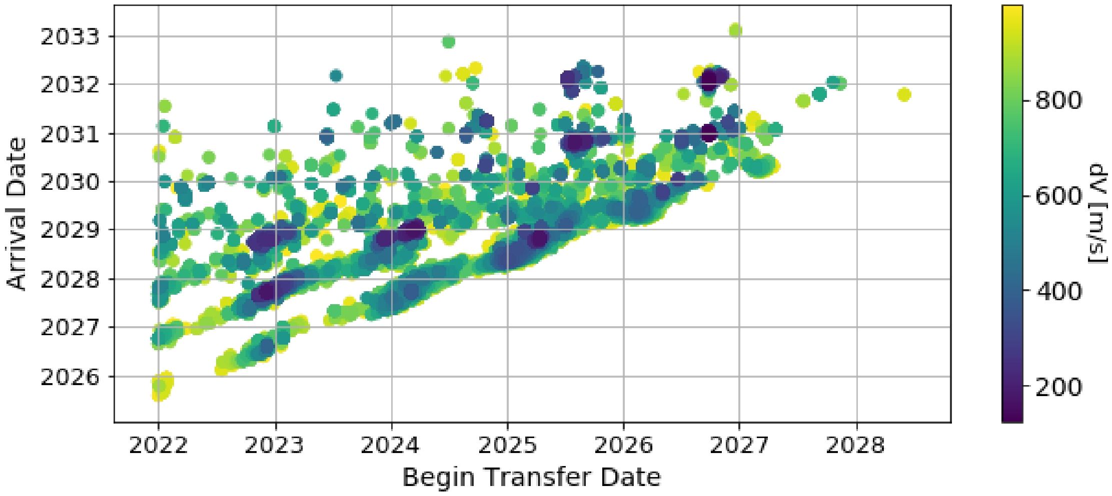

(b) South halo

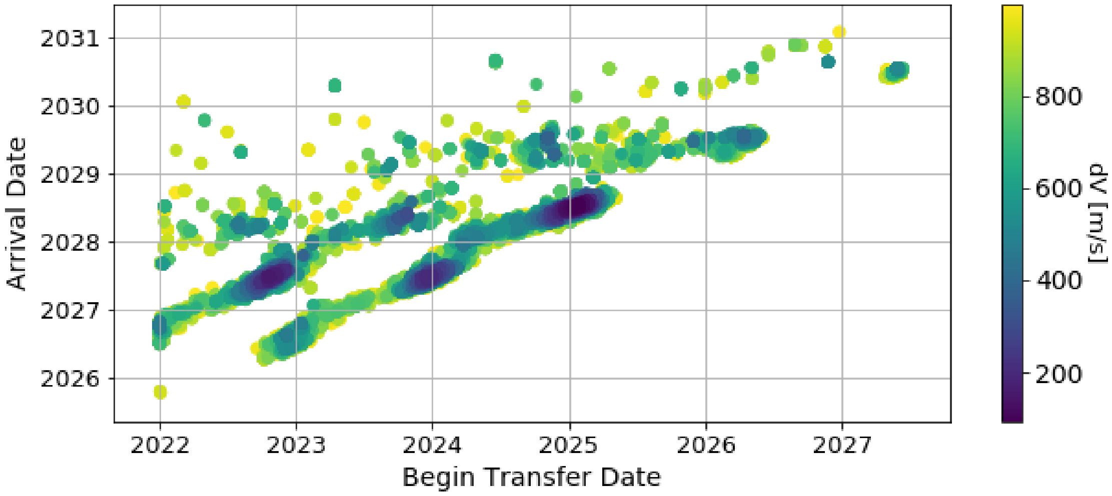

(c) Vertical

Figure 7.13: Departure-arrival maps for two revolutions and all quasi-periodic families for 2006 RH120.

7.1.8. Comparison with other's work

The feasibility of transferring NEAs to Earth's vicinity has been studied in the past by other authors, as explained in Chapter 2. A small part of these studies also studied 2006 RH120 in particular. In this section, we will compare the results that were obtained in the past with the ones we obtained using quasi-periodic invariant tori.

In 2017, Tan et al. [116] studied the possibility of transferring NEAs to the stable manifold emanating from periodic orbits about the libration points of the Earth-Moon system. Their problem was parameterized by 5 parameters, in contrast to the 11 that were used in this work. They found that using the invariant manifolds provided cheaper opportunities for NEA transfer than otherwise, so this scenario was not tested in this work by itself, but it is included in the general problem. They found also that transferring to a halo orbit was the most promising option, which interestingly coincides with our results. Moreover, they found that a total ΔV of 454.63 m/s would be required to transfer 2006 RH120 from its orbit to a halo orbit about L_2 in the Earth-Moon system, which is around 20 times larger than the most attractive value that we obtained in this work.

Table 7.4: Comparison of results of best ΔV values to transfer 2006 RH120 to Earth, by different authors.

Author	**Best ΔV [m/s]**	**Peculiarities**
This work	22	L_2 north-halo quasi-periodic orbits in Sun Earth system
J. P. Sánchez [116]	54	L_2 north-halo orbits in Sun-Earth system
Tan et al. [107]	454.63	L_2 north-halo orbits in the Earth-Moon system

J. P. Sánchez has devoted some studies to this same issue. In 2012 [107] he explored the possibility of using the invariant manifolds emanating from periodic orbits in the Sun-Earth system as a means of transport for NEAs. They used Lambert orbits as well to connect the asteroid's orbit with the manifold. However, they constrained the insertion into the manifold to happen before a plane located at $\pm\pi/8$ or 22.5°. They found that, again, manifolds emanating from north-halo orbits were the most suitable ones for capturing 2006RH120. They achieved a minimum $\Delta V = 54$ m/s for trajectories leading to north-halo orbits, 107 m/s when using south-halo orbits, and 187 m/s when using vertical periodic orbits. In this work, transfers at a lower cost have been obtained by using the manifolds emanating from quasi-periodic orbits for all families. Furthermore, the optimal value found in this work is half the previously known better solution. In 2016, Sánchez et al. approached the problem again, this time using all the new small bodies that had been discovered in the previous years and exploring the possibility of retrieving such bodies using low thrust. In any case, no improvements were made of the ΔV value required to retrieve 2006 RH120.

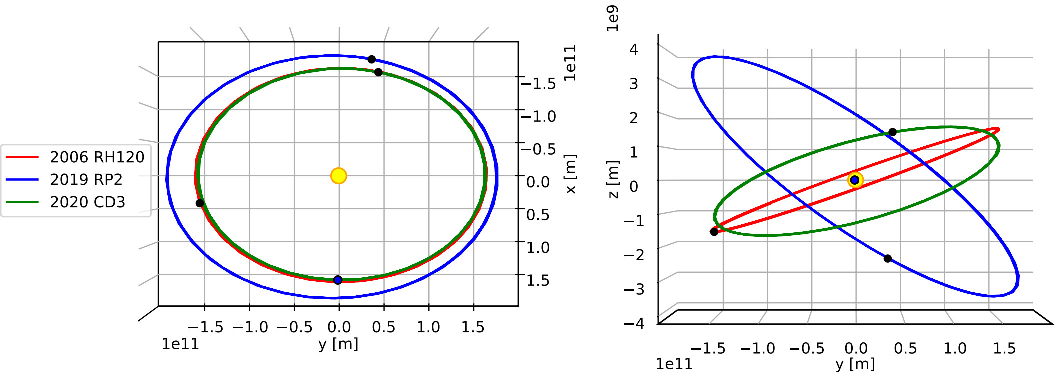

(a) $x-y$ plane view.

(b) $y-z$ plane view.

Figure 7.14: Orbits of the three NEAs considered for this work as potential candidates for retrieval.

7.2. 2019 RP2

The NEA 2019 RP2 was analyzed in the same manner as 2006 RH120, as mentioned only the most interesting results will be presented here. Table 7.5 displays the best individuals obtained for each family and the number of revolutions for 2019 RP2. It is noticeable that the minimum ΔV obtained is around 1.2 km/s, which is far above the limits established to catalog 2019 RP2 as an Easy Retrievable Object (ΔV < 500 km/s). That means that even though 2019 passed the pruning, it is indeed not a good candidate to retrieve from the NEA population.

Table 7.5: Best individuals for each family and number of revolutions for 2019 RP2.

Family	**Rev**	**Jac Idx**	**Cont Idx**	θ_1 **[deg]**	θ_2 **[deg]**	t_{begin} **[year]**	t_{trans} **[year]**	θ_m **[deg]**	ΔV **[m/s]**	**TOF [year]**
North Halo	1	41	29	266.56	103.85	1.34	1.93	25.50	1210.59	3.0190
North Halo	2	38	29	251.44	13.85	0.16	3.13	22.85	1192.20	4.15
South Halo	1	38	29	242.77	6.92	1.55	1.52	7.52	1251.83	2.27
South Halo	2	36	29	287.44	166.15	0.15	3.07	19.76	1219.29	4.05
Vertical	1	39	29	138.0	166.15	1.47	1.79	15.22	1271.42	2.69
Vertical	2	38	29	141.23	0.0	0.12	3.03	49.30	1270.43	5.09

This large difference is caused by the orbital configuration of this particular asteroid. Figure 7.14 shows the orbits of the three NEAs that we are studying through this work. On the left, it can be seen that the orbit of 2019 RP2 is the most eccentric one, and has a different semi-major axis than the other two, which are closer to the Earth's orbit. In any case, the driving factor for the observed difference is thought to be the inclination difference between the orbit of 2019 RP2 and the ecliptic. As it is well known, changes in inclination are an expensive maneuver and, in this case, the inclination of 2019 RP2 almost doubles the other two asteroids.

7.3. 2020 CD3

As was seen in the previous section, the orbit of 2020 CD3 is very similar to that of 2006 RH120. Therefore, a large part of the discussion for 2006 RH120 will be directly applicable to 2020 CD3. Others like the promising regions on the tori will simply adapt to a slightly different configuration, and others such as the beginning and transfer windows will change completely from one to the other.

Table 7.6 shows the best individuals obtained out of the optimization. It can be seen that transfers with very low values, around 46 m/s have been obtained. Analogously to what we found with 2006 RH120, the halo family seems to provide the best transfers, and among them, the north halo family yielded the minimum ΔV. However, note that these very low ΔV transfers also have associated large TOFs. For the minimum ΔV a TOF of 11.82 years is required, which is a rather long mission time. In that sense, maybe it could be interesting to use a more energetic transfer in order to reduce the TOF. Also, connecting with vertical invariant tori could be an interesting alternative.

Table 7.6: Best individuals for each family and number of revolutions for 2020 CD3.

Family	**Rev**	**Jac Idx**	**Cont Idx**	θ_1 **[deg]**	θ_2 **[deg]**	t_{begin} **[year]**	t_{trans} **[year]**	θ_m **[deg]**	ΔV **[m/s]**	**TOF [year]**
North Halo	1	46	13	186.0	103.85	14.86	1.80	166.64	45.47	11.82
South Halo	1	56	29	0.0	145.38	22.46	1.77	97.34	65.73	9.82
North Halo	1	41	22	42.0	34.62	24.94	1.78	56.66	67.16	5.62
North Halo	2	46	7	155.44	0.0	21.66	2.89	86.64	80.56	8.93
South Halo	2	57	13	240.0	138.46	21.43	2.80	100.48	81.91	10.68
South Halo	1	54	25	146.77	173.08	24.99	1.83	72.65	84.05	6.99
North Halo	2	37	29	117.23	13.85	23.93	2.84	44.18	113.11	5.65
South Halo	2	53	29	191.44	103.85	24.28	2.29	81.01	205.02	8.82
Vertical	2	44	5	98.77	0.0	23.92	2.90	29.75	208.78	4.68
Vertical	1	45	7	96.56	152.31	24.91	1.71	57.76	215.0	4.69

Figure 7.15 shows the porkchop-like plots for 2020 CD3. It is remarkable that in this case, some good solutions for large values of θ_m arose, which on the other hand, cause the long transfer times. Again, the orientation of these curves is upper diagonal, and the diagonal represents the transfers that do not make use of very few of the manifolds. In that sense, it can be seen that the vertical family is the one that less exploits its manifolds, while for the halo orbit, interesting results are found in these regions. These plots could be used to envision and determine the main specification of a retrieval mission to 2020 CD3 by exploiting the invariant manifolds of the quasi-periodic orbits.

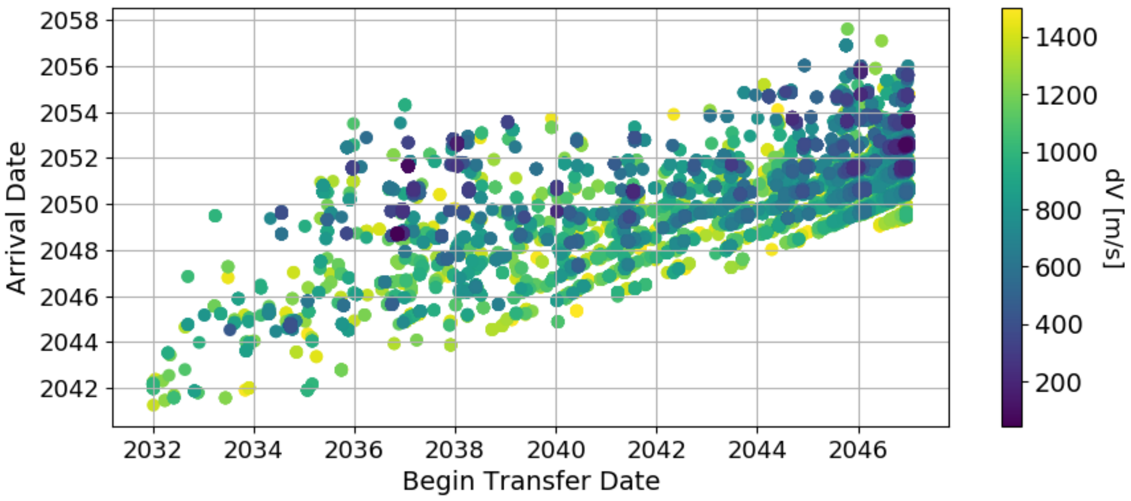

(a) North halo

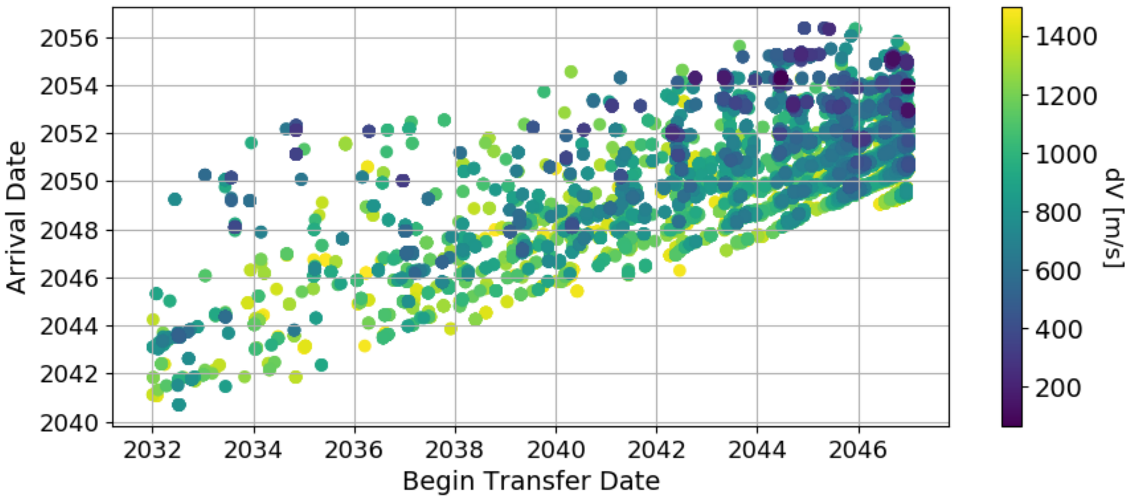

(b) South halo

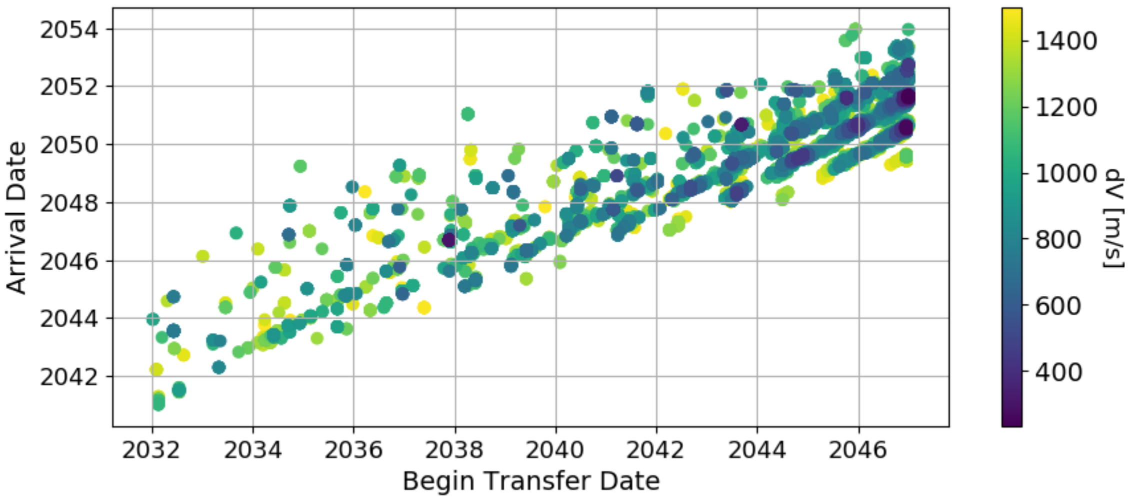

(c) Vertical

Figure 7.15: Departure-arrival maps for two revolutions and all quasi-periodic families for 2020 CD3.

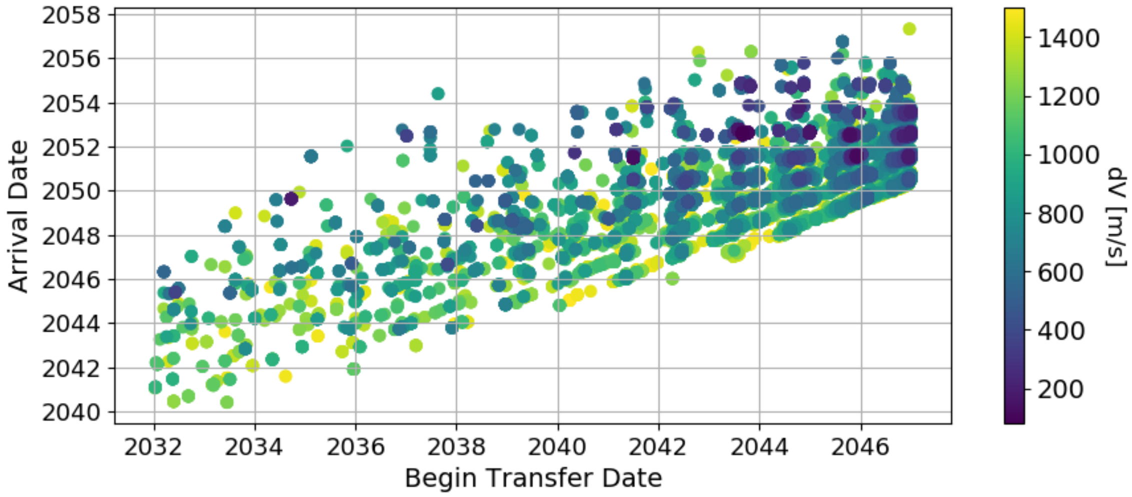

(a) North halo

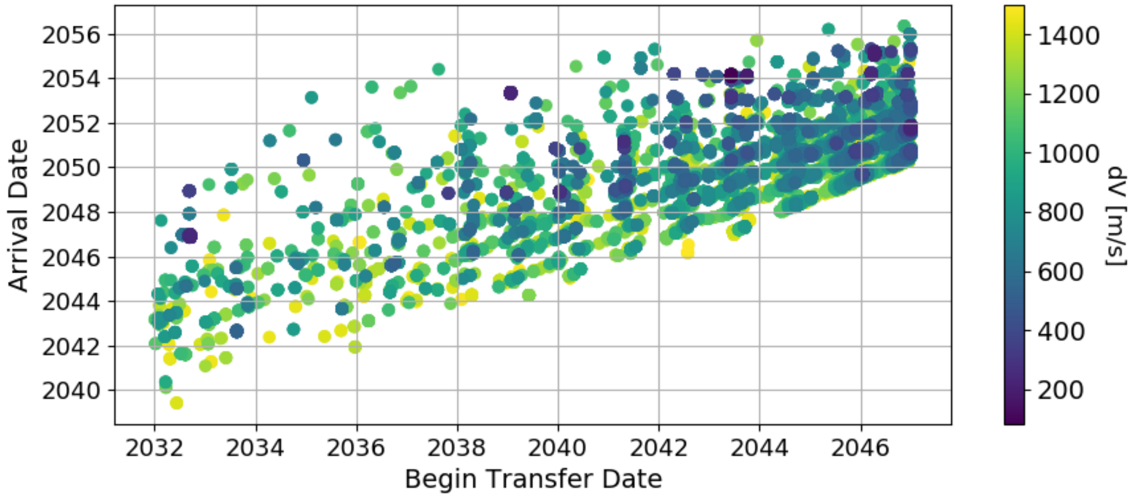

(b) South halo

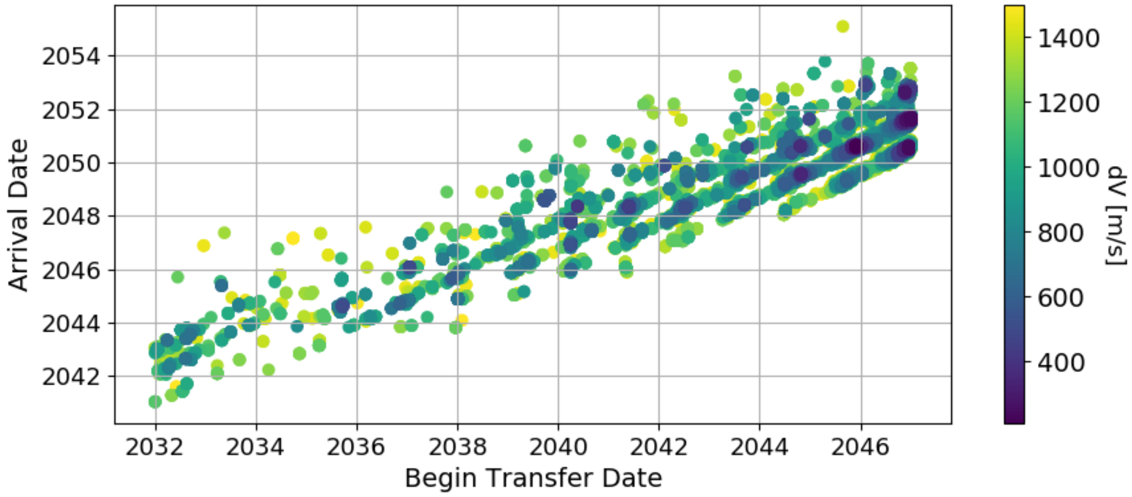

(c) Vertical

Figure 7.16: Departure-arrival maps for two revolutions and all quasi-periodic families for 2020 CD3.

8

Validation

In this chapter, the main intermediate results that were computed for this work are validated. In the most favorable scenario, reference cases from literature are emulated and the numerical results are compared. This is the case when validating the computation of the equilibrium points and periodic orbits. However, for more complex objects, such as the quasi-periodic tori and its manifolds, it is not possible to find those kinds of reference tables. Then, those cases will be validated by emulating some case from a reference paper or thesis and trying to replicate relevant graphs that reflect the evolution of any of the parameters. By comparing both figures we will validate our implementation. In the least favorable case, for validating the manifolds, a three-dimensional graph with the configuration space will be used. Finally, the transformation of ephemerides, and propagation of the asteroid will be validated using graphs from the JPL small-body database. The validation of the CR3BP reference frame to the ecliptic J2000 is done using geometric arguments.

8.1. Equilibrium Points

The equilibrium points of the Earth-Sun CR3BP are the first numerical result computed for this work. They are the basis on which the rest of the results is built upon. They are explained in the CR3BP formulation about equilibrium points ,Subsection 3.1.2, and they are used to derive the analytical approximation of the periodic orbits afterwards.

The equilibrium points were found by solving Equation 3.11, and using a gravitational parameter $\mu = \mu_E/(\mu_S + \mu_E) = 3.0404390358 \cdot 10^{-6}$ [84]. Bear in mind that at good starting point is important for the convergence of the root finder, as stated in Section 3.2.

Table 8.1: Computed position of the equilibrium points in dimensionless units.

	L_1	L_2	L_3	L_4	L_5
x	0.989985965	1.010075217	-1.00000076	0.499996970	0.499996970
y	0.0	0.0	0.0	0.86602540	-0.86602540

Table 8.2: Location of the Lagrange points in the Sun-Earth CR3BP, from [39]

	L_1	L_2	L_3	L_4	L_5
x	0.98998598	1.01007520	-1.00000127	0.49999696	0.49999696
y	0.0	0.0	0.0	0.86602540	- 0.86602540

Table 8.1 contains the computed position of the equilibrium points, while Table 8.2 displays the values used by Deccia in his master thesis [39]. As can be seen, for L_1 and L_2, which are the Lagrange points that will be used for this work, the differences appear at the 8th decimal position. The differences between both tables may arise for different μ considerations, in our case it includes also the Moon, or by using different sources to obtain the gravitational parameter of the primaries. Since the error between the useful values from both tables is $\sim 10^{-6}$ % we can consider as validated these results.

8.2. Periodic Orbits

The second result that was computed for this work were the different families of periodic orbits. The aim was to create a large database of periodic orbits that would serve as a starting point to create the quasi-periodic orbits, and from that the invariant tori. For that reason, it is necessary to validate that the implementation which computes the periodic orbits works correctly. The periodic orbit solver was firstly implemented in Python and it was based on shooting methods. However, as has been seen, shooting methods present some convergence problems, Subsection 3.5.3. For that reason, a second implementation in C++ was made based on collocation methods. The main advantage of this choice is that the solver could be inherited from a general collocation solver class so that a large part of the code was shared between the periodic orbit and quasi-periodic tori solvers. The initial guess for each of the families were created following the formulation in Section 3.4.

The validation of these kinds of solution is more complex than with the equilibrium points. Luckily, in his master thesis, Grebow [58] includes an abundant number of converged initial conditions to generate the main periodic orbit families in the Earth-Moon system. In order to validate our periodic orbit solver, we will recompute the Lagrange points using $\mu = 0.0121505856$ as indicated in [58]. Then we use the Jacobi constant that corresponds with the initial condition provided by Grebow to generate an analytic approximation from which the exact orbit will be computed using our solver. Once the member is found, we will compare the initial state provided by Grebow with the state of our orbit at θ_0, if they match, then the solver is validated for that family.
Take into account that the implementation of the solver is generic and so, the convergence of one member of any family would suffice to validate it. However, in this way we intend to validate also the initial approximations that will be used to initialize the solver.

Table 8.3: Computed initial state vs reference planar Lyapunov orbit with almost equal period

		Computed	Reference
L_1	$\mathbf{x}_0$	$(0.8197, 0.0028, 0, 0.0026, 0.1741, 0)$	$(0.8189, 0, 0, 00.175, 0)$
	T	2.7970	2.7959
L_2	$\mathbf{x}_0$	$(1.1836, 0, 0, 0, -0.18115, 0)$	$(1.1843, 0, 0, 0-0.1818, 0)$
	T	3.4329	3.4341

Table 8.3 contains the comparison between a computed periodic about L_1 and L_2, and the reference value provided by Grebow. As mentioned, the orbit was found by using the energy of the reference initial state to generate the initial guess. In both cases (L_1 and L_2) the differences appear at the 3rd decimal, and this small difference can be caused by two effects. First, the period of both orbits is not exactly the same, so they do not represent exactly the same member, although they are very close. Secondly, Grebow computed these periodic orbits using shooting, while ours were obtained via collocation, so the ’initial point’ may not be exactly the same. These two sources can

explain the small differences between the computed and reference states. Nonetheless, it can be seen that the solver works properly. Moreover, by inspecting Table 8.3, it can be seen that when the period of the computed orbit is slightly larger than the reference, the error in the states are also larger. This agrees with the physical intuition that when the family moves away from the Lagrange points, the period increases, which strengthens our confidence in the solver.

Table 8.4: Computed initial state vs reference north halo orbit with almost equal period.

		Computed	Reference
L_1	$\mathbf{x}_0$	$(0.8241, 0, 0.0221, 0, 0.1336, 0)$	$(0.8234, 0, 0.0224, 00.1343, 0)$
	T	2.7476	2.7464
L_2	$\mathbf{x}_0$	$(1.1800, -0.0030, 0.0139, 0, -0.1562, 0.0006)$	$(1.1807, 0, 0.0139, 0-0.157, 0)$
	T	3.4139	3.4126

Table 8.4 contains the computed and reference initial state for a north halo orbit. Again, there are small deviations that can be explained by the same arguments as in the planar case. The south halo orbit validation will not be included here because north and south halo orbits are symmetric, so if the initial approximation of the north is valid, the south one will equally be.

Table 8.5: Computed initial state vs reference vertical orbit with almost equal period.

		Computed	Reference
L_1	$\mathbf{x}_0$	$(0.8573, -0.0007, -0.0048, -0.0048, 0.0549, 0.3628)$	$(1.0118, 0, 0.1739, 0-0.0799, 0)$
	T	3.45533	5.0950
L_2	$\mathbf{x}_0$	$(1.1113, 0.0031, -0.0074, 0.0140, -0.1820, 0.4354)$	$(1.1119, 0, 0, 0-0.1812, 0.4358)$
	T	4.4222	4.43906

Table 8.5 contains the reference and computed value for the two equilibrium point we are studying, now for a vertical orbit. Again, the value about L_2 matches reasonably well. However, the values at L_1 do not match. This is odd, because the solver has already been validated, and the equations that are used to compute the vertical initial guess are the same for both equilibrium points.

After careful consideration, it was concluded that the values provided in this case by Grebow are erroneous, as can be proved by geometric arguments. Since in the Earth-Moon system $\mu = 0.0121505856$, and vertical orbits around L_1 do not surpass the smaller primary in x, see Figure 3.4. In dimensionless units the Earth is at $x = 0.9878$ so then, the reference position given has to be erroneous. Furthermore, the fact that the period is higher at L_1 than at L_2, while the values that used Grebow were always lower, gives us a clue that the reference data is in fact wrong.

8.3. Quasi-periodic invariant tori

The quasi-periodic tori are a central part of this work. The collocation solver used to obtain them inherits from a class that the periodic orbit solver also uses, so some of the functionalities have already been validated there. However, the evaluation of the system of equations and it associated Jacobi constant is the most cumbersome and difficult part, and consequently, error-prone.

On top of that, validating these kinds of objects is a difficult task since it is not common to find a table of initial conditions or file containing the exact tori states for a given parametrization and configuration. Indeed such information could not be found. For that reason a different approach had to be adopted to validate our quasi-periodic collocation solver.

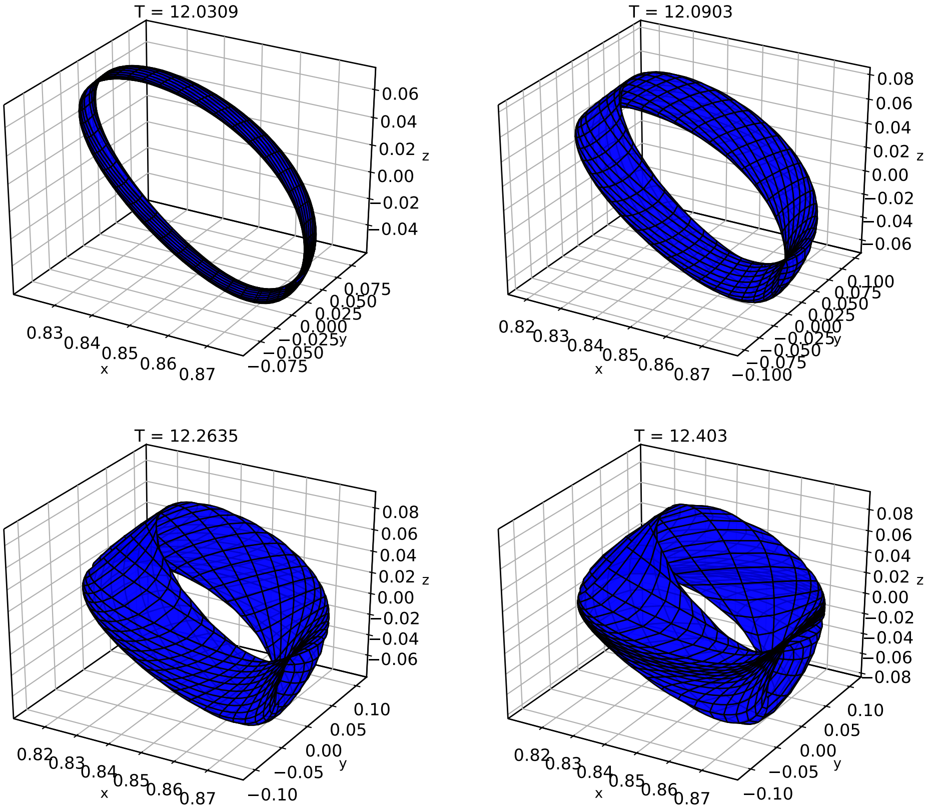

Figure 8.1: Set of invariant tori about L_1 in the Earth-Moon system computed emulating the set generated by McCarthy, [88]

McCarthy presented in his master thesis [88] a collection of tori that represent the continuation evolution of a family of tori with the same constant value ($C = 3.1389$) in the Earth-Moon system. He provides the period T of each of these tori, and an extra graph displaying the evolution of the torus amplitude with respect to the mapping time or period. The approach that we will use to validate our solver is the following. The same set of tori will be computed; this is possible because the Jacobi constant and period fully characterize each of the tori, because they exist in two-dimensional families. Then, this set of tori will be used to create a graph similar to the one that McCarty presented. If they match then the tori are the same, and our implementation would be validated.

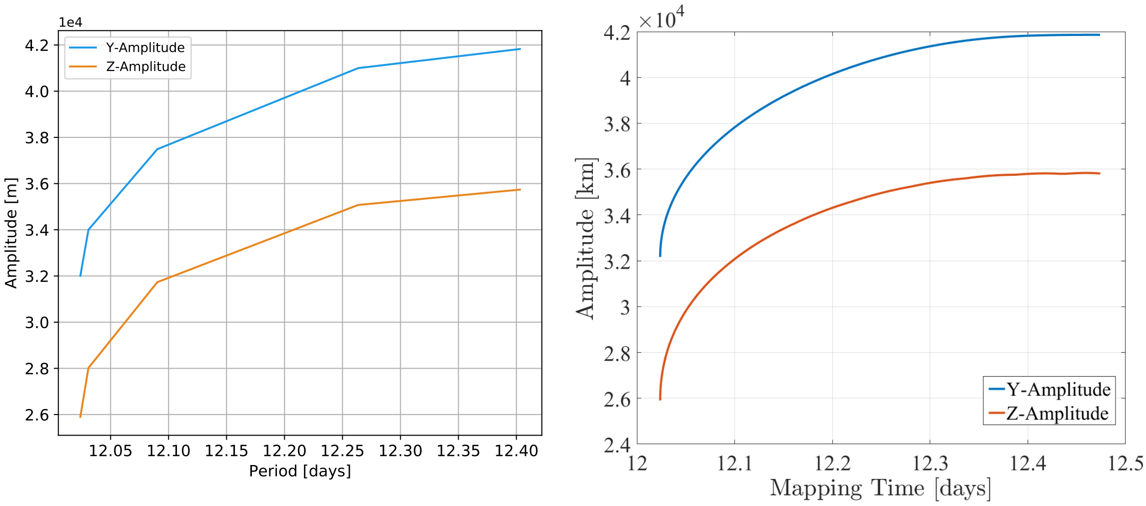

(a) Computed

(b) Reference

Figure 8.2: Computed vs reference amplitudes for a set of tori.

Figure 8.1 shows our set of tori emulating the ones that McCarthy computed for his master thesis. By taking the maximum y- and z-values of each of the tori we can generate Figure 8.2. On the left we have the values obtained using our solver, and on the right side the reference one. As can be clearly seen, both figures look very similar, the values are almost the same and the shapes also are alike. The small deviations are mainly due to the fact that the tori with specific periods had to be found iteratively, so the period may not be exactly the same. This is because the solver we are using allows to fix the Jacobi constant but not the period, and this parameter is defined in the continuation procedure.

8.4. Invariant tori manifolds

If validating the quasi-periodic tori was difficult, validating their manifolds is even more difficult. It was not possible to find any literature values to use as a reference. The good news is that if the solver scheme works correctly, as it has been already verified, then only a few algebraic operations and the evaluation of the eigenvalues, Section 4.8, occur before we obtain the manifolds. Nonetheless, we needed to verify that our results make sense in order to begin computing the large database that was required for the optimization problem, Section 4.9. For that, the master thesis of McCarthy has been used again to obtain at least a qualitative reference. There, he shows the evolution the tori manifolds for a given integration times and for a torus with a given Jacobi constant $C = 3.1389$. Figure 8.3 shows in black the original torus and in red the torus that is created when integrating each points on the torus along their unstable manifold for a given amount of time.

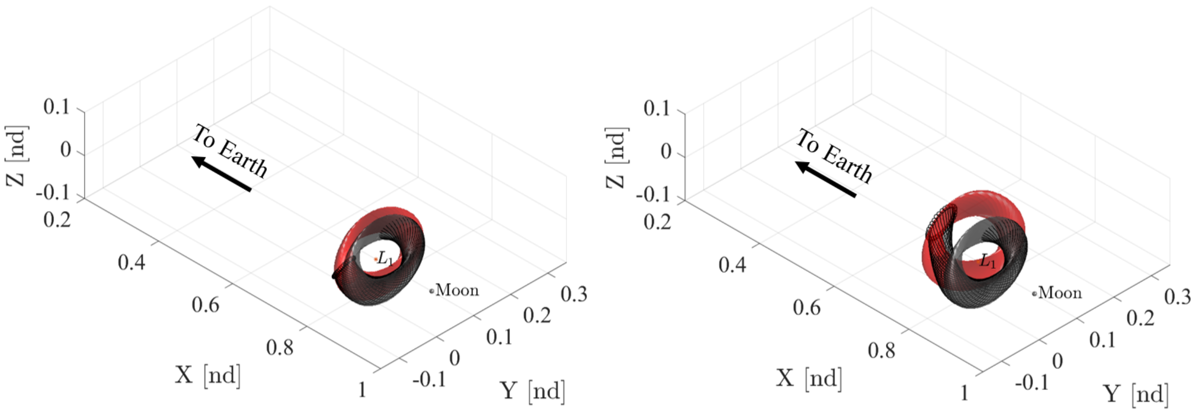

(a) $t = 7.79$ days (b) $t = 9.75$ days

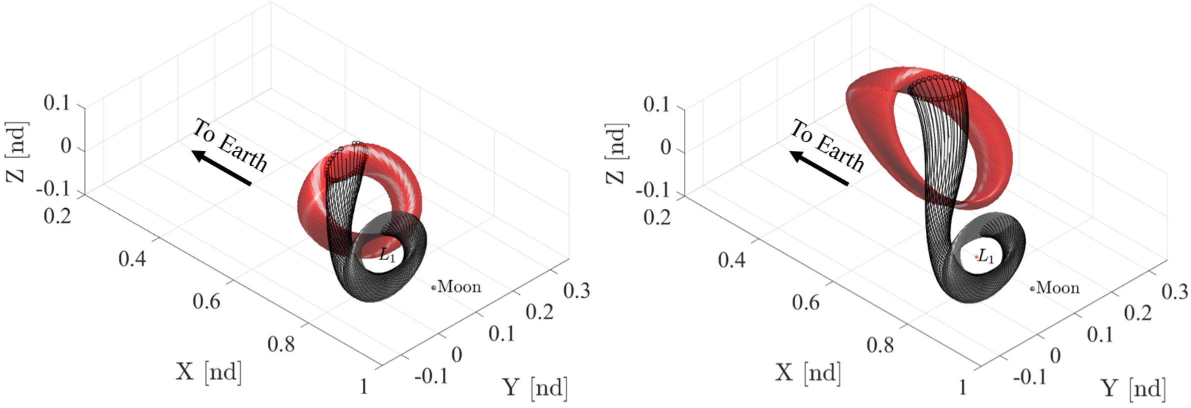

(c) $t = 11.39$ days (d) $t = 13.02$ days

Figure 8.3: Unstable manifold in the x-direction for tori in the Earth-Moon system [88].

Figure 8.5 displays the same case but using our implementation of the solver. Also the original torus appears in black, the invariant manifolds of one of its sections in blue and in red the propagation along the unstable manifolds. As can be seen by comparing both figures the evolution of the torus is very similar. Small differences can exist because the full parametrization, providing the period T for instance, of the original torus was not provided in McCarthy's thesis, and so a similar one had to be found iteratively until the dimensions of both were very close. Another source of error can come from the value of the perturbation that is applied to the hyperbolic eigenvectors that are chosen. In any case, the shape and values of the unstable manifolds match well, so we confirm that the solver computes the manifolds correctly. Note that in the case we are interested in, we will be using the stable manifolds instead of the unstable, however there is no difference concerning the implementation, so they do not need to be validated independently.

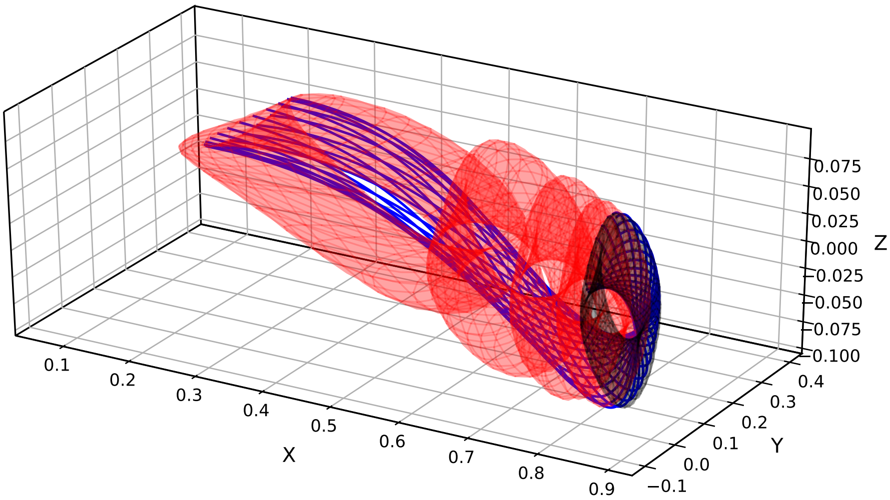

Figure 8.4: Evolution of the manifold of a north-halo quasi-periodic torus ($C = 3.1389$) about L_1 at times $t = 7.79, 9.75, 11.39, 13.02$ days. In black the original torus, in red the propagated ones along the unstable manifold and in blue the manifolds of a section.

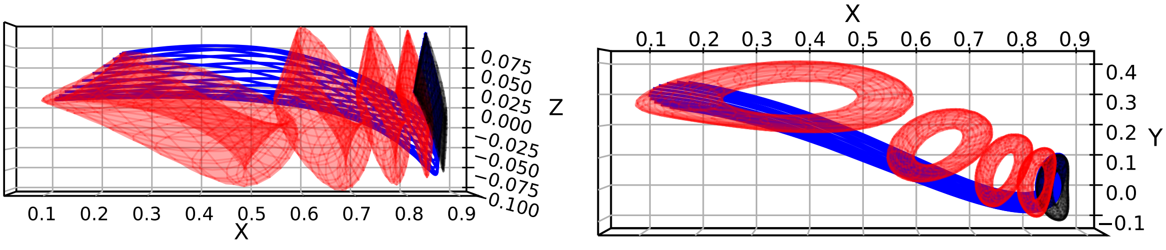

(a) View from $y-$axis.

(b) View from $x-$axis.

Figure 8.5: Different perspective of Figure 8.5.

8.5. Reference frame transformations

The last part that will be validated concerns the harmonization of all the data that was created into the same reference and unit system. On one hand, all the elements that are related with the CR3BP are expressed with respect to a synodical reference frame and in non-dimensional units. On the other hand, the state of the asteroid is given in the JPL Small-Body database by its Kepler elements at a fixed epoch, which is given in either Julian or Modified Julian Days and with respect to the JPL 51 reference frame, in other words the heliocentric ecliptic J2000.

As was already seen, the cost function that was created for our optimization problem creates a unified framework in which the Lambert transfer between an asteroid at t_{begin} and a stable manifold of a torus at $t = t_{begin} + t_{transfer}$ can be computed. In order to verify that the transformations are correctly implemented the following approach will be employed. The value of t_{begin} will be selected to match the 20th of March of 2022. This day corresponds to the spring vernal equinox[1] which is used to define the orientation of the ecliptic J2000 reference frame. On that day, the Earth is located on the negative $x-$axis. So it will be simple to check if the ephemerides are being retrieved correctly. Furthermore, a time of transfer equal to 1 year will be used so that we can use the position of the Earth at t_{begin} to check if the transfer point on the manifold is correctly transformed. This can be simply checked by looking whether the angle between this point and the line between the Sun and the Earth matches the input value.

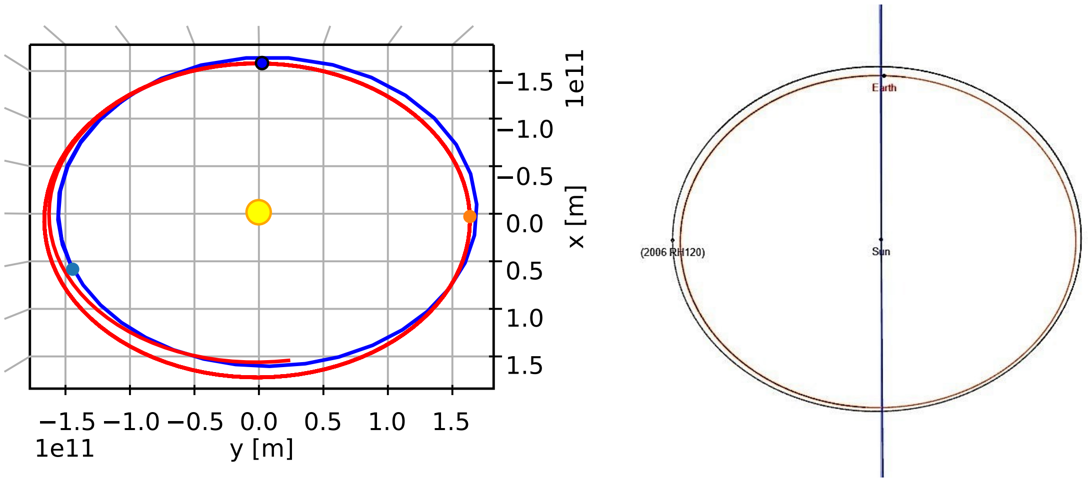

(a) From model

(b) From NASA

Figure 8.6: Earth and asteroid ephemerides. Computed state (left) and the one provided by the JPL database (right).

---

[1] The spring vernal equinox is the time in the spring when the sun crosses the equator, and when night and day are of equal length.

Figure 8.6 shows on the left the most important elements in our model. The yellow and blue dots represent the position of the Sun and the Earth respectively. On a brighter blue dot, there is the position of the asteroid. All these elements are represented at the epoch 20th of March 2022. On the right we can see the same elements, but given by the JPL Small-Body database webpage based on their own ephemerides. It is clear that the relative and absolute position of these bodies with respect to the Solar System barycenter at the ecliptic J2000 reference frame has been correctly implemented.

The left-hand figure also shows an orange dot which represents the point at which the Lambert arc will transfer to the stable invariant manifold the 20th March 2023. The input angle was 270° which is measured from the Sun-Earth axis and clockwise for L_1 departing orbits, and anti-clockwise for L_2 departing orbits. The transfer point, and hence the manifold evolution, has been then correctly transformed from the synodical dimensionless reference frame to the one in which the ephemerides of the rest of the bodies are expressed. So we can ensure that the Lambert arc computations that have been performed do reflect physical reality.

9

Conclusions and Recommendations

9.1. Conclusions

This research intended to study the feasibility and advantages of using the invariant manifolds emanating from quasi-periodic orbits in the Sun-Earth system as a means of transport of Near-Earth Asteroids.

Dynamical environment: The general concepts to compute periodic solutions in the CR3BP were reviewed, which are also applicable to the quasi-periodic orbits. In order to improve the basin of attraction and convergence of the solvers, the collocation method was chosen, despite its more complex implementation. Moreover, the pseudo-arclength continuation method was used for it accounts for the local shape of the solution curve, and improves convergence.

Quasi-periodic orbits: The quasi-periodic invariant tori were computed using the stroboscopic method, adding a series of constraints and extending the flow with unfolding parameters to obtain a unique solution for each set of equations. By computing the eigenvalues of a large series of periodic orbits the domain of existence of quasi-periodic orbits was bounded. In order to speed up the computations during the optimization, a comprehensive database was created, where the state of the manifold of each torus can be accessed as in a look-up table. The number of tori families for a fixed Jacobi constant was computed dynamically, by adjusting the error between consecutive members, the continuated family was fixed to 30 members for simplicity; this value would introduce errors between tori of about $\sim 10^{-4}$. Finally, the parametrization of the tori was addressed to find a compromise between accuracy and computational efficiency. The difference between adjacent eigenvectors and the computing time was used to find the best parametrization for our use, which turned out to be $N_1 = 30, m = 5$, and $N_2 = 26$.

Near-Earth Asteroids: The most promising asteroids to be retrieved from the NEA population were obtained first using simple graphical methods by comparing the maximum inclination that a family of tori with equal Jacobi constant can provide with the Tisserand parameter and inclination of the NEA. After that, using a three-layer filter (energy, orbital parameters, and diameter < 15 m), three promising candidates were found, which were also obtained in the graphical analysis at a much lower computational cost.

Tuning: The optimization problem was defined using Lambert arcs to connect the asteroid's orbits with the stable manifolds of quasi-periodic orbits, and it was seen that can be completely parameterized by 11 parameters. It was seen that the $n-$body integration of the asteroid worked better with a variable step-size Bulirsch-Stoer integrator with a tolerance value of 10^{-10}, because it allows to use very large time-steps. Furthermore, we included the accelerations of all the planets, the Moon and (estimated) radiation pressure were included in the simulations, because they contribute to errors of at least $\sim 10^7$ m over the integration times of decades that were used.
The integration of the manifolds in the CR3BP was done using Runge-Kutta 4 integrator and a time-step of two days seemed to offer the best results.

It was seen that some of the simulations can yield errors, which can be caused by the Lambert solver, manifold integration and initial state angle (negligible). Using a Monte-Carlo analysis, it was concluded that, out of the 11 parameters of the problem, four ($t_{begin}, t_{trans}, L_i$, and n_{rev}) could be further constrained in order to speed up the convergence of the optimization.
Building upon the work of fellow TU Delft students, the optimizator MOEA/D was selected. In order to ensure its good performance, it was tuned and a population of 500 individuals, weighted decomposition method, and $CR = 0.8$ seemed to offer the best results.

Optimization: For 2006 RH120, transfers with very low ΔV were found ($\sim$ 22 m/s), and north halo tori seemed to offer the best transfers. Since this asteroid had already been studied in literature

for retrieval, we compared our results with theirs, and the minimum obtained in this work turns out to be between 20 and 2 times better than any previous result found. It was then proved that quasi-periodic orbits are able to provide NEA retrieval trajectories with extraordinary low values of ΔV, and relatively good TOF. The effect of each of the parameters was analyzed. It was seen that tori further from the periodic orbit, that is, larger tori seemed to offer the best transfers. Moreover, it was shown that using quasi-periodic tori allows for more flexible transfer windows for a fixed value of ΔV. The relationship between TOF, dV and θ_m was explained and related to the multi-objective optimization we were performing. It was also seem that the Jacobi constant of the asteroid alone is not enough to obtain the Jacobi constant of the best tori, and that the relative inclination between them has also to be taken into account. Finally, the fact that some regions on the tori produce considerable better transfers was verified and explained using its manifold geometry.
On the other hand, 2019 RP2 did not offered good enough results to classify it as an Easy Retrievable Object, due to its orbital parameters. Finally, it has shown that 2020 CD3 could be retrieved at extremely low ΔV as well. For the two promising asteroids, departure-arrival graphs were presented in order to be used for mission design and illustrate all the results obtained.

9.2. Recommendations

In this section, we will address some recommendations and questions that would need further research in the field of designing transfers using the quasi-periodic invariant tori. Some of them will be related to tools that would need to be created in order to facilitate the work for future investigation and some others will dive into more technical questions that need to be studied.

- In this work, the TU Delft Astrodynamic Toolbox (TUDAT) was used for creating the cost function for the optimization problem. Nonetheless, the tools for creating the database were developed independently in C++. A TUDAT implementation similar to the one used for this work should be done, for it will help many students in the future to speed up greatly the first steps of the research when working in the context of the CR3BP. The following architecture is suggested: in the CR3BP namespace, create a class for periodic orbit and quasi-periodic orbit. Each class is able to contain the state, parametrization, and other parameters such as period, stability index, and others. The periodic orbit class should be able to be initialized by creating an approximation of the solution which could be later converged using a solver. Two solvers could be implemented, both collocation and shooting. Then each solver function could be specialized for each of these classes. The solver could also compute the manifold eigenvectors, which could be stored in each object for later use. Providing a functional and thorough environment to compute in the context of the CR3BP, could not only be useful for research but also for educational purposes in some subjects taught at the university.

- In the last years some NEA asteroids that had fallen into the Earth's influence sphere have been discovered, this is the case of 2006 RH120 and 2020 CD3. A different approach to bound the motion of these asteroids could be to transfer them directly to a quasi-periodic orbit, while they are under the Earth's gravitational influence. These kinds of transfers would require to be known beforehand at what moment an asteroid will fall under its influence, and because only small asteroids could be retrieved nowadays, and these are difficult to detect, this is a difficult task at least for now.

- In the first place, we intended to explore the possibility of connecting the NEA orbits to the manifolds by using also low-thrust transfers. However, due to the very different nature of the problem, and in order to focus on a single problem, it was discarded in the end. The study of these transfers, but using low thrust, could provide more and better solutions. It is expected that the total TOF would also increase considerably, but in any case, it would be interesting to study.

- In this work, three different models are used at different parts of the simulations: two-body, CR3BP, and full dynamics. The Lambert arc could be substituted by a more representative model of the full dynamics. Studying the entire problem by including all the accelerations at all times would make the results more realistic and useful for future mission designs.

- In a more general context, we would have liked to study the behavior of these quasi-periodic orbits around NEAs with irregular shapes and feeble gravity fields. Quasi-periodic orbits around similar bodies like Phobos [108] and some asteroids [70] have already been studied. Nonetheless, studying the invariant manifolds that arrive at quasi-periodic tori around these asteroids could be used for the design of the first part of the mission.

- In the context of asteroid deflection it could be also interesting to study the behavior of such tori in binary asteroids when the state of one of them is modified abruptly.

Having a simple database available, from which their states could be retrieved as a look-up table could be a good idea, to avoid having to recompute the same results by different people for the most popular systems, namely the Sun-Earth and Earth-Moon systems. In general, the use of quasi-periodic orbits in mission design could improve the performance and create new opportunities, as has been proven through this work.

Bibliography

[1] Paul A Abell, BW Barbee, RG Mink, DR Adamo, CM Alberding, DD Mazanek, LN Johnson, DK Yeomans, PW Chodas, AB Chamberlin, et al. The Near-Earth object human space flight accessible targets study (NHATS) list of near-Earth asteroids: identifying potential targets for future exploration. In *Lunar and Planetary Science Conference*, 2012.

[2] Yuki Akiyama, Mai Bando, and Shinji Hokamoto. Periodic and quasi-periodic orbit design based on the center manifold theory. *Acta Astronautica*, 2019.

[3] Elisa Maria Alessi et al. *The Role and Usage of Libration Point Orbits in the Earth-Moon System.* Universitat de Barcelona, 2010.

[4] Brian D Anderson and Martin Lo. Dynamics of asteroid 2006 RH120: temporary capture phase. In *2018 Space Flight Mechanics Meeting*, 2018.

[5] Brian D Anderson and Martin W Lo. Dynamics of asteroid 2006 RH120: pre-capture and escape phases. 2016.

[6] Astronomy Answers. Synodical periods between all planets, 2020. URL `https://www.aa.quae.nl/en/reken/synodisch.html`.

[7] Vladimir Igorevich Arnol'd. *Mathematical methods of classical mechanics.* Springer Science & Business Media, 2013.

[8] Kendall Atkinson, Weimin Han, and David E Stewart. *Numerical solution of ordinary differential equations.* John Wiley & Sons, 2011.

[9] Giulio Avanzini. A simple Lambert algorithm. *Journal of guidance, control, and dynamics*, 2008.

[10] Paul B Bailey and LF Shampine. On shooting methods for two-point boundary value problems. *Journal of Mathematical Analysis and Applications*, 1968.

[11] He-Xi Baoyin, Yang Chen, and Jun-Feng Li. Capturing near Earth objects. *Research in Astronomy and Astrophysics*, 2010.

[12] Nicola Baresi, Daniel J Scheeres, and Hanspeter Schaub. Bounded relative orbits about asteroids for formation flying and applications. *Acta Astronautica*, 2016.

[13] Nicola Baresi, Zubin P Olikara, and Daniel J Scheeres. Fully numerical methods for continuing families of quasi-periodic invariant tori in astrodynamics. *The Journal of the Astronautical Sciences*, 2018.

[14] Richard P Binzel, Alan W Harris, Schelte J Bus, and Thomas H Burbine. Spectral properties of near-Earth objects: Palomar and IRTF results for 48 objects including spacecraft targets (9969) Braille and (10302) 1989 ML. *Icarus*, 2001.

[15] Francesco Biscani and Dario Izzo. A parallel global multiobjective framework for optimization: PAGMO. *Journal of Open Source Software*, 2020.

[16] Bryce T Bolin, Christoffer Fremling, Timothy R Holt, Matthew J Hankins, Tomás Ahumada, Shreya Anand, Varun Bhalerao, Kevin B Burdge, Chris M Copperwheat, Michael Coughlin, et al. Characterization of temporarily captured minimoon 2020 CD3 by keck time-resolved spectrophotometry. *The Astrophysical Journal Letters*, 2020.

[17] Claudio Bombardelli, Hodei Urrutxua, Andres Galvez, and Ian Carnelli. The SIROCO asteroid deflection demonstrator. In *AAS/AIAA Space Flight Mechanics Meeting, Charleston, South Carolina*, 2012.

[18] William F Bottke Jr, Alessandro Morbidelli, Robert Jedicke, Jean-Marc Petit, Harold F Levison, Patrick Michel, and Travis S Metcalfe. Debiased orbital and absolute magnitude distribution of the near-Earth objects. *Icarus*, 2002.

[19] Edward Bowell, Bruce Hapke, Deborah Domingue, Kari Lumme, Jouni Peltoniemi, and Alan W Harris. Application of photometric models to asteroids. *Asteroids II*, 1989.

[20] R Brasser and P Wiegert. Asteroids on Earth-like orbits and their origin. *Monthly Notices of the Royal Astronomical Society*, 2008.

[21] John V Breakwell and John V Brown. The ‘halo’ family of 3-dimensional periodic orbits in the Earth-Moon restricted 3-body problem. *Celestial mechanics*, 1979.

[22] Hendrik W Broer, George B Huitema, and Mikhail B Sevryuk. *Quasi-periodic motions in families of dynamical systems: order amidst chaos.* Springer, 2009.

[23] John R Brophy, Louis Friedman, and Fred Culick. Asteroid retrieval feasibility. In *2012 IEEE Aerospace Conference*. IEEE, 2012.

[24] Pablo Calla, Dan Fries, and Chris Welch. Asteroid mining with small spacecraft and its economic feasibility. 2018.

[25] E Canalias, M Gidea, and JJ Masdemont. Numerical evidence for obstructions against integrability in a planar circular restricted three body problem.

[26] Julyan HE Cartwright and Oreste Piro. The dynamics of Runge–Kutta methods. *International Journal of Bifurcation and Chaos*, 1992.

[27] KH Chang. Chapter 5 - Multiobjective optimization and advanced topics, design theory and methods using CAD/CAE. 2015.

[28] Clark R Chapman. The hazard of near-Earth asteroid impacts on Earth. *Earth and Planetary Science Letters*, 2004.

[29] Alain Chenciner. Poincaré and the three-body problem. In *Henri Poincaré, 1912–2012*. Springer, 2015.

[30] Andrew F Cheng, Andrew S Rivkin, Patrick Michel, Justin Atchison, Olivier Barnouin, Lance Benner, Nancy L Chabot, Carolyn Ernst, Eugene G Fahnestock, Michael Kueppers, et al. AIDA DART asteroid deflection test: Planetary defense and science objectives. *Planetary and Space Science*, 2018.

[31] Steven R Chesley, Paul W Chodas, Andrea Milani, Giovanni B Valsecchi, and Donald K Yeomans. Quantifying the risk posed by potential Earth impacts. *Icarus*, 2002.

[32] PW Chodas and SR Chesley. 2000 SG344: the story of a potential Earth impactor. In *AAS/Division of Dynamical Astronomy Meeting*, 2001.

[33] Charles C Conley. On the ultimate behavior of orbits with respect to an unstable critical point i. oscillating, asymptotic, and capture orbits. *Journal of Differential Equations*, 1969.

[34] Samuel Daniel Conte and Carl De Boor. *Elementary numerical analysis: an algorithmic approach*. SIAM, 2017.

[35] John Danby. Fundamentals of celestial mechanics. *Richmond: Willman-Bell*, 1992.

[36] George Darwin. On certain families of periodic orbits. *Monthly Notices of the Royal Astronomical Society*, 1909.

[37] George Howard Darwin. Periodic orbits. *Acta mathematica*, 1897.

[38] Kathryn E Davis, Rodney L Anderson, Daniel J Scheeres, and George H Born. Optimal transfers between unstable periodic orbits using invariant manifolds. *Celestial Mechanics and Dynamical Astronomy*, 2011.

[39] CMA Deccia. Analysis of the sun-Earth lagrangian environment for the new worlds observer (nwo). 2017.

[40] Nicolas Delsate and Audrey Compere. Nimastep: a software to modelize, study, and analyze the dynamics of various small objects orbiting specific bodies. *Astronomy & Astrophysics*, 2012.

[41] E.J Doedel D.J. Dsichmann and R.C. Paffenroth. *The computation of periodic solutions of the 3-body problem using the numerical continuation software AUTO.*

[42] Eusebius Doedel, Herbert B Keller, and Jean Pierre Kernevez. Numerical analysis and control of bifurcation problems (i): bifurcation in finite dimensions. *International journal of bifurcation and chaos*, 1991.

[43] Eusebius J Doedel. Auto: A program for the automatic bifurcation analysis of autonomous systems. *Congr. Numer*, 1981.

[44] Eusebius J Doedel, Volodymyr A Romanov, Randy C Paffenroth, Herbert B Keller, Donald J Dichmann, Jorge Galán-Vioque, and André Vanderbauwhede. Elemental periodic orbits associated with the libration points in the circular restricted 3-body problem. *International Journal of Bifurcation and Chaos*, 2007.

[45] Robert W Easton. Introduction to hamiltonian dynamical systems and the n-body problem. *SIAM Review*, 1993.

[46] Ken Erickson. Optimal architecture for an asteroid mining mission: equipment details and integration. In *Space 2006*. 2006.

[47] Stavros C Farantos. Pomult: A program for computing periodic orbits in hamiltonian systems based on multiple shooting algorithms. *Computer physics communications*, 1998.

[48] Robert W Farquhar and Ahmed A Kamel. Quasi-periodic orbits about the translunar libration point. *Celestial mechanics*, 1973.

[49] Robert W Farquhar, David W Dunham, Yanping Guo, and James V McAdams. Utilization of libration points for human exploration in the Sun-Earth-Moon system and beyond. *Acta Astronautica*, 2004.

[50] RW Farquhar. The control and use of libration-point satellites, Ph. D. Dissertation, Dept. of aeronautics and astronautics, Stanford University. Stanford, ca. 1968.

[51] Grigori Fedorets, Marco Micheli, Robert Jedicke, S Naidu, Davide Farnocchia, Mikael Granvik, Nicholas Moskovitz, M Schwamb, Robert Weryk, Kacper Wierzchos, et al. Characterization of 2020 CD3, Earth's second minimoon. In *AAS/Division for Planetary Sciences Meeting Abstracts*, 2020.

[52] Joseph E. Flaherty. Lecture notes in ordinary differential equations, Lecture 9 - collocation methods. Spring 1999.

[53] Yang Gao. Near-Earth asteroid flyby trajectories from the Sun-Earth L2 for Chang'e-2's extended flight. *Acta Mechanica Sinica*, 2013.

[54] Evan S Gawlik, Jerrold E Marsden, Stefano Campagnola, and Ashley Moore. Invariant manifolds, discrete mechanics, and trajectory design for a mission to Titan. 2009.

[55] Gerard Gómez and Josep M Mondelo. The dynamics around the collinear equilibrium points of the RTBP. *Physica D: Nonlinear Phenomena*, 2001.

[56] Gerard Gómez, Josep-Maria Mondelo, and Carles Simó. A collocation method for the numerical Fourier analysis of quasi-periodic functions. I: Numerical tests and examples. *Discrete & Continuous Dynamical Systems-B*, 2010.

[57] Mikael Granvik, Jeremie Vaubaillon, and Robert Jedicke. The population of natural Earth satellites. *Icarus*, 2012.

[58] Daniel Grebow. Generating periodic orbits in the circular restricted three-body problem with applications to lunar south pole coverage. *MSAA Thesis, School of Aeronautics and Astronautics, Purdue University*, 2006.

[59] John Guckenheimer and Philip Holmes. *Nonlinear oscillations, dynamical systems, and bifurcations of vector fields.* Springer Science & Business Media, 2013.

[60] Ernst Haier, Christian Lubich, and Gerhard Wanner. *Geometric Numerical integration: structure-preserving algorithms for ordinary differential equations.* Springer, 2006.

[61] Alan W Harris. Near-Earth asteroid surveys. In *Collisional Processes in the Solar System.* Springer.

[62] AW Harris. The hg asteroid magnitude system: Mean slope parameters. In *Lunar and Planetary Science Conference*, 1989.

[63] Zaki Hasnain, Christopher A Lamb, and Shane D Ross. Capturing near-Earth asteroids around Earth. *Acta Astronautica*, 2012.

[64] Vide Hellgren. Asteroid mining: a review of methods and aspects. *Student thesis series INES*, 2016.

[65] Michael E Henderson. Multiple parameter continuation: Computing implicitly defined k-manifolds. *International Journal of Bifurcation and Chaos*, 2002.

[66] Kathleen Connor Howell. Three-dimensional, periodic, 'halo'orbits. *Celestial mechanics*, 1984.

[67] Kathleen Connor Howell and ET Campbell. Three-dimensional periodic solutions that bifurcate from halo families in the circular restricted three-body problem. *Advances in the astronautical sciences*, 1999.

[68] Arieh Iserles. *A first course in the numerical analysis of differential equations.* Cambridge University Press, 2009.

[69] Dario Izzo, Marek Ruciński, and Francesco Biscani. The generalized island model. In *Parallel Architectures and Bioinspired Algorithms.* Springer, 2012.

[70] Yu Jiang, Hexi Baoyin, Junfeng Li, and Hengnian Li. Orbits and manifolds near the equilibrium points around a rotating asteroid. *Astrophysics and Space Science*, 2014.

[71] Angel Jorba. Numerical computation of the normal behaviour of invariant curves of n-dimensional maps. *Nonlinearity*, 2001.

[72] Angel Jorba. *The Lagrangian Solutions.* 2015.

[73] Angel Jorba and Josep Masdemont. Dynamics in the center manifold of the collinear points of the restricted three body problem. *Physica D: Nonlinear Phenomena*, 1999.

[74] Jun'ichiro Kawaguchi, Akira Fujiwara, and Tono Uesugi. Hayabusa—its technology and science accomplishment summary and Hayabusa-2. *Acta Astronautica*, 2008.

[75] Egemen Kolemen, N Jeremy Kasdin, and Pini Gurfil. Multiple poincaré sections method for finding the quasiperiodic orbits of the restricted three body problem. *Celestial Mechanics and Dynamical Astronomy*, 2012.

[76] Wang Sang Koon, Martin W Lo, Jerrold E Marsden, and Shane D Ross. Dynamical systems, the three-body problem and space mission design. World Scientific, 2000.

[77] Wang Sang Koon, Martin W Lo, Jerrold E Marsden, and Shane D Ross. Heteroclinic connections between periodic orbits and resonance transitions in celestial mechanics. *Chaos: An Interdisciplinary Journal of Nonlinear Science*, 2000.

[78] Bernd Krauskopf, Hinke M Osinga, and Jorge Galán-Vioque. *Numerical continuation methods for dynamical systems*. Springer, 2007.

[79] Tomasz Kwiatkowski, Agnieszka Kryszczyńska, Magdalena Polińska, DAH Buckley, D O'Donoghue, PA Charles, L Crause, S Crawford, Y Hashimoto, A Kniazev, et al. Photometry of 2006 RH120: an asteroid temporary captured into a geocentric orbit. *Astronomy & Astrophysics*, 2009.

[80] Kieran G Larkin, Michael A Oldfield, and Hanno Klemm. Fast Fourier method for the accurate rotation of sampled images. *Optics communications*, 1997.

[81] Chris Lewicki, Peter Diamandis, Eric Anderson, Chris Voorhees, and Frank Mycroft. Planetary resources—the asteroid mining company. *New Space*, 2013.

[82] Martin Lo and Jeffrey Parker. Unstable resonant orbits near-Earth and their applications in planetary missions. In *AIAA/AAS Astrodynamics Specialist Conference and Exhibit*, 2004.

[83] Martin W Lo, Bobby G Williams, Williard E Bollman, Dongsuk Han, Yungsun Hahn, Julia L Bell, Edward A Hirst, Robert A Corwin, Philip E Hong, Kathleen C Howell, et al. Genesis mission design. *The Journal of the Astronautical Sciences*, 2001.

[84] Brian Luzum, Nicole Capitaine, Agnès Fienga, William Folkner, Toshio Fukushima, James Hilton, Catherine Hohenkerk, George Krasinsky, Gérard Petit, Elena Pitjeva, et al. The IAU 2009 system of astronomical constants: the report of the IAU working group on numerical standards for fundamental astronomy. *Celestial Mechanics and Dynamical Astronomy*, 2011.

[85] NJ Mallon. Collocation: a method for computing periodic solutions of ordinary differential equations. 2002.

[86] R Timothy Marler and Jasbir S Arora. Survey of multi-objective optimization methods for engineering. *Structural and multidisciplinary optimization*, 2004.

[87] JJ Masdemont. High-order expansions of invariant manifolds of libration point orbits with applications to mission design. *Dynamical Systems*, 2005.

[88] Brian P McCarthy. *Characterization of quasi-periodic orbits for applications in the Sun-Earth and Earth-moon systems.* PhD thesis, Purdue University Graduate School, 2019.

[89] A Milani, M Carpino, G Hahn, and AM Nobili. Dynamics of planet-crossing asteroids: Classes of orbital behavior: Project spaceguard. *Icarus*, 1989.

[90] Giorgio Mingotti, JP Sánchez, and CR McInnes. Combined low-thrust propulsion and invariant manifold trajectories to capture NEOs in the Sun-Earth circular restricted three-body problem. *Celestial mechanics and dynamical astronomy*, 2014.

[91] José Manuel Montilla García. Auto-based numerical study of three body problem orbits and trajectories with applications to the lunar deep space gateway. 2018.

[92] Andres Moreno Gonzalez. Characterisation of shape-based methods and combination with coasting arcs. 2020.

[93] Forest Ray Moulton, Daniel Buchanan, Thomas Buck, Frank Loxley Griffin, William Raymond Longley, and William Duncan MacMillan. Periodic orbits. *Washington*, 1920.

[94] ZE Musielak and Billy Quarles. The three-body problem. *Reports on Progress in Physics*, 2014.

[95] NASA. Near shoemaker, 2021. URL `https://nssdc.gsfc.nasa.gov/nmc/spacecraft/display.action?id=1996-008A`.

[96] Zubin P Olikara and Daniel J Scheeres. Numerical method for computing quasi-periodic orbits and their stability in the restricted three-body problem. *Advances in the Astronautical Sciences*, 2012.

[97] Zubin Philip Olikara. Computation of quasi-periodic tori and heteroclinic connections in astrodynamics using collocation techniques. *Ph. D. Thesis*, 2016.

[98] Lawrence Perko. *Differential equations and dynamical systems*. Springer Science & Business Media, 2013.

[99] Henri Poincaré. *Les méthodes nouvelles de la mécanique céleste*. Gauthier-Villars, 1899.

[100] Werner C Rheinboldt. *Numerical analysis of parametrized nonlinear equations*. Wiley-Interscience, 1986.

[101] David L Richardson. Analytic construction of periodic orbits about the collinear points. *Celestial mechanics*, 1980.

[102] Shane D Ross. Near-Earth asteroid mining. *Space*, 2001.

[103] RD Russell and Lawerence F Shampine. A collocation method for boundary value problems. *Numerische Mathematik*, 1972.

[104] Joan-Pau Sanchez and Colin McInnes. Asteroid resource map for near-Earth space. *Journal of Spacecraft and Rockets*, 2011.

[105] Joan Pau Sanchez and Daniel Garcia Yárnoz. Asteroid retrieval missions enabled by invariant manifold dynamics. *Acta Astronautica*, 2016.

[106] Joan-Pau Sanchez Cuartielles and Colin McInnes. On the ballistic capture of asteroids for resource utilisation. In *62nd International Astronautical Congress 2011*, 2011.

[107] Joan-Pau Sanchez Cuartielles, Daniel Garcia Yarnoz, Elisa Maria Alessi, and Colin McInnes. Gravitational capture opportunites for asteroid retrieval missions. In *63rd International Astronautical Congress*, 2012.

[108] DJ Scheeres, Z Olikara, N Baresi, et al. Dynamics in the Phobos environment. *Advances in Space Research*, 2019.

[109] Frank Schilder, Hinke M Osinga, and Werner Vogt. Continuation of quasi-periodic invariant tori. *SIAM Journal on Applied Dynamical Systems*, 2005.

[110] Carl L Siegel and Jürgen K Moser. Lectures on celestial mechanics: Reprint of the 1971 edition. 2012.

[111] Priscilla A Sousa Silva and Maisa O Terra. Diversity and validity of stable-unstable transitions in the algorithmic weak stability boundary. *Celestial Mechanics and Dynamical Astronomy*, 2012.

[112] Mark Joseph Sonter. The technical and economic feasibility of mining the near-Earth asteroids. *Acta Astronautica*, 1997.

[113] spacereference.org. 2006 rh120, very small apollo-class asteroid, 2021. URL `https://www.spacereference.org/asteroid/2006-rh120`.

[114] Elis Strömgren. Forms of periodic motion in the restricted problem and in the general problem of three bodies, according to researches executed at the observatory copenhagen. *Publikationer og mindre Meddeler fra Kobenhavns Observatorium*, 1922.

[115] V Szebehely. Theory of orbits: the restricted three body problem. 1967.

[116] Minghu Tan, Colin McInnes, and Matteo Ceriotti. Direct and indirect capture of near-Earth asteroids in the Earth–moon system. *Celestial Mechanics and Dynamical Astronomy*, 2017.

[117] Kim Taylor. Where can we find asteroids and comets?, 2019. URL `https://letstalkscience.ca/educational-resources/backgrounders/where-can-we-find-asteroids-and-comets`.

[118] Hodei Urrutxua, D Scheeres, Claudio Bombardelli, Juan L Gonzalo, and Jesús Peláez. What does it take to capture an asteroid? a case study on capturing asteroid 2006 RH120. In *24th AAS/AIAA Space Flight Mechanics Meeting, Santa Fe, New Mexico*, 2014.

[119] L van der Heyden. Exploring the kuiper belt: Design of trajectories for long-term Kuiper belt exploration. 2020.

[120] Massimiliano Vasile and Marco Locatelli. A hybrid multiagent approach for global trajectory optimization. *Journal of Global Optimization*, 2009.

[121] Ferdinand Verhulst. *Nonlinear differential equations and dynamical systems*. Springer Science & Business Media, 2006.

[122] ACJ Vermeulen, Farshad Goldoust, M Sirenko, Daniela Hallak, Brennan Lutkewitte, Lenka Husárová, Kelvin F Long, and FM Brazier. Simulating the construction of conceptual space architecture to explore the potential of combined asteroid mining and space-based 3d manufacturing. In *Proceedings of the International Astronautical Congress, IAC*, 2019.

[123] Angelo Vermeulen. E| A| S (Evolving Asteroid Starships): TEC ART 2018. In *TEC ART 2018*, 2018.

[124] Richard Wainscoat. The Pan-STARRS search for near Earth objects. In *2016 IEEE Aerospace Conference*. IEEE.

[125] Karel F Wakker. Fundamentals of astrodynamics. 2015.

[126] Daniel Wilczak and Piotr Zgliczynski. Heteroclinic connections between periodic orbits in planar restricted circular three-body problem–a computer assisted proof. *Communications in mathematical physics*, 2003.

[127] Edward L Wright, Amy Mainzer, Joseph Masiero, Tommy Grav, and James Bauer. The albedo distribution of near Earth asteroids. *The Astronomical Journal*, 2016.

[128] D García Yárnoz, Joan-Pau Sánchez, and Colin R McInnes. Easily retrievable objects among the NEO population. *Celestial Mechanics and Dynamical Astronomy*, 2013.

[129] Lewei Zhao. Spectral methods for hamiltonian systems and their applications. 2019.

[130] AK Zimmer. Investigation of vehicle reusability for human exploration of near-Earth asteroids using Sun-Earth libration point orbits. *Acta Astronautica*, 2013.